



Publicly Accessible Penn Dissertations


2017

Shedding Light On General Anesthesia: Uncovering The Molecular Mechanisms For Propofol And Volatile Anesthetics

Kellie Ann Woll

University of Pennsylvania, kwooll@mail.med.upenn.edu

Follow this and additional works at: <https://repository.upenn.edu/edissertations>

 Part of the [Molecular Biology Commons](#), [Neuroscience and Neurobiology Commons](#), and the [Pharmacology Commons](#)

Recommended Citation

Woll, Kellie Ann, "Shedding Light On General Anesthesia: Uncovering The Molecular Mechanisms For Propofol And Volatile Anesthetics" (2017). *Publicly Accessible Penn Dissertations*. 2641.
<https://repository.upenn.edu/edissertations/2641>

This paper is posted at ScholarlyCommons. <https://repository.upenn.edu/edissertations/2641>
For more information, please contact repository@pobox.upenn.edu.

Shedding Light On General Anesthesia: Uncovering The Molecular Mechanisms For Propofol And Volatile Anesthetics

Abstract

General anesthetics have played a pivotal role in the history of medicine. Despite accounts of their use within the earliest of human records, our understanding of anesthetic mechanisms remains unclear. Understanding these molecular mechanisms would be a significant advance toward enhanced drug design and optimal the clinical use of these potentially hazardous agents. Recent advances in chemical and molecular biology, including photoaffinity labeling, have allowed enhanced appreciation of the complex interactions anesthetic's have with their macromolecular substrates. This work is dedicated to further define the protein interactions of the frequently administered volatile anesthetics sevoflurane and isoflurane, as well as the most commonly used intravenous anesthetic, propofol. A novel photoaffinity ligand for sevoflurane was validated and applied to uncover the unique mechanism of sevoflurane positive modulation of mammalian Shaker Kv1.2 channels. This novel sevoflurane photoaffinity ligand was in addition to a previously developed photoaffinity ligand for isoflurane, further applied to determine the anesthetic binding sites within a vital protein target, synaptic GABAA receptors. The molecular recognition elements for propofol-protein interactions were probed using a novel hydrogen-bond null derivative. It was determined that the propofol 1-hydroxyl is key for molecular interactions that contribute to anesthetic endpoints, such as synaptic GABAA receptor positive modulation, while less significant for other known biological effects like decreasing muscle contractility. The range of propofol-binding proteins within synaptosomes was further defined with the synthesis of a novel photoaffinity tandem click chemistry-active ligand and the development of a quantitative affinity-based protein profiling workflow. Results of the investigation indicated a highly complex pool of propofol-specific proteins including an unbiased, selective binding of specific synaptic GABAA receptor subunits. The likely propofol binding cavities and the underlining molecular recognition features that contribute to the selective GABAA receptor subunit binding were examined using molecular dynamics simulations and photoaffinity protection studies. Together these series of studies suggest that general anesthetics bind a to range of molecular substrates that cumulatively result in general anesthesia phenotypes and that multiple, functionally distinct, binding sites can be present within a single protein target.

Degree Type

Dissertation

Degree Name

Doctor of Philosophy (PhD)

Graduate Group

Pharmacology

First Advisor

Max B. Kelz

Keywords

Chemical Biology, General Anesthetics, Isoflurane, Photoaffinity Labeling, Propofol

Subject Categories

Molecular Biology | Neuroscience and Neurobiology | Pharmacology

SHEDDING LIGHT ON GENERAL ANESTHESIA:
UNCOVERING THE MOLECULAR MECHANISMS OF PROPOFOL AND
VOLATILE ANESTHETICS

Kellie Ann Woll

A DISSERTATION

in

Pharmacology

Presented to the Faculties of the University of Pennsylvania

in

Partial Fulfillment of the Requirements for the

Degree of Doctor of Philosophy

2017

Supervisor of Dissertation:

Roderic G. Eckenhoff, MD, Austin Lamont Professor of Anesthesiology & Critical Care

Graduate Group Chairperson:

Julie A. Blendy, PhD, Professor of Pharmacology

Dissertation Committee:

Max B. Kelz, MD PhD, David E. Longnecker Associate Professor of Anesthesiology and Critical Care

Ivan J. Dmochowski, PhD, Professor of Chemistry

Benjamin A. Garcia, PhD, Presidential Professor of Biochemistry and Biophysics

Vladimir R. Muzykantov, MD PhD, Professor of Pharmacology

SHEDDING LIGHT ON GENERAL ANESTHESIA: UNCOVERING THE
MOLECULAR MECHANISMS OF PROPOFOL AND VOLATILE ANESTHETICS

COPYRIGHT

2017

Kellie Ann Woll

ACKNOWLEDGEMENTS

I have been fortunate enough to have encountered and continue to be surrounded by the most amazing people, and they are largely responsible for allowing me to reach this stage in my life and career. At the forefront I must thank Rod and Maryellen Eckenhoff for their support and guidance. Under their mentorship I have not only developed as a scientist, but also as a person. I will forever be grateful for the astounding opportunities that they have provided me and will continue look up to them for the rest of my life.

The UPenn Anesthesiology Department as a whole has been a strong force in pushing me forward. In all honestly the ‘JMB3 Attic’ ended up as home-away-from-home for the past four years, and the individuals that work here became like family. Thank you all for your mentorship and friendship; I will always be in-debt to you.

I would also like to thank the previous mentors and peers that significantly changed the course of my life, and ultimately lead me into science research. These include my undergraduate mentor Debbie Crans as well as my steadfast friend Robin Ward. I can’t tell you how much you have impacted my life and I thank you so much for helping me find my passion.

Finally, and most importantly, I would like to thank those who have supported me throughout my life. I have put my family through quite a bit; despite this they have always stood behind me and encouraged me to reach for my dreams. I struggle to put into words how much your support and love has helped me find my way in the most trying times of my life. I hope to make you at least half as proud as I am of all of you.

Thank you.

- ‘Persist & persevere’-

ABSTRACT

SHEDDING LIGHT ON GENERAL ANESTHESIA: UNCOVERING THE MOLECULAR MECHANISMS OF PROPOFOL AND VOLATILE ANESTHETICS

Kellie A. Woll

Roderic G. Eckenhoff

General anesthetics have played a pivotal role in the history of medicine. Despite accounts of their use within the earliest of human records, our understanding of anesthetic mechanisms remains unclear. Understanding these molecular mechanisms would be a significant advance toward enhanced drug design and optimal the clinical use of these potentially hazardous agents. Recent advances in chemical and molecular biology, including photoaffinity labeling, have allowed enhanced appreciation of the complex interactions anesthetic's have with their macromolecular substrates. This work is dedicated to further define the protein interactions of the frequently administered volatile anesthetics sevoflurane and isoflurane, as well as the most commonly used intravenous anesthetic, propofol. A novel photoaffinity ligand for sevoflurane was validated and applied to uncover the unique mechanism of sevoflurane positive modulation of mammalian *Shaker* Kv1.2 channels. This novel sevoflurane photoaffinity ligand was in addition to a previously developed photoaffinity ligand for isoflurane, further applied to determine the anesthetic binding sites within a vital protein target, synaptic GABA_A receptors. The molecular recognition elements for propofol-protein interactions were probed using a novel hydrogen-bond null derivative. It was determined that the propofol 1-hydroxyl is key for molecular interactions that contribute to anesthetic endpoints, such as synaptic GABA_A receptor positive modulation, while less significant for other known

biological effects like decreasing muscle contractility. The range of propofol-binding proteins within synaptosomes was further defined with the synthesis of a novel photoaffinity tandem click chemistry-active ligand and the development of a quantitative affinity-based protein profiling workflow. Results of the investigation indicated a highly complex pool of propofol-specific proteins including an unbiased, selective binding of specific synaptic GABA_A receptor subunits. The likely propofol binding cavities and the underlining molecular recognition features that contribute to the selective GABA_A receptor subunit binding were examined using molecular dynamics simulations and photoaffinity protection studies. Together these series of studies suggest that general anesthetics bind a to range of molecular substrates that cumulatively result in general anesthesia phenotypes and that multiple, functionally distinct, binding sites can be present within a single protein target.

TABLE OF CONTENTS

ACKNOWLEDGEMENTS.....	iii
ABSTRACT.....	iv
LIST OF TABLES.....	x
LIST OF ILLUSTRATIONS.....	xi
CHAPTER 1: INTRODUCTION TO GENERAL ANESTHESIA & PHOTOAFFINITY LABELING.....	1
<i>1.1 Brief Historical Sketch.....</i>	2
1.1.1. An Ancient Realm.....	2
1.1.2 The Chemical Era and Empirical Domination.....	3
1.1.3 What's the Point of a Molecular Hunt?.....	6
1.1.4 Conclusions.....	8
<i>1.2. Photoaffinity labeling: Shining-light on hidden anesthetic binding sites.....</i>	8
1.2.1. Anesthetic-Photoaffinity Ligand Development: Making an 'A-PAL'	8
1.2.2. Micro-level investigations	18
1.2.3. Macro-level investigations	25
1.2.4. Conclusions	28
CHAPTER 2: SEVOFLURANE AND ISOFLURANE INHALATIONAL ANESTHETIC MECHANISMS	28
<i>2.1. Novel Photoaffinity ligand for sevoflurane reveals sites of voltage-gated ion channel modulation</i>	29
2.1.1. Synthesis and characterization of azisevoflurane(1a)	31
2.1.2. Photoaffinity labeling of purified Kv1.2 channel	36

2.1.3. Validation of sevoflurane Kv1.2 channel binding site by electrophysiology	39
2.1.4. Conclusions.....	42
2.1.5. Experimental Methods	42
2.2. Mechanistic basis for synaptic GABA_A receptor modulation by volatile general anesthetics	52
2.2.1. <i>a</i> -PAL competition for $\alpha_1\beta_3\gamma_{2L}$ GABA _A receptor photomodification	55
2.2.2. Volatile <i>a</i> -PAL photoaffinity labeling of purified $\alpha_1\beta_3$ GABA _A receptors	59
2.2.3. Volatile anesthetic binding in $\alpha_1\beta_3\gamma_{2L}$ GABA _A receptor models	62
2.2.4. Conclusions	72
2.2.5. Experimental Methods	73
CHAPTER 3: MOLECULAR MECHANISMS OF PROPOFOL AND ALKYLPHENOL-BASED ANESTHETICS	79
3.1. Role for the propofol hydroxyl in anesthetic protein target molecular recognition.80	
3.1.1. Synthesis and characterization of propofol(1b)	82
3.1.2. Propofol(1b) pharmacological and functional activity	86
3.1.3. Conclusions	92
3.1.4. Experimental Methods	93
3.2. Novel bifunctional alkylphenol anesthetic allows identification of the alkylphenol binding synaptic proteome	101
3.2.1. Synthesis and characterization of <i>AziPm-click</i> (1c)	102
3.2.2. Affinity-based protein profiling (ABPP) of alkylphenol synaptic protein targets.	106
3.2.3. Conclusions	109
3.2.4. Experimental Methods	110

3.3. Characterization of alkylphenol anesthetic selective GABA_A receptor subunit binding in synaptosomes	115
3.3.1. $\alpha_1\beta_2\gamma_{2L}$ GABA _A receptor modulation by AziPm-click(1c)	117
3.3.2. Alkylphenol anesthetic selective GABA _A receptor subunit binding	117
3.3.3. Conclusions	123
3.3.4. Experimental Methods	124
CHAPTER 4: CONCLUSIONS	129
APPENDIX	
A.1. Equations	134
A.2. Detailed synthetic methods	135
A.2.1. 3-(Difluoro((1,1,1,3,3,3-hexafluoropropan-2-yl)oxy)methyl)-3H-diazirine; Azisevoflurane (1a)	135
A.2.2. 2-fluoro-1,3-diisopropylbenzene; Fropropofol (1b)	137
A. 2.3. 2-((prop-2-yn-1-yloxy)methyl)-5-(3-(trifluoromethyl)-3H-diazirin-3-yl)phenol; AziPm-click (1c)	137
A.3. Mass spectrometry protein coverage	141
A.3.1. αF coverage photoaffinity labeled by azisevoflurane(1a)	141
A.3.2. Kv1.2 coverage photoaffinity labeled by azisevoflurane(1a)	141
A.3.3. $\alpha_1\beta_3\gamma_{2L}$ GABA _A receptor coverage photoaffinity labeled by azisevoflurane(1a).141	
A.3.4. $\alpha_1\beta_3\gamma_{2L}$ GABA _A receptor coverage photoaffinity labeled by aziisoflurane	142
A.3.5. $\alpha_1\beta_3$ GABA _A receptor coverage photoaffinity labeled by azisevoflurane(1a)	143
A.3.6. $\alpha_1\beta_3$ GABA _A receptor coverage photoaffinity labeled by aziisoflurane	144
A.4. Mass spectra	146

A.4.1. Apo-ferritin (<i>aF</i>) peptides photoaffinity labeled by azisevoflurane(1a)	146
A.4.2. Kv1.2 peptide photoaffinity labeled by azisevoflurane(1a)	148
A.4.3. $\alpha_1\beta_3\gamma_{2L}$ GABA _A receptor peptides photoaffinity labeled by azisevoflurane(1a) .	148
A.4.4. $\alpha_1\beta_3\gamma_{2L}$ GABA _A receptor peptides photoaffinity labeled by aziisoflurane	154
A.4.5. $\alpha_1\beta_3$ GABA _A receptor peptides photoaffinity labeled by azisevoflurane(1a)	159
A.4.6. $\alpha_1\beta_3$ GABA _A receptor peptides photoaffinity labeled by aziisoflurane	167
<i>A.5. Table of Propofol-specific proteome as determined by AziPm-click(1c) activity-based protein profiling</i>	175
BIBLIOGRAPHY	176

LIST OF TABLES

- Table 1. Summary of adducted residues by anesthetic photoaffinity ligands using amino acid sequencing methods (pg. 14)
- Table 2. Physicochemical properties of sevoflurane and azisevoflurane(**1a**) (pg. 32)
- Table 3. Apo-Ferritin (*aF*) sevoflurane and azisevoflurane (**1a**) binding parameters (pg. 34)
- Table 4. Tadpole studies with sevoflurane and azisevoflurane (**1a**) (pg. 36)
- Table 5. Physicochemical parameters and binding properties of propofol and fropofol(**1b**) (pg. 83)
- Table 6. Physicochemical properties of propofol and *AziPm-click*(**1c**) (pg. 103)
- Table 7. Equilibrium binding parameters of propofol and *AziPm-click*(**1c**) to *aF* (pg. 105)
- Table 8. Tadpole studies with propofol and *AziPm-click*(**1c**) (pg. 108)
- Table 9. Binding affinities of propofol bound to one of four GABA_A receptor interfacial sites (shown in Figure 31, interfaces notated counter-clockwise), calculated using Alchemical Free Energy Perturbation algorithm. (pg. 120)

LIST OF ILLUSTRATIONS

Figure 1. Chemical and spherical structures of general anesthetics and corresponding photoaffinity ligands (pg. 10)

Figure 2. Simplified schemes for the major methods used in micro-level anesthetic photoaffinity labeling (pg. 18)

Figure 3. Schematic representation of the steps involved in the most basic mechanism of parent anesthetic protection of anesthetic photoaffinity labeling experiments (pg. 23)

Figure 4. Chemical structures of sevoflurane and azisevoflurane(**1a**) (pg. 30)

Figure 5. Photoactivation of azisevoflurane (**1a**) (pg. 33)

Figure 6. Sevoflurane and azisevoflurane (**1a**) binding to *apoferritin* (*aF*) (pg. 34)

Figure 7. Sevoflurane and azisevoflurane (**1a**) pharmacological activity (pg.35)

Figure 8. Photoaffinity labeling of mammalian Shaker Kv1.2 channel by azisevoflurane (**1a**) (pg. 37)

Figure 9. Lowest energy azisevoflurane(**1a**) docking pose viewed towards the S4-S5 linker and S6 cavity (pg. 38)

Figure 10. Positive modulation of Kv1.2 conductance by sevoflurane and azisevoflurane (**1a**) is dampened by the Leu-317-Ala mutation (pg. 40)

Figure 11. The Leu-317-Ala mutation under basal conditions induces a parallel leftward shift in the *G-V* curve. (pg. 41)

Figure 12. Chemical structures of volatile anesthetics and corresponding anesthetic-photoaffinity ligands. (pg. 54)

Figure 13. Inhibition [³H]AziPm photoaffinity radiolabeling of FLAG- $\alpha_1\beta_3\gamma_{2L}$ -(L3)-1D4 GABA_A receptor by azisevoflurane(**1a**) and aziisoflurane (pg. 57)

Figure 14. Locations of the photomodified residues by azisevoflurane(**1a**) and aziisoflurane from FLAG- $\alpha_1\beta_3\gamma_{2L}$ -(L3)-1D4 or FLAG- $\alpha_1\beta_3$ GABA_A GABA_A receptor photoaffinity labeling studies. (pg. 62)

Figure 15. Sevoflurane and isoflurane docking poses in the $\alpha_1\beta_3\gamma_{2L}$ GABA_A receptor at the α^+/γ^- TMD interface with photoaffinity labeled residues (pg. 64)

Figure 16. Sevoflurane and isoflurane docking poses in the $\alpha_1\beta_3\gamma_{2L}$ GABA_A receptor at the γ^+/β^- TMD interface with photoaffinity labeled residues. (pg. 65)

Figure 17. Sevoflurane and isoflurane docking poses in the $\alpha_1\beta_3\gamma_{2L}$ GABA_A receptor at the β^+/α^- TMD interface with photoaffinity labeled residues. (pg. 67)

Figure 18. Sevoflurane and isoflurane docking poses in the $\alpha_1\beta_3\gamma_{2L}$ GABA_A receptor at the α^+/β^- TMD interface with photoaffinity labeled residues. (pg. 69)

Figure 19. Chemical structures of propofol and fropofol(**1b**) (pg. 81)

Figure 20. Propofol and fropofol(**1b**) horse spleen apo-ferritin (*aF*) binding (pg. 84)

Figure 21. Propofol and fropofol(**1b**) human serum albumin (hSA) binding. (pg. 85)

Figure 22. Propofol and fropofol(**1b**) *in vivo* activity (pg. 87)

Figure 23. Propofol and fropofol(**1b**) GABA_A receptor activity (pg. 89)

Figure 24. Influence of propofol and fropofol(**1b**) on trabecular muscle force generation (pg. 91)

Figure 25. Chemical structures of propofol and AziPm-*click*(**1c**) (pg. 102)

Figure 26. AziPm-*click* (**1c**) geometry and photoreactivity. (pg. 105)

Figure 27. Anesthetic activity of AziPm-*click*(**1c**) (pg. 105)

Figure 28. Fluorescent profiling of propofol proteome (pg. 106)

Figure 29. Affinity-based propofol profiling of alkylphenol binding proteins in native

synaptosomes (pg. 108)

Figure 30. *AziPm-click(1c)* $\alpha_1\beta_2\gamma_{2L}$ GABA_A receptor activity (pg. 117)

Figure 31. Selectivity of intersubunit propofol binding in an $\alpha_1\beta_3\gamma_2$ GABA_A receptor as predicted by molecular dynamics simulations using the Alchemical Free Energy Perturbation algorithm (pg. 118)

Figure 32. Intersubunit propofol and *AziPm-click(1c)* occupancy in an $\alpha_1\beta_3\gamma_2$ GABA_A receptor as predicted by AutoDock Vina simulations (pg. 119)

Figure 33. Sequence variation in interfacial binding sites of an $\alpha_1\beta_3\gamma_2$ GABA_A receptor heteropentamer. (pg. 121)

Figure 34. Ligand protection of synaptic GABA_A receptor capture (pg.122)

Figure 35. Schematic of the major conclusions presented in this work. (pg. 133)

CHAPTER 1: INTRODUCTION TO GENERAL ANESTHESIA RESEARCH AND PHOTOAFFINITY LABELING

General anesthesia is among the oldest medical practices exercised by man. Despite this continual underlining application throughout our history, general anesthetics still maintain a strong stance as a ‘black-box drug’; our lack of understanding of their actual mechanisms of action, pharmacological endpoints and side effects is overshadowed by their current common use. Starting with joint hypothesis by Overton and Meyer in 1899 and 1901, which relates anesthetic potency with solubility in olive oil^{1,2}, there has been a push to gain insight into how these drugs work in order to improve their design and/or administration. The movement to further our understanding has truly started to gain momentum within the last half-century resulting in the solidification of anesthesiology research as a field in medical science.

The objective of this work is to add to this field by contributing a series of investigations focused on defining the molecular mechanisms of two inhalational or volatile anesthetics, sevoflurane and isoflurane, and one intravenous anesthetic, propofol. Photoaffinity labeling, a technique first introduced in the 1970s³⁻⁵, has shown to be very useful in anesthesiology research. The first section of this chapter includes a concise summary on the historical background for general anesthetic development and discovery as well as short perspective. The second section examines all aspects of photoaffinity labeling within anesthesiology research, including the current methodologies and ligand design, characterization, and deployment. This section also includes points of consideration and highlights the future outlook as more photoaffinity ligands emerge within this field.

1.1. Brief Historical Sketch

Behind every drug class is a story of ‘discovery’ and the individuals that contributed to each drug’s development. This holds true for general anesthetics particularly with their extensive, and rather turbulent, history. It is significant to have a fair understanding of a drug class’s history to grasp the background behind the current and the potential future understanding of drug mechanisms. Furthermore, it provides an appreciation for the achievements of these agents, and the persons that ultimately brought about modern medical practices as we see it today.

1.1.1. An Ancient Realm

General anesthesia, with the multiple components therein (eg. hypnosis, amnesia and immobility) ⁶, allows for a patient to undergo normally painful medical procedures without recall. The induced immobility enables the acting medical professional to conduct a procedure with considerably less physical hindrance. Because of our natural avoidance of pain, anesthesia’s ancient history is no surprise. Translations of carotid in Greek (*karotida*) and Russian (*sonnaya areteriya*) are derived from ‘sleep’ or ‘stupor,’ suggesting that even our primitive ancestors may have applied compression to carotid arteries in order to physically produce a state similar to anesthesia.

The ancient civilizations, from Egyptians to the early Greeks and Romans as well as the ancient Arabians, Hindus, and Chinese, all show records for inducing the anesthesia state with use of Indian Hemp, poppy, and/or mandrogora, alone or within complicated preparations ^{7,8}. Pedanius Dioscorides, a pharmacologist, physician, and botanist of the Roman Empire describes a preparation within *De Materia Medica* (“On Medical Material”), the first pharmacopeia, using mandrogora and sweet wine. This preparation

that would cause a patient to be “thrown into a deep sleep, [where] they do not feel any pain.”⁹ Records of anesthesia during surgical practices also exist for the Middle Ages, including inhalational administration with ‘*spongia somnifera*’, or the ‘sleeping sponge’¹⁰. Theodoric, the son of a 15th century Tuscan Physician, described that when applied over the nose and mouth, the sleeping sponge was so effective that some patients would not awaken for several days unless a countering medicinal agent like vinegar was used^{7,10}.

While recorded, the frequency in the use of general anesthesia in early history would be considered scarce compared to modern day. This could be attributed to a variety of reasons such as the lack of widespread knowledge, as well as poor availability. It is likely, however, that the main cause for the lesser use stemmed from the unpredictability in potency of the plant-based preparations^{7,8}. Lord Nelson of the British Royal Navy provides an account of the variability when he requested that the surgeon had a pot of hot water ready so, if the anesthetic failed, at worst he would feel a warm knife during the amputation of his right arm during the French Revolutionary Wars¹¹. Because of the lack of knowledge and inconsistency, general anesthesia would have likely faded from medical practice. If it were not for the advances that occurred mostly in the 1800’s now dubbed the ‘Chemical Era of General Anesthetics’, general anesthesia as we now see it would not exist. During this era, modern anesthetics started to emerge and these drugs were pushed to the forefront to eventually become amongst the most important advances within medicine.

1.1.2. The Chemical Era of Empirical Domination

The increased understanding of gases and vapors within the later 1700's led to the isolation of nitrous oxide. The discovery of the of the gas's analgesic and anesthetic effects accredited to Humphry Davy ^{12,13}. Professor Thompson of Glasgow further demonstrated the anesthetic properties of nitrous oxide and sulpheric ether by administering the gases to volunteering students as a form of entertainment to his students (and himself) ⁷. However, application of these chemicals within practical medical purposes was not fully appreciated until almost half a century later.

Dentist Horace Wells is recognized as the leading advocate for the use of nitrous oxide as the earliest form of modern general anesthesia when he himself was treated while getting a tooth pulled by Dr. G.Q. Colton ⁷. However, foretelling future troubles with this class of drug, Dr. Wells was unable to successfully administer the agent during a formal medical demonstration. This unfortunate event resulted in the denouncement of nitrous oxide, the procedure, and Dr. Wells ¹⁴.

Years later the combined effort of Charles Jackson and W.T.G. Morton eventually accumulated to the first successful surgical operation demonstration with ether on Friday, October 16, 1846 at Massachusetts General Hospital ^{7,15}. The amphitheater was packed with medical professionals and the success of the procedure, which took no more than five minutes, propelled general anesthesia and anesthetics into the limelight. The event is forever immortalized in the Robert Hinckley oil painting "First Operation Under Ether" and with the amphitheater being renamed the 'Ether Dome'.

In the first few decades following ether's acceptance into medicine, hundreds of other anesthetic gases were considered and many were tried. These attempts were all by trial and error with risks being particularly high. Two gases emerged with the highest

potential; chloroform and the re-discovered nitrous oxide, however both were very expensive, difficult to administer, and displayed many unwanted side effects ¹⁶.

A third gas, cyclopropane, also showed promise as an anesthetic if not for the coinciding extremely high explosive property ^{17,18}. Nevertheless cyclopropane, while in no way safe to use during surgical cautery and/or the age of electric monitoring, did provide vital insight for future drug chemotypes. John C. Krantz Jr. of the University of Maryland added his knowledge of halogenation, which decreases flammability relative to the hydrocarbon, and opened the door to a new series of compounds as potential general anesthetics ¹⁹. With shotgun empirical approaches led by various chemists, halothane emerged and gained worldwide acclaim as the prime general anesthetic in the mid-to-late 1900s. Then, due to an associated side effect called ‘Halothane hepatitis’¹⁸, halothane decreased in favor allowing for fluorinated ethers to come forth as an optimal volatile anesthetic chemotype with isoflurane (1972), desflurane (1992) and sevoflurane (1994) being introduced into clinical use ^{16,20}.

Parallel with the development of volatile agents, alternative routes for administering general anesthetics were also being considered. The first intravenous anesthetic, chloral hydrate, was demonstrated in 1872, however the agent did not gain much popularity due to a relative mild anesthetic effect compared to the unwanted side effects ²¹. It was not until the concept of ‘balanced anesthesia’ proposed by Dr. John Lundy (i.e. administration of combinations of anesthetic agents at lower doses reduces undesired side effects), the discovery of sodium thiopental ²⁰, and a push for agents that could be more readily transported and applied on the battle field^{11,22} that intravenous anesthetics became more conventional. The development of intravenous anesthetics

gradually progressed, much like their volatile counterparts, with the laborious synthesis of huge chemical libraries and empirically based pharmacological screening. Eventually agents including ketamine (1964) and later etomidate (1975) were discovered and administered to induce anesthesia²³⁻²⁵ in combination with volatile agents to maintain anesthesia. It was not until propofol (1977)²⁶ that total intravenous anesthesia (or the “TIVA” method)²⁷ was applied. Intravenous anesthetics also, to varying degrees, resulted in specific unwanted side effects compared to volatile agents, namely cardiovascular depression²⁸.

From the use of the carotid artery to sevoflurane and propofol, the majority of the advances within general anesthetic development have been by serendipity and empiricism with no systematic evaluation of the actual molecular mechanism(s) or the state of general anesthesia. Indeed Professor James Simpson and his assistants would, after a long day of work, sit down and inhale vapors of their various compounds out of tumblers to eventually come across chloroform⁷. The professor in the neighboring office commented on his fears of what he may find when he came in the next morning⁷. Therefore it is not surprising that by this method various harmful drugs like phencyclidine (or PCP)²⁰ were exposed to wide populations or how acceptable drugs were dismissed, delayed, and/or stigmatized. Fortunately an alternative approach in anesthesiology research has arisen, with the science community focusing on furthering our understanding of what the anesthesia state entails and determining the underlining mechanisms.

1.1.3. What's the Point of a Molecular Hunt?

General anesthetics are used at least an estimated 200 million times per year in the United States alone²⁹. In total, undergoing general anesthesia is considered to be a

relatively safe experience when administered by the appropriate, highly trained medical professional, an anesthesiologist. As a result of this, in combination with the cost of drug development, there has been a lack of interest to invest in anesthesiology research, particularly in the pharmaceutical industry, adopting a natural viewpoint of, '*Why fix what's not broken?*'

It still remains that general anesthetics are among the most dangerous drugs currently used in medicine. Even the modern clinical agents still display very narrow therapeutic indices (LD₅₀/ED₅₀) such as 6-12 and 2-4 for propofol and sevoflurane respectively ^{30,31}. Much of the observed toxicity is from the overt acute side effects, notably respiratory and cardiovascular depression ²⁸. Ample opportunities for improving administration and/or drug design exist to reconcile these known adverse effects. Furthermore, increasing evidence suggests other, lesser-known side effects might be present, including those on neurodevelopment and neurodegeneration ³²⁻³⁴. While research on these effects is not conclusive, these and other acute or chronic impacts on health -particularly within sensitive populations- are a cause for concern and warrant further investigation.

An additional avenue to apply a further understanding of anesthetic mechanisms is within precision medicine, also known as personalized, predictive, preventive and participatory ('P4') medicine ³⁵. While treatment strategies that account for individual variability are by no means a new concept, P4 medicine is gaining in popularity particularly with a large push for drug repurposing and the development of more robust personalized treatment predictions. Drug repurposing has already shown promise with general anesthetic ketamine, which has displayed signs as a useful antidepressant ³⁶.

Finally, much within neurobiology remains a mystery, and given that general anesthetics are capable of inducing multiple interesting behaviors, likely through distinct pathways, these drugs can be applied to further probe the underlining molecular contributors.

1.1.4. Conclusions

General anesthetics are considered very old drugs with a presence reaching the earliest recorded history^{7,8}. It is interesting how, regardless of this, we know so little of anesthetic mechanisms of action. In a sense our practiced expertise in administration of these difficult and dangerous agents has stalled investigations. However, the increasing concerns, a need for better care, as well as healthy scientific curiosity kindled a fire to extend our understanding. In combination with technological advances, we have the potential to gain insight into the workings of the ‘black-box’ that is general anesthesia and to further our understanding of neurobiology.

1.2. Photoaffinity labeling: Shining-light on hidden binding sites

Studying the interactions between general anesthetics and their macromolecular targets is crucial to the understanding of the biochemistry for these drugs. In recent years the application of photoaffinity labeling for this purpose has gained popularity. Traditionally the objectives of this method are to allow researchers to identify the binding site(s) within established targets (micro-level) and, to a lesser extent, determine novel binding molecules and distribution within a given biological system (macro-level). Within anesthesia research there has been significant advancement in the development of PALs (photoaffinity ligands), from the initial use of neat halothane³⁷ to complex syntheses of bifunctional PALs allowing for affinity-based protein profiling (ABPP)^{38,39}.

1.2.1. Anesthetic-Photoaffinity Ligand Development: Making ‘a-PAL’

In the current process of photoaffinity labeling, the chemical structure of the drug of interest (parent ligand) is modified to incorporate a photoreactive group that, upon ultra-violet (UV) irradiation, generates a highly reactive chemical intermediate. This intermediate then chemically ‘modifies’ or ‘labels’, by covalent insertion to a bond in close proximity, such as solvent components or an occupied macromolecule. In the instance of a PAL bound to a macromolecule, the covalent insertion acts as a traceable modification that can be used to investigate ligand-target interactions and/or ligand distribution within the organ or tissue. A critical advantage that PALs provide for general anesthetics is that they mitigate the relative lower binding affinities, generally micromolar, associated with this particular class of drugs. They accomplish this by dramatically prolonging drug unbinding rates -to irreversibility-, thereby providing a snapshot of these otherwise transient interaction(s). On the other hand, the inherent high dissociation constants of anesthetics remains an experimental hurdle chiefly by adding to the difficulty in validation of specific binding sites in photoaffinity labeling studies.

Several factors are considered during the design of an anesthetic PAL or *a*-PAL; most notably that introduction of the photoreactive group into the anesthetic chemical structure does not significantly alter the biochemical and pharmacological properties of the parent drug. Diazirines are nearly universal as the photoreactive group incorporated within *a*-PALs (Figure 1). With UV irradiation, diazirines undergo photoactivation, resulting in the release of an inert dinitrogen molecule and the generation of carbene chemical species that indiscriminately inserts into the nearest molecule. The popularity

of this particular photoreactive group can be largely attributed to the less damaging UV wavelength needed for photoactivation, its relative stability and smaller size, and highly reactive intermediate product, the carbene. In combination, these attributes allow for lesser deviation of binding properties compared to the parent anesthetic. Past reviews further discuss the development and use of PALs and photoreactive groups^{5,40–42} in detail.

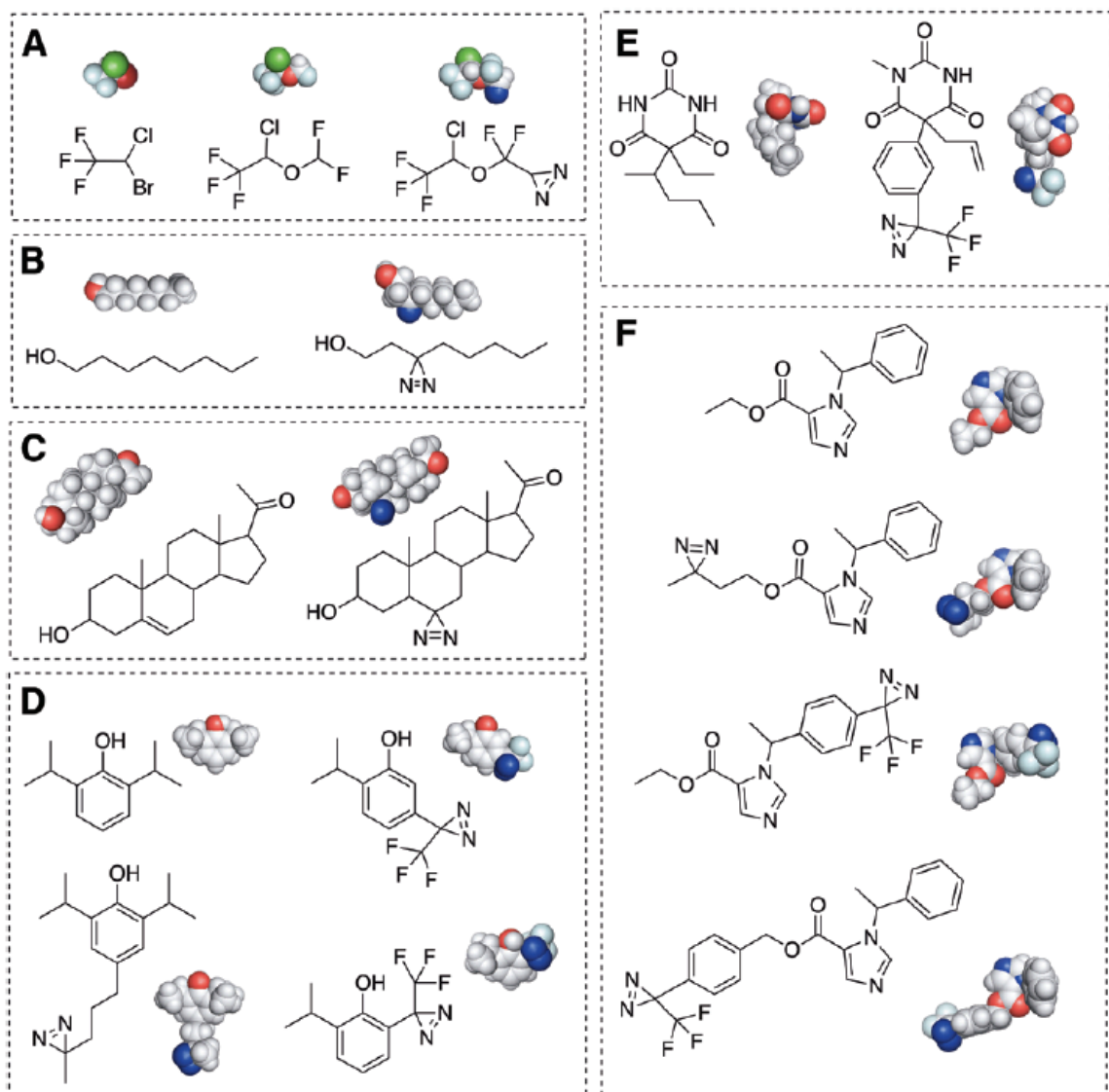


Figure 1. Chemical and spherical structures of general anesthetics and corresponding photoaffinity probes. With the exception of halothane, a diazirine serves as the photoreactive group. Halothane and Haloethers (a); halothane (left), isoflurane (middle), aziisoflurane (right). Alcohols (b): octanol (left), 3-azioctanol (right). Neurosteroids (c); pregnenolone (left), 6-azipregnenolone

(right). Alkylphenols (d); propofol (top left), meta-azipropofol (top right), para-4-azipropofol (bottom left), ortho-propofol diazirine (bottom right). Barbiturates (e); pentobarbital (left), m-TFD-mephobarbital (right). Imidazoles (f); etomidate (top), azietomidate (upper middle), pTFD-etomidate (lower middle), TDBzl-etomidate (bottom)

In practice, the design and synthesis of *a*-PAL to effectively mimic a general anesthetic can be arguably the most difficult process due to the challenging synthesis of stable molecules containing unstable photoreactive groups, and the lack of in-depth knowledge of molecular recognition elements between anesthetics and their important macromolecular targets. The small size and relatively featureless nature of most general anesthetics makes any chemical modification, even a diazirine, a relatively large perturbation. As it stands, even the best-designed *a*-PAL requires considerable chemical deviation from the parent anesthetic structure (exception being halothane³⁷) and alone cannot definitively determine a binding target and/or site for the parent drug.

After incorporation of the diazirine into the anesthetic chemical structure, the resulting changes in physicochemical properties require careful characterization before experimental deployment of the *a*-PAL. The stability and photoactivation efficiency of the diazirine (or any incorporated photoreactive group) are unique to each developed *a*-PAL. The diazirine moiety should produce a distinctive and pronounced UV absorbance^{5,43} that decays with increasing exposure to the appropriate UV wavelength^{44,45}. The rate of decay provides an estimate of photoactivation efficiency within the given buffer. A basic equation (Eq. 1)⁴ can give the half-life of photoactivation ($T_{1/2}$) with relationship to the intensity of the lamp (I_0) applied, molar extinction coefficient (ϵ) and quantum yield of photoactivation (Ψ).

*Equation 1.*⁴

$$T_{1/2} = 0.3 / (\Psi I_0 \epsilon)$$

The chemical nature of the subsequent reactive intermediate generated by photoactivation is also unique to each α -PAL. The reactivity of the intermediate directly influences the propensity to covalently insert into near-by molecules or, depending on ligand chemical structure, itself (e.g. *intramolecular* reactions). For example, studies of 6-azipregnanolone, an α -PAL derivative for pregnanolone, reported that major photoactivation products were likely generated from internal rearrangement or bimolecular insertion reactions⁴⁶. As a result, some macromolecular sites would not be sufficiently represented to allow for detection due to low to zero yield of adducted intermolecular products.

Assuming that a photoactivated ligand intermediate demonstrates sufficient probability for intermolecular interactions, it is generally considered that most carbenes do not demonstrate significant preference for covalent insertion. This includes solvent molecules that, under usual conditions, are in far greater abundance than a target macromolecule. For example, the singlet carbene intermediate is readily quenched by covalent insertion into adjacent water molecules⁴⁷. Similarly, amphipathic molecules of perhaps less interest than proteins, such as lipids and/or detergents, have also been shown to be readily adducted⁴². Weiser *et. al.* demonstrated that the tritiated propofol derivative [³H]*meta*-azipropofol ([³H]AziPm), while showing preference towards synaptic dense regions (and therefore presumably protein), ubiquitously labeled whole rat brain, implying that lipids also act as a considerable photomodified product⁴⁸.

Increasing evidence has suggested that proteins are a significant contributor to anesthetic mechanisms. As such, α -PALs have been applied toward understanding protein binding sites of anesthetics. Table 1 gives the list of photoadducted residues of halothane

and diazirine-containing anesthetic PALs with protein targets. To our knowledge, there has not been a systematic investigation on an anesthetic photoaffinity ligand that conclusively demonstrates preferential insertion into selected amino acids within a protein or polypeptide. Indeed previous work has demonstrated that, while the efficiency (defined as mole of PAL per mole of stationary pure amino acid) of labeling of specific amino acids may be greater for a given PAL (e.g. Cys, Trp, His, Phe), a carbene can covalently insert into all amino acids even within a transmembrane domain^{42,49}. It should be noted that backbone atoms within a protein, not just side chains, can act as potential insertion sites. Indeed, previous evidence with azisoflurane modification of apoferritin (*aF*) implies that backbone atoms (such as the carbonyl oxygen) are suitable photomodification sites⁵⁰.

An exception to preferential residue labeling arises with aliphatic-diazirines and their increased predisposition to undergo diazo isomerization, an alternative *intramolecular* rearrangement. The diazo isomerization of the diazirine can lead to the generation of a carbocation, rather than a carbene, an intermediate that preferentially undergoes electrophilic attack of electron dense (nucleophilic) residues⁴³. The fraction of the PAL generated by isomerization is specific to the chemical properties of the PAL, with the event being debated for some aliphatic-diazirines⁵¹. Regardless, the propensity of labeling Asp, Glu, His, and Tyr by azietomidate^{52,53} led to the development of the etomidate derivatives pTFD-etomidate⁵⁴ and TDBzl-etomidate⁵⁵, both of which contain trifluoromethyl diazirine and trifluoromethylaryl diazirine respectively. These additional chemical groups chemically favor carbene generation, rather than diazo isomerization,

Table 1. Summary of adducted residues by anesthetic photoaffinity ligands (*a*-PALs) using amino acid sequencing methods

Parent anesthetic	Anesthetic photoaffinity ligand	Amino acid sequencing method ^a	Protein	Residue	Ref.
halothane	halothane	Edman degradation (14C)	apo-ferritin	Trp-15	56
			nAChR	α Tyr-213, γ Tyr-111, δ Phe-206 δ Tyr-228	57
octanol	3-azioctanol	Edman degradation (3H, 1H)	nAChR	α Tyr-190, α Tyr-198, α Glu-262, α His-408, α Cys-412	53
			MS/MS	adenylate kinase	His-36
		neural cell adhesion molecule L1		Glu-33, Tyr-418	59
		protein kinase C δ		Tyr-236, Lys-40, Glu-2	60
		protein kinase C ϵ		Tyr-176, Tyr-238, Tyr-250	61,62
		japanese firefly luciferase	Glu-313	63	
isoflurane	aziisoflurane	MS/MS	apo-ferritin	Arg-59	50
			lymphocyte function associated antigen-1	Leu-135, Glu-137, Tyr-257, Leu-302, Lys-304, Lys-305	50,64
			platelet receptor integrin α IIb β 3	Asp-158, Lys-159	65
etomidate	azietomidate	Edman degradation (3H)	nAChR	α Tyr-98, α Tyr-190, α Glu-262, α Glu-390, α Cys-412, β Asp-268, δ Asp-59, δ Ser-258, δ Cys-236, δ Ser-262, δ Gln-276	52,66
			GABA _A receptor	α 1Met-236, β 1Met-286	67-69
	pTFD-etomidate	Edman degradation (3H)	nAChR	α Leu-251, α Ser-252, α Val-255, α Leu-258, β Leu-257, β Leu-261, δ Leu-265, δ Val-269	54
	TDBzl-etomidate	Edman degradation (3H)	nAChR	α Leu-251, α Ser-252, α Val-255, γ Met-299, δ Leu-265, δ Val-269, δ Leu-272, δ Leu-273, δ Gln-276	70
			GABA _A receptor	α 1Cys-234, α 1Met-236, β 3Met-286, β 3Cys-288, β 3Val-290	71
	barbituate	(R)-(-)- <i>m</i> TFD-mephobarbital	Edman degradation (3H)	nAChR	α Leu-231, α Met-242, α Cys-412, β Met-249, β Ser-254 β Leu-257, β Val-261, β Leu-265, γ Cys-252, γ Met-299, δ Met-257, δ Ser-258,

				δ Ser-262, δ Leu-265, δ Val-269	
			GABA _A receptor	α 1Ala-291, α 1Tyr-294, β 3Met-227, β 3Met-227, γ 2Ser-301	⁷³
pregnanolone	6-azipregnanolone	MS/MS	tubulin	Cys-354	⁴⁶
			GABA _A receptor	β 3Phe-301	⁷⁴
propofol	<i>meta</i> -azipropofol	Edman degradation (3H, 1H)	nAChR	α Ser-248, α Ser-252, δ Arg-277, δ Phe-232, δ Cys-236, δ Val-269, δ Thr-274	⁷⁵
			GABA _A receptor	α 1Met-236, α 1Ile-239, β 3Met-227, β 3Met-286	⁷⁶
			GLIC	Met-205, Tyr-254, Met-261, Asn-307	⁷⁷
		MS/MS	apo-ferritin	Leu-24, Leu-81	⁷⁸
			lymphocyte function associated antigen-1	Ile-254, Tyr-257, Ile-258, Lys-287, Leu-302, Lys-304	⁷⁹
			SIRT2 deacetylase	Tyr-139, Phe-190, Met-206	⁸⁰
			VDAC	Gly-56, Val-184	⁸¹
		<i>para</i> -4-aziC5-propofol ^b		nAChR	
	<i>ortho</i> -propofol diazirine	MS/MS	human serum albumin	Lys-41, Trp-111, Lys-525, His-535, Lys-536	⁸³
			GABA _A receptor	β His-267	⁸³

(nAChR) nicotinic acetylcholine receptor; (GABA_A) γ -aminobutyric acid type A; (GLIC) gloeobacter ligand-gated ion channel; (SIRT2) sirtuin-2 ; (VDAC) voltage-dependent anion channel. ^a Noted in () with Edman degradation amino acid sequencing method are the isotopes used for photoaffinity ligand detection. ^bpara-4-aziC5-propofol was not applied in amino acid sequencing however displayed adduction to nAChR by gel electrophoresis and autoradiography

leading to the desired indiscriminate covalent insertions^{5,43,84}. The synthetic changes of etomidate *a*-PALs resulted in a broader range of labeled residues, including hydrophobic residues^{55,85,86}. However whether these modifications were due to changes in photochemistry and/or to altered equilibrium binding due to the changes in chemical structure is unclear.

It is universally agreed that any novel anesthetic derivative, including *a*-PALs, requires a thorough investigation of biochemical and pharmacological activities to assure

retention of parent drug characteristics. These studies can be placed in three basic groups; 1) equilibrium binding to anesthetic protein models, 2) isolated functional studies, and 3) *in vivo* demonstration of pharmacological endpoints.

Initial determination of similar equilibrium binding to model proteins provides some evidence towards the retention of basic molecular recognition elements (hydrophobic forces, hydrogen bonding, van der Waals (vdW) volumes and electrostatic forces, etc.) between the parent drug and developed PAL. Well characterized anesthetic protein models previously crystalized in complex with the parent anesthetic at high resolution, such as apo-ferritin (*aF*)^{87,88} and human serum albumin (hSA)^{89,90}, are often used.

The *a*-PAL should demonstrate similar functional effect(s) within an established protein target as the parent general anesthetic. For many micro-level studies, the targets considered include the cys-loop pentameric ligand gated ion channels, such as the nicotinic acetylcholine receptor (nAChR) and γ -amino butyric acid type A (GABA_A) receptor. Functional characterization therefore requires electrophysiology. Within these studies investigators often observe changes in potency and/or efficacy dependent on the type and position of chemical modifications made to turn the parent anesthetic into an *a*-PAL, as observed with the *meta*- and *ortho*- trifluoromethyl-diazirine substitutions on propofol photoaffinity ligands^{78,83}. Similarly the different *a*-PAL derivatives of etomidate show altered activity on nAChR including approximately 5-fold differences in potency between azietomidate and pTFD-etomidate for inhibition^{54,91}. Because the contributions of these individual targets to the desired effect (anesthesia) is not known, it is not clear *a priori* how important these subtle changes in potency are for the

interpretation of photoaffinity labeling data. Regardless, these studies aim to demonstrate that the ligand retains the functional activity as the parent anesthetic. However this demonstration, while necessary, is not sufficient to indicate a shared binding site, particularly with these relatively lower affinity agents, in that the α -PAL may act as a functionally active ligand but at other distinct site(s).

In addition to retention of activity in a reductionist system, retention of *in vivo* activity is also considered a necessary form of validation of the α -PAL. These studies usually include tadpole immobility assays or rodent loss of righting reflex. Since the mechanisms by which any of the general anesthetics produce their *in vivo* endpoints remain unclear, the retention of *in vivo* activity alone is insufficient evidence to support binding and action at specific protein targets. An interesting demonstration of this is TDBzl-etomidate, an etomidate α -PAL derivative. TDBzl-etomidate demonstrates comparable potency for tadpole immobility and more potent potentiation of the GABA_A receptor relative to the parent anesthetic⁵⁵. However unlike etomidate, this α -PAL acts as a positive modulator of nAChR,⁵⁴ indicating that caution is required when attempting to correlate *in vivo* potency and a shared binding site within a specific target macromolecule. Additionally it should also be noted that the above noted *in vivo* models, and the overt endpoint(s) that are generally used (ie. immobility), do not represent the all components of anesthesia or adverse effects.

Each of the biochemical and pharmacological investigations can be extended to provide evidence to confirm an α -PAL's capabilities to successfully insert into the bound targets after photoactivation. For example photoaffinity labeling of model proteins with halothane³⁷, isoflurane⁵⁰, or propofol^{78,83} α -PAL derivatives have demonstrated

insertion into residues lining the crystallographically confirmed site of hSA or *a*F. Irreversible enhancement of GABA_A receptor gating and desensitization has been reported upon azietomidate photoactivation⁹². *Meta*-azipropofol (*AziPm*) photoactivation *in vivo* has shown significant prolongation of emergence, nearly 10-fold, of tadpole immobility⁹³ suggesting successful covalent insertion into a sufficient mass or number of targets that contribute to an anesthetic endpoint. While the absence of this ‘optoanesthesia’ feature does not negate the validity of an *a*-PAL, its presence is strong evidence for validity and utility. Evidence for reliable photomodification can be considered just as important as the studies demonstrating retention of biochemical and pharmacological activity in that this characteristic is directly responsible for the identification of novel binding partners.

1.2.2. Micro-level Photoaffinity Labeling

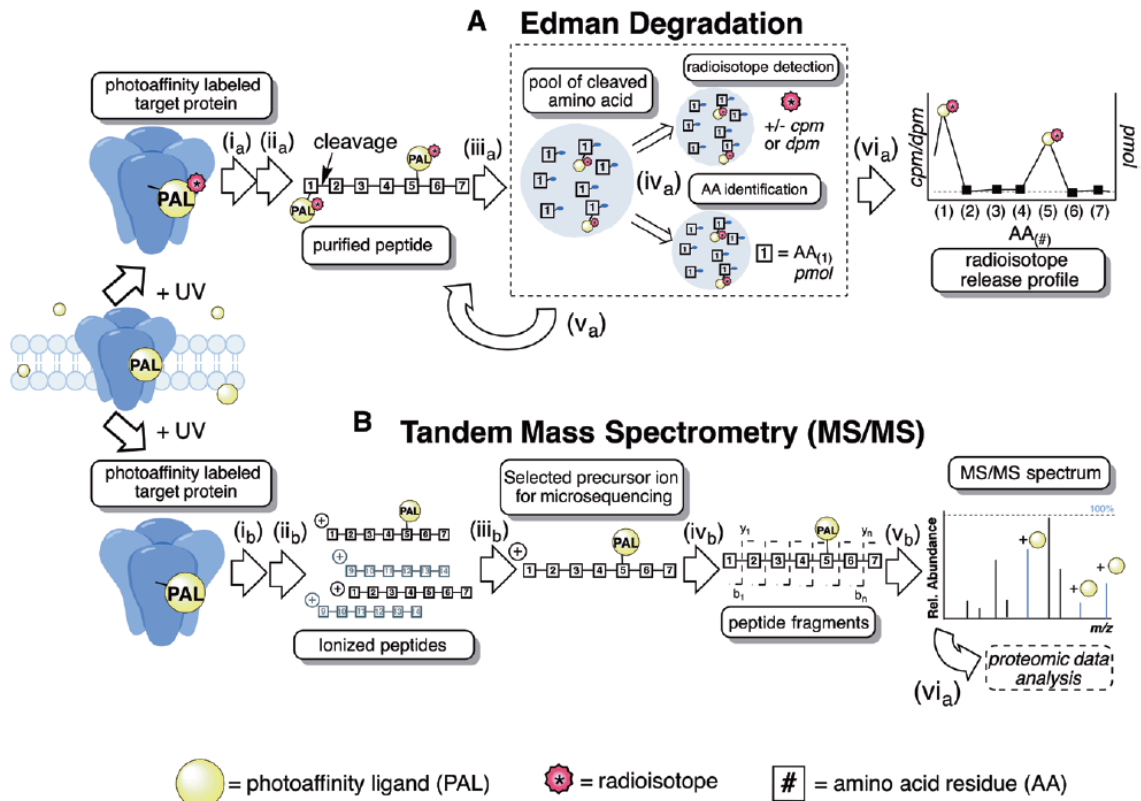


Figure 2. Simplified schemes for the major methods used in micro-level anesthetic photoaffinity labeling; a) Edman degradation b) Tandem mass spectrometry (MS/MS). a) Edman degradation; i_a) enriched target protein is photoaffinity labeled with radiolabeled (*) anesthetic photoaffinity ligand (PAL) and protein(s) are separated and digested into peptides; ii_a) peptides are isolated and rigorously purified; iii_a) the first amino acid from the N-termini is cleaved from purified peptide via Edman reaction; iv_a) the cleaved amino acid is isolated, quantified and separated into two pools for (*top*) radioisotope detection by scintillation counting and (*bottom*) amino acid identification by chromatography; v_a) the cycle is repeated, gradually sequencing the entire purified peptide; vi_a) the amino acid sequence is plotted against radioactivity (cpm, counts per minute, or dpm, disintegrations per minute) resulting in radioisotope release profile. b) Tandem mass spectrometry (MS/MS); i_b) enriched target protein is photoaffinity labeled with anesthetic photoaffinity ligand (*a*-PAL) and protein(s) are separated and digested into peptides that are further separated by on- and/or offline chromatography methods; ii_b) peptides undergo ionization generally by electrospray ionization (ESI) or matrix-assisted laser desorption/ionization (MALDI); iii_b) precursor ions are separated by mass/charge (*m/z*) within MS1 (aka. MS1 precursor ion); iv_b) MS1 precursor ion undergoes mass fragmentation often by collision-induced dissociation (CID) resulting in largely b or y fragment ions; v_b) mass spectrometry software are used for data acquisition, database search analysis and representation.

The majority of studies currently represented in the literature use *a*-PALs to determine anesthetic binding sites within a specific pre-selected protein target, termed as a ‘micro-level’ approach. The identification and characterization of drug binding sites promotes increased understanding of the molecular mechanism(s) within pharmacological targets and, potentially, drug modifications to improve the drug safety profile.

Two different methodologies of protein microsequencing are commonly used to identify protein binding sites photoaffinity labeled by an *a*-PAL. These include Edman degradation (ED) and mass spectrometry (MS), both of which determine binding sites to the amino acid level. Simplified schematics for both methods are shown in Figure 2A-B. ED and MS have been used extensively for multiple types of potential protein targets, soluble and insoluble, over the entire range of *a*-PALs (see Table 1) and much has been learned in terms of binding site location, specificity and actual mechanism of protein dysfunction. Depending on the characteristics and size of the investigated protein target,

both ED and MS can become complex. For example, larger multimeric membrane proteins may require additional steps of precipitation, separation and protease digestions in order to achieve sufficient coverage of the sequence to confidently reveal or exclude photomodified sites.

While the fundamental endpoint result of either method is identical (e.g. identification of the photomodified amino acid), the means to gather the results are notably different. For ED, individual amino acids are sequentially and chemically cleaved (e.g. Edman reaction) from pools of purified peptide fragments from the digested target protein. The resulting pool of the cleaved amino acid is then separated into two smaller pools; one used for the identification of the amino acid using high-performance liquid chromatography (HPLC), the other to detect whether this amino acid contains a radiolabeled *α*-PAL modification. It should be noted that when a backbone atom is labeled by the radiolabeled *α*-PAL, the Edman reaction (or prior peptide cleavages) might be retarded. Although this has not been systematically studied, evidence in support of the possibility is the frequent observation that subsequent amino acid yield decreases after a radiolabeled amino acid.

In contrast, in the MS approach, the *α*-PAL modification is detected by the change the label imparts to the molecular mass-to-charge (m/z) ratio of a peptide fragment. For amino acid level localization of the modification, second level (MS/MS) or higher order data is required. Most often ion traps, quadrupole mass filters, and mass analyzers are combined to the electrospray source for detection. The recent development of orbitrap and Fourier Transform Ion Cyclotron Resonance has resulted in very high mass accuracy, resolution, and dynamic range of detection for the MS method^{94,95,63}. These recent

advances in MS technology and the non-dependence on radioactivity have contributed to the increased use of MS as a method for detection in photoaffinity labeling studies.

The protein binding sites identified by *a*-PAL labeling require several levels of validation to have confidence that the revealed site is the same as that of the parent anesthetic. According to pharmacological convention, *specific* photoaffinity labeling would be irreversible labeling by the *a*-PAL, within a *saturable* protein binding site. For the purposes of this review, we define *anesthetic-specific* photoaffinity labeling as when this same labeled saturable site would be shared by the parent anesthetic. In contrast, *nonspecific* photoaffinity labeling is a result of random modification, such as to peripheral, solvent accessible, or lipid exposed regions of a protein. Nonspecific labeling could also occur with the migration of the reactive intermediate after photoactivation in solvent, lipid, or protein matrix to a random and remote site. All these forms of labeling will occur over the course of a single experiment, but in general nonspecific labeling is challenging to detect in most conditions due to the large number of potential modification sites, generally lower affinity and therefore lower occupancy, and random nature. Further, non-specific labeling should have lower reproducibility, so to categorize sites as ‘specific’ requires several experiments.

Validation of an *anesthetic-specific* over an ‘*a*-PAL’-specific binding site is also required for a target protein. Notably, it should be recognized that both instances may contribute to a mechanism or component of ‘anesthesia’, however only parent anesthetic-specific modified sites are of interest and relevance to clinical medicine. Generally the initial step includes reconciling the labeled residues against existing crystal structures or developed models to identify potential localization within a protein cavity, interface, or

pore site. The characteristics of these sites may indicate potential mechanisms as well as the likelihood for shared binding by the parent anesthetic. For example, the photomodified site of aziiisoflurane in platelet receptor integrin $\alpha\text{IIb}\beta\text{3}$ resided near a calcium binding site, a critical region for regulation of the protein. This proximity immediately suggests a potential mechanism for isoflurane-induced attenuation of platelet aggregation ⁶⁵.

Another common form of validation is by mutagenesis of the photomodified residue(s), followed by functional studies and perhaps repeated photoaffinity labeling experiments. These studies, while indirect, allow association of the photomodified residue and site to the functional activity of the parent anesthetic within the protein. However, common to all mutagenesis investigations, the change in residue might also alter protein structure or dynamics, altering the protein's response to the anesthetic instead of changing the affinity for the binding site. Furthermore, since the photomodification might be side chain independent, mutagenesis studies may not provide a clear interpretation of the site.

Finally, direct evidence of a parent anesthetic-specific modified site would be represented by successful inhibition of PAL labeling through competitive binding, or 'protection', by the parent anesthetic ⁴. Although intuitive, protection from photoaffinity labeling is complicated by the non-equilibrium nature of most photoaffinity labeling experiments. A kinetic mechanism for protection of a parent anesthetic-specific site from photoaffinity labeling is described in Figure 3, and is similar to that previously described for photoaffinity agents and other protection experiments for non-equilibrium systems ^{4,96}. The model has simultaneous dependence on the two different affinities of the ligands

(e.g. protecting ligand and α -PAL) for the protein target, and the photoreactivity of the α -PAL (which is highly dependent on the experimental conditions noted in section 2.2). Since the photoaffinity labeling event is irreversible, in contrast to the parent ligand, binding sites will be gradually depleted. Further, the α -PAL will also be gradually depleted by solvent labeling. Therefore, multiple consecutive and competing rates, unique to the target protein, protecting ligand and α -PAL, are present within a typical protection experiment. As a result, protection experiments require careful attention; otherwise, results can be misinterpreted.

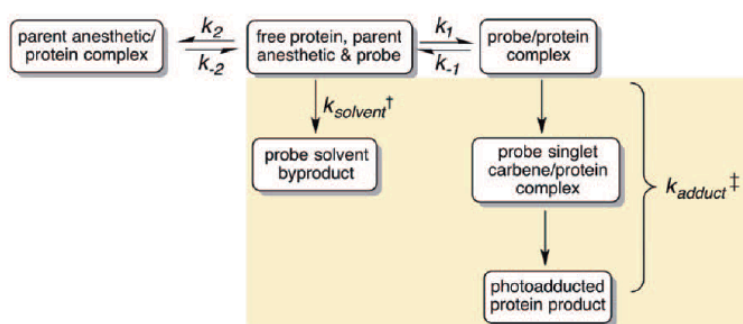


Figure 3. Schematic representation of the steps involved in the most basic mechanism of parent anesthetic protection of anesthetic photoaffinity labeling experiments. Highlighted region denotes the non-equilibrium reactions upon UV irradiation. $^{\dagger}(k_{solvent})$ Rate of solvent quenching of the ligand, given that carbenes are readily quenched by water the rate is limited by photoactivation of the ligand and therefore a first order rate constant. $^{\ddagger}(k_{adduct})$ Rate of photoadduction represents two consecutive first order reactions, the photoactivation of the ligand and the insertion by the singlet carbene into the protein.

Some physicochemical limitations of the α -PAL or the method for label detection may prevent quantitative assessment of protection. For example, a relatively high molar ratio of the parent anesthetic to α -PAL is generally required for protection (>100:1). However, such a high concentration may not be possible due to limitations in parent anesthetic solubility as reported previously⁷⁴, making interpretation of protection experiments a challenge. Quantitative detection by MS also poses limitations, particularly

for label-free quantification that requires considerable protection for significance under most experimental conditions ⁹⁷. However with continuing advancement of the technique, such as isobaric labeling methods ^{98,99}, quantification of protection experiments by MS will be possible.

The potential for in-depth knowledge of the molecular mechanisms of anesthesia and/or drug side effects is reflected by the wide range of developed *a*-PALs and their numerous micro-level investigations. A previous published review ⁴⁰ provides a comprehensive overview of all developed anesthetic PALs and studied protein targets. In addition Table 1 may be referred to for additional information. The following are selected significant findings that focuses on examples of insights given by the photoaffinity labeling.

The majority of studies using volatile anesthetic *a*-PALs in micro-level investigations include neat halothane and azeisoflurane, the *a*-PAL for isoflurane. Permitted by ¹⁴C-labeled halothane, ED identified halothane modification of extracellular and transmembrane domains within *Torpedo* nAChR ⁵⁷. In particular, isoflurane protected halothane photoaffinity labeling of Tyr-228 within the δ subunit in a state-dependent manner. This finding highlighted a potential pocket formed within the receptor's desensitized state that can accommodate either anesthetic and, through stabilization of the state, may contribute to the functional inhibition of nAChR. A similar trend of potential state-dependent binding was suggested by azeisoflurane labeling of lymphocyte function associated antigen-1 (LFA-1) ⁶⁴. The labeling of Ile-135 and Glu-137 within the LFA-1 β 1 domain by azeisoflurane suggested a closed state-dependent binding. The stabilization of this conformation by the volatile anesthetic may contribute

to the impaired lymphocyte arrest and the anti-inflammatory actions displayed by isoflurane^{100–102}.

The *α*-PAL derivative of mephobarbital, (R)-(-)-*m*TFD-mephobarbital, was shown to act as a particularly potent positive modulator of the GABA_A receptor; approaching the potencies of etomidate and propofol¹⁰³. As such, (R)-(-)-*m*TFD-mephobarbital was used to uncover binding sites of barbiturate anesthetics. When compared to azietomidate, photoaffinity labeling studies suggested distinct sites within the GABA_A receptor for the two anesthetics⁷³. Both (R)-(-)-*m*TFD-mephobarbital and azietomidate labeled intersubunit sites, and at a similar depth within the transmembrane region; however, the different anesthetics targeted different subunit interfaces. *m*TFD-mephobarbital selectively labeled γ -/ α + while azietomidate selectively labeled β -/ γ + or α +/ β - with the GABA_A receptors⁷³. These studies demonstrate the heterogeneity of anesthetic chemical structures are reflected by different site locations within the same target. Indeed, with the likely joint use of multiple *α*-PALs, a progressive understanding of the molecular mechanisms for anesthetics within complex target proteins can be achieved.

1.2.3. Macro-level Photoaffinity Labeling

Macro-level photoaffinity labeling is a much less prevalent method compared to the application of micro-level photoaffinity labeling within anesthesiology research. Despite this, macro-level investigations are becoming recognized as a useful tool within chemical biology due to the increased need to uncover druggable targets, matched with the dawning awareness of how promiscuous many drugs are. Anesthetics can be considered a prime example of the current paradox in drug development in that there is

an urgent calling for optimized chemical designs in order to improve potency or decrease toxicity. Unfortunately, many of the molecular targets leading to any endpoints remain elusive. The following section overviews selected studies and perspectives of α -PALs in macro-level studies.

Previously the labeling of rat brain membranes with [^3H]6-azipregnanolone provided an unbiased, affinity-based picture of neurosteroid targets within a complex biological system ¹⁰⁴. Based on radioactivity of slices from a subsequent SDS-PAGE separation of proteins, specific labeling of a few gel bands was observed. Two proteins, tubulin and voltage-dependent anion channel-1 (VDAC-1), were subsequently identified and further investigated as potential protein targets. Micro-level studies found that photomodification of tubulin was at Cys-354 ⁴⁶, a residue within the colchicine binding site, and consistent with the ability of 6-azipregnanolone and pregnanolone to inhibit tubulin polymerization ⁴⁶. Other work using the non-clinical α -PALs azidoanthracene has also implicated tubulin as a potential anesthetic target ¹⁰⁵. Similarly, further work on VDAC-1 found that it was unlikely to be an important target in the VDAC-1/GABA_A receptor interaction pathway ¹⁰⁶. VDAC-1 might however be responsible for alternative pathways and/or anesthetic side effects.

VDAC-1 was also identified as a specific anesthetic binding protein target in a macro-level investigation using [^3H]AziPm ⁹³. The subsequent micro-level investigation found that VDAC gating was modulated by propofol, and two binding sites were identified ⁸¹. In addition to VDAC-1, synaptosomal-associated protein- 25kDa (SNAP-25) was identified as a labeled protein within the macro-level investigation ¹⁰⁷. The SNARE complex has potential as an anesthetic target, with volatile anesthetics and

propofol inhibiting neurotransmitter release by interactions with the complex^{108,109}.

These few examples demonstrate how photoaffinity labeling has provided unexpected molecular targets that should provide opportunities for drug improvement when the associated physiology is understood.

It is anticipated that many protein targets involved in anesthesia are low abundance integral membrane proteins such as ion channels and receptors. Both characteristics result in complications for macro-level detection using classical PAL techniques^{104,107}. However, over the past decade advancements in the photoaffinity labeling field has shown successful coupling of photoaffinity labeling and bioorthogonal reactions; a recent review¹¹⁰ provides an excellent discussion of these developments in chemical biology methods. Recent tandem anesthetic photoaffinity-click chemistry conjugation involves the additional incorporation of a biologically inert alkyne into the *a*-PALs structure^{38,39}. The additional chemical group allows for affinity-based protein profiling (ABPP) of the anesthetic. This technology has numerous powerful applications from micro- to macro-level protein profiling and imaging investigations within complex systems.

General anesthetics are often considered to have low affinity for their targets relative to most other drugs. As such, the simplified view of ‘one drug, one target’ for these drugs is exceedingly improbable. While the diversity of targets opens up new avenues for further development, it also presents significant challenges with respect to characterization and validation. Challenges associated with these macro-level investigations are similar, if not greater, to that of micro-level investigations; sufficient *a*-PAL development and validation of identified protein targets. As the science moves

towards systems biology and ‘P4’ medicine, the precise target-interaction profiles for each general anesthetic become increasingly necessary.

1.2.4. Conclusions

An ultimate the goal of anesthesiology research is to identify the biochemistry of these drugs that leads to the observed pharmacological phenotypes, both the desired and less desired effects. It is apparent that the popularity of photoaffinity labeling studies has increased in anesthesiology research and further progress is inevitable. *A*-PALs have contributed to this goal by providing evidence of molecular recognition elements for more informed design of future anesthetic agents as well as the identification of targets that may contribute to altered sensitivity within population groups. The obtained evidence has permitted refined hypotheses, and new directions with respect to molecular targets. This knowledge should allow educated improvements in drug design by enhancing or diminishing affinities for targets that lead to desired and adverse effects respectively and/or for selective administration of an anesthetic to distinct populations. The mechanisms of anesthesia have remained elusive for nearly two centuries and increasing evidence has suggested a highly complex process. In combination with other advancing techniques, the use of *a*-PALs continues to be a significant tool in shedding light on this puzzle in medicine.

CHAPTER 2: SEVOFLURANE AND ISOFLURANE VOLATILE ANESTHETIC MECHANISMS

Efforts to develop a safe, nonflammable volatile anesthetic started to gain momentum in the 1930s when it was found that the halogenation of compounds lowered

the boiling point, enhanced the solubility and generally decreased the toxicity of most agents¹¹¹. In addition to Krantz Jr., Earl McBee of Purdue University applied his knowledge of fluorination, which he gained from his involvement in the “Manhattan” atomic bomb project, to develop a range of fluorine-containing compounds.

Unfortunately none of these agents were appropriate clinical application^{112,113}. In 1951 the synthesis of halothane by Charles Suckling lead to an increased push to develop better volatile anesthetic compounds¹¹⁴. Many of the halogenated inhaled agents that we associated with general anesthesia today were prepared in the 1960s from a library of over 700 compounds including enflurane, isoflurane, and desflurane¹⁷.

The halogenated methyl ethyl ethers sevoflurane and isoflurane demonstrate many favorable pharmacological characteristics that were significant enough to eventually compensate for their alleged toxicity and relatively difficult synthesis at the time^{115–117}. However, both volatile anesthetics still require millimolar plasma concentrations to induce their desired pharmacological effects suggesting very rapid ligand-target protein off-times¹¹⁸. Therefore, conventional binding assays are unlikely to confidently provide drug binding sites for these ligands and application of alternative techniques are required. The first section of this chapter focuses on the development of the first sevoflurane *a*-PAL called azisevoflurane(**1a**), and its application within a unique sevoflurane protein target, mammalian *Shaker* potassium (Kv1.x) channels. The second section within this chapter centers on the application of azisevoflurane along-side a previously published isoflurane *a*-PAL, aziisoflurane⁵⁰, in the identification of binding sites in synaptic γ -aminobutyric acid Type A (GABA_A) receptors, a likely major general anesthetic target.

2.1. Novel Photoaffinity ligand for sevoflurane reveals sites of voltage-gated ion channel modulation

Sevoflurane (Figure 4) was first synthesized by Regan of Travenol Laboratories in 1968 and was later reported by fellow co-workers in 1971¹¹⁹. The Travenol group continued on to animal studies and characterized the new anesthetic's clinical properties. Despite some resistance brought on from claims of toxic effects (later shown to be a result of poor experimental design) as well as the drug's biotransformation in soda lime (used to remove CO₂ from breathing gases), favorable clinical properties kept sevoflurane afloat as a potential clinical general anesthetic^{115,116}. Sevoflurane was finally accepted for clinical use in 1990 in Japan, later followed by approval by the Food and Drug Association. To date sevoflurane holds a spot as being amongst the youngest accepted volatile general anesthetics administered within the United States.

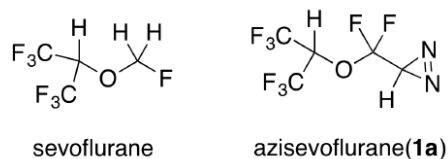


Figure 4. Chemical structures of sevoflurane and azisevoflurane(**1a**)

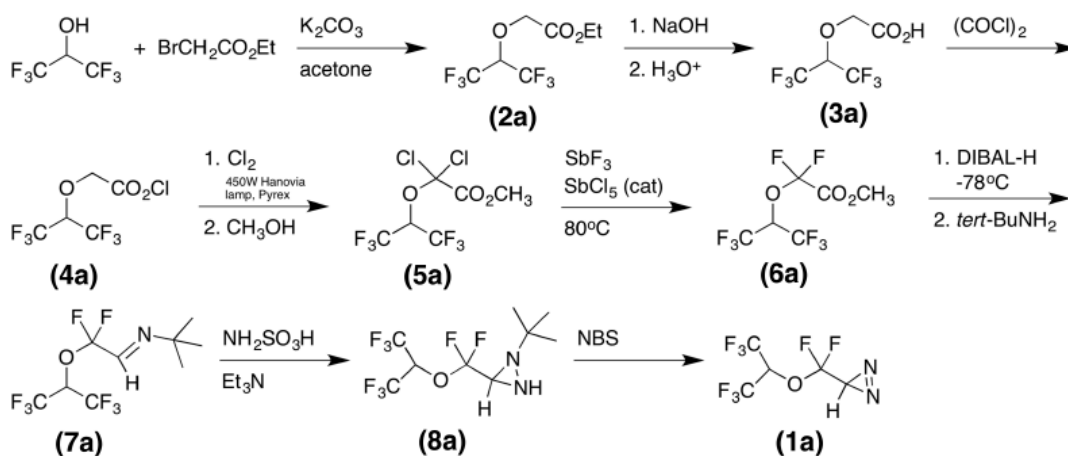
The favorable properties that sustained the interest in sevoflurane as a potential anesthetic included hemodynamic stability, rapid induction and emergence, as well as a marked decrease in pungency, or respiratory irritation¹¹⁵. This combination of clinical properties has made sevoflurane the preferred anesthetic in pediatric care^{120,121} where inhalational inductions are common. Most of the early reports on sevoflurane center on these pharmacokinetic observations, while the molecular mechanisms of sevoflurane anesthetic action remain unclear. There has been growing concerns regarding adverse

effects of anesthetics on neurodevelopment and cognition, both being applicable for sevoflurane anesthesia due to their largely sensitive patient population.

Here, the synthesis and characterization for the first PAL developed for sevoflurane, 3-{difluoro[(1,1,1,3,3,3-hexafluoropropan-2-yl)oxy]methyl}-3H-diazirine or azisevoflurane (**1a**) (Figure 4) is presented. Azisevoflurane (**1a**) displayed the same functional and pharmacological activity as sevoflurane. The use of azisevoflurane (**1a**) in the *Shaker* voltage-gated potassium channel Kv1.2, a unique target for this anesthetic chemotype, allowed for the unbiased identification of a sevoflurane active site, complementing previously suggested mechanisms of action. This result indicates that azisevoflurane (**1a**) will be useful to identify further contributing mechanism(s) for this important drug.

2.1.1. Synthesis and characterization of azisevoflurane

Scheme 1.



The alkyldiazirine photoreactive group was used to generate azisevoflurane (**1a**) due to previous use in developing alkyldiazirine-based PAL derivatives for general anesthetics^{50,78,122}. The synthesis of 3-(difluoro[(1,1,1,3,3,3-hexafluoropropan-2-yl)oxy]methyl)-3H-diazirine or azisevoflurane (**1a**) is shown in Scheme 1. The synthesis

started with the reaction between hexafluoroisopropanol and ethyl bromoacetate in the presence of anhydrous potassium carbonate. The resulting ester **2a** is saponified and converted to acid chloride **4a** using oxalyl chloride and a catalytic amount of DMF. Photochemical chlorination of **4a** followed by reaction with methanol converts **4a** to the dichloro-ester **5a**. Fluorination of **5a** using SbF₃ with a catalytic amount of SbCl₅¹²³ converts it to octafluoro-ester **6a**. A more direct route to **6a** using the reaction between hexafluoroisopropanol and 2-iodo- or 2-bromo- or 2-chloro-2,2-difluoroacetic acid derivatives was unsuccessful under a wide variety of conditions. This is in contrast to the reaction between 3,3,3-trifluoroethanol and 2-chloro-2,2-difluoroacetic acid in the presence of aqueous base¹²⁴.

Further conversion of methyl ester **6a** to diazirine **1a** followed standard procedures¹²⁵. Thus, reduction of ester **6a** with DIBAL-H at low temperature followed by immediate condensation with tert-butylamine in refluxing benzene formed imine **7a**. Treatment of **7** with hydroxylamine-O-sulfonic acid in ethanol in the presence of triethylamine produced diaziridine **8a** which was converted to diazirine **1a** using N-bromosuccinimide in dichloroethane. Final purification of **1a** was accomplished using preparative gas chromatography.

Table 2. Physicochemical properties of sevoflurane and azisevoflurane(**1a**)

	MW (Da)	Density (22-23°C; g/mL)	Van Der Waals, (Å ³)	cLogP
sevoflurane	200	1.51	123	2.42
azisevoflurane (1a)	258	1.48	151	2.47

The physiochemical properties of sevoflurane and azisevoflurane(**1a**) are reported in Table 2. Compared to sevoflurane, azisevoflurane(**1a**) showed a modest increase in

hydrophobicity. The absorption spectrum of the alkyldiazirine shows the distinctive double-peak at 280-330 nm that decreased with increasing 300 nm exposure, indicating photoreactivity (Figure 5). The $t_{1/2}$ of photoreactivity using a 300 nm RPR-3000 Rayonet lamp through a 295 nm glass cutoff filter was 6 min (in methanol).

Despite the chemical modifications to incorporate the photoreactive group, azisevoflurane(**1a**) retained protein binding interactions and pharmacological activity of

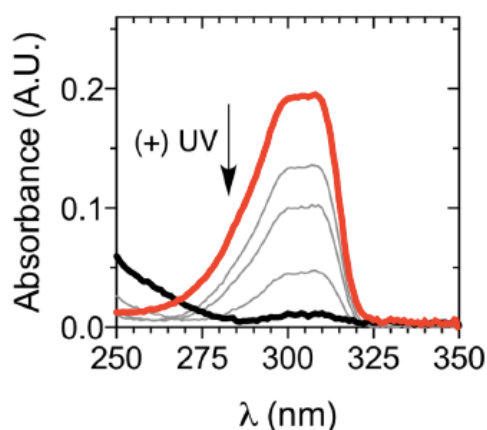


Figure 5. Photoactivation of azisevoflurane (**1a**). Absorbance spectrum of azisevoflurane (**1a**) diazirine with exposure to 300 nm UV light from $t=0$ (red line) and $t=n$ (gray/black lines).

sevoflurane. Previously it has been shown that *aF* serves as a soluble model for anesthetic binding to the four-helix bundles motifs found in consensus general anesthetic protein targets, such as the GABA_A receptor^{87,88}. Multiple volatile general anesthetics have been crystallized within the *aF* ‘anesthetic site’ including the haloether anesthetic isoflurane⁸⁸. Equilibrium binding affinity of sevoflurane and azisevoflurane(**1a**) to *aF* was determined by 1-aminoanthracene (1-AMA) fluorescence competition¹²⁶ and isothermal titration calorimetry (ITC). Results from both methods were in agreement and are provided in Table 3 and in Figure 6A-B. Azisevoflurane (**1a**) demonstrates a small (50-70%) increase

in binding affinity relative to sevoflurane, consistent with the increased hydrophobicity

88

Two animal models were employed to evaluate *in vivo* pharmacological activity of azisevoflurane(**1a**). Because of limitations imparted by low synthetic yield (~2%), the clinical route of administration (e.g. inhalation) was not feasible for azisevoflurane(**1a**). The common tadpole immobility assay^{50,127} was employed to determine the potency of azisevoflurane(**1a**) as compared to sevoflurane. An Intralipid®-based formulation for

Table 3. Apo-Ferritin (*aF*) sevoflurane and azisevoflurane (**1a**) binding parameters

	sevoflurane		azisevoflurane (1)	
	ITC	Fluorescence Competition	ITC	Fluorescence Competition
K _D (μM; 95% CI)	36 (23-49)	15 (9.5-24)	19 (13-24)	8.4 (5.2-14)
Hill Slope (Mean ± SEM)	-	-1.0 ± 0.22	-	-1.5 ± 0.43

intravenous (IV) administration of volatile anesthetics¹²⁸ was also employed to test anesthetic efficacy in mice. Sevoflurane and azisevoflurane(**1a**) displayed similar hypnotic potency in *Xenopus laevis* tadpoles with the induction of a reversible loss of spontaneous movement (Figure 7A). Azisevoflurane (**1a**) demonstrated a ~50% increase in potency relative to sevoflurane (Table 4) and no toxicity, again consistent with the small increase in hydrophobicity².

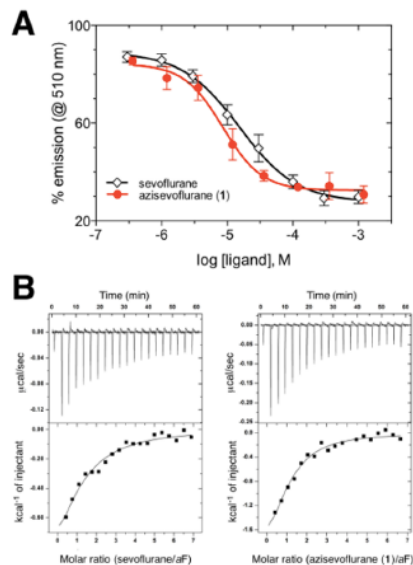


Figure 6. Sevoflurane and azisevoflurane (**1a**) binding to *apoferritin*. A) Equilibrium fluorescence competition from *apoferritin* (*aF*) anesthetic binding site using 1-aminoanthracene (1-AMA). Titration of the *aF* and 1-AMA combination with either sevoflurane (open diamonds) or azisevoflurane (**1a**) (red filled circles) produced inhibition of fluorescence indicating competition for binding. Graph values are given in Table 2. B) Isothermal titration calorimetry profiles of *aF* interaction with sevoflurane (left) or azisevoflurane (**1a**) (right) using sequential titrations. Top: time response heat change from addition of ligand. Bottom: best fit attained from a single site binding model (best χ^2 statistic) fitted to a 1:1 stoichiometry for *aF*.

Mouse IV administration of sevoflurane in 20% Intralipid® by bolus tail vein injection resulted in reversible hypnosis determined by Loss Of Righting Reflex (LORR). No toxic effects or irritation at injection site were observed. The EC_{50} and Hill Slope for emulsified sevoflurane were 0.36 g/kg (0.35-0.39 g/kg; 95% CI) and 11 ± 2.9 respectively. The EC_{99} dose (based on sevoflurane) of azisevoflurane (**1a**) (0.51-0.53 g/kg) was administered to two mice, resulting in reversible LORR with no observable toxicity. The time to regain righting reflex for emulsified azisevoflurane(**1a**) was longer (180 ± 21 s, mean \pm SD, n=2) than for sevoflurane (40 ± 18 s, mean \pm SD, n=4). The extended hypnotic times are consistent with azisevoflurane(**1a**) activity as a more potent anesthetic than sevoflurane, although the small cohort precluded statistical significance. At a minimum, azisevoflurane(**1a**) is a reversible anesthetic with potency and efficacy

similar to sevoflurane.

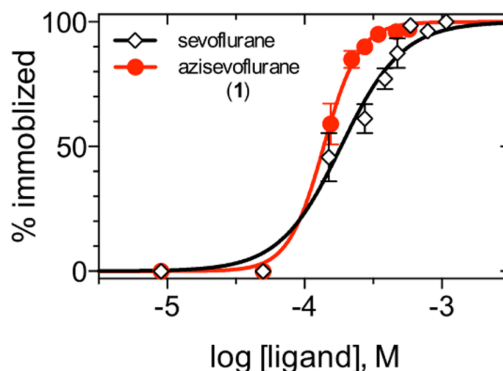


Figure 7. Sevoflurane and azisevoflurane (**1a**) pharmacological activity. A) Tadpole immobility assay dose-response relationship for sevoflurane (open diamonds; n=80) and azisevoflurane (**1a**) (red filled circles; n=100). Lines represent best fit Hill slopes, constraining the bottom to 0% immobility. Graph values are given in Table 3.

Table 4. Tadpole studies with sevoflurane and azisevoflurane (**1a**)

	EC 50 (μ M; 95% CI)	Hill Slope (Mean \pm SEM)
sevoflurane	192 (166-221)	2.1 \pm 0.26
azisevoflurane (1a)	130 (120-141)	2.9 \pm 0.26

As a final means to evaluate azisevoflurane (**1a**) as a reliable PAL for sevoflurane, *aF* was photoaffinity labeled to determine whether the ligand could report sevoflurane binding site(s) at the residue level. Peptides accounting for 96.57% sequence coverage of *aF* light chain were detected by mass spectrometry (see appendix A.3.1). Azisevoflurane(**1a**) modifications were identified in 4 unique peptides on 4 different residues Arg-25, Arg-59, Leu-81 and Gln-82 (see appendix A.4.1). All residues were located within the crystallographically defined *aF* ‘anesthetic site’, with Arg-59 and Leu-81 previously labeled by the isoflurane and propofol *a*-PAL derivatives^{50,78}.

2.1.2. Photoaffinity labeling of purified *Kv1.2* channels

Sevoflurane at pharmacologically relevant concentrations, potentiates *the Shaker-*

type Kv1.2 channel by left-shifting the conductance-voltage (G - V) curve and increasing the maximum conductance (G_{\max})^{129,130}. The positive modulation of Kv1.2 channels by sevoflurane is in contrast to other anesthetic chemotypes that mainly show weak inhibitory activity¹³⁰ making Kv1.2 a uniquely specific target of this chemotype. Investigating such distinct differences in functional activity between general anesthetics is critical in understanding the multiple mechanisms that lead to the ‘same’ anesthesia endpoints. For example, previous studies have shown that characteristic burst suppression patterns observed during deep anesthesia differ between general anesthetics, including sevoflurane¹³¹. Such findings strongly suggest that the various general anesthetics distinctly perturb molecular targets that influence neuronal excitability of which Kv1.x channels are known key regulators¹³². Indeed, previous studies have shown that inhibition of Kv1.x channels restored righting reflex in rodents under sevoflurane anesthesia^{133,134}.

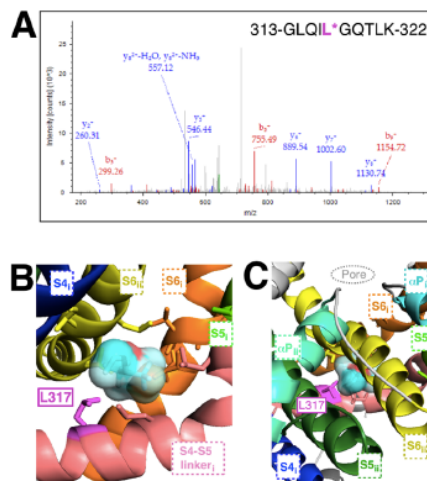


Figure 8. Photoaffinity labeling of mammalian Shaker Kv1.2 channel by azisevoflurane (**1a**). A) MS2 data for the peptide 313-GLQILGQTLK-322 peptide labeled with azisevoflurane (**1a**)(L*) (red: assigned b⁺ ions; blue: assigned y⁺ ions; green: assigned precursor ion). (B-C) Lowest energy sevoflurane docking pose viewed towards the S4-S5 linker and S6 cavity (B) and from the cytoplasm (C) of the lowest free energy docking pose of sevoflurane (stick/surface structure) within Kv1.2 (PDB code: 3LNM) transmembrane domain. S4 to S6 helices, pore-helix (α P) and S4-S5 linker are denoted as the same subunit (X_i) or the adjacent subunit (X_{ij}). The L317

(corresponding to L313 in 3LNM) photolabeled residue is represented in magenta stick structure.

Therefore, azisevoflurane(**1a**) was used to locate binding sites in this ubiquitously expressed central nervous system channel. Homotetrameric His-tagged rat Kv1.2 channels were heterologously expressed in Sf9 cells and purified before the introduction of 1 mM azisevoflurane(**1a**), with or without UV light. Mass spectrometry analysis resulted in the detection of peptides covering 74.0% of the full sequence; 57% of the 6 transmembrane domains (see appendix A.3.1). In the photolabeled sample, only Leu-317, part of the S4-S5 linker region, was identified as modified by azisevoflurane(**1a**) modification (Figure 8A; see appendix A.4.2).

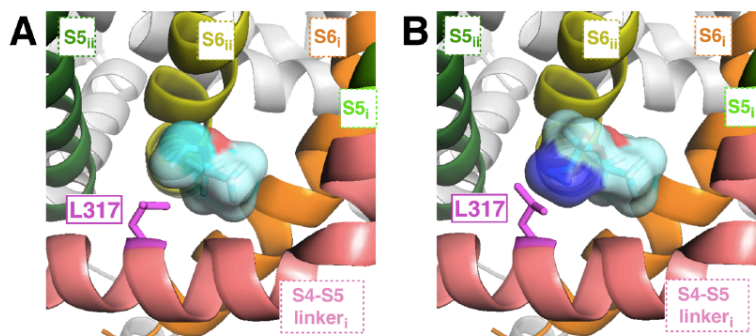


Figure 9. Lowest energy azisevoflurane(**1a**) docking pose viewed towards the S4-S5 linker and S6 cavity. (A-B) Lowest energy sevoflurane (A) and azisevoflurane (**1a**) (B) (stick/surface structure) docking pose viewed towards the S4-S5 linker and S6 cavity within Kv1.2 (PDB code: 3LNM) transmembrane domain. S5 to S6 and the S4-S5 linker are denoted as the same subunit (X_i) or the adjacent subunit (X_{ii}). The L317 (corresponding to L313 in 3LNM) photolabeled residue is represented in magenta stick structure.

For further evaluation of the azisevoflurane (**1a**) photolabeled site within Kv1.2 channels, docking simulations using sevoflurane and azisevoflurane (**1a**) were conducted with AutoDockVina¹³⁵. Mammalian *Shaker* K1.x channels consist of four α -subunits that are arranged to form a pore as tetramers. Each subunit contains six transmembrane helical segments (S1–S6), with a membrane-reentering loop (P-loop) and a ‘hinge’ helix

between the S4 and S5 called the S4-S5 linker¹³². The simulations contained the entirety of the cavity formed by the S4-S5 linker and S4-S6 helices of the same and adjacent subunit of a Kv1.2 homodimer (PDB ID: 3LNM). The lowest free energy value for the complex was -5 kcal mol^{-1} orienting the monofluoro- methyl group of sevoflurane 3.1-3.5 Å from L317 (Figure 8 B-C). Azisevoflurane(**1a**) docking simulations revealed a lowest free energy value of $-5.9 \text{ kcal mol}^{-1}$ with the diazirine carbon remaining 3.2-4.0 Å from Leu-317 (Figure 9). The highest scored poses placed the trifluoro-methyl moieties of both ligands in a pocket formed by the S4-S5 linker and the S5 and S6 helices of one subunit as well as the S6 from the adjacent subunit (Figure 8-9).

2.1.3. Validation of sevoflurane Kv1.2 channel binding site by electrophysiology

Compared to sevoflurane, azisevoflurane(**1a**) retained a unique ability to induce positive modulation of the Kv1.2 channel by significantly potentiating heterologously expressed Kv1.2 channels in *X. leavis* oocytes at 0.3 mM which corresponds to ~ 1 MAC (minimum alveolar concentration) (Figure 10A-B). Relative to sevoflurane, azisevoflurane(**1a**) is modestly more potent, a difference particularly evident when comparing the increase in G_{\max} .

To assess the importance of L317 in the positive modulation of Kv1.2 by sevoflurane and azisevoflurane(**1a**), we investigated the electrophysiological properties of the Leu-317-Ala mutant. This mutation affected Kv1.2 gating by inducing a modest parallel G - V curve leftward shift of the order of -10mV . Furthermore, the Leu-317-Ala mutation dampened the sevoflurane- or azisevoflurane(**1a**)-induced leftward shifting of the G - V curve without affecting the G_{\max} increase (Figure 10). Accordingly, the effect of the anesthetics on the mutant half activation voltage ($V_{1/2}$) was no longer significant

(Figure 11). The magnitude of the anesthetic effect and the impact of the Leu-317-Ala mutant can be directly assessed by examining the conductance ratio-plots for either ligand (Figure 10). At -30 mV, the anesthetics increase the Kv1.2 conductance ~1.5 – 2.5-fold, and at positive membrane potentials corresponding to the G_{\max} , the increment decays and levels off at ~1.1 – 1.2-fold. Whereas Leu-317-Ala reduces the fold change at biologically relevant negative voltages, it does not affect it at positive voltages (Figure 10).

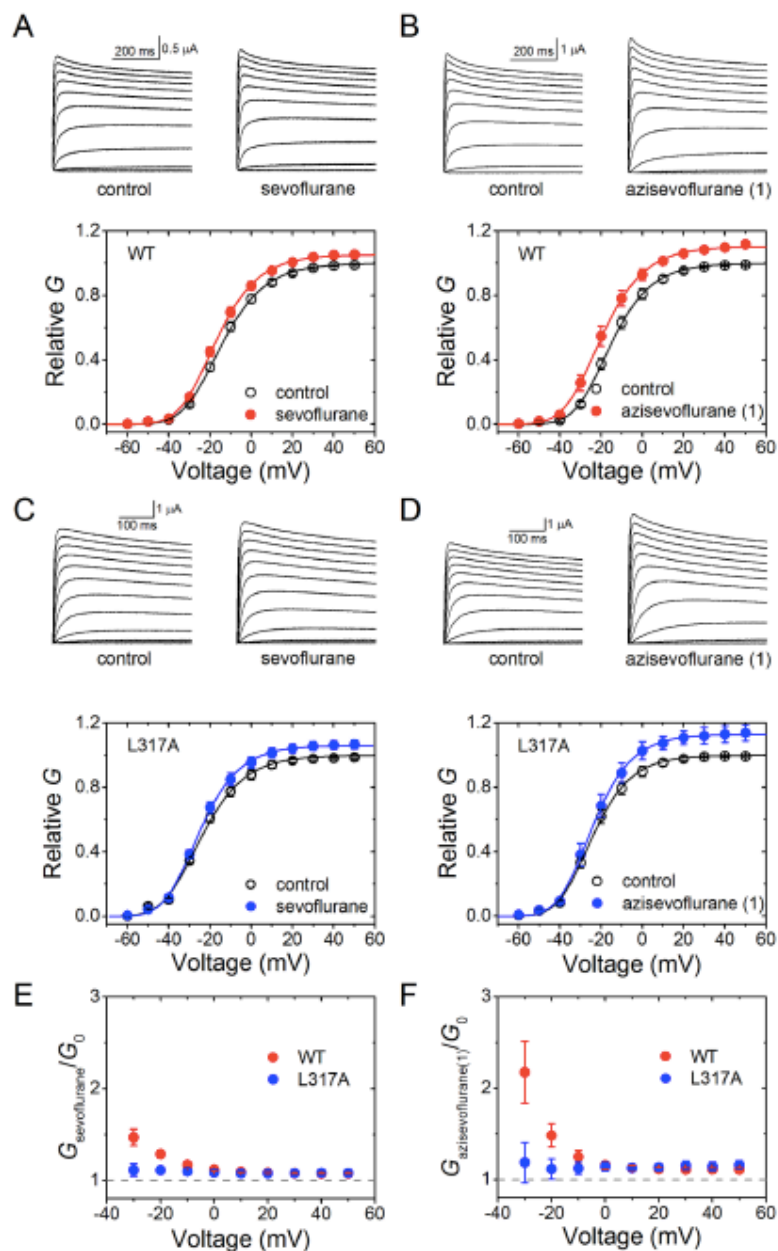


Figure 10. Positive modulation of Kv1.2 conductance by sevoflurane and azisevoflurane (**1a**) is dampened by the L317A mutation. (A) Kv1.2 wild-type currents in the absence and presence of sevoflurane, and the corresponding relative conductance-voltage plots. From a holding voltage of -100 mV, currents were evoked in 10-mV increments by step depolarizations from -90 to +50 mV. Relative conductance is defined as the conductance G at a given voltage in the absence or presence of sevoflurane over the maximum conductance (G_{max}) in the absence of the anesthetic.

Solid lines represent the best-fit Boltzmann functions. (B) Kv1.2 wild-type currents in the absence and presence of azisevoflurane (**1a**), and the corresponding relative conductance-voltage plots. Each symbol and error bars represent the mean \pm SEM ($n = 13$ and 9 , for sevoflurane and azisevoflurane (**1a**), respectively). (C-D) Kv1.2 L317A mutant currents in the absence and presence of 0.3 mM sevoflurane and 0.3 mM azisevoflurane (**1a**), and the corresponding relative conductance-voltage plots. Each symbol and error bars represent the mean \pm SEM ($n = 6$ and 5 ,

for sevoflurane and azisevoflurane (**1a**), respectively). (E-F) Conductance ratio-voltage plots of the ligands on wild-type and L317A mutant channels. At each voltage, these plots evaluate the fold conductance change ($G_{\text{anesthetic}}/G_{\text{control}}$) induced by the anesthetic. Each symbol and error bars represent the mean \pm SEM (n is the same as above).

Cumulatively, the results indicate that Leu-317 and the S4-S5 linker, plays a significant role in the voltage-dependent aspect of the anesthetic-induced Kv 1.2 channel positive modulation, but a distinct site might be responsible for the increase in G_{max} . These findings align with previous mutagenesis studies investigating anesthetic modulation *Shaker*-type Kv 1.2 channels^{129,130,136–138} and suggest that the G_{max} increase is governed by occupancy of a distinct site not detected in our photoaffinity labeling-experiments (~25% of the sequence was not detected). More provocative mutations of Leu-317 (Leu-317-Ser or Leu-317-Thr) resulted in either no expression or conductance, a result consistent the critical role in of the S4-S5 linker in Kv1.2 dynamics^{139–142}. Therefore, the application of an unbiased experimental methodology based on photoaffinity labeling strongly supports the conclusion that the S4-S5 linker is part of an allosteric sevoflurane site through direct evidence of ligand binding, rather than a region of the channel highly sensitive to remote perturbations.

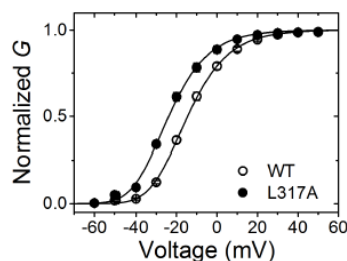


Figure 11. The L317A mutation under basal conditions induces a parallel leftward shift in the G - V curve. *Solid* lines represent the best-fit 4th power Boltzmann function. Each symbol and error bars represent the mean \pm SEM (n = 22 and 11, for wild-type and L317A mutant, respectively).

A crystal structure of the closed-state Kv1.x channel has yet to be reported making it a challenge to determine the exact molecular mechanism of modulation. Current models suggest that, following the ‘upward’ movement of the S4 voltage sensor, the final cooperative transition to the open state involves an interaction between the S4-S5 linker and the S6 tail, becoming more closely packed to create a cavity or pocket^{139,140}. Based on our evidence and previous work, it is likely that sevoflurane binds to a pocket formed by the S4-S5 linker and the S6 helix and thereby stabilizes the open conformation in its conducting state¹³⁸.

2.1.4. Conclusion

Understanding the unique mechanisms for sevoflurane is significant as it is the preferred anesthetic for children and concerns for anesthetic influences on neurodevelopment have arisen. However, identification of the molecular targets using conventional methods has been difficult due largely to the drug’s volatility and low binding affinities. Thus, a trifluoro-diazirine photoaffinity derivative of sevoflurane, or azisevoflurane(**1a**) was synthesized. Azisevoflurane(**1a**) was applied to investigate a pharmacological target distinct to sevoflurane, the voltage-gated Shaker Kv1.2 potassium channel, to identify the binding site(s) that lead to the observed positive modulation of the mammalian channel. Further application of azisevoflurane(**1a**) should provide an improved understanding of the full- repertoire of sevoflurane protein targets and binding sites and thereby a further understanding of volatile anesthetic molecular mechanisms.

2.1.5. Experimental methods

General Synthetic Procedures- Reagents and solvents were all acquired from commercial sources. ¹H, ¹³C NMR spectra were obtained on a Bruker DMX 500 MHz nuclear

magnetic resonance spectrometer and ^{19}F NMR spectra were obtained on a Bruker DMX 360 MHz nuclear magnetic resonance spectrometer.

Physicochemical properties- The density of azisevoflurane(**1a**) was calculated using triplicate measurements of the volume/mass relationship within sealed vials. The UV spectrum and extinction coefficient ($\Sigma_{305\text{ nm}} = 115\text{ M}^{-1}$) of the diazirine absorption were determined from methanolic solutions of azisevoflurane(**1a**) at known concentration. The maximal water solubility ($S_w = 1.25\text{ mM}$) was determined by triplicate titrations into phosphate buffered saline (pH 7.4) and calculated from the extinction coefficient. The rate of photoactivation was determined by reduction of the azisevoflurane(**1a**) diazirine peak within a methanolic solution during the course of 300 nm UV light exposure using a 1 cm pathlength quartz cuvette 5 cm from light source. The octanol/water partition coefficients were calculated using XLOGP3 with default settings ¹⁴³.

Horse Spleen apo-Ferritin (aF) fluorescence competition- The affinity of azisevoflurane(**1a**) was determined by equilibrium binding of increasing amounts of sevoflurane in the presence of constant concentrations of 1-aminoanthracene (1-AMA) and *aF*. Total volume 200 μL of 10 μM *aF*, 10 μM 1-AMA and concentrations of sevoflurane or azisevoflurane(**1a**) (0.3 μM -1 mM) in phosphate buffered saline (PBS) pH 7.4 were combined in 96-well plate on ice. The fluorescence spectrum of 1-AMA in each solution well was determined with 380 nm excitation and emission of 510 nm at 10°C. The fluorescence was corrected by simple math subtractions of baseline 1-AMA and *aF* fluorescence. Fluorescence intensity versus concentration data were fitted to variable slope Hill models. The Cheng-Prusoff equation was used to correct for the presence of the 1-AMA competitor ¹²⁶.

Isothermal titration calorimetry (ITC)- ITC studies were generated using a MicroCal™ iTC200 System (GE Healthcare Life Sciences). The calorimeter reference cell contained ddH₂O. 25 μM of apoferritin (*aF*) dimer in 0.22 μm filtered 130 mM NaCl, 20 mM sodium phosphate (pH 7.0) was centrifuged for 10 min at 14, 000 x g before being added into the calorimeter sample cell (200 μL). Sevoflurane or azisevoflurane(**1a**) were solubilized to 0.8 mM concentration in the same buffer. Either sevoflurane or azisevoflurane(**1a**) were titrated into the sample cell horse spleen *aF* solution from a 39.9 μL volume syringe. An initial 0.6 μL volume over 1.2 s was titrated followed by 2 μL volumes over 4 s thereafter with 3 min intervals between each injection. The measurements were carried out at 25 °C and data was corrected for heats generated from buffer into buffer, sevoflurane or azisevoflurane(**1a**) into buffer and buffer into *aF*. Enthalpy measurements generated were fit using Origin 5.0 (MicroCal, Inc.) to a single set of independent sites^{87,88}.

Tadpole immobility assay- Albino *Xenopus leavis* tadpoles were used to determine the relative anesthetic potency of azisevoflurane(**1a**) compared to sevoflurane. Groups of 10 tadpoles were placed in a 25 mL sealed glass Hamilton syringe containing 10mL of non-drugged pond water. A sealed 25mL glass syringe containing 25 mL of either 1.67 mM sevoflurane or 1 mM or azisevoflurane(**1a**) was connected using a two-way valve. Gently the tadpoles were exposed to set volumes of the drug-containing solution for 5 min. After 5 min the tadpoles were assessed for spontaneous moment as defined previously^{50,78}. After final exposure the tadpoles were removed from the syringe and allowed to recover in petri dishes containing non-drugged water. Tadpoles were observed the following day for toxicity.

Preparation of emulsified volatile anesthetics- Neat sevoflurane or azisevoflurane(**1a**) was added to 20% Intralipid® using gas-tight Hamilton syringes. Emulsions were formed via shear stress provided by passing the solutions through a 26-gauge needle between two gas-tight Hamilton syringes 20-30 times at 20-22°C. Emulsified sevoflurane and azisevoflurane(**1a**) were quantified using reverse phase-high performance liquid chromatography (rpHPLC) with a C-18 analytical column and a refractive index detector. Using an isocratic gradient (44:14:41.5 acetonitrile: isopropanol: 20 mM phosphate in ddH₂O) with 1 mL/min flow rate (20-22°C), sevoflurane had a retention time of 5.7 min. Emulsified azisevoflurane(**1a**) was quantified using diazine UV absorbance at 305 nm. Azisevoflurane(**1a**) had a retention time of 19.2 min with an isocratic gradient (35:12:53 acetonitrile: isopropanol: 20 mM phosphate in ddH₂O) at 1 mL/min flow rate (20-22°C). An initial preparation of 3.2 mg/mL azisevoflurane(**1a**) in Intralipid® provided 2.1 ± 0.1% (v/v%; mean ± SD) emulsified azisevoflurane(**1a**) determined by chromatography. Excess emulsified azisevoflurane(**1a**) from each rodent exposure was analyzed immediately after administration to confirm dosage.

Rodent studies- Emulsified sevoflurane 2.0 ± 0.2% (v/v%; mean ± SD) or azisevoflurane(**1**) 2.1 ± 0.1% (v/v%; mean ± SD) in 20% Intralipid® were introduced into 8-14 week CD-1 male mice via tail vein bolus injection. The hypnotic effects of emulsified anesthetics were measured using the loss of righting reflex (LORR) assay immediately after injection. Mice were placed in a supine position within a mouse chamber and the time at which the mice were able to right themselves was recorded. Mice were observed for 24-48 hr for toxicity.

Photolabeling of Horse spleen apoferritin (aF)- 50 µg of aF was suspended to 1 mg/mL in phosphate buffered saline (pH 7.4) with 0.5 mM azisevoflurane(**1a**). Samples were equilibrated in the dark for 5 min prior to being exposed to 300 nm RPR-3000 Rayonet lamp in 1-mm path length quartz cuvettes at through a WG295 295 nm glass filter (Newport Corporation) for 15 min. An exclusion list was generated from separate experiment where a sample was exposed to same filtered UV light without the presence of azisevoflurane(**1a**).

Shaker Kv1.2 channel plasmid construction and expression- A C-terminal Arg-Gly-Ser-His₁₀ tag was appended to the sequence of rat Kv1.2 using PCR, and the resulting gene was subcloned into the EcoRI and NotI sites of pFastBac1. This plasmid was then used to generate recombinant baculovirus. Kv1.2, which were both expressed in Sf9 cells by the Protein Expression Facility of the Wistar Institute (Philadelphia, PA, USA). Cells were incubated for 48-60 h post-infection.

Shaker Kv1.2 channel purification- All purification steps were carried out at 4 °C. A cell pellet from a one-liter growth was rapidly thawed and resuspended in 50 mL of lysis buffer (250 mM KCl, 25 mM imidazole, 50 mM potassium phosphate, 10 mM 2-mercaptoethanol, pH 7.6) containing 5 mM MgCl₂, 2 mM tris(2-carboxyethyl)phosphine (TCEP), 1 µg/mL each of DNase and RNase, and 1x protease inhibitor cocktail (Sigma-Aldrich). Cells were lysed by three strokes in a Potter-Elvehjem homogenizer. 10% (w/v) dodecyl-maltoside (DDM) was then added to the lysate to a final concentration of 1.5%, and the suspension was stirred for 1hr. Cell debris and insoluble material were removed by ultracentrifugation (164,000 x g, 1 hr). The resultant supernatant was syringe-filtered twice, first with a 5 µm PVDF filter and then with a 0.45 µm MCE filter. The doubly

filtered supernatant was loaded at 1 mL/min onto a 1 mL HiTrap IMAC HP column (GE Healthcare) equilibrated with buffer A (250 mM KCl, 25 mM imidazole, 50 mM potassium phosphate, 10mM 2-mercaptoethanol, 0.2% DDM, pH 7.6). The column was washed with 15 mL of 5% buffer B (identical to buffer A, except with 325 mM imidazole), followed by 15 mL of 15% buffer B. Protein was then eluted from the column with a 25 mL gradient from 15-100% buffer B. The column was washed with 25 mL of 100% buffer B to complete protein elution.

Fractions were analyzed by Western blotting, using HRP-conjugated anti-His antibody (Proteintech). Positive fractions were pooled and dialyzed against IEX start buffer (20 mM Tris-Cl, 0.1% DDM, 10 mM 2-mercaptoethanol (β ME), pH 8). The dialyzed protein was loaded at 1 mL/min onto a 1mL HiTrap Q HP column (GE Healthcare) previously equilibrated with IEX start buffer. The column was washed with 20 mL of IEX start buffer, and then eluted with a 50 mL gradient from 0-100% IEX elution buffer (start buffer + 500mM KCl). The column was washed with 20 mL of 100% IEX elution buffer. Fractions were analyzed by SDS-PAGE, using both Western blot analysis and Coomassie staining. Fractions containing protein were pooled and concentrated using 50-100kDa MWCO concentrators.

Photolabeling of Shaker Kv1.2 channel.- 25 μ g of Kv 1.2 were diluted to 0.5 mg/mL containing final concentrations of 20 mM TrisHCl, pH 7.2, 5 mM KCl, 5 mM β ME containing 1.75% DDM with or without 1 mM azisevoflurane (**1a**). Samples were equilibrated in the dark for 5 min prior to being exposed to 300 nm RPR-3000 Rayonet lamp in 1-mm path length quartz cuvettes through a WG295 295nm glass filter (Newport

Corporation) for 15 min. Exclusion lists were generated using samples exposed to same filtered UV light without the presence of azisevoflurane(**1a**).

In-solution digestion of proteins- 20 µg of protein was participated with chilled acetone and air dried for 3-5 min. Proteins were solubilized and digested with ProteaseMax™ Surfactant trypsin enhancer using product instructions. For detailed methods, see supporting information. Pellet was first solubilized in 20 uL 0.2% (w/v %) ProteaseMax™ Surfactant in 50 mM NH₄HCO₃ for 1 hr at room temperature and then diluted with 73.5 uL 50 mM NH₄HCO₃. Following 1 uL 0.5 M DTT was added and sample was incubated at 56° C for 20 min. 2.7 uL of 0.55 M iodoacetamide was then added and protein sample was incubated at room temperature in the dark for 15 min. After 1 uL of 1% (w/v%) ProteaseMax™ Surfactant was added followed by CaCl₂ to 1 mM final concentration. 1.8 uL of 1 µg/µL porcine sequencing trypsin (Promega) was added and samples were incubated at 37 °C for 3 hr with mild agitation. Samples were centrifuged for 10 min at 16, 000 x g, the supernatant was removed and trifluoroacetic acid (TFA) was added to a final concentration of 0.5% (v/v %). Samples were incubated at room temperature for 5 min. Samples were snap frozen with dry ice and stored at -80 °C until further processing. 20 µg of sample was desalted using C18 stage tips prepared in house and the elution was dried by speed vac. Prior to MS analysis the peptide digestion was resuspended in 0.1% formic acid.

Mass spectrometry- Digested protein preparations were analyzed by Orbitrap Elite™ Hybrid Ion Trap-Orbitrap Mass Spectrometer (MS) coupled to an Easy-nanoLC 1000 system with a flow rate of 3 µL/min. Data dependent acquisition mode was applied with a dynamic exclusion of 45 s. in every cycle, one full MS scan was collected with a scan

range of 350 to 1500 m/z . An exclusion list of MS1 precursor ions of non-photolabeled protein sample was imported into the precursor mass parameter in Xcalibur allowing for a 10 min retention window. Spectral analysis was conducted using Thermo Proteome Discoverer 2.0 (Thermo Scientific) and the Mascot Daemon search engine using horse ferritin light chain sequence provided by UniProt database (UniProtKB: P02791) or a customized database containing the sequence for the expressed rat Kv1.2 with appended Arg-Gly-Ser-His10 tag. All analyses included dynamic oxidation of methionine (+15.9949 m/z) and static alkylation of cysteine (+57.0215 m/z ; iodoacetamide alkylation). Photolabeled samples were run with the additional azisevoflurane(**1a**) modification (+230.0559 m/z), the false discovery rate of 0.01% allowing for up to 2 missed cleavages and setting a fragment ion mass tolerance of 0.500 Da and a parent ion tolerance of 10 ppm.

Docking . Horse spleen apo-ferritin (aF)- The biological assembly of the aF dimer complex with pentobarbital (PDB code: 3RAV) solved at 1.9 Å resolution was used for docking simulations. Prior to docking pentobarbital, sulfate, and Cd⁺ were removed using PYMOL. For docking the protein, hydrogens and Kollman charges were added and nonpolar hydrogens were merged using AutodockTools4. Molecular coordinates for sevoflurane were downloaded from the ZINC small molecule library¹⁴⁴ using provided physical representations. The molecular coordinates for azisevoflurane(**1a**) were generated using MarvinSketch version 16.3.28.0. In AutodockTools4 Geisteiger charges were added and nonpolar hydrogens were merged. A maximum of 4 and 5 torsions were allowed for sevoflurane and azisevoflurane(**1a**) respectively (i.e., ligands were fully flexible). Residue side chains projecting towards the cavities were flexible during

docking runs with AutoDock Vina. The grid box was centered within the *aF* monomer interfacial region or within the *aF* dimer interface sized to 22x24x22 points with 1 Å resolution for both experiments. For either ligand, 30 docking results were generated using an exhaustiveness of 300, other genetic algorithm search parameters and docking protocol were set as default. Scores were evaluated based off the upper bound RMSD values. Images and distance measurements were prepared using PYMOL.

Docking Kv1.2 transmembrane region. The biological assembly of rat F233W mutant of the Kv2.1 paddle-Kv1.2 chimera channel crystal structure (PDB code: 3LNM) solved at 2.9 Å resolution was used for docking simulations. Prior to docking water, NADP⁺, potassium and phosphatidylglycerol were removed using PYMOL. To focus on the transmembrane domain of Kv1.2 subunit interfaces within docking studies, we removed L36-E120 from the B chain and the full A, C and D chains and joined two subunits in the same biological assembly provided¹⁴⁵ before loading into AutoDockTools¹⁴⁶. AutoDockTools¹⁴⁶ preparation of the Kv1.2 assembly and sevoflurane for docking were completed as mentioned above. For docking, the grid was targeted the S4-S5 linker and S6 interaction region at the interface of the two subunits. Flexible residue side chains and AutoDock Vina¹⁴⁷ were programmed as mentioned above.

Heterologous Kv1.2 channel expression in Xenopus oocytes. Plasmid maintenance, mutagenesis, sequence, RNA synthesis and oocyte microinjection were carried out as previously described¹³⁰. Briefly, defolliculated stage V-VI *Xenopus laevis* (*X. laevis*) oocytes were microinjected with *in vitro* transcribed cRNA (mMessage mMachine kit, Ambion, Austin, TX). Oocytes were incubated at 18°C for 1-2 days before electrophysiological characterization. All animal care and experimental procedures

involving were carried out according to a protocol approved by the IACUC of Thomas Jefferson University.

Electrophysiological characterization of Kv1.2 expressed in Xenopus oocytes- Whole-oocyte currents were recorded at room temperature (21-23°C) under two-electrode voltage-clamping conditions (OC-725C, Warner Instrument, Hamden, CT). The microelectrodes were filled with 3 M KCl and recordings were completed as previously reported¹³⁰. Briefly, a stable current baseline was determined by repeating voltage steps to +40 mV from a holding potential of -100 mV while oocytes were bathed in ND96 (in mM: 96 NaCl, 2 KCl, 1 MgCl₂, 1.8 CaCl₂, 5 HEPES, 2.5 Na-Pyr, pH 7.4 with NaOH). Responses were collected once currents reached a stable level. ND96-based solutions of sevoflurane or azisevoflurane(**1a**) were freshly prepared by sonication under gas-tight conditions. Solution delivery was conducted with a gas-tight syringe and Teflon tubing. Data acquisition, leak subtraction and initial analysis were performed using pClamp 10.3 (Molecular Devices, Sunnyvale, CA).

G-V curves were described by assuming this form of the 4th order Boltzmann equation:

Equation 2.

$$G = \frac{G_{max}}{\left(1 + e^{\frac{(V_c - V_s)}{k}}\right)^4}$$

Where *G* is the peak chord conductance; *G*_{max} is the maximum conductance; *k* is the slope factor; *V*_{*c*} is the command voltage; and *V*_{*s*} is the activation midpoint voltage of a single subunit. *V*_{1/2}, the midpoint voltage of the peak conductance curve, was calculated as follows:

Equation 3.

$$V_{1/2} = 1.665 k + V_s$$

The equivalent gating charge (z) was calculated as follows:

Equation 4.

$$z = RT/Fk = 25.5/k$$

Where R , T and F are the gas constant, absolute temperature and Faraday constant, respectively.

To display the results from different oocytes and estimate the magnitude of relative changes, individual G - V relations were normalized to the control G_{\max} before exposure to sevoflurane/azisevoflurane(**1a**) because all data were obtained from paired experiments (same oocyte in the absence and presence of the anesthetics). Accordingly, a relative $G = 1$, <1 and >1 indicates no change, inhibition and potentiation, respectively. Data analysis, plotting and curve fitting were performed in OriginPro 9.1 (OriginLab, Northampton, MA).

Statistics- GraphPad Prism 7, unless otherwise noted, was used for preparation and statistical data analysis.

Study Approval- All animal care and experimental procedures involving *X. laevis* tadpoles and rodents were carried out according to a protocol approved by the IACUC of University of Pennsylvania. All animal care and experimental procedures involving *Xenopus* frogs were carried out according to a protocol approved by the IACUC of Thomas Jefferson University.

2.2. Mechanistic basis for $GABA_A$ receptor modulation by volatile general anesthetics

γ -aminobutyric acid (GABA) is well established as the major inhibitory neurotransmitter within the adult mammalian brain. The majority of GABA inhibitory activity is a consequence of binding to the GABA Type A (GABA_A) receptors, a member of the pentameric ligand-gated channel (pLGIC) superfamily. GABA_A receptors are largely heteromeric protein complexes composed of five homologous subunits. These subunits are expressed in a pseudosymmetric manner to form a chloride-selective pore. Numerous investigations have indicated that synaptic GABA_A receptors are vital in for postsynaptic hyperpolarization and contribute to presynaptic neurotransmitter release^{148–151}. Synaptic GABA_A receptors are predominately a 2 $\alpha_{(1-3)}$:2 $\beta_{(1-3)}$:1 $\gamma_{(1-3)}$ stoichiometry^{152,153} organized in an alternating order (e.g. $\gamma\alpha\beta\alpha\beta$ anti-clockwise as seen from synaptic cleft)^{152–154}. As a consequence, numerous potential ligand binding sites exist including at least four distinct subunit interfaces; $\alpha+\gamma-$, $\alpha+\beta-$, $\beta+\alpha-$, and $\gamma+\beta-$.

Since the mid-20th century, mounting evidence has suggested that GABA_A receptors are significant functional protein targets involved general anesthetic mechanisms^{155–158}. The majority of general anesthetics enhance receptor activity at clinically relevant concentrations⁶. Within the past decade the focus has largely been on identifying binding sites for intravenous anesthetics, such as propofol and etomidate¹⁵⁹; however the sites for volatile anesthetics remains unclear. Sevoflurane and isoflurane (Figure 12) are volatile anesthetics widely used in clinics. Both anesthetics have been shown to effect synaptic transmission within the central nervous system and enhance synaptic GABA_A receptor activity^{156,160}. It has been reported that α_1 mutations can influence isoflurane and sevoflurane positive modulation of the receptor¹⁶⁰. Isoflurane at clinical concentrations has shown to prolong both fast and slow forms of phasic GABA_A

receptor-mediated inhibition in mouse hippocampal neurons¹⁶¹ and ‘knock-in’ mutations within α_1 or β_3 subunits within mice have resulted in, to varying degrees, right-shifts of anesthesia endpoints for volatile anesthetics^{162,163}. These studies, while providing evidence for the role of synaptic GABA_A receptors in sevoflurane and isoflurane mechanisms of action, do not define the direct binding site(s) of these ligands within the receptor. Indeed, it is unclear whether the mutated proteins provide suitable model systems and/or the inhibition is a product of allosterically perturbing the binding site(s). Furthermore mutagenesis leaves some ambiguity to the location of the anesthetic binding cavity relative to the mutated residue; therefore complementary methodologies are necessary.

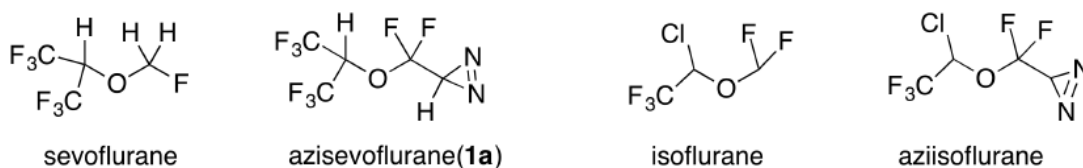


Figure 12. Chemical structures of volatile anesthetics and corresponding anesthetic-photoaffinity ligands.

It is critical to define these sites for volatile agents in synaptic GABA_A receptors due to 1) the likely significant contribution that these and other pLGICs within volatile anesthetic mechanisms and 2) to determine underlining mechanisms that may lead to potential receptor subunit selectivity of these agents. Within the following investigation two *α*-PALs for the volatile anesthetics sevoflurane and isoflurane, azisevoflurane(**1a**) and aziisoflurane⁵⁰ respectively (Figure 12), were applied to identify binding sites within human $\alpha_1\beta_3\gamma_{2L}$ and $\alpha_1\beta_3$ GABA_A receptors. Azisevoflurane(**1a**) and aziisoflurane labeled multiple sites within $\alpha_1\beta_3\gamma_{2L}$ and $\alpha_1\beta_3$ GABA_A receptors largely located within the

transmembrane domain (TMD). Photoaffinity labeled residues strongly suggests a shared volatile anesthetic binding site within the β +/ α - interface that overlaps with a previous positive modulatory site identified for intravenous anesthetics. Selective interfacial photoaffinity labeling within the α +/ β - interface aligns with previous mutagenesis studies implicating this interface as a volatile anesthetic binding site. Potential intra- and/or interfacial volatile anesthetic binding within γ subunit-containing sites were identified, however functional contributions of the occupancy of these sites remain to be further defined.

2.2.1. Purified $\alpha_1\beta_3\gamma_{2L}$ GABA_A receptor generation and volatile α -PAL competition for photoaffinity radiolabeling

$\alpha_1\beta_3\gamma_{2L}$ GABA_A receptors are considered among the most abundant synaptic GABA_A receptors within the adult mammalian brain¹⁴⁸. These receptors are also noted to be difficult to heterologously express as functionally active receptor, in particular the γ_2 subunit has been reported to be difficult to incorporate during assembly^{164,165}. A previously successful tetracycline-inducible HEK293 cell line was applied that includes a (GGG)₃GK (or L3) linker and 1D4 epitope to the C-terminus of the γ_{2L} GABA_A receptor subunit¹⁶⁴. The additional 1D4 epitope within the FLAG- $\alpha_1\beta_3\gamma_{2L}$ -(L3)-1D4 GABA_A receptor allows for enhanced affinity purification and validation of γ_{2L} containing receptor. The full, assembled FLAG- $\alpha_1\beta_3\gamma_{2L}$ -(L3)-1D4 GABA_A receptor was validated by the proper stoichiometry (2:1) of [³H]muscimol (a GABA-mimetic that shares binding sites within the two β +/ α - interfaces per receptor) and [³H]flunitrazepam (a benzodiazepine that binds within a single α +/ γ - interfacial binding site per receptor) binding. The additional affinity tags have shown to have no significant effect on the

functional activity of the receptor, including response to positive modulators¹⁶⁴. To solubilize the receptors from membrane preparations, n-dodecyl- β -D maltopyranoside (DDM) was used¹⁶⁴. The receptors were then purified with anti-FLAG and/or anti-1D4 affinity columns before reconstitution directly from the beads with washes using 3-[(3-cholamidopropyl)dimethylammonio]-1-propanesulfonate (CHAPS)/asolectin. Approximant specific activity and purification were determined by [³H]muscimol binding.

Previously, photoaffinity radiolabeling with radioactive isotope-containing *a*-PALs has been used to demonstrate photomodification(s) of proteins^{93,57,80}, unfortunately due to significant synthetic challenges, a radioactive isotope could not be incorporated into the volatile *a*-PAL structures. Protection from or competition for photoaffinity radiolabeling using various anesthetics or *a*-PALs have also been used to gather further evidence for protein binding sites^{166,69,76}. Indeed propofol and the corresponding PAL *meta*-azipropofol (AziPm) inhibit [³H]azietomidate photoaffinity radiolabeling within $\alpha_1\beta_3$ GABA_A receptors and likely have shared and/or overlapping binding site(s) within $\alpha_1\beta_3\gamma_{2L}$ GABA_A receptors^{159,76}. Similarly it has been shown that isoflurane was able to protect from [³H]azietomidate photoaffinity radiolabeling of GABA_A receptor purified from bovine brain⁶⁹. Likely due to the differences in binding affinity as well as the multiple factors that interplay during photoaffinity labeling protection (see section 1.2.2.), such studies utilizing volatile anesthetics and [³H]AziPm have not been realized for GABA_A receptors. Therefore we applied azisevoflurane(**1a**) and aziisoflurane as competing *a*-PALs during the [³H]AziPm photoaffinity radiolabeling of purified $\alpha_1\beta_3\gamma_{2L}$ GABA_A receptors.

FLAG- $\alpha_1\beta_3\gamma_{2L}$ -(L3)-1D4 GABA_A receptors were equilibrated with 1:25 molar ratio of [³H]AziPm: azisevoflurane(**1a**) or aziisoflurane in the presence of GABA. Receptors were simultaneously irradiated with two UV lamps with two optimal transmission wavelengths, 300 nm (associated with a 295 nm low pass filter) and 350 nm (associated with a 305 nm low pass filter) for volatile *a*-PAL and [³H]AziPm photoactivation respectively. The irradiated receptors were separated by SDS-PAGE and excised bands were counted for radioactivity. With the addition of the low pass filters no overt damage to the FLAG- $\alpha_1\beta_3\gamma_{2L}$ -(L3)-1D4 GABA_A receptor subunits by the UV irradiation was observed as displayed by SDS-PAGE. Predominate bands spanning above the 50kDa molecular weight marker were present corresponding with the expected molecular weight for subunits are 52-55kDa¹⁶⁴.

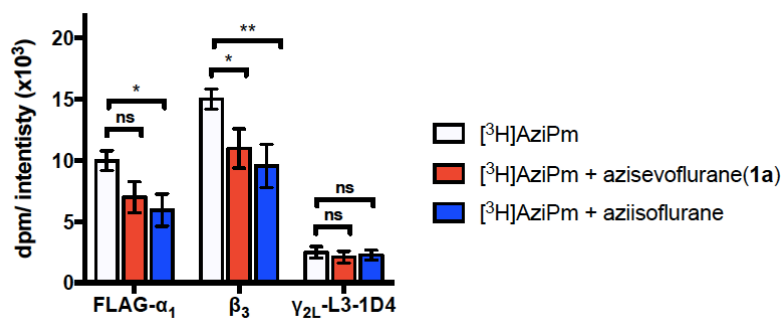


Figure 13. Inhibition [³H]AziPm photoaffinity radiolabeling of FLAG- $\alpha_1\beta_3\gamma_{2L}$ -(L3)-1D4 GABA_A receptor by azisevoflurane(**1a**) and aziisoflurane. Competition radiolabeling labeling assay with [³H]AziPm, azisevoflurane(**1a**) and aziisoflurane photoaffinity labeling of FLAG- $\alpha_1\beta_3\gamma_{2L}$ -(L3)-1D4 GABA_A receptor subunits separated by SDS-PAGE. Dpm represents disintegrations per minute, intensity was measured as the optical density of the coomassie blue stained bands multiplied by the band area (mm²). Results were analyzed by 2way-ANOVA with Dunnett's multiple comparisons test comparing photoaffinity competition samples to [³H]AziPm control, (*, p<0.05; **, p<0.01; ns, not significant). Error values are represented as mean ± SEM

Azisevoflurane(**1a**) and aziisoflurane both inhibited [³H]AziPm photoincorporation into FLAG- α_1 and β_3 subunits of FLAG- $\alpha_1\beta_3\gamma_{2L}$ -(L3)-1D4 GABA_A receptors (Figure 13). Within bands at molecular weight corresponding to the FLAG- α_1

subunit, aziisoflurane significantly decreased the [³H]AziPm radiolabeling by ~41% (p-value = 0.0280; two-way ANOVA Dunnett's multiple comparisons test). A ~30% inhibition in [³H]AziPm photoaffinity radiolabeling was observed when azisevoflurane(**1a**) was included however these results did not reach significance (p-value = 0.1167; two-way ANOVA Dunnett's multiple comparisons test). Within bands corresponding to the molecular weights of the β₃ subunit, both azisevoflurane(**1a**) and aziisoflurane significantly decreased [³H]AziPm photoincorporation by ~27% (p-value = 0.0275; two-way ANOVA Dunnett's multiple comparisons test) and ~36% (p-value = 0.0030; two-way ANOVA Dunnett's multiple comparisons test) respectively. Neither volatile *a*-PALs significantly inhibited [³H]AziPm photoincorporation into the γ_{2L}-(L3)-1D4 subunit (Figure 13); although considering the relative lower levels of photoaffinity radiolabeling by [³H]AziPm and/or potential alternative unshared binding site(s), this study does not rule out potential azisevoflurane(**1a**) or aziisoflurane photoaffinity labeling of the γ subunit residues.

Together the inhibition of [³H]AziPm photoaffinity radiolabeling indicates successful photoaffinity labeling of FLAG- α₁ and/or β₃ subunit residues by the volatile *a*-PALs. Furthermore the competition for [³H]AziPm photoaffinity labeling aligns with previous evidence suggesting shared and/or overlapping binding sites between the intravenous and volatile anesthetics within synaptic GABA_A receptors^{160,69,76}. While providing an initial assessment for volatile *a*-PAL binding to α₁β₃γ_{2L} GABA_A receptors, the results from this study cannot be fully extended to localization of or affinity for volatile anesthetic binding sites. The observed competition by azisevoflurane(**1a**) and aziisoflurane for [³H]AziPm photoaffinity radiolabeling, albeit considered unlikely due to

the low EC50s¹¹⁸, might be a result of an allosteric mechanism resulting in decreased [³H]AziPm binding. Furthermore the differences in quantum yield of photoactivation or Ψ (see section 1.2.1) between all three α -PALs as well as the effect of the cumulative exposure of multiple UV wavelengths prevents accurate quantitative evaluation of binding affinity. Protein microsequencing would be necessary to identify the volatile α -PAL photomodified residues and provide evidence for potential volatile anesthetic binding sites within $\alpha_1\beta_3\gamma_{2L}$ GABA_A receptors.

2.2.2. Volatile α -PAL photoaffinity labeling of $\alpha_1\beta_3\gamma_{2L}$ & $\alpha_1\beta_3$ GABA_A receptors

For the micro-level identification of volatile α -PAL photomodification sites reverse phase High Performance Liquid Chromatography coupled tandem mass spectrometry (rpHPLC-MS/MS) for protein microsequencing was employed. Purified FLAG- $\alpha_1\beta_3\gamma_{2L}$ -(L3)-1D4 GABA_A receptors were prepared as above. Aziseovflurane(**1a**) or aziisoflurane were directly solubilized into the receptor containing sample and allowed time to equilibrate within the system before UV irradiation with 300 nm UV lamp with the addition of a 295 nm low pass filter. After irradiation, receptors were concentrated and subjected to either in-solution or in-gel sequential trypsin/chymotrypsin protease digests. The resulting spectra from rpHPLC-MS/MS were analyzed using a customized database containing the heterologously expressed receptor sequences¹⁶⁷.

There was sufficient coverage of each GABA_A receptor subunit with 95:85:78% (FLAG- $\alpha_1:\beta_3:\gamma_{2L}$ -(L3)-1D4 % coverage) for aziseovflurane(**1a**) and 95:88:84%(FLAG- $\alpha_1:\beta_3:\gamma_{2L}$ -(L3)-1D4 % coverage) for aziisoflurane photoaffinity experiments (see appendix A.3.3.-A.3.4.). Within aziseovflurane(**1a**) photoaffinity labeled receptor, a total of eight residues within seven unique peptides were identified to contain the mass to

charge (m/z) change indicative of the α -PAL photomodification. The FLAG- α_1 subunit contained the highest relative degree of photomodification by aziseovflurane(**1a**) with five residues demonstrating modification (Ser-276/241, Arg-290/255, Val-295/260, Thr-296/261 and Thr-300/265; residues corresponding FLAG/non-FLAG tagged α_1 subunit) within four unique peptides. The β_3 subunit displayed the least detected aziseovflurane(**1a**) photomodified residues with the single Ala-248 detected as containing photomodification. Within the γ_{2L} -(L3)-1D4 subunit, two aziseovflurane photomodified residues, Leu-268 and Gly-269, on two unique peptides were identified (see appendix A.4.3.). A total of nine aziisoflurane modified residues within seven unique peptides were detected in photoaffinity labeled FLAG- $\alpha_1\beta_3\gamma_{2L}$ -(L3)-1D4 GABA_A receptors. Comparatively the β_3 subunit displayed the highest number of modified residues detected with five residues (Ile-222, Gln-224, Trp-226, Ile-255, and Ile-264) on three unique peptides. Three modified residues were detected within the FLAG- α_1 subunit (Glu-285/250, Ser-311/276, and Pro-313/278; residues corresponding FLAG/non-FLAG tagged α_1 subunit) on three unique peptides. Finally only one residue within the γ_{2L} -(L3)-1D4 subunit (Trp-241) was detected with an aziisoflurane modified residue (see appendix A.4.4.).

It should be noted that in the case of the γ_{2L} subunit, relative to the other subunits, showed the least protein coverage (~4-18% less than the FLAG- α_1 or β_3 subunits) within both aziseovflurane(**1a**) and aziisoflurane photoaffinity labeled receptor; therefore some photomodified residues might not be represented. Multiple factors could have contributed to the decrease including the relative subunit abundance, protease digest efficiency and/or the photomodifications themselves as discussed in section 1.2.2. Notably the γ_{2L} subunit

third transmembrane domain (TMD) helix (γ M3) consistently was not detected within photoaffinity labeled receptors with ~40-78% coverage. This is in contrast to FLAG- α_1 and β_3 subunits that showed 100% and 93-100% coverage despite being within the same experiments and having fair homology. As such we cannot rule out further photoaffinity labeled residues within this region of the subunit.

A difficulty when evaluating potential photoaffinity labeled sites within a complex oligomer is that single protein interface can be present in multiple distinct binding cavities. Within $\alpha_1\beta_3\gamma_{2L}$ GABA_A receptors, the $\alpha+$ and $\beta-$ subunit interfaces are present in two of three separate interfacial sites ($\alpha+/\beta-$ and $\alpha+/\gamma-$ or $\gamma+/\beta-$). In order further resolve these sites, heterologously expressed $\alpha_1\beta_3$ GABA_A receptors were photoaffinity labeled with azisevoflurane(**1a**) or aziisoflurane. Removing the γ subunit from the system provides evidence for of $\alpha+/\beta-$ interfacial binding without interference from $\alpha+/\gamma-$ or $\gamma+/\beta-$ interfacial binding. Purified and functionally active human FLAG- $\alpha_1\beta_3$ GABA_A receptors were generated using a previously published tetracycline-inducible HEK293 cell line with receptor solubilization and purification methods similar to that described above¹⁶⁷. The FLAG-tagged receptor maintains a stable cell line with concentration dependent response to GABA comparable to that of $\alpha_1\beta_3$ GABA_A receptors and positive modulation by anesthetics is also retained by the FLAG-tagged receptors¹⁶⁷. The system composition used during photoaffinity labeling and downstream sample preparation and MS microsequencing of photoaffinity labeled FLAG- $\alpha_1\beta_3$ GABA_A receptors was the same as FLAG- $\alpha_1\beta_3\gamma_{2L}$ -(L3)-1D4 GABA_A receptors noted above.

Both FLAG- α_1 and β_3 GABA_A receptor subunits displayed ample coverage with 92: 89% (FLAG- α_1 : β_3 % coverage) for azisevoflurane(**1a**) and 91: 81% (FLAG- α_1 : β_3 %

coverage) for aziisoflurane photoaffinity labeling experiments (see appendix A.3.5-A.3.6). A total of four residues on four unique peptides within the FLAG- α_1 subunit (Gly-139/104, Cys-269/234, Pro-288/253, and Val-292/257; residues corresponding FLAG/non-FLAG tagged α_1 subunit) and five residues on four unique peptides within the β_3 subunit (Glu-179, Pro-184, Trp-241, Ala-249, Thr-256, and Leu-417) were photolabeled by azisevoflurane(**1a**) (see appendix A.4.5.). Seven aziisoflurane photomodified residues (Asn-138/103, Thr-265/230, Ile-274/239, Leu-275/240, Val-287/252, Ile-306/271 and Ser-307/272; residues corresponding FLAG/non-FLAG tagged α_1 subunit) on five unique peptides were detected within FLAG- α_1 subunit of FLAG- $\alpha_1\beta_3$ GABA_A receptors. Within the β_3 subunit three residues (Ala-45, Thr-266 and Val-290) on three unique peptides were detected with aziisoflurane photomodifications (see appendix A.4.6.).

2.2.3. Volatile anesthetic binding in $\alpha_1\beta_3\gamma_{2L}$ GABA_A receptor homology models

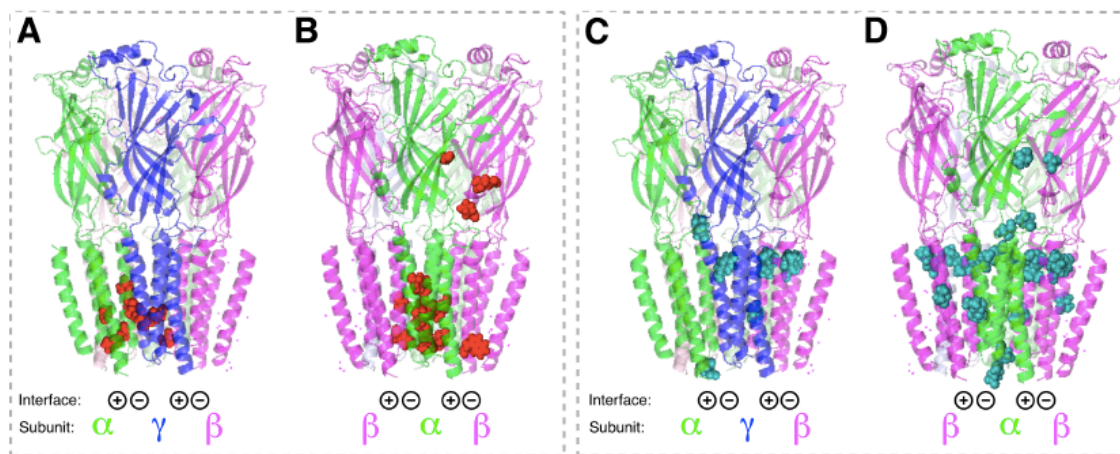


Figure 14. Locations of the photomodified residues by azisevoflurane(**1a**) and aziisoflurane from FLAG- $\alpha_1\beta_3\gamma_{2L}$ -(L3)-1D4 and/or FLAG- $\alpha_1\beta_3$ GABA_A receptor photoaffinity labeling studies. Detected photomodified residues (spherical structure) by azisevoflurane(**1a**) (A-B; red) or aziisoflurane (C-D; teal) within $\alpha_1\beta_3\gamma_{2L}$ -(L3)-1D4 (A-D) and FLAG- $\alpha_1\beta_3$ (B,D) GABA_A receptors.

The locations of the photomodified residues by azisevoflurane(**1a**) and aziisoflurane from all GABA_A receptors photoaffinity labeling studies are shown in Figure 14 using a previously published homology model of the $\alpha_1\beta_3\gamma_2$ GABA_A receptor¹⁶⁸ based-off the glutamate-gated chloride channel (GluCl) of *Caenorhabditis elegans* (PDB ID: 3RHW). For each FLAG- $\alpha_1\beta_3\gamma_{2L}$ -(L3)-1D4 or FLAG- $\alpha_1\beta_3$ GABA_A GABA_A receptor the 8-10 residues were detected to contain volatile *a*-PAL photomodification. It is likely that the multiple but largely localized photomodifications reflects the high motility and lower binding affinities of these volatile anesthetics within protein cavities^{87,88}. Volatile anesthetics and *a*-PALs generally show higher flexibility with more rotatable bonds compared to their nearest sized intravenous anesthetic counterparts. Therefore it is likely for the volatile *a*-PALs to insert into a range of potential residues within a single binding site.

The majority of detected photoaffinity labeled residues by the volatile *a*-PALs appear to be within or near the membrane spanning helices of each subunit. Previous evidence has indicated that the majority of the likely pharmacologically relevant binding sites for intravenous anesthetics are likely located in TMD of GABA_A receptors¹⁵⁹ and the selective photoaffinity labeling of the TMD residues by azisevoflurane(**1a**) and aziisoflurane extends this hypothesis to volatile anesthetics. To investigate the potential of the anesthetics to occupy the cavities within the TMD, docking experiments with sevoflurane and isoflurane were conducted for each of the binding cavities provided by the four distinct GABA_A receptor subunit dimers (α/γ , α/β , β/α , and γ/β) using AutoDock Vina¹⁴⁷. Docking included the one intersubunit and two intrasubunit cavities present within the dimer and all cavity-facing residues made flexible.

Views of sevoflurane and isoflurane docking poses within α/γ cavities are shown in (Figure 15) with corresponding α -PAL labeled residues within the interfacial cavity forming helices (Figure 16A). All of the generated docked poses for sevoflurane were located within the $\alpha+\gamma$ - interfacial cavity (Figure 15B-C). Docking experiments appeared to correlate well with FLAG- $\alpha_1\beta_3\gamma_{2L}$ -(L3)-1D4 GABA_A receptor photoaffinity labeling experiments with poses being within at least 3 Å of at least one residue labeled by

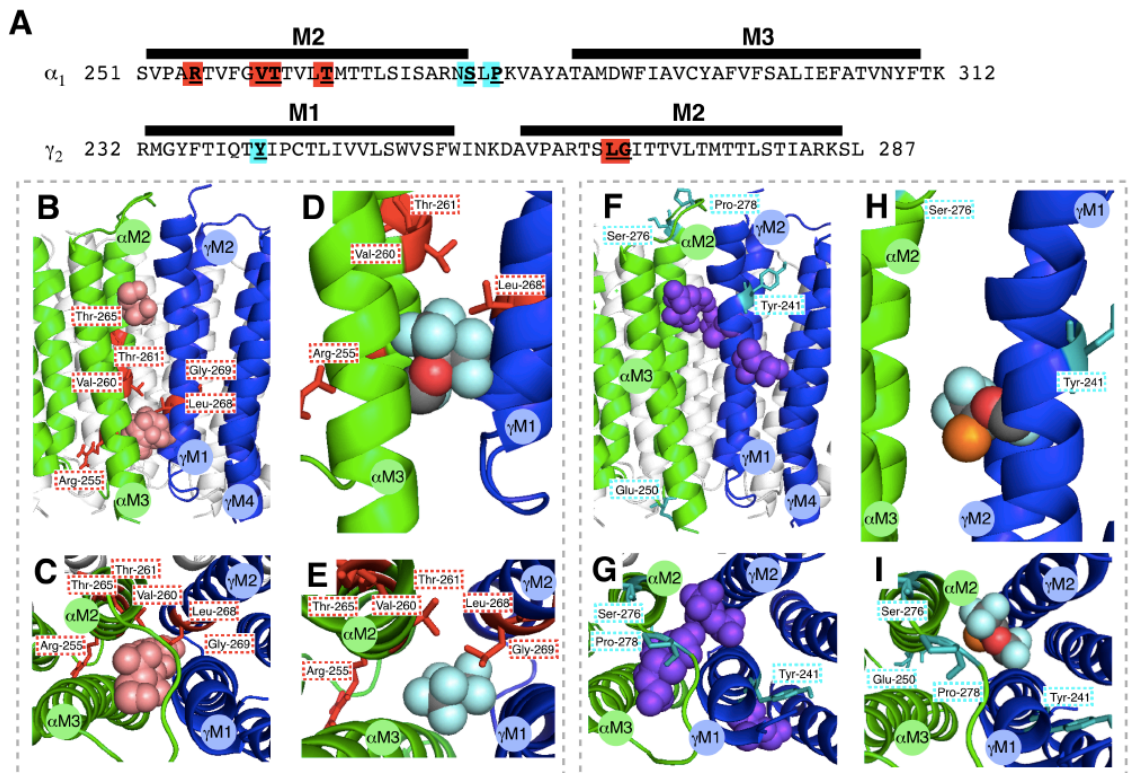


Figure 15. Sevoflurane and isoflurane docking poses in the $\alpha_1\beta_3\gamma_{2L}$ GABA_A receptor at the $\alpha+\gamma$ -TMD interface with photoaffinity labeled residues. Sequences (A) of $\alpha+\gamma$ -TMD interfacial helices (α_1 M2-M3 and γ_{2L} M1-M2) are shown with corresponding residues (bold, underlined) labeled within $\alpha_1\beta_3\gamma_{2L}$ GABA_A receptors by azisevoflurane(1a) and aziisoflurane highlighted in red and cyan respectively. Views of the $\alpha+\gamma$ -TMD interface of an $\alpha_1\beta_3\gamma_{2L}$ GABA_A receptor homology model¹⁶⁸ based-off the glutamate-gated chloride channel (GluCl) of *Caenorhabditis elegans* (PDB ID: 3RHW) from the lipid (B,D, F,H) or the base of the extracellular domain (C,E,G,I) with the α and γ subunit shown in green and blue respectively and TMD helices labeled within colored circles. Five scored docking poses are shown in spherical representations for sevoflurane (B-C; salmon) and isoflurane (F-G; purple). The highest scored docking pose for sevoflurane (D-E) and isoflurane (H-I) are shown as spherical representations with carbon, oxygen, fluorine, and chloride colored as gray, red, cyan, and orange respectively.

Corresponding azisevoflurane(1a) labeled residues within $\alpha_1\beta_3\gamma_{2L}$ (red dashed boxes) GABA_A receptors are shown as red stick representations at highest scored docking poses. Corresponding

aziisoflurane labeled residues within $\alpha_1\beta_3\gamma_{2L}$ (cyan dashed boxes) GABA_A receptors are shown as teal stick representations at highest scored docking poses and labeled in dashed boxes.

azisevoflurane(**1a**). This included the lowest energy pose for sevoflurane (Figure 15D-E) that was $< 2.5 \text{ \AA}$ from the azisevoflurane(**1a**) modified residue γ Leu-268. The majority of isoflurane docking poses were also located within the α^+/γ^- interfacial cavity (Figure 15F-G) including the lowest energy docking pose (Figure 15H-I). However it should be noted that the second highest scoring pose was located at the exterior of the dimer situated within a small cavity formed by the γ M1 and γ M4 helices. In contrast to the sevoflurane docking experiments, generated docking poses for isoflurane were a relative fair distance $> 5 \text{ \AA}$ from any detected aziisoflurane photomodified residue.

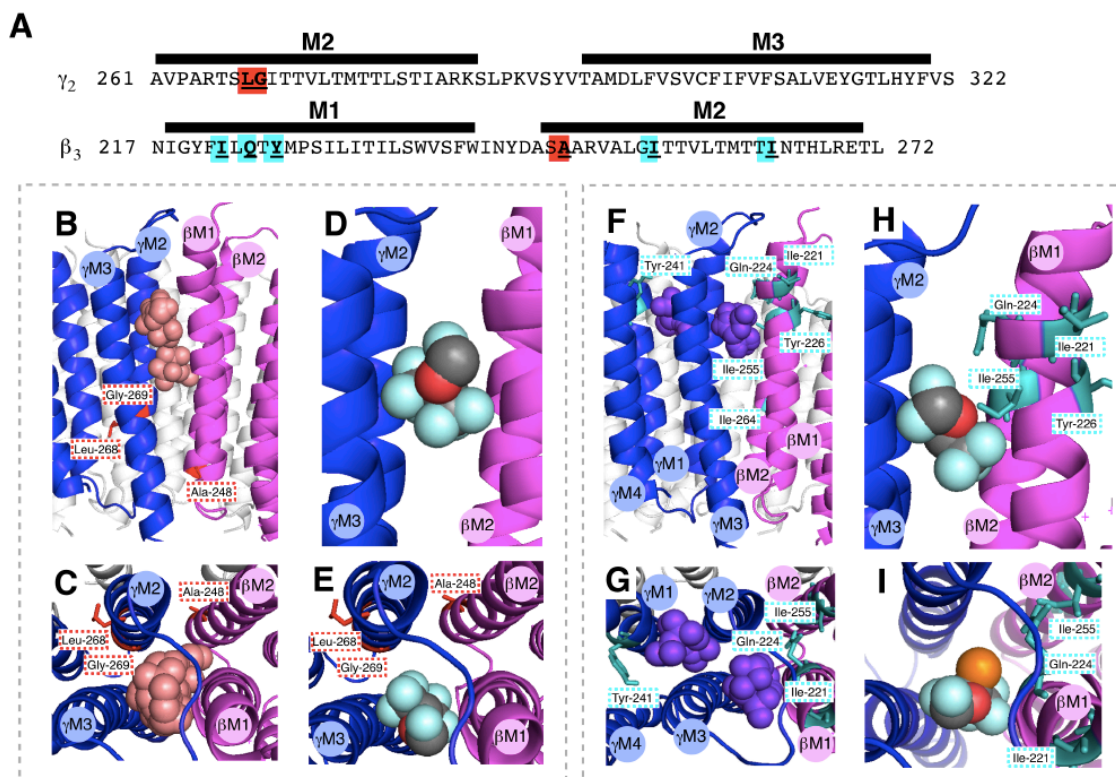


Figure 16. Sevoflurane and isoflurane docking poses in the $\alpha_1\beta_3\gamma_{2L}$ GABA_A receptor at the γ^+/β^- TMD interface with photoaffinity labeled residues. Sequences (A) of γ^+/β^- TMD interfacial helices (γ_{2L} M2-M3 and β_3 M1-M2) are shown with corresponding residues (bold, underlined) labeled within $\alpha_1\beta_3\gamma_{2L}$ GABA_A receptors by azisevoflurane(**1a**) and aziisoflurane highlighted in red and cyan respectively. Views of the γ^+/β^- TMD interface of an $\alpha_1\beta_3\gamma_{2L}$ GABA_A receptor homology model¹⁶⁸ based-off the glutamate-gated chloride channel (GluCl) of *Caenorhabditis*

elegans (PDB ID: 3RHW) from the lipid (B,D, F,H) or the base of the extracellular domain (C,E,G,I) with the α and γ subunit shown in green and blue respectively and TMD helices labeled within colored circles. Five scored docking poses are shown in spherical representations for sevoflurane (B-C; salmon) and isoflurane (F-G; purple). The highest scored docking pose for sevoflurane (D-E) and isoflurane (H-I) are shown as spherical representations with carbon, oxygen, fluorine, and chloride colored as gray, red, cyan, and orange respectively. Corresponding azisevoflurane(1a) labeled residues within $\alpha_1\beta_3\gamma_{2L}$ (red dashed boxes) GABA_A receptors are shown as red stick representations at highest scored docking poses and labeled in dashed boxes. Corresponding aziisoflurane labeled residues within $\alpha_1\beta_3\gamma_{2L}$ (cyan dashed boxes) GABA_A receptors are shown as teal stick representations at highest scored docking poses.

Docking within the γ/β GABA_A receptor TMD dimer is shown in Figure 16.

Compare to the α/γ dimer, the generated poses for sevoflurane in the γ/β dimer were further ($> 5.5 \text{ \AA}$) from detected azisevoflurane photomodified residues (Figure 16A-E) however all were still within the interfacial cavity. Two of the five generated poses (second and fifth lowest relative energy) for isoflurane were situated within the γ intrasubunit region (Figure 16A,F-I). The intrasubunit sites were in closest proximity ($<2.5 \text{ \AA}$) to an aziisoflurane labeled residue within the γ M1 helix, γ Tyr-241 (Figure 15A). Previously intrasubunit binding within pLGICs has been associated with inhibition¹⁶⁹. It is unclear whether this identified site within the γ subunit represents a competing antagonistic action within synaptic GABA_A receptors, however this finding does provide an interesting prospect for volatile anesthetic molecular mechanisms. The lowest energy pose generated for isoflurane was located within the γ^+/β^- interfacial cavity (Figure 16H-I). The interfacial poses for isoflurane were a fair distance ($<4.0 \text{ \AA}$) of a detected aziisoflurane photomodified residue within the β_3 subunit, namely β Gln-224.

It is necessary to consider that the portion of the γ M3 helix (γ Tyr-292/Val-300 to γ Ile-305; see appendix A.3.5- A.3.6) that consistently displayed poor coverage within both *a*-PAL photoaffinity labeling experiments would be included within γ^+/β^- interfacial binding cavity. Anticipated alterations by the volatile *a*-PALs to this peptide segment (ex.

increased hydrophobicity) could be responsible for the continual lack of coverage within this region. Ultimately volatile anesthetic binding within the γ +/ β - interfacial cavity cannot be excluded from consideration due to potential of unrepresented photoaffinity labeled residues within the γ M3 helix. Indeed binding by intravenous anesthetics has been suggested within the γ +/ β - interfacial cavity^{159,170}, with an (R)-(-)-*m*TFD-mephobarbital photomodification detected on γ Ser-301 of the γ M3 helix⁷³.

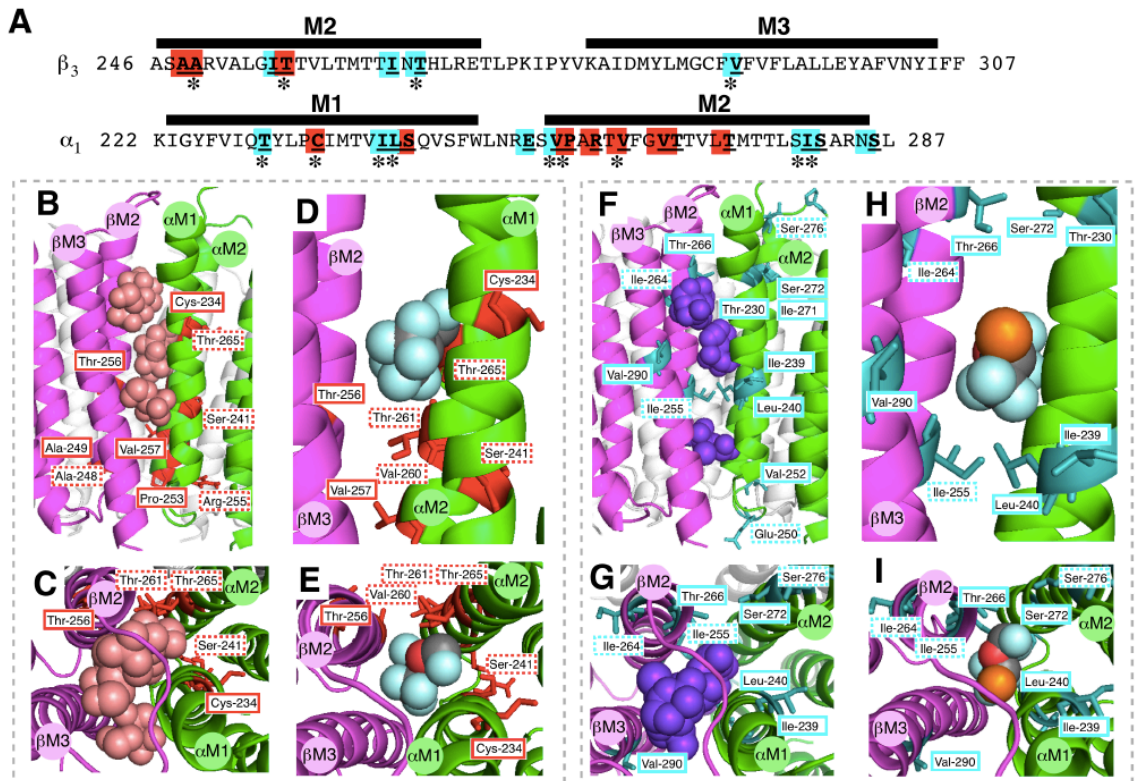


Figure 17. Sevoflurane and isoflurane docking poses in the $\alpha_1\beta_3\gamma_{2L}$ GABA_A receptor at the β +/ α -TMD interface with photoaffinity labeled residues. Sequences (A) of β +/ α -TMD interfacial helices (β_3 M2-M3 and α_1 M1-M2) are shown with corresponding residues (bold, underlined) labeled within $\alpha_1\beta_3$ (*) or $\alpha_1\beta_3\gamma_{2L}$ GABA_A receptors by azisevoflurane(1a) and aziisoflurane highlighted in red and cyan respectively. Views of the β +/ α -TMD interface of an $\alpha_1\beta_3\gamma_{2L}$ GABA_A receptor homology model¹⁶⁸ based-off the glutamate-gated chloride channel (GluCl) of *Caenorhabditis elegans* (PDB ID: 3RHW) from the lipid (B,D, F,H) or the base of the extracellular domain (C,E,G,I) with the α and γ subunit shown in green and blue respectively and TMD helices labeled within colored circles. Five scored docking poses are shown in spherical representations for sevoflurane (B-C; salmon) and isoflurane (F-G; purple). The highest scored docking pose for sevoflurane (D-E) and isoflurane (H-I) are shown as spherical representations with carbon, oxygen, fluorine, and chloride colored as gray, red, cyan, and orange respectively. Corresponding azisevoflurane(1a) labeled residues within $\alpha_1\beta_3$ (bold boxes) or $\alpha_1\beta_3\gamma_{2L}$ (dashed

boxes) GABA_A receptors are shown as red stick representations at highest scored docking poses. Corresponding aziisoflurane labeled residues within $\alpha_1\beta_3$ (cyan bold boxes) or $\alpha_1\beta_3\gamma_{2L}$ (cyan dashed boxes) GABA_A receptors are shown as teal stick representations at highest scored docking poses.

Figure 17 displays the docking poses for the volatile anesthetics within the β/α TMD dimer. The β/α dimer is expected to form the $\beta+/\alpha-$ interface that represents two of the five potential interfaces within most native synaptic $\alpha_1\beta_3\gamma_{2L}$ GABA_A receptors and in photoaffinity labeled FLAG- $\alpha_1\beta_3\gamma_{2L}$ -(L3)-1D4 and FLAG- $\alpha_1\beta_3$ GABA_A receptors (Figure 17A). Sevoflurane docking poses were located within the $\beta+/\alpha-$ interface (Figure 17B-E) with the lowest energy docking poses agreeing (< 2.5 Å distance) with α M1 (α Cys-234), α M2 (α Thr-261 and/or α Thr-260) or β M2 (β Thr256) helical residues photomodified by azisevoflurane(**1a**) (Figure 17D-E). Isoflurane docking poses were also near (<2.5 Å distance) aziisoflurane photomodified residues detected within the α M1 (α Ile-239 and/or α Leu-240), β M2 (β Ile-255) or β M3 (β Val-290) helices (Figure 17A, F-I).

The $\beta+/\alpha-$ interfacial site has been implicated as a likely positive modulatory site for the comparatively more potent intravenous anesthetics propofol and etomidate¹⁵⁹. Indeed residues previously labeled by these intravenous *a*-PALs are in close proximity to residues labeled by the volatile *a*-PALs. This includes residues photoaffinity labeled by aziisoflurane that were also detected to contain a photomodification by AziPm (α Ile-239)⁷⁶ and TDBzl-etomidate (β Val-290)⁷¹. Together with previous protection studies^{69,76} and above photoaffinity radiolabeling competition studies with [³H]AziPm, the evidence suggests a shared or overlapping general anesthetic binding site within the $\beta+/\alpha-$ interface of synaptic GABA_A receptors. Based off published mutagenesis studies and the binding

of more potent modulators, it is likely that the β^+/α^- interfacial site contributes to the positive modulation of GABA_A receptors by the volatile anesthetics sevoflurane and isoflurane.

The docking results and photoaffinity labeled residues within the α/β subunit dimer are shown in Figure 18. As the α^+ and β^- interfaces are present within α^+/β^- and

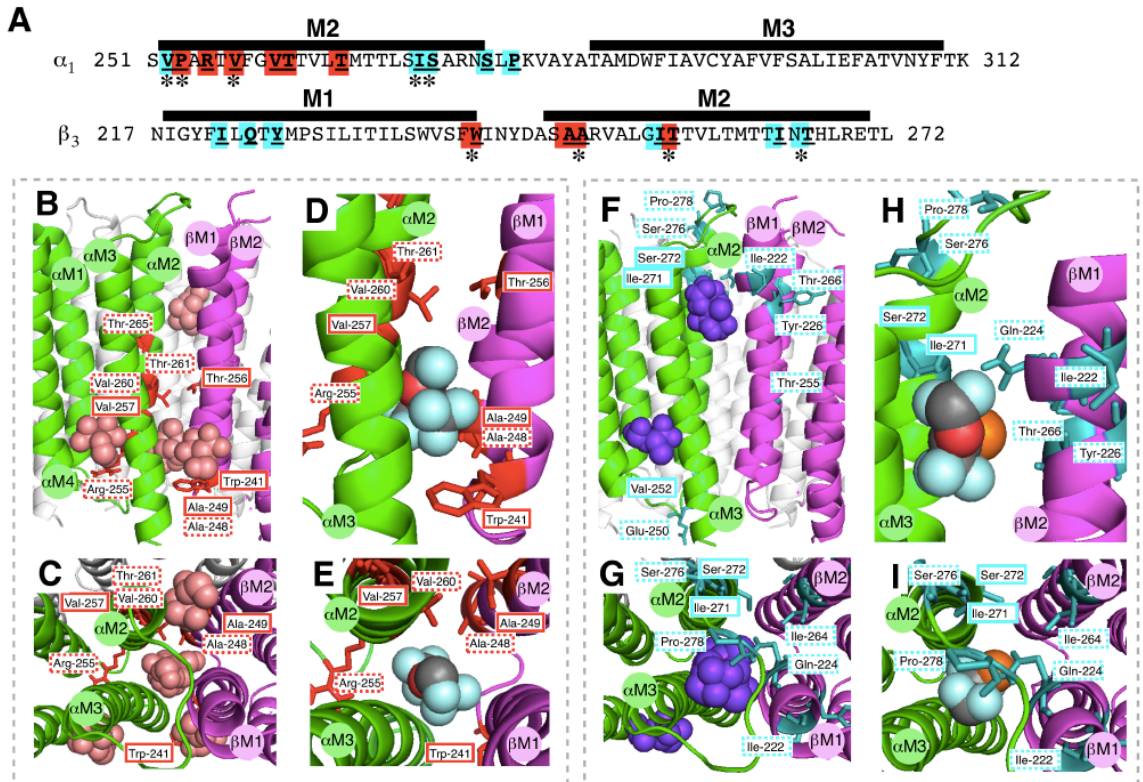


Figure 18. Sevoflurane and isoflurane docking poses in the $\alpha_1\beta_3\gamma_{2L}$ GABA_A receptor at the α^+/β^- TMD interface with photoaffinity labeled residues. Sequences (A) of α^+/β^- TMD interfacial helices (α_1 M2-M3 and β_3 M1-M2) are shown with corresponding residues (bold, underlined) labeled within $\alpha_1\beta_3$ (*) or $\alpha_1\beta_3\gamma_{2L}$ GABA_A receptors by azisevoflurane(1a) and aziisoflurane highlighted in red and cyan respectively. Views of the α^+/β^- TMD interface of an $\alpha_1\beta_3\gamma_{2L}$ GABA_A receptor homology model¹⁶⁸ based-off the glutamate-gated chloride channel (GluCl) of *Caenorhabditis elegans* (PDB ID: 3RHW) from the lipid (B,D, F,H) or the base of the extracellular domain (C,E,G,I) with the α and γ subunit shown in green and blue respectively and TMD helices labeled within colored circles. Five scored docking poses are shown in spherical representations for sevoflurane (B-C; salmon) and isoflurane (F-G; purple). The highest scored docking pose for sevoflurane (D-E) and isoflurane (H-I) are shown as spherical representations with carbon, oxygen, fluorine, and chloride colored as gray, red, cyan, and orange respectively. Corresponding azisevoflurane(1a) labeled residues within $\alpha_1\beta_3$ (red bold boxes) or $\alpha_1\beta_3\gamma_{2L}$ (red dashed boxes) GABA_A receptors are shown as red stick representations at highest scored docking poses. Corresponding aziisoflurane labeled residues within $\alpha_1\beta_3$ (cyan bold boxes) or $\alpha_1\beta_3\gamma_{2L}$

(cyan dashed boxes) GABA_A receptors are shown as teal stick representations at highest scored docking poses.

the α +/ γ - or γ +/ β - interfacial sites within $\alpha_1\beta_3\gamma_{2L}$ GABA_A receptors, photoaffinity labeling of FLAG- $\alpha_1\beta_3\gamma_{2L}$ -(L3)-1D4 GABA_A receptor alone cannot fully distinguish photomodified residues within the α +/ β - interface. To examine the α +/ β - interfacial site under further isolation, FLAG- $\alpha_1\beta_3$ GABA_A receptors were photoaffinity labeled with the volatile α -PALs. The detected photomodified residues by azisevoflurane(**1a**) and aziisoflurane from both experiments are shown in Figure 18A. The docking poses for sevoflurane within the α / β subunit dimer were in agreement with photomodified residues that were detected in both GABA_A receptors (Figure 18B-E). Accordingly the selective photoaffinity labeling by azisevoflurane(**1a**), in particular those residues photomodified within the FLAG- $\alpha_1\beta_3$ GABA_A receptors (α Pro-253, α Val-257, β Trp-241, β Ala-249 and β Thr-256), suggests binding within the lower region of the α +/ β - interface. Similarly the residues photomodified with aziisoflurane were in good agreement with docking poses generated within the α / β subunit dimer with poses within close proximity (< 3 Å) of α Ser-272 and α Ile-271 that were detected with photomodifications within FLAG- $\alpha_1\beta_3$ GABA_A receptors (Figure 18F-I).

Previously mutations of α Ser-270, which is located within the α M2 helix and projects into the α +/ β - interface, to either Trp and Ile has shown to enhance receptor sensitivity to GABA. Furthermore α Ser-270 mutations have been shown to significantly decrease the positive modulation by volatile anesthetics including sevoflurane and, to a greater extent, isoflurane. Based on things findings, the α +/ β - interface, specifically this region of the interface, had been put forth to contain volatile anesthetic binding site(s). The volatile α -PAL photoaffinity labeling experiments largely complement this

hypothesis, particularly for the site identified with aziisoflurane. Residues photomodified by azisevoflurane(**1a**) are located near the final residues of the α M2 helix and the final and leading residues of the β M2 and β M3 respectively (Figure 18A). Mutations near the α Ser-270 residue will likely influence the conformation and/or dynamics of the surrounding protein structure. Given the lower inhibition of positive modulatory activity by α Ser-270 mutations for sevoflurane compared to isoflurane¹⁶⁰, it is reasonable to conclude that regions identified by azisevoflurane(**1a**) photoaffinity labeling located within the same interface could be more selective for sevoflurane binding.

Some photomodified residues by the volatile α -PALs were detected outside the TMD of the FLAG- $\alpha_1\beta_3$ GABA_A receptors. A total of three extracellular domain (ECD) residues, one within the FLAG- α_1 (α Gly-139/104; residues corresponding FLAG/non-FLAG tagged α_1 subunit) and two within β_3 (β Glu-179 and β Pro-184) subunit, were detected with an azisevoflurane(**1a**) photomodification. Two extracellular domain residues were detected with an aziisoflurane photomodification, α Asn-138/103 (residues corresponding FLAG/non-FLAG tagged α_1 subunit) and β Ala-45. Within the applied homology model of the $\alpha_1\beta_3\gamma_2$ GABA_A receptor¹⁶⁸ all the volatile α -PAL photomodified residues are focused within a single site at the α +/ β - interface of ECD (Figure 14). This ECD site is distinct from the GABA and benzodiazepine binding sites that are located at the β +/ α - and α +/ γ - interfaces respectively. These photomodified residues correspond with the ketamine binding site crystalized within bacterial homolog of pLGICs from *Gloeobacter violaceus* (GLIC)¹⁷¹. Both ketamine and volatile anesthetics inhibit GLIC^{171,172}, however the functional relevance of this site for GABA_A receptors (i.e. whether it may act as a potential functional site within all pLGICs) is unclear. One residue (β Leu-

417) located within the intracellular loop between the β M3 and β M4 helices was detected as an azisevoflurane(**1a**) photomodified residue. This residue is located near the clathrin adaptor 2 protein (AP2) binding motif that acts as a vital phosphorylation site that regulates GABA_A receptor endocytosis¹⁷³. Whether a potential anesthetic binding cavity exists within the intracellular loop is not apparent and the potential effect it may have in a biological system is unclear; however, this finding opens the possibility for potential alternative anesthetic molecular mechanisms, other than direct modulation of ion flux, that could affect receptor activity.

2.2.4. Conclusions

General anesthetics have long been shown to enhance the GABA_A receptor activity at clinically relevant concentrations. The bulk of recent investigations to determine the mechanism(s) behind the positive modulation have been focused on intravenous anesthetics while studies for inhaled anesthetics have been, in comparison, limited. In this study two *a*-PALs for sevoflurane and isoflurane to identify binding sites within human $\alpha_1\beta_3\gamma_{2L}$ and/or $\alpha_1\beta_3$ GABA_A receptors. In total, the multiple localized photomodified residues by either volatile *a*-PAL exemplifies the motility of these comparatively highly flexible and mobile ligands within these cavities and likely contributes to their lower protein binding affinity. The labeled residues suggested that the *a*-PALs likely bind within both α +/ β - and β +/ α - subunit interfaces, with the β +/ α - interfacial site overlapping with previously suggested intravenous anesthetic binding site. Azisevoflurane(**1a**) and aziisoflurane demonstrated potential preferential labeling, and therefore occupancy of the α +/ β - interface. Labeling of γ subunit residues suggests binding within γ -containing interface(s) and the potential for an intrasubunit site. Further

studies are required to determine the functional significance of detected binding sites. However photoaffinity experiments do support previous investigations suggesting binding site(s) within the α +/ β - and β +/ α - subunit interfaces that likely contribute to volatile anesthetic positive modulation of synaptic GABA_A receptors.

2.2.5. Experimental methods

Construction and stable cell line generation. The genes encoding GABA_A receptor α ₁, β ₃, and γ _{2L} subunits were respectively cloned into expression vectors containing independent antibiotic selection. Preparation of the plasmids FLAG-bGABA_AR α ₁/pcDNA4/TO-Zeocin, hGABA_AR β ₃/pcDNA3.1/TO-Hygro1 and hGABA_AR γ ₂-(GGG)₃GK-1D4/pACMV/TO-blasticidin was performed as previously described^{164,167}. Transfection using 293fectin and colony selection and amplification were conducted as previously reported. Optimal inducible cell lines were validated and chosen based on quantitative reverse-transcription polymerase chain reaction (RT-PCR), Western blotting, growth rate and the number of [³H]muscimol and/or [³H]flunitrazepam sites.

Immunoaffinity purification of GABA_A receptor. Protein purification and reconstitution were performed as previously described^{164,167}. Briefly stably transfected HEK293-TetR cells were grown, induced with tetracycline and 5 mM sodium butyrate, harvested and lysed, and membrane suspensions were collected. Membrane pellets were solubilized by dropwise addition of (in mM) 50 Tris-HCl (pH 7.4), 150 NaCl, 2 CaCl₂, 5 KCl, 5 MgCl₂, and 4 EDTA supplemented with 10% (v/v%) glycol, protease inhibitors and DDM (final concentration 1.5% m/v%) to a final protein concentration of 1 mg/mL. Insoluble material was removed by ultracentrifugation and the supernatant was loaded on to prepared anti-FLAG or anti-1D4 affinity columns. CHAPS/asolectin replaced DDM by

repeated washes and 1 hr equilibration. The columns were then washed with asolectin (0.025-0.86 mM as required) and CHAPS (5 mM) prior to elution by 90 min equilibration in one column volume of the same solution supplemented with 0.1 mM FLAG or 0.15 mM 1D4 peptide. The eluate was collected and the elution process was conducted a total of 3 to 4 times. The eluted protein fractions were frozen in liquid nitrogen and stored at -80 °C.

Radiophotoaffinity labeling of purified FLAG- $\alpha_1\beta_3\gamma_{2L}$ -L3-1D4 GABA_A receptor. 1250:1 (ligand:protein molar ratio) of azisevoflurane(**1a**) or aziisoflurane and 50:1 (ligand:protein molar ratio) [³H]*meta*-azipropofol was added to 1 μ g FLAG- $\alpha_1\beta_3\gamma_{2L}$ -L3-1D4 GABA_A receptor in 200 μ M 2:1 (asolectin: cholesterol), 5 mM CHAPS and 1 μ M GABA using methanol vehicle (<0.5% v/v%). The sample was equilibrated on ice in the dark for 5 min prior to being simultaneously exposed to 350 nm and 300 nm RPR-3000 Rayonet lamp in quartz cuvettes through a WG305 305 nm glass filter (Newport Corporation) at the 350 nm face and WG295 295 nm glass filter (Newport Corporation) at the 300 nm face for 30 min. Samples were concentrated to ~15-20 μ L using 10kDa MWCO Amicon Ultra Centrifugal Filters (Millipore). An equal volume of SDS loading buffer was added to the sample containing a final concentration 80 mM DTT, samples were vortexed vigorously then incubated at room temperature for 60 min before separation by 7.5% SDS-PAGE. The gel was stained by Coomassie Blue G250 (BioRad), destained and washed with ddH₂O. Identified bands spanning from ~60-50kDa were excised. Prior to band cutting, gels were scanned on a Bio-Rad GS-800 calibrated densitometer with quantitation performed using the accompanying Quantity One Software. Mean background was subtracted with a box drawn between 50- 60 kDa

molecular mass marker. The mean optical density multiplied by the band area (mm²) was recorded. Each excised band was placed into scintillation vials containing 2 mL 30% hydrogen peroxide (v/v%) and incubated at 65 °C to digest the polyacrylamide. Samples were allowed to cool to ambient temperature before 10 mL of scintillation fluid was added. The disintegrations per minute (dpm) from each vial were corrected with a non-UV irradiated control and normalized to the corresponding optical density measurement. Values are represented as the mean ± SEM of four replicate experiments.

Photoaffinity labeling of FLAG- $\alpha_1\beta_3$ or FLAG- $\alpha_1\beta_3\gamma_{2L}$ -L3-1D4 GABA_A receptor for protein microsequencing. 1250:1 (ligand:protein molar ratio) of aziseovflurane(**1a**) or aziisoflurane was added to 4 µg FLAG- $\alpha_1\beta_3\gamma_{2L}$ -L3-1D4 and/or 6 µg of FLAG- $\alpha_1\beta_3$ GABA_A receptor in 200 µM 2:1 (asolectin: cholesterol), 5 mM CHAPS and 1 µM GABA using DMSO vehicle (<0.01% v/v%). The sample was equilibrated on ice in the dark for 5 min prior to being exposed to 300 nm RPR-3000 Rayonet lamp in 1-mm path length quartz cuvettes at through a WG295 295nm glass filter (Newport Corporation) for 25 min.

In-Solution Protein Digestion. Photolabeled samples were concentrated to ~15-20 µL using 10kDa MWCO Amicon Ultra Centrifugal Filters (Millipore). ProteaseMAX™ Surfactant (Promega) was added to 0.2% and the samples were vortexed vigorously for 30 s. Samples were diluted to 93.5 µL to a final concentration of 50 mM NH₄HCO₃. Following 1 µL 0.5 M dithiothreitol (DTT) was added and samples were incubated at 56 °C for 20 min. 2.7 uL of 0.55 M iodoacetamide was then added and protein samples were incubated at room temperature in the dark for 20 min. After, 1 µL of 1% (w/v%) ProteaseMax™ Surfactant was added followed by CaCl₂ to 1 mM final concentration.

Sequencing grade-modified trypsin (Promega) was added to a final 1:20 protease: protein ratio (w/w). Proteins were digested overnight at 37°C. Trypsin digested peptides were diluted to 200 μ L with final concentration of 100 mM NH_4HCO_3 and 0.2% ProteaseMAX Surfactant prior to the addition of sequencing grade chymotrypsin (Promega) to a final 1:20 protease:protein ratio (w/w). Proteins were digested overnight at 37°C.

Trifluoroacetic acid (TFA) was added to 0.5% (v/v) and the peptide digests were incubated at room temperature for 10 min prior to centrifugation at 16, 000 x g for 20 min before desalting using C18 stage tips prepared in house. Samples were dried by speed vac and resuspended in 0.1% formic acid immediately prior to mass spectrometry analysis.

In-Gel Protein Digestion. Photolabeled receptor samples were concentrated to \sim 20 μ L using 10kDa MWCO Amicon Ultra Centrifugal Filters (Millipore). SDS loading buffer was added to the sample containing a final concentration 80 mM DTT, samples were vortexed vigorously then incubated at room temperature for 45 min before the entire sample was separated by SDS-PAGE. Resulting gels were stained with Coomassie Blue G250 (BioRad). Gels were destained and washed with ddH₂O; identified protein bands between \sim 50-60kDa, corresponding to FLAG- α_1 , β_3 , or γ_{2L} -(L3)-1D4 GABA_A receptor subunits, were excised. Excised bands were destained, dehydrated and dried by speed vac before proteins were reduced by incubation at 56° C for 20 min in 5 mM DTT and 50 mM NH_4HCO_3 . The DTT solution was removed and proteins were then alkylated by the addition of 55 mM iodoacetamide in 50 mM NH_4HCO_3 and incubation at room temperature in the dark. Bands were dehydrated and dried by speed vac before resuspension in 100 μ L 0.2 % ProteaseMAX™ surfactant, 1 mM CaCl_2 and 50 mM NH_4HCO_3 solution containing trypsin at a 1:20 protease:protein ratio (w/w). Proteins

were digested overnight at 37°C. After, samples were diluted to 200 µL with final concentration of 100 mM NH₄HCO₃ and 0.2% ProteaseMAX™ Surfactant prior to the addition of sequencing grade chymotrypsin (Promega) to a final 1:20 protease:protein ratio (w/w). Proteins were digested overnight at 37°C. To increase hydrophobic peptide retrieval from the gel, multiple peptide extractions were performed. First the initial peptide digest solution was removed and 100 µL 30% acetonitrile and 5% formic acid in ddH₂O (v/v%) was added. Samples were sonicated for 20 min. The second peptide extraction was removed before 100 µL 70% acetonitrile and 5% formic acid in ddH₂O (v/v%) was added. Samples were sonicated for 20 min. All peptide digests were pooled and dried by speed vac before resuspension in 0.5% TFA and desalting using C18 stage tips prepared in house. Samples were dried by speed vac and resuspended in 0.1% formic acid immediately prior to mass spectrometry analysis.

Mass spectrometry. Desalted peptides were analyzed on an Orbitrap Elite™ Hybrid Ion Trap-Orbitrap Mass Spectrometer (MS) coupled to an Easy-nanoLC 1000 system with a flow rate of 300 nL/min. Peptides were eluted with 100 min with linear gradients from 2% to 40% ACN (85 min), from 40% to 85% ACN (5 min) and finally 85% (10 min) ACN in 0.1% formic acid (v/v). Data dependent acquisition mode was applied with a dynamic exclusion of 45 s, in every 3 s cycle, one full MS scan was collected with a scan range of 350 to 1500 m/z, a resolution of 60K and a maximum injection time was 50 ms and AGC of 500000. Then MS2 scans were followed on parent ions from the most intense ones. Ions were filtered with charge 2-5. An isolation window of 1.5 m/z was used with quadrupole isolation mode. Ions were fragmented using collision induced dissociation (CID) with collision energy of 35%. Iontrap detection was used with normal

scan range mode and rapid iontrap scan rate. AG was set to be 10000 with a maximal injection time of 100 ms.

Mass spectrometry analysis. Analysis was performed similar to as previously reported¹⁷⁴. Spectral analysis was conducted using Thermo Proteome Discoverer 2.0 (Thermo Scientific) and the Mascot Daemon search engine using a customized database containing GABA_A receptor protein sequences supplied for heterologous expression or the human proteome UniProt database (UniProtKB: P28472). All analyses included dynamic oxidation of methionine (+15.9949 *m/z*) and N(Q) deamidation (+0.98402 Da, when PNGase F-specific, defined as N(Q) deglycosylation) as well as static alkylation of cysteine (+57.0215 *m/z*; iodoacetamide alkylation). Photolabeled samples were run with the additional dynamic azisevoflurane (+230.0559 *m/z*) or aziisoflurane (+195.97143 *m/z*) modifications. A mass variation tolerance of 10 ppm for MS and 0.8 Da for MS/MS were used. Both the in-solution and in-gel sequential trypsin/chymotrypsin digests were searched without enzyme specification with a false discovery rate of 0.01%. Samples were conducted in triplicate and samples containing no photoaffinity ligand were treated similarly to control for false positive detection of photoaffinity ligand modifications.

Docking. $\alpha_1\beta_3\gamma_2$ GABA_A receptor transmembrane interfaces. A homology model of the $\alpha_1\beta_3\gamma_2$ GABA_A receptor was built by mutating 31 residues in the β subunits from an $\alpha_1\beta_1\gamma_2$ GABA_A Model 3 reported in Hénin et al., 2014¹⁶⁸. The mutations were made using the MUTATOR plugin of VMD¹⁷⁵. Molecular coordinates for isoflurane and sevoflurane were downloaded from the ZINC small molecule library¹⁴⁴ using provided physical representations. The maximum torsions were allowed (i.e., ligands were fully flexible). Each unique subunit dimer (ie. α/γ , α/β , β/α , or γ/β) underwent individual

docking runs with each ligand with docking runs using AutoDock Vina¹⁴⁷. Grid boxes were set to contain the two intrasubunit and single intersubunit cavities present in the dimer and all residue side chains projecting towards the intra- and interface cavities were made flexible. Each dimer docking experiment was set to output 5 docking modes, all other settings were assigned with default parameters. Figures and measurements were generated using PYMOL.

Statistics- GraphPad Prism 7, unless otherwise noted, was used for preparation and statistical data analysis.

CHAPTER 3: PROPOFOL AND ALKYLPHENOL-BASED ANESTHETIC MOLECULAR MECHANISMS

Propofol, or 2,6-diisopropylphenol, was the 31st of 51 alkylphenols synthesized and tested as candidate general anesthetic compounds within a primary structure-activity assessment by Dr. R. James in 1980¹⁷⁶. Since then propofol has become the most widely used intravenous general anesthetic for the induction and maintenance of anesthesia. Although considered a more potent agent compared to the volatile anesthetics discussed within the previous chapter, the micromolar EC₅₀ concentrations still suggest very transient interactions with molecular targets. The first section of this chapter contains a study on the key molecular feature(s) that contribute to propofol biological effects including the introduction of the novel hydrogen-bonding null propofol derivative called fropofol(**1b**). The second section introduces a novel bioorthogonal *α*-PAL for propofol termed AziPm-click(**1c**) that, coupled with a quantitative mass spectrometry workflow, allows the identification of propofol and alkylphenol-based general anesthetics binding

proteome within synaptosomes. The third and final section of this chapter focuses on propofol and alkylphenol binding within a suggested major target, synaptic GABA_A receptors.

3.1. Role for the propofol hydroxyl in anesthetic protein target molecular recognition

The first major proposal for a mechanism of anesthetic-induced hypnosis arose when a relationship between anesthetic lipophilicity and potency was independently observed by Meyer and Overton^{1,2}. This correlation led to various hypotheses for membrane mediated mechanisms of anesthesia; however, evidence that anesthetics bind and cause functional effects through specific sites on multiple protein targets has steadily emerged. Crystallized anesthetic-protein complexes^{88,90,177}, recognition of highly specific and selective responses by ion channels^{6,178}, and elucidation of receptor binding site character using α -PALs^{40,179} have propelled the concept of protein-mediated mechanisms to general acceptance.

The binding affinity of a drug for a protein site is generally mediated by multiple specific non-covalent interactions in a process known as molecular recognition. Drug occupancy of a target protein site results in alteration(s) in protein conformation and/or dynamics that reflect (or produce) changes in the protein's activity. General anesthetic ligands are a unique class of drugs in that they share only broad physicochemical features, such as low molecular weight and hydrophobicity. While causing similar desired endpoints including hypnosis, immobility, and amnesia, and adverse effects including cardiovascular depression, nausea, and hyperthermia, the drug concentrations to achieve the effects can be considerably different between anesthetics. These observations suggest that a penchant of an individual anesthetic for a pharmacological

effect may be reliant on distinctive chemical features giving rise to a relative higher affinity for particular protein target(s). It is therefore essential to characterize the molecular interactions between proteins and anesthetics to successfully design new anesthetic agents that selectively cause the desirable effects through specific targets.

While a fairly simple compound, propofol contains a particular feature within its chemical structure, a 1-hydroxyl, that is capable of distinctive intermolecular interactions¹⁸⁰⁻¹⁸². The hydrophilic group permits hydrogen bonding to both aqueous solvent and to amino acids within protein targets, which contribute to solvation and specific molecular recognition, respectively. Solvation is critical for hydrophobic ligands to gain access to protein target(s)¹⁸³. Previous studies that examined various substitutions on the alkylphenol backbone could not rigorously attribute the changes in ligand efficacy to molecular recognition or to solvation^{184,185}. To achieve this, a modification of propofol that removes hydrogen bonding propensity while retaining solvation properties, and then a comparison of both ligand activity and binding, is essential.

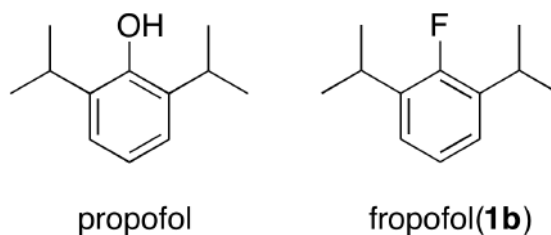


Figure 19. Chemical structures of propofol and fropofol(**1b**)

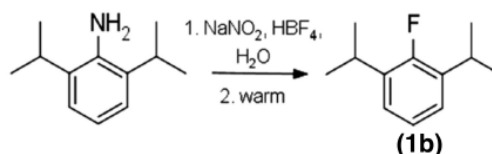
Thus, the 1-hydroxyl of propofol was substituted with a fluorine atom to produce 2-fluoro-1,3-diisopropylbenzene, or fropofol(**1b**) (Figure 19). This otherwise physicochemically similar analogue to propofol allowed us to explicitly link the 1-hydroxyl to protein affinity and, most importantly, to multiple *in vivo* consequences. The

investigation indicates that hydrogen bonding plays a surprisingly dominant role in molecular recognition for propofol-protein interactions that contribute to hypnosis, whereas the loss of the hydrophilic feature did not prevent binding to targets that lead to less favorable endpoints.

3.1.1. Synthesis and characterization of fropofol(**1b**)

To directly evaluate the contribution of the 1-hydroxyl in propofol molecular recognition an analogue that selectively weakens the hydrogen bond capability while retaining other physiochemical properties of propofol was designed. The synthesis of fropofol involved the diazotization of 2,6-diisopropylaniline, precipitation of the tetrafluoroborate salt, and dediazotization-fluorination under mild vacuum overnight (Scheme 2).

Scheme 2.



The physiochemical properties of propofol and fropofol(**1b**) are reported in Table 5. The calculated van der Waals molecular volumes were similar between the two compounds with fropofol(**1b**) (189 Å³) being marginally smaller than propofol (192 Å³). Based on the Meyer-Overton rule, the increase in hydrophobicity by calculated octanol/water partition coefficients for fropofol(**1b**) (3.96) relative to propofol (3.79) predicted a modest increase in the compound's anesthetic potency^{1,2}. Consistent with the cLogP value, the measured maximum aqueous concentration achieved by fropofol(**1b**) was 116 ± 4.4 μM, approximately 5-fold less than propofol; however, the solubility of

fropofol(**1b**) exceeded or was within the same range of halogenated alkylphenols that retain activity; 2,4-diethylphenol bromide and 4-iodo-2,6-diisopropylphenol ¹⁸⁵.

Initial studies started with comparing propofol and fropofol(**1b**) binding to two model proteins. Previously, anesthetic binding to horse spleen apoferritin (*aF*) had been found to correlate strongly with GABA_A receptor potentiation and tadpole loss of righting reflex (LORR) ^{87,186}. Anesthetic binding to a single site on *aF* is exothermic and mediated by electrostatic and hydrophobic interactions ⁸⁷; a hydrogen bond was not apparent in the crystal structure of the complex with propofol. Propofol and fropofol(**1b**) bound *aF* with low micromolar K_D values (Figure 20A-B; Table 5); however, fropofol(**1b**) had a 4 to 5-fold increase in affinity (K_D= 1.7 μM (0.5 - 2.9) (95% CI)) relative to propofol (K_D= 9.0 μM (7.1 - 11) (95% CI)).

Table 5. Physicochemical parameters and binding properties of propofol and fropofol(**1b**)

Physicochemical Properties	Propofol (2,6-diisopropylphenol)		Fropofol(1b) (2-fluoro-1,3-diisopropylbenzene)	
	Molecular Weight	178.27Da		180.26Da
van der Waals Volume	192 Å		189 Å	
cLogP	3.79		3.96	
Density	0.96g/cm ³		0.9 g/cm ³	
Protein Affinities (μM) †	<i>aF</i> [‡]	hSA	<i>aF</i> [‡]	hSA
ITC	9 (7.1 - 11)	43 (36 - 50)	1.7 (0.5 – 2.9)	91 (72-110)
1-AMA Competition	10 (7-15)	-	0.7 (0.3 -1.5)	-

† Values are represented as mean (95% CI); ‡ Stoichiometry of *aF* sites were fixed at N=1; † K_D Fluorescence data derived from Cheng–Prusoff equation

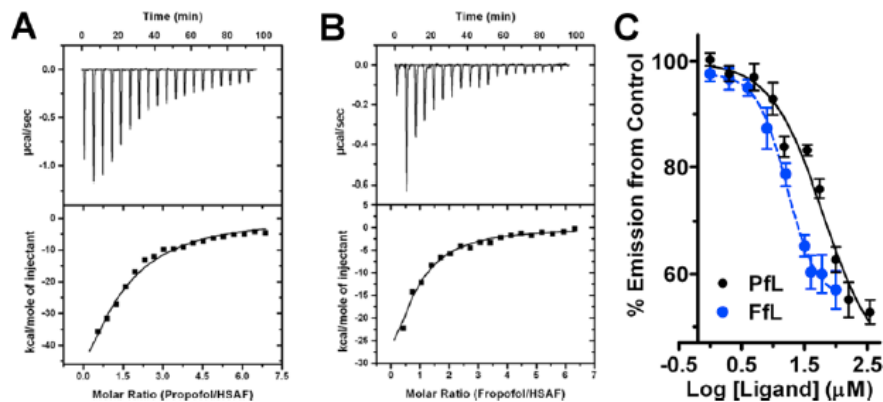


Figure 20. Propofol and fropofol(**1b**) horse spleen apoferritin (*aF*) binding. Isothermal titration calorimetry profiles of *aF*(A-B) interaction with propofol (A) or fropofol(**1b**) (B) using sequential titrations. Top: time response heat change from addition of ligand. Bottom: best fit attained from a single site binding model (best χ^2 statistic) fitted to a 1:1 stoichiometry for *aF*. Drug affinities (K_D) for HSAF site were $9\mu\text{M}$ and $1.7\mu\text{M}$ for propofol and fropofol(**1b**) respectively. (C) *aF* fluorescence competition using 1-aminoanthracene with titrations of either propofol (PfL; black circles) or fropofol(**1b**) (FfL; blue circles). Intensity was corrected for ambient ligand and protein fluorescence (see table 5).

The propofol *a*-PAL *meta*-azi-propofol (AziP*m*) has been shown to photolabel the crystallographically-determined propofol site on *aF*¹⁸⁷. Therefore, [³H]AziP*m* was used in photoradiolabeling with and without competing ligands to definitively determine the fropofol(**1b**) -*aF* binding site. $1\mu\text{M}$ propofol or fropofol(**1b**) caused a 31% and 61% reduction in [³H]AziP*m* binding to *aF*, respectively. 1-Aminoanthracene (1-AMA) also binds the same site on *aF*¹²⁶. 1-AMA decreases in fluorescence when displaced from the *aF* site, and this feature allows calculation of ligand K_D values through competition experiments. Calculated K_D values from 1-AMA fluorescence competition (Figure 20A) correlated well with ITC and photoradiolabel competition studies for both propofol ($K_D=10\mu\text{M}$ (7 - 15) (95% CI)) and fropofol ($K_D=0.7\mu\text{M}$ (0.3 - 1.5) (95% CI)). Cumulatively, the data show that propofol and fropofol(**1b**) bind within the same hydrophobic cavity on *aF*⁸⁷; however, fropofol(**1b**) consistently demonstrated an

approximately 3- to 5-fold increase in affinity, presumably due to the modest increase in hydrophobicity.

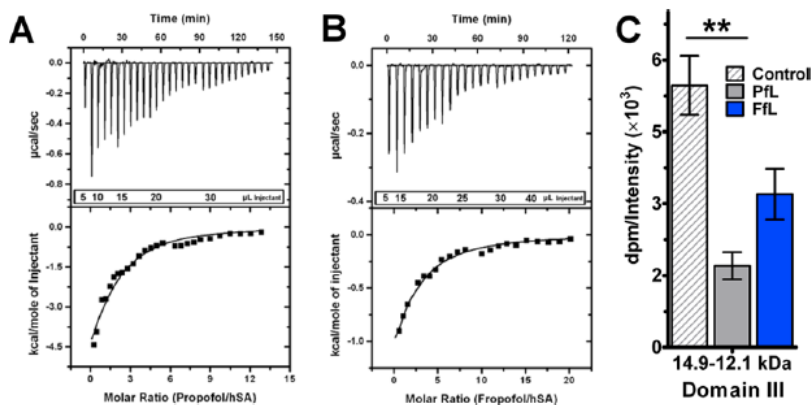


Figure 21. Propofol and fropofol(**1b**) human serum albumin (hSA) binding. Isothermal titration calorimetry profiles of hSA interaction with propofol (A) or fropofol (B) using incremental titrations. Top: time response heat change from addition of ligand. Bottom: best fit attained from a single site binding model (best χ^2 statistic) resulting in roughly 1:2 stoichiometry for hSA for fropofol(**1b**) ($n=1.3 \pm 0.9$) and propofol ($n=1.4 \pm 0.5$). Affinity (K_D) for the hSA sites were $43\mu\text{M}$ and $91\mu\text{M}$ for propofol and fropofol(**1b**) respectively (see table 5). (C) Protection binding assay with [³H]AziPm photoradiolabeling of hSA hSA CNBr 14.9-12.1 kDa domain III digestion fragment with DMSO control or $75\mu\text{M}$ propofol (PFL) or fropofol(**1b**) (FFL) protection. Quantitation of dpm was normalized to averaged relative lane intensities of Coomassie blue (CB) stain. Data sets are represented as normalized mean \pm normalized SEM and were analyzed by one-way ANOVA with Bonferroni's post hoc test ($p < 0.05$) comparing significance in protection to fragment control (*).

Propofol has also been shown with crystallography to bind two sites within domain III of human serum albumin (hSA)¹⁸⁸. Within each site there resides hydrogen bonding partners that facilitate propofol binding¹⁸⁸. Similar to *aF*, ITC measurements showed propofol and fropofol(**1b**) bound to hSA exothermically (Figure 21A-B; Table 5). The cumulative K_D of propofol binding to hSA was determined as $43\mu\text{M}$ (36-50) (95% CI), with stoichiometry being dominated by the higher affinity complex¹⁸⁹. Fropofol(**1b**) demonstrated similar stoichiometry but with a cumulative K_D of $91\mu\text{M}$ (72-110) (95% CI).

[³H]AziPm photoradiolabeling protection experiments were also performed with hSA, and these experiments were supplemented with CNBr digestion to specifically study binding to domain III. Within the isolated domain III fragments, propofol significantly decreased radiolabel incorporation to about $67 \pm 5\%$ of the control [³H]AziPm photolabeling, while fropofol(**1b**) inhibited it by only half as much ($37 \pm 12\%$ (mean \pm SEM); Figure 21C). This suggests that the substitution of the 1-hydroxyl results in lower affinity to the specific propofol hSA binding sites that contain hydrogen bonding partners.

Together, our data with *aF* and hSA demonstrate a contribution of the propofol hydroxyl for specific molecular recognition of model proteins. Our results demonstrate that propofol binds with higher affinity than fropofol(**1b**) to sites that contain hydrogen bond interactions, but that in the absence of hydrogen bond partners, fropofol(**1b**) binds with higher affinity. The relatively high affinities of these interactions also suggest that this result is independent of the solubility of the ligands.

It bears mentioning that substitution for the 1-hydroxyl would also result in electronic changes that could modulate binding. It is very difficult to entirely separate this possibility from the hydrogen bonding hypothesis, but it seems an unlikely explanation for the large differences measured and the generally weaker van der Waals interactions that would be influenced. Halogens can also serve as weak hydrogen bond acceptors. However fluorine, due to its high electronegativity and lack of polarizability^{190,191}, is generally excluded from this form of interaction¹⁹².

3.1.2. Fropofol(**1b**) pharmacological and functional activity

Next, to characterize the relevance of the hydroxyl on pharmacological activity, several *in vivo* experiments were performed. The pharmacological activity of fropofol(**1b**) within albino *X. laevis* tadpoles was evaluated over the course of 60 and 90 min exposure periods. When administered 3-100 μM fropofol, none of the *X. laevis* tadpoles within any dose group exhibited the standard loss-of-mobility endpoints. In contrast, excitatory phenotypes¹⁹³ were observed in some tadpoles (~11%) at 40-60 min with greater than 30 μM concentrations, and longer (80-90 min) exposures to these high concentrations produced this behavior in ~70% of the tadpoles. This excitatory behavior included continuous tight circular and/or ‘darting’ swimming patterns, previously reported as indicators of lower class seizures in *X. laevis*¹⁹³. When fropofol(**1b**)-containing water was exchanged for fresh pond water, normal swimming behaviors resumed within 10-15 min.

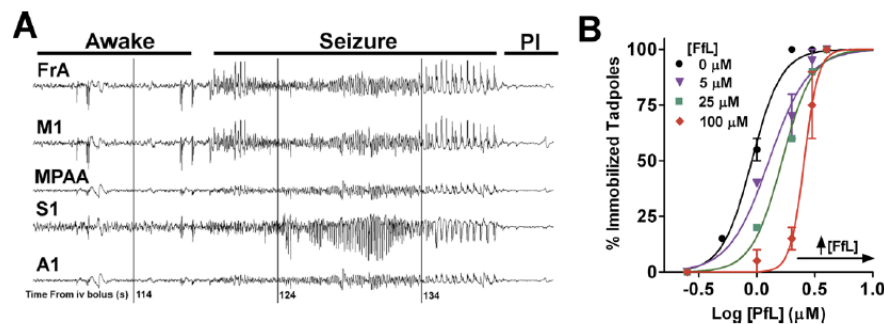


Figure 22. Propofol and fropofol(**1b**) *in vivo* activity. (A) EEG recording 1.75-2.4min after injection of 200 mg/kg fropofol(**1b**). Phenotypical seizure activity observed within frontal association (FrA), primary motor (M1), medial parietal association area (MPAA), primary somatosensory (S1) and primary auditory (A1) traces. Postictal state (PI) was observed after seizing activity. (B) Propofol dose-response curves with the co-administration of 0 μM (black circles), 5 μM (violet triangles), 25 μM (green squares) and 100 μM (red diamonds) of fropofol(**1b**) within *X. laevis* tadpoles. Immobility was measured as loss of spontaneous movement.

The excitatory activity was similarly observed within a mammalian model. Wild type C57/Bl6 mice were given bolus tail vein injections of fropofol(**1b**) dissolved in 10% lipid emulsion. At low dose (96 mg/kg), no observable effects were noted. At higher

dose (180 mg/kg), electroencephalography (EEG) recordings and physical observation showed generalized tonic-clonic seizure-like activity 2 min post injection (Figure 22A), after which a lethargic postictal state was observed. Mice resumed normal activity within 2-3 hr, and no toxicity was observed within the following days post-injection. Loss of righting reflex, the standard endpoint for general anesthetics was produced with 20 mg/kg of propofol, but not with even the highest doses of fropofol(**1b**).

To assure that fropofol(**1b**) accessed the brain, some mice were euthanized at 45 s and at 10 min after IV bolus injection of 96 mg/kg and 200mg/kg respectively. After perfusion and removal, the fropofol(**1b**) content in the brain was assayed by reverse phase-high performance liquid chromatography. At both time points, fropofol(**1b**) was detectable within processed brain samples at 38 µg/gram of brain tissue and 51 µg/gram of brain tissue for the lower and higher doses, respectively. These concentrations are higher than propofol concentrations that result in hypnosis¹⁹⁴. When combined with the obvious central nervous system-derived behavioral change, this confirms that exclusion by either the blood-brain-barrier or through active pumps does not explain the absence of a fropofol(**1b**) hypnotic action.

Finally, in order to determine whether fropofol(**1b**) has subhypnotic activity¹⁹⁵, tadpoles were exposed to increasing concentrations of propofol in the presence of four fixed concentrations of fropofol(**1b**) (0, 5, 25 and 100 µM). Rather than demonstrating an additive effect, fropofol induced a right-shift in the propofol dose-response curve (Figure 22B) indicating antagonism towards propofol induced hypnosis at all concentrations.

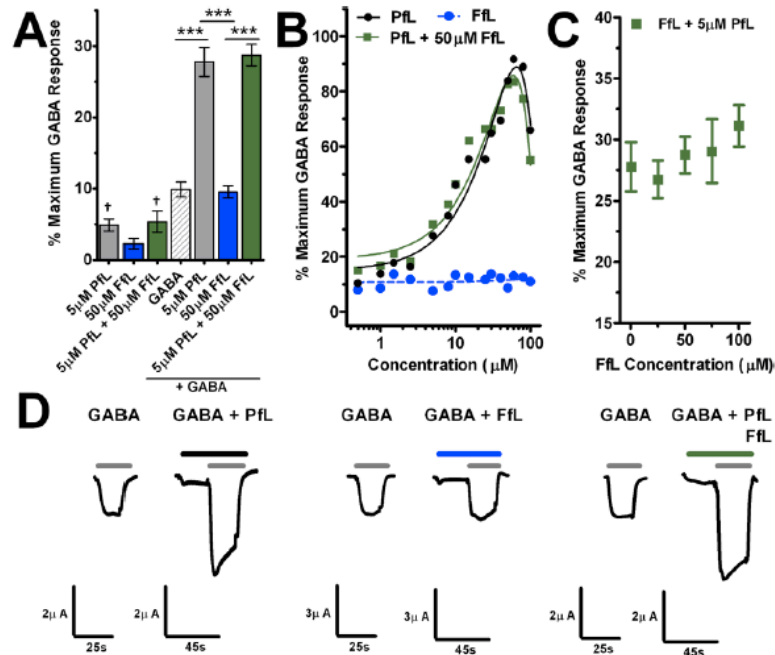


Figure 23. Propofol and fropofol(**1b**) GABA_A receptor activity. (A) Effect on current by concentrations of propofol (Pfl; n=3), fropofol(**1b**) (Ffl; n=5) or propofol and fropofol(**1b**) (n=5) without GABA EC10 and propofol (n=5), fropofol (n=8), or propofol and fropofol with (n=6) GABA EC10 within *X. laevis* oocytes expressing $\alpha_1\beta_2\gamma_{2L}$ GABA_A receptor. GABA represents initial control EC10 exposure for modulation studies (n=19). Data is normalized to maximum GABA response and represented as mean \pm SEM. Data were analyzed by one-way ANOVA with Bonferroni's post hoc test ($p < 0.05$) showing significant differences in fropofol(**1b**) or propofol or propofol and fropofol(**1b**) modulation (*) or significance from EC00 (†). (B) Propofol (Pfl; black circles), fropofol(**1b**) (Ffl; blue circles), or propofol with 50 μ M fropofol(**1b**) (green squares) concentration-response curves for $\alpha_1\beta_2\gamma_{2L}$ GABA_A receptor positive modulation in the presence of GABA EC10. Each point represents individually tested oocytes. Lines represent polynomial (Pfl/black solid; Pfl+ 50 μ M Ffl/ green solid) and linear (Ffl/ blue dash) best fit curves. (C) Response to fropofol (Ffl) concentrations in the presence of 5 μ M propofol represented as mean \pm SEM (n=3-6). (D) Representative traces of evoked current by GABA EC10 control and following combined of GABA EC10 and 5 μ M propofol (Pfl; left); GABA EC10 control and following combined of GABA EC10 and 50 μ M fropofol(**1b**) (Ffl; middle); GABA EC10 control and following combined of GABA EC10, 5 μ M propofol and 50 μ M fropofol(**1b**) (Pfl+Ffl; right) exposures within individual *X. laevis* oocytes expressing $\alpha_1\beta_2\gamma_{2L}$ GABA_A receptor.

To test the hypothesis and determine a potential mechanism for fropofol(**1b**) excitatory activity and antagonism of propofol induced hypnosis, the influence of these agents on recombinantly-expressed GABA_A receptors was investigated. Propofol has been shown to be a strong positive modulator of GABA_A receptors¹⁹⁶, which likely contributes to its hypnotic action. Perfusion with propofol in the absence of GABA

caused minor direct activation, consistent with previous literature (Figure 23A)¹⁹⁶. Also consistent with previous studies, co-exposure to propofol and GABA resulted in a concentration-dependent increase in current up to 80 μM (Figure 23B); positive modulation began to decline at propofol concentrations of 100 μM ^{196,197}. In contrast, 5 μM and 50 μM fropofol(**1b**) elicited no significant direct activation of the receptor (Figure 23A). Furthermore fropofol(**1b**), at any concentration, demonstrated no significant modulation or inhibition of the $\alpha_1\beta_2\gamma_{2L}$ GABA_A receptor at solubility permitted concentrations (Figure 23).

To determine whether the antagonistic action of fropofol(**1b**) on propofol hypnosis was mediated through GABA_A receptors, recombinant ion channels were exposed to all three ligands (GABA, propofol and fropofol(**1b**)). The introduction of 50 μM fropofol(**1b**) resulted in no significant change of propofol positive modulation of the GABA_A receptor (Figure 23A-B, D), and exposure of saturating concentrations of fropofol(**1b**) displayed no significant alteration of 5 μM propofol potentiation of GABA_A receptor currents (Figure 23C-D).

In total, fropofol(**1b**) had no influence whatsoever on propofol positive modulation of the $\alpha_1\beta_2\gamma_{2L}$ GABA_A receptor. Because propofol has shown similar potency across most synaptic GABA_A receptor subtypes^{197,198}, these data suggest that fropofol(**1b**) *in vivo* excitatory activity and antagonism of propofol hypnosis were via a non-GABAergic mechanism. However, we examined only a single sub-type, and thus cannot completely rule out GABAergic antagonism as underlying fropofol(**1b**) excitation. Fropofol(**1b**) might be a useful tool to characterize GABA_A receptor specificity. In addition, these data suggest that our previous demonstration of the

correlation of affinity for α F “anesthetic site”, GABA_A receptor potentiation, and LORR⁸⁷ represents only a portion of the molecular recognition features required for transducing a likely major component for the pharmacological effect. While α F provides a convenient model amenable to high throughput screening, which is a considerable improvement over previous approaches, like the Meyer-Overton rule^{1,2}, these fropofol(**1b**) data strongly indicate an additional requirement for a hydrogen bond within synaptic GABA_A receptor site(s).

As fropofol(**1b**) does not partake in the molecular recognition features that lead to hypnosis, we decided to examine whether the propofol 1-hydroxyl was similarly vital for mechanisms resulting in an alternative pharmacological endpoint. A known adverse effect of propofol is cardiovascular depression, which previous reports suggest is at least partially caused by a direct effect on myocardial contraction^{199,200}. The influence of propofol and fropofol(**1b**) on myocardial contractility was measured by the change in

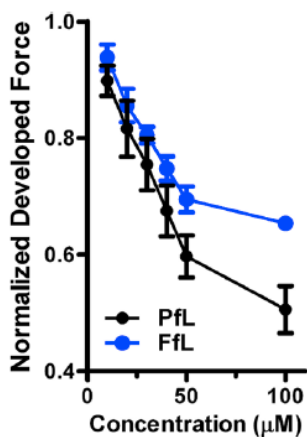


Figure 24. Influence of propofol and fropofol(**1b**) on trabecular muscle force generation. Force development by intact trabecular muscle over a range of propofol (PfL; n=8) and fropofol(**1b**) (FfL; n=3) concentrations. Force development was normalized to initial force development without agent exposure. Values are represented at normalized mean \pm SEM.

force development of isolated, intact rat trabecular muscle. 100 μ M propofol depressed maximum force development by $49 \pm 4\%$ (Figure 24), and 100 μ M fropofol(**1b**) exposure resulted in a similar effect with a $35 \pm 1\%$ reduction (Figure 24). These results suggest that the molecular interactions that lead to the decrease in myocardial contractility are less dependent on the 1-hydroxyl, and likely hydrogen bond interactions, in contrast to GABA_A receptor potentiation. These data indicate that fropofol(**1b**) would be an effective tool to dissect interactions within these different molecular targets and tissues.

The cardiovascular and excitatory activity of fropofol(**1b**) emphasizes the importance of distinguishing different forms of molecular recognition involved in the pharmacology of propofol. Our evidence suggests that more degenerate, apolar binding sites may transduce either no effect or are associated with certain adverse effects. Furthermore, we demonstrate that these alternative non-hydrogen bonding dependent pathways that fropofol(**1b**) unveils are probably non-GABAergic. By expanding the repertoire of recognized propofol targets, and relating molecular recognition features with the functional effect, further progress in anesthetic development is possible.

3.1.3. Conclusion

In summary, we synthesized a propofol analogue with fluorine replacing the 1-hydroxyl to result in the loss of hydrogen bond capabilities. The compound, fropofol(**1b**), displayed analogous physiochemical properties and specific binding to commonly employed anesthetic-site protein models. Within a protein site defined primarily by hydrophobic forces, fropofol(**1b**) showed greater affinity than propofol. However, within a model containing cavities with clear hydrogen bonding residues, fropofol(**1b**)

demonstrated lower affinity. Within animal models, fropofol(**1b**) administration resulted in no hypnotic activity, but rather weak excitatory activity. The excitatory activity and antagonism of propofol efficacy was determined not to be mediated by direct postsynaptic GABAergic signaling. On the other hand, fropofol(**1b**) induced myocardial depression like that of propofol. These data indicate that hydrogen bonding is a critical molecular recognition feature for propofol protein binding sites that transduce hypnosis, and that fropofol(**1b**) may be used to identify and distinguish these sites.

3.1.4. Experimental methods

General Synthetic Procedures- Solvents and reagents used were purchased from commercial sources unless otherwise noted. Proton and ^{13}C NMR spectra were recorded using Bruker DMX 500 MHz NMR spectrometer and ^{19}F NMR spectra was recorded using Bruker DMX 360 MHz NMR spectrometer. Purity of fropofol(**1b**) was determined using reverse phase-high performance liquid chromatography (rpHPLC) with C-18 analytical column. An isocratic gradient (67:28:5:0.1 acetonitrile: ddH₂O: isopropanol: trifluoroacetic acid) with a 1 mL/min flow at ambient temperature (21-22°C) was applied, and fropofol(**1b**) was monitored for UV-vis absorbance at 210 nm and 205 nm. The retention time for fropofol(**1b**) was observed at 8.5 min with a purity of >98%.

Physicochemical Properties- The density of fropofol(**1b**) was determined from triplicate measurements of the volume/mass relationship. The extinction coefficient ($\Sigma_{270}=10611/\text{M}$) was calculated through the UV (Varian Cary 300 Bio UV-vis spectrophotometer) benzene absorption at 270 nm within a methanolic solution of known concentrations. The maximal water solubility ($116 \pm 4.4 \mu\text{M}$; mean \pm SD) was calculated from the extinction coefficient after 24 hr titration and incubation in double distilled

water (ddH₂O). Octanol/water partition coefficients were calculated using XLOGP3¹⁴³. Molecular volume was calculated using NAMD program developed by the Theoretical Biophysics Group in the Beckman Institute for Advanced Science and Technology at the University of Illinois at Urbana-Champaign²⁰¹.

Isothermal Titration Calorimetry- Isothermal titration calorimetry (ITC) permits the calculation of the binding affinity and entropy based on measurement of binding enthalpy. Propofol and fropofol(**1b**) injections into the soluble protein models horse spleen apoferritin (*aF*) and human serum albumin (hSA) were conducted similar to previously reported procedures⁸⁷ and were resolved using a VP-ITC microcalorimeter (MicroCal, Inc., Northampton, MA, U.S.A). For all ITC studies, 20 mM sodium phosphate buffer containing 130 mM NaCl (pH 7.0) was used and referenced against ddH₂O. The sample cell (1.43 mL) contained either 5 μM or 2.5 μM HSAF or 20 μM hSA solution at 20°C or 26°C based on pilot studies respectively. The injectate solution (286 μL) was either propofol (160 μM) or fropofol(**1b**) (75 μM). Injections were titrated (15 μL) into the sample cell for *aF*. Because of the low-affinity interaction(s) with hSA, and the limited solubility of the ligand(s), sequential titrations were performed to achieve near complete occupancy of the binding site(s). This was accomplished by loading and titrating (10-40 μM) with the same ligand, propofol (0.55 mM) or fropofol(**1b**) (85 μM) without removal from the sample cell until the titration signal was near constant. The titrations were linked together prior to data analysis using ConCat32 software provided by MicroCal, Inc. The signals of buffer into buffer, ligand to buffer, and buffer to protein were subtracted after separate titrations. Origin 5.0 software was used to best fit thermodynamic parameters to the heat profiles.

Fluorescence competition with aF- A fluorescence competition assay utilizing 1-aminoanthracene (1-AMA) allowed comparison of ligand-protein binding in *aF*. The extent of 1-AMA fluorescence inhibition has been previously reported as a reliable measurement of anesthetic occupation of hydrophobic protein cavities^{126,186}. All solutions were prepared in 20 mM sodium phosphate buffer containing 130 mM NaCl (pH 7.2) in 1 mL quartz cuvettes. For competition with the *aF* anesthetic site⁸⁷, samples containing 5 μ M *aF* and 5 μ M 1-AMA were mixed with increasing concentrations of propofol (1-350 μ M) or propofol(**1b**) (1-100 μ M). The 1-AMA fluorescence was determined with 380 nm excitation and emission monitoring between 400 nm and 700 nm. The fluorescence curves were corrected by subtraction of the 1-AMA/protein, ligand/protein and ligand/ 1-AMA baseline emission post acquisition. The fluorescence intensity versus concentration data were fitted to variable slope Hill models to obtain the IC₅₀ and Hill slope. The K_D was calculated using the Cheng-Prusoff equation¹²⁶ to correct for the presence of the 1-AMA competitors.

[³H]meta-Azipropofol Photolabel Competition with aF- In addition to 1-AMA, we employed radiophotolabel competition using tritiated *meta*-Azipropofol (³H]AziPm) to confirm occupancy of the *aF* propofol site. In 1 mm quartz cuvettes, 3 μ M *aF* and 1 μ M [³H]AziPm respectively in ddH₂O were combined with 10 μ M propofol(**1b**) or propofol, or vehicle control (DMSO). After 5 min equilibration, the sample was irradiated for 10min with ~340-375 nm light generated by filtering a 100 W arc mercury lamp through broadband (~340-625 nm) and UV bandpass (~250-375 nm) filters (lamp and filters from Newport, Stratford, CT). After precipitation with 4X volume cold acetone and two additional cold acetone washes (1 mL each), the dried pellet was suspended in 1% SDS,

1% Triton-X, and 5 mM Tris (pH 7.6) to achieve 12 μ M *aF* (BCA Protein Assay Kit using *aF* as standard). A sample volume of 5 μ L was scintillation counted using Ecolite (+) liquid scintillation cocktail (MP Biomedicals) with a PerkinElmer Tri-Carb 2800TR instrument. The final dpm were normalized to protein content.

[³H]meta-Azipropofol Photolabel Competition with hSA- Similar competition experiments were used for hSA, except that CNBr protein digestion was used after photolabeling. Thus, after irradiation of 5 μ M hSA (>98%; Fluka) and 2 μ M [³H]Azipm with 75 μ M propofol(**1b**) or propofol or vehicle control (DMSO), samples were diluted to 1.5 μ M hSA with 0.1 M Tris-HCl (pH 8.0) and 3% SDS. DTT was then added to achieve 2 mM and samples were heated for 2 min at 96°C. CNBr and formic acid were added to produce a 9 mM CNBr, 70% formic acid solution. These samples were left at room temperature for 24 hr, followed by the addition of 200 μ L N-ethylmorpholine (97%, Sigma). Following acetone precipitation and drying under nitrogen, the pellets were resuspended in 1.5% SDS, 50 mM Tris pH 7.0. Protein content was determined with the BCA Protein Assay Kit using hSA as standard. A total of 30 μ g of digested protein was separated on 4-15% SDS-gels. After electrophoresis, the gel was stained with Coomassie blue G-250 and imaged using Kodak Image Station 4000mm Pro. Bands were excised and the polyacrylamide dissolved with 30% H₂O₂ for ~ 3 hr at 65-70°C. The sample volume was scintillation counted using Ecolite (+) liquid scintillation cocktail with a PerkinElmer Tri-Carb 2800TR instrument. The final dpm were normalized to the Coomassie blue stain intensity relative to the total sample lane. In a parallel study, bands were excised and submitted to the Proteomics Core Facility at the University of Pennsylvania for mass spectrometry to verify band peptide content.

Activity in Tadpoles- Behavioral activity was initially determined in albino *X. laevis* tadpoles (stages 45-47) as previously described^{187,193}. Tadpoles (n= 240) were incubated in Petri dishes (10 tadpoles/dish) with concentrations (3 μ M, 30 μ M, 70 μ M and 100 μ M) of fropofol(**1b**) dissolved in pond water, containing <0.01% DMSO vehicle, for 60 or 90 min. Because loss of righting was not observed with any fropofol(**1b**) concentration, fropofol(**1b**) was co-administered with propofol to look for pharmacological additivity. Tadpoles (n= 630) were incubated with varying concentrations of fropofol(**1b**) (0 μ M, 5 μ M, 25 μ M and 100 μ M) and propofol (0.25-3 μ M) dissolved in pond water containing <0.01% DMSO vehicle and were evaluated after 30 min. Hypnosis was defined as the percentage of tadpoles that did not demonstrate spontaneous movement over the course of a 30 s period preceding each time point. After both study conditions, the tadpoles were transferred to fresh pond water and observed overnight for signs of toxicity. The water temperature remained between 21-22°C throughout the experiments. All animal care and experimental procedures involving *X. laevis* tadpoles were carried out according to protocol approved by the IACUC of University of Pennsylvania.

Pharmacological Activity in Mice. Fropofol(**1b**) was dissolved in 10% lipid emulsion to 30 g/L and two dosages, 96 mg/kg (n= 2) and 180 mg/kg (n= 2), were introduced into 12-20 week C57/B6 mice via tail vein bolus injection. Mice were then monitored for changes in behavior immediately and over the following days post injection. Some mice were euthanized by cervical dislocation within 45 s or 10 min post injection, and the brain was rapidly removed and frozen for subsequent fropofol extraction. Fropofol(**1b**) extraction proceeded according to methods published for propofol (41). Briefly, 2

volumes of 0.22 μm filtered PBS buffer was added to weighed brain samples. The brain was homogenized for 5 s using a Polytron PT 1300D handheld homogenizer (Kinematica), vortexed for 30 s, and centrifuged for 20 min at 14,000 x g. The supernatant was removed and 2 volumes of HPLC-grade acetonitrile was added. Samples were vortexed for 30 s and centrifuged for 20 min at 14,000 x g. Fropofol(**1b**) amount was quantified using the same rpHPLC method as mentioned above. All brain tissue extractions were conducted within 12 hr of rpHPLC quantification and the fropofol(**1b**) peak was clearly distinguishable from tissue peaks with the determined retention time of 8.5 min. Generated standard curves with neat fropofol(**1b**) in methanol provided absolute concentration values. Based on an average (n= 4) of fropofol spiked brain tissue samples, recovery from tissue was determined to be $4.8 \pm 0.2\%$ for both 210 nm and 205 nm wavelengths (similar for propofol).

Electroencephalography (EEG) recording. 12-20 week C57/B6 male mice (n= 2) were placed under general anesthesia maintained with isoflurane and implanted with 5 right-sided chronically indwelling silver ball EEG electrodes over frontal association cortex (2.6 mm anterior to bregma, 1.0 mm lateral), primary motor cortex (2.0 mm anterior to bregma, 2.0 mm lateral), the medial parietal association area (1.7 mm posterior to bregma, 1.2 mm lateral), primary somatosensory cortex (2.0 mm posterior to bregma, 2.6 mm lateral) and primary auditory cortex (2.3 mm posterior to bregma, 4.0 mm lateral); the leads were secured with dental cement. After a minimum of a two-week recovery, a tail vein catheter was placed in the lateral tail vein of an implanted mouse and secured. After recording a 5 min baseline EEG, 200 mg/kg fropofol(**1b**) in 10% lipid emulsion was injected over 3 s through the catheter, and the catheter was flushed with 100 μL

normal saline. Acqknowledge (Biopac Systems Inc., Golea, CA) was used for processing with a 0.8-59 Hz software bandpass filter. All animal care and experimental procedures involving mice were carried out according to protocol approved by the IACUC of the University of Pennsylvania.

Electrophysiology. $\alpha_1\beta_2\gamma_{2L}$ γ -Aminobutyric acid type A ($GABA_A$) receptor expression within oocytes- cDNAs for $GABA_A$ receptor α_1 , β_2 , and γ_{2L} subunits were kindly provided by Dr. Robert Pearce (University of Wisconsin). Defolliculated stage V-VI *Xenopus laevis* (*X. laevis*) oocytes were microinjected with 2.8 ng of *in vitro* transcribed cRNA (mMessage mMachine kit, Ambion, Austin, TX) of $\alpha_1/\beta_2/\gamma_{2L}$ subunits at a 1:1:10 weight ratio respectively. Oocytes were incubated at 18°C in a gentamycin supplemented ND96 solution (in mM: 96 NaCl, 2 KCl, 1 MgCl₂, 1.8 CaCl₂, 5 HEPES, 2.5 Na-Pyr, pH 7.4 with NaOH) for 16-24 before use. All animal care and experimental procedures involving *X. laevis* frogs were carried out according to a protocol approved by the IACUC of Thomas Jefferson University.

Oocyte Electrophysiology Recordings- $GABA_A$ receptor whole-oocyte currents were recorded at room temperature (21-23°C) under two electrode voltage clamp (TEVC) conditions (OC-725C, Warner Instrument, Hamden, CT). All recordings were made at a holding voltage of -80 mV. Oocytes were continuously perfused with ND96-based solutions using gravity-driven perfusion system with an approximate perfusion rate 2-4 mL/min. The perfusion system was outfitted with Teflon® tubing for drug exposure studies. γ -Aminobutyric acid (GABA; Sigma) solutions were prepared daily in ND96. Propofol and fropofol(**1b**) were directly dissolved in ND96 facilitated by sonication. Initially each oocyte was exposed to 2.5-5 μ M GABA for the effective concentration

(EC) 7-13 of maximum GABA_A receptor activation. Maximum GABA response was determined by a 10 mM GABA perfusion post drug exposure and washout. To determine modulatory activity oocytes were perfused for 20 s with the test compound(s) immediately followed by 20 s perfusion with the test compound and GABA at determined EC10. Oocytes continuously perfused in ND96 solution or fropofol ND96 based solution prepared as noted above. Data acquisition and initial analysis were performed using pClamp 9.2/10.3 (Molecular Devices, Sunnyvale, CA). Macroscopic currents were low-pass filtered at 1 kHz and digitized at 2 kHz. Expression of $\alpha_1\beta_2\gamma_{2L}$ cRNA within *X. laevis* oocytes generated GABA_A receptors that demonstrated a GABA EC50 of 33 μ M (95% CI, 29 - 38) with a Hill coefficient of 0.87 ± 0.04 (mean \pm SEM) within 18-24 hr post microinjection.

Trabeculae preparation- Drug effects on myocardial contractility were conducted as previously reported²⁰². Briefly LBN/F1 rats (250–300g, Harlan Laboratories, Indianapolis, IN) were anesthetized by intra-peritoneal injection of pentobarbital (100 mg/kg); the heart was exposed by sternotomy and rapidly removed. After transfer to a dissection dish, the aorta was cannulated and the heart perfused in a retrograde fashion with dissecting Krebs-Henseleit (K-H) solution (in mM: 120 NaCl, 20 NaHCO₃, 5 KCl, 1.2 MgCl₂, 10 glucose, 0.5 CaCl₂, and 20 2,3-butanedione monoxime (BDM) (pH 7.35–7.45); equilibrated with 95% O₂ and 5% CO₂). The trabecular muscle was dissected from the right ventricle and mounted between a force transducer and a motor arm. The muscle was superfused with K-H solution without BDM at \sim 10 ml/min, and stimulated at 0.5 Hz. A transducer (KG7, Scientific Instruments GmbH, Heidelberg, Germany) was used to measure the developed force, and expressed as millinewtons per square millimeter of

cross-sectional area. The muscles underwent isometric contractions with a set resting muscle length that was set at 15% of the total force development corresponding to resting sarcomere length of 2.20-2.30 μm as determined by laser diffraction²⁰³. Propofol or propofol(**1b**) were added to non-BDM containing K-H solution at desired concentrations during the experiments. Similar force depression was observed at both 37°C and room temperature (20-22°C); the experiments reported herein were performed at room temperature. Animal care and experimental protocols were approved by the Animal Care and Use Committee of The Johns Hopkins University School of Medicine. Data is represented as mean \pm SEM of experiments normalized to initial force development without drug exposure.

Statistics- GraphPad Prism5, unless otherwise noted, was used for preparation and statistical data analysis. Details are given in the figure legends.

3.2. Novel bifunctional alkylphenol anesthetic allows identification of the alkylphenol binding synaptic proteome

While demonstrating higher potency compared to volatile anesthetics, propofol still requires micromolar plasma concentrations to induce observable behavioral effects⁴⁰. Evidence suggests the likelihood of protein targets as major contributors towards the mechanisms of propofol with *in vitro* studies demonstrating functional influence at pharmacologically relevant concentrations^{6,178}. Regardless, direct identification of propofol interactions with protein targets in more physiologically relevant biological systems has been a scientific challenge. Forming an understanding of likely binding sites of potential clinical relevance within protein targets is vital for the characterization of propofol. Therefore a development of a means to study a biological system that

demonstrates physiologically relevant protein distribution and molecular environment is significant.

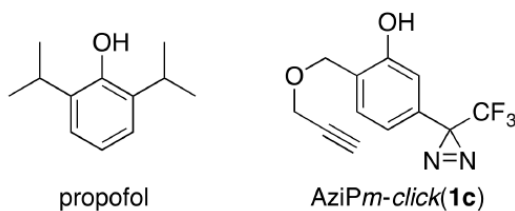


Figure 25. Chemical structures of propofol and AziPm-click(1c)

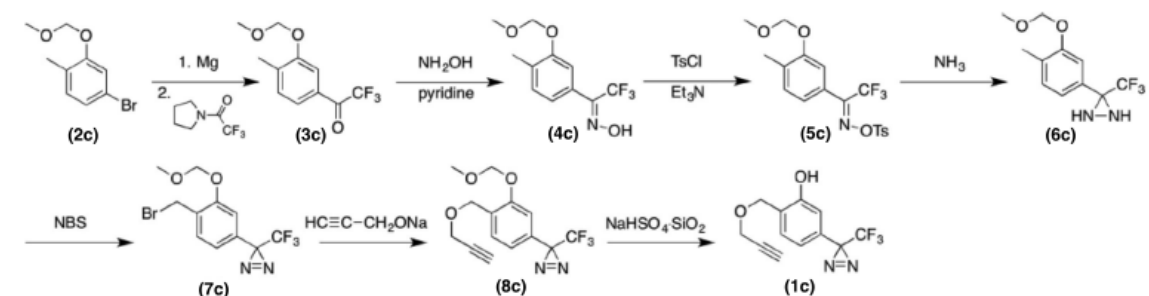
Herein an affinity-chemoproteomic strategy is presented to expand the current range of approaches for anesthetic protein target identification within non-recombinant tissue. A novel propofol analogue, *ortho*-alkynyl-*meta*-azipropofol or AziPm-click(1c) (Figure 25), was synthesized this compound contains two chemically-active groups; 1) a photoactive group for direct and immediate labeling of protein targets and 2) a ‘click chemistry’ partner for designed attachment of affinity tags for target protein enrichment. Within this study an alkylphenol-based anesthetic pharmacoproteome composed of 196 propofol-binding proteins, or approximately 4% of the mouse synaptosomal proteome, was identified.

3.2.1. Synthesis and characterization of AziPm-click(1c)

To identify the alkylphenol binding proteins within the synaptic proteome, 2-((prop-2-yn-1-yloxy)methyl)-5-(3-(trifluoromethyl)-3H-diazirin-3-yl)phenol, or AziPm-click (1c), a photoaffinity tandem bioorthogonal alkylphenol anesthetic ligand was developed. AziPm-click (1c) was designed to integrate two chemically active groups that allow for affinity-based protein profiling (ABPP): 1) a diazirine photoreactive group to covalently label protein-interaction sites and 2) an alkynyl group for covalent attachment

of a reporter tag by 1,3-dipolarcycloaddition reaction (e.g. ‘Click Chemistry’) in order to capture and identify photoaffinity-labeled proteins within the synaptic proteome.

Scheme 3.



Synthesis of *AziPm-click* (**1c**), shown in Scheme 3, starts with the previously reported 4-bromo-2-(methoxymethoxy)-1-methylbenzene (**2c**)²⁰⁴. Conversion of **2c** to the Grignard reagent using magnesium in THF followed by treatment with pyrrolidine trifluoroacetamide produced trifluoromethyl ketone **3c**. Conversion of **3c** to the oxime **4c**

Table 6. Physicochemical properties of propofol and *AziPm-click*(**1c**)

	MW, Da	Density, g/mL	cLogP
<i>AziPm-click</i> (1c)	270	1.19	3.55
propofol	178	0.96	3.79

and oxime tosylate **5c** followed standard procedures. Treatment of **5c** with excess liquid ammonia produced diaziridine **6c** which was oxidized to the diazirine **7c** using pyridinium dichromate (PDC). Benzylic bromination using N-Bromosuccinimide (NBS) produced **8c**, which was treated with the sodium salt of propargylic alcohol in Tetrahydrofuran (THF) to provide **9c**. Removal of the methoxymethyl protecting group in the presence of the propargylic ether required carefully controlled conditions and was finally accomplished using sodium hydrogen sulfate impregnated silica gel in methylene chloride²⁰⁵.

The physicochemical characteristics of propofol and *AziPm-click* (**1c**) are summarized in Table 6 and the geometry-optimized structure is shown in Figure 26A.

Table 7. Equilibrium binding parameters of propofol and *AziPm-click*(**1c**) to *aF*

	Propofol		<i>AziPm-click</i> (1c)	
	ITC	1-AMA displacement ^b	ITC	1-AMA displacement ^b
K_D (95% CI; μM)	9 (7.1 - 11)	2.4 (1.3-4.4)	22 (20- 24)	4.0 (1.8 – 8.7)
Hill slope (Mean \pm SEM)	1 ^a	-1.1 \pm 0.33	1 ^a	-0.97 \pm 0.39

^a Stoichiometry of *aF* sites were modeled for one site therefore the Hill slope is fixed at 1; ^b K_D Fluorescence data derived from Cheng–Prusoff equation

The UV absorption spectrum of *AziPm-click* (**1c**) shows a well-defined peak between 330- 400 nm due to the diazirine group (methanol extinction coefficient ($\Sigma_{365\text{nm}}$) of 580 /M). Over the course of UV irradiation using a Rayonet RPR-3500 lamp within aqueous solution, the *AziPm-click* (**1c**) diazirine absorbance band decreased intensity indicating photoactivation (Figure 26B). The time-dependent photoreactivity of *AziPm-click* (**1c**) in aqueous solution was a single exponential decay with a half-life ($t_{1/2}$) of 25 min (95% CI; 20-33) within a 1 cm path-length cuvette and 6 cm from the lamp. To confirm retention of other major molecular recognition features, we compared equilibrium binding affinities of applied alkylphenol general anesthetics with the model protein *aF* by ITC and 1-AMA competition^{187,206}. The affinities of alkylphenols for *aF* have shown to be well correlated with GABA_A receptor potentiation^{87,88,186}; results are summarized in Table 7.

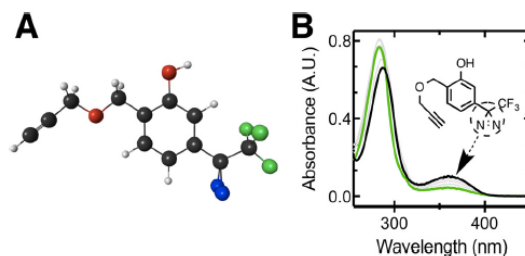


Figure 26. *AziPm-click* (**1c**) geometry and photoreactivity. A) Ball and stick structure of *AziPm-click* (**1c**) in predicted lowest energy conformation (gray: carbon, red: oxygen, blue: nitrogen, green: fluorine). B) UV absorption spectra of *AziPm-click* (**1**) (175 μ M) in double distilled water (black line) over the course of UV irradiation time points (gray and green lines).

Propofol and *AziPm-click* (**1c**) demonstrated similar pharmacological endpoints within *Xenopus laevis* (*X. laevis*) tadpoles, inducing reversible hypnosis with no observable toxicity summarized in Table 8 and shown in Figure 27. To indicate photoaffinity labeling of pharmacologically relevant targets, we demonstrated that *AziPm-click* (**1c**) produced sustained anesthetic endpoints (immobility) *in vivo* after UV irradiation⁹³. *X. laevis* tadpoles were exposed to 12 μ M *AziPm-click* (**1c**) or 3 μ M propofol for 30 min. Tadpoles were then exposed to 10 min of low intensity UV irradiation or were maintained as a 10 min non-UV control. Similar to our previous reports for *AziPm*⁹³, only tadpoles exposed to *AziPm-click* (**1c**) and 10 min UV displayed prolonged immobility after drug washout (Figure 27).

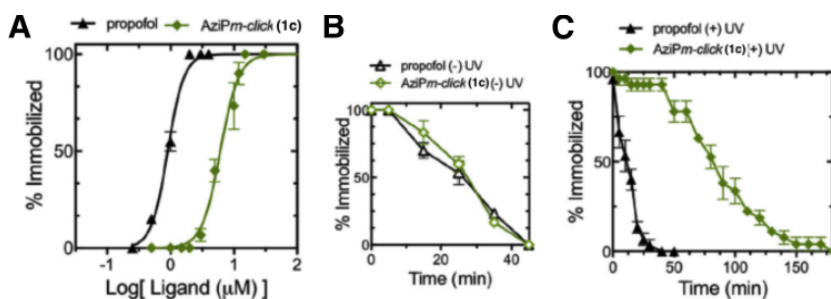


Figure 27. Anesthetic activity of *AziPm-click*(**1c**) A) Dose-response curves for propofol (n= 210; black circle) and *AziPm-click* (**1c**) (n= 300; green diamond) for loss of spontaneous movement in tadpoles. Data was fitted to a sigmoidal dose response curve with variable Hill Slope and the EC₅₀ and Hill slope values are represented in Table 8. B) Time course of recovery for *Xenopus laevis* tadpoles following propofol (n=30; black open circle) or *AziPm-click* (**1c**) (n=30; green open diamond) equilibration and 10 min no UV treatment control. E) Time course of recovery for

tadpoles following propofol (n=30; black filled circle) or AziPm-*click* (**1c**) (n=30; green filled diamond) equilibration and 10 min of low intensity UV irradiation.

Table 8. Tadpole studies with propofol and AziPm-*click*(**1c**)

	EC ₅₀ (95% CI; μ M)	Hill slope (Mean \pm SEM)
AziPm- <i>click</i> (1c)	6.1 (5.1-7.4)	3.0 \pm 0.54
propofol	0.90 (0.84 -0.97)	3.4 \pm 0.31

3.2.2. Affinity-based protein profiling (ABPP) of alkylphenol synaptic protein targets

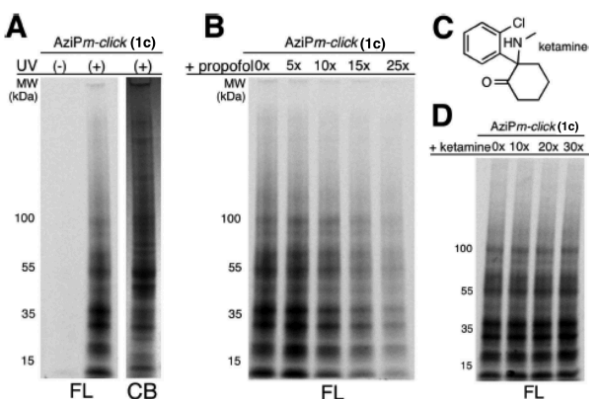


Figure 28. Fluorescent profiling of propofol proteome. A) Fluorescent image (FL) of SDS-PAGE gel of synaptosomes exposed to AziPm-*click* (**1c**) with or without UV irradiation and corresponding Coomassie blue (CB) stain of UV irradiated synaptosomes. B) Protection from AziPm-*click* (**1c**) labeling of synaptosomes by propofol at 5x (75 μ M), 10x (150 μ M), 15x (225 μ M) and 25x (375 μ M). C) Chemical structure of ketamine. D) Protection from AziPm-*click* (**1c**) labeling of synaptosomes by ketamine at 10x (150 μ M), 20x (300 μ M) and 30x (450 μ M). All experiments were conducted in triplicate.

To confirm the functionality of both the chemically active groups for downstream ABPP, AziPm-*click* (**1c**) was employed within mouse synaptosomes using an azide-PEG3-Alexa 488 fluorophore as a reporter tag. The fluorescent labeling of proteins was reliant on UV exposure (Figure 28A). Fluorescent labeling was decreased with increased concentrations of propofol indicating protection of alkylphenol-binding proteins within synaptosomes (Figure 28B). To control for potential ‘inner-filter’ of UV light, ketamine was employed as a protecting ligand (Figure 28C), which conferred no changes in fluorescence intensity seen in Figure 28D.

The ABPP workflow using *AziPm-click* (**1c**) with relative quantification, is summarized in Figure 29A. Azide-PEG3-biotin was employed as the reporter tag for streptavidin-affinity isolation of photoaffinity labeled protein targets. Tandem Mass Tag (TMT) isotopic labeling and three-stage mass spectrometry (MS3)²⁰⁷ was coupled to ABPP for quantitative assessment of capture and propofol protection. The totals for identified proteins are summarized in Figure 29B. The *AziPm-click* (**1c**) proteome contained a discernible group of proteins that demonstrated a high degree of capture efficiency with a greater than 10 enrichment factor (Figure 29C). Of the higher capture group, the majority of proteins displayed propofol specificity with a greater than 50% protection, and a decrease of at least 5 in enrichment factor (Figure 29D, see appendix A.5.).

It is unlikely that a given drug will only bind and act on a single protein target within a proteome. In particular, the small general anesthetic molecules have been shown to bind to many different proteins²⁰⁸. While propofol is thought to have higher affinity for specific protein targets relative to volatile anesthetics, the projected affinities for

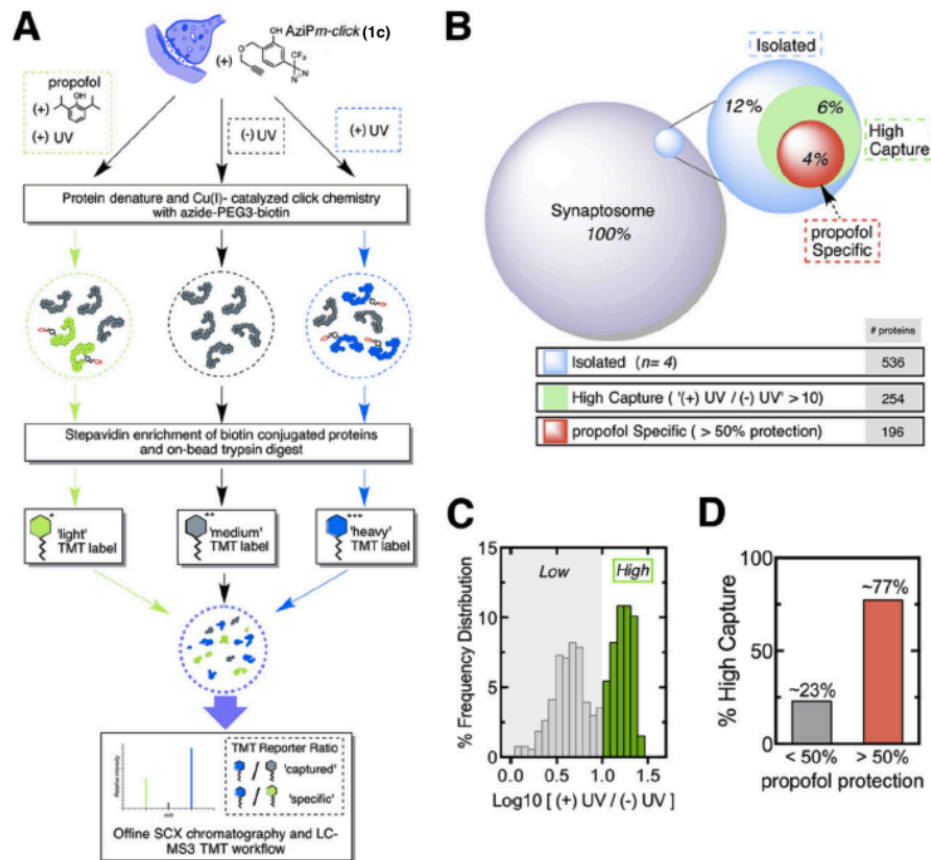


Figure 29. Affinity-based propofol profiling of alkylphenol binding proteins in native synaptosomes. A) Scheme for capture and analysis of AziPm-click (1c) labeling profiles in synaptosomes by biotin-streptavidin methods, tandem mass tag (TMT) labeling for relative quantification, strong cation exchange chromatography (SCX) and Nanoliquid chromatography - three-stage mass spectrometry (NanoLC-MS3) analysis. B) Distribution of protein groups for the AziPm-click (1c) capture and approximant percentage of full synaptosomal proteome, with a summary of group's threshold requirements. Proteomic experiments were conducted in quadruplicate; the log₂ standard deviation between datasets was calculated as 0.28 for heavy over intermediate TMT labeled samples and 0.17 for heavy over light TMT labeled samples. C) TMT ratio frequency distribution (Log₁₀ scale) of UV versus no UV with high capture efficiency threshold. D) Percent of high capture group proteins that demonstrated less then or greater then 50% protection by propofol.

major targets, such as the GABA_A receptor, still remain in the low micromolar range³⁹.

Therefore, it is not surprising that a number of targets (196) were captured due to the promiscuous binding associated with the general anesthetic. Whether the activity of every identified protein is altered upon alkylphenol binding is not clear and not likely.

However, some captured targets have been reported as being influenced by propofol.

Examples include a likely major target synaptic GABA_A receptor¹⁵⁹, syntaxin-1A¹⁰⁹, N-methyl-D-aspartate receptor (NMDA 1)²⁰⁹, potassium/sodium hyperpolarization-activated cyclic nucleotide-gated channel 1 (HCN 1)²¹⁰ as well as voltage-gated calcium channels²¹¹ and potassium channels¹²⁹ all of which may contribute to desirable and/or undesirable pharmacological effects.

3.2.3. Conclusions

Propofol has been widely administered for over a quarter century in general anesthesia and for rapid sedation. Regardless, the drug's mechanism of action remains elusive however mounting evidence has suggested that multiple pathways contribute to propofol's pharmacological effects. Most of the proposed protein targets, such as ion channels and ligand-gated receptors^{138,212}, are low abundance but functionally important proteins. To uncover these significant targets, we synthesized a bioorthogonal propofol *α*-PAL, AziPm-click(**1c**). The introduction of an *ortho*-alkynyl group allows for the attachment of affinity tags for the designed capture of photomodified proteins by copper catalyzed 1,3-dipolar cycloaddition, or Click chemistry. AziPm-click(**1c**) maintains the physiochemical, biochemical and *in vivo* properties of propofol. After the unbiased photoaffinity labeling of bound targets, the *ortho*-alkynyl click moiety successfully undergoes click chemistry reactions with azide-containing tags within mouse synaptosomes. Coupled with a quantitative mass spectrometry workflow, the study provided a strategy for labeling and capture of low abundance protein targets for propofol. Ultimately AziPm-click(**1c**) highlighted the expansive group of alkylphenol-based anesthetic bound proteins within synapses and indicated the likely complex nature of propofol mechanisms of action.

3.2.4. Experimental methods

Physicochemical properties. The UV spectrum and extinction coefficient of the AziPm-click (**1c**) diazirine absorption were obtained from known concentrations in methanolic solutions and gathered from the Varian Cary 300 Bio UV-visible spectrophotometer. Photoactivation of the diazirine was measured by the disappearance of the diazirine UV absorption peaks when exposed to 350 nm light (Rayonet RPR-3500 lamp) ~ 6 cm from the light source. Maximum water solubility was approximated using the extinction coefficient. Calculated octanol/ water partition coefficients were generated using XLOGP3 software²² with default settings. The geometry-optimized structures for AziPm-click (**1c**) was calculated at the B3LYP/6-311+G (2d,p) level of theory using t pH 7.4) before decapitation. Brains were extracted and homogenized in ice cold isolation buffer (IB; 0.32 M sucrose/ 2.5 mM 4-(2-hydroxyethyl)-1-piperazineethanesulfonic acid (HEPES), 1 mM ethylenediaminetetraacetic acid (EDTA) (pH 7.4)) (10% w/v%) in the presence of protease and phosphatase inhibitors. The homogenate was centrifuged at 1,000 x g for 10 min at 4° C. The resulting supernatant was decanted and pellet was homogenized with equal volume IB and centrifuged at 1,000 x g for 10 min at 4° C. Both supernatants were pooled were centrifuged at 1,000 x g for 10 min at 4° C. The supernatant was decanted and centrifuged at 12,000 x g for 20 min at 4° C. The pellet was washed twice by resuspension of the pellet in 2X volumes of IB and centrifugation at 12,000 x g for 15 min at 4°C. The resulting crude preparation of synaptosomes, now entirely free of the euthanizing isoflurane, was used in following experiments. All following protein contents are measured using BCA assay (Thermo Scientific). Animal

care and experimental procedures involving mice were carried out according to a protocol approved by the IACUC of University of Pennsylvania.

Synaptosomal photoaffinity labeling. Synaptosomes were resuspended to 1 mg protein/mL in HEPES buffer medium (in mM: 140 NaCl, 5 KCl, 5 NaHCO₃, 1.2 NaH₂PO₄, 1 MgCl₂, 10 glucose, and 10 HEPES (pH 7.4)). Concentrations of AziPm-click (**1c**) with or without the presence of concentrations of competitive ligands (propofol or ketamine) in dimethyl sulfoxide (DMSO) vehicle (<0.3% v/v) were added and synaptosomes were gently vortexed for 10 s. The samples were allowed to equilibrate for 5 min before being transferred to a parafilm-sealed 1 mm path-length quartz cuvette. The sample was then irradiated for 20 min at a peak band-width of 350 nm (Rayonet RPR-3500 lamp) ~ 6 cm from the light source. Non-irradiated samples were left in the dark at ambient temperature (22-25°C) for 20 min. All remaining procedures were conducted with restricted light exposure.

Fluorophore conjugation for proteome detection. To 150 µg of photolabeled or control synaptosomes, 8 µL of 10% sodium dodecyl sulfate (SDS) in water and 2 µL of 1 mM dithiothreitol (DTT) in water were added. Samples were vortexed and heated at 65° C for 10 min. After brief cooling final concentrations of 30 µM azide-PEG3-Fluor 488 (Click Chemistry Tools), 2 mM tris(3-hydroxypropyltriazolylmethyl)amine (THTPA) (Sigma), 1 mM ascorbic acid (Sigma), and 1 mM CuSO₄* 5H₂O (Sigma) were added to each sample and vortexed vigorously. The samples were left in the dark for 1 hr. After, 4X volume of chilled methanol, 1.5X of chilled chloroform, and 3X of chilled ddH₂O were added and vortexed vigorously. Samples were centrifuged at 1,300 x g for 30 min and both liquid layers were carefully removed. The protein pellet was washed with 500 µL of

1:1 (v:v) methanol: chloroform and centrifuged at 14,000 x g for 20 min at 4° C. Washed pellets were air dried for 10 min and resuspended in 25 µL of 1% SDS and 1% Triton-X in 50 mM TrisBase buffer. An equal volume of 2X SDS Laemmli buffer was added and 25 µg of protein was loaded without boiling to 4-15% SDS-PAGE gel. Proteins were directly visualized within the gel using fluorescence and then stained with Coomassie G250 stain. Fluorescent studies were normalized to Coomassie stain band intensity.

Hypnotic activity and In vivo photolabeling in Xenopus laevis Tadpoles- Behavioral activity was initially determined in albino *X. laevis* tadpoles (stages 45-47) as previously described^{93,187}. All animal care and experimental procedures involving *X. laevis* tadpoles were carried out according to a protocol approved by the IACUC of the University of Pennsylvania

Biotin conjugation- To 750 µg of photolabeled or control synaptosome sample, 40 µL of 10% SDS and 2 µL of 5 mM DTT in water were added. Samples were then vortexed, heated for 10 min at 65°C, and then briefly cooled. Final concentrations of 150 µM azide-biotin (Click Chemistry Tools), 2 mM THPTA (Sigma), 1 mM ascorbic acid (Sigma), and 1 mM CuSO₄* 5H₂O (Sigma) were added to each sample and vortexed vigorously. The samples were left in the dark at ambient temperature (22-25° C) for 1 hr with mild agitation. Directly to each sample 4X volume chilled methanol, 1.5X chilled chloroform and 3X chilled ddH₂O were added. Samples were vortexed vigorously and centrifuged at 1,400 x g for 30 min at 4°C. Both liquid layers were carefully removed and the protein pellet was washed with 2 mL of 1:1 (v:v) chilled methanol: chloroform. Samples were centrifuged at 3,500 x g for 30 min at 4° C. Protein pellets were briefly air dried before further processing.

Sample processing for affinity-based protein profiling (ABPP) mass spectrometry

studies- 750 µg of biotin conjugated protein sample was resuspended in 500 µL of 25 mM NH₄HCO₃ and 6 M urea in water. Next, 150 µL 5% Triton-100X in water, 50 µL 10% SDS in water and 1.5 µL 0.5 M DTT were added. The samples were heated for 15 min at 65° C. After briefly cooling, 14 µL of 0.5 M iodoacetamide in water was added and the sample was left in the dark for 45 min. Insoluble debris was separated by centrifugation for 10 min at 14,000 x g. The supernatant was diluted to 4 mL with PBS and 2 mL of PBS containing 100 uL of 50% strepavidin-agarose resin (Thermo Scientific) was added. Biotinylated proteins within the sample were captured over resin overnight at 4° C with mild agitation. The resin was first washed with 6 mL of 1% SDS in PBS, then 7 mL of 0.1 M urea in PBS followed by 10 mL PBS. The resin underwent a final wash with 0.9 mL 50 mM Tris-HCl and 1 mM CaCl₂ in water (pH 8.0) and then resuspended in 200 uL of 50 mM Tris-HCl, 1 mM CaCl₂ in water (pH 8.0) and 2 µg of porcine sequencing grade trypsin (Promega). Samples were digested overnight at 37° C. Samples were then centrifuged at 2,000 x g for 4 min and digest supernatant was decanted. Beads were washed in 100 µL PBS centrifuged at 5,200 x g for 5 min and the wash was combined with the digest supernatant. To the combined sample, trifluoroacetic acid (TFA) was added to 0.4% (v/v) or until pH < 2. The sample was desalted with Oasis C18 10 mg columns (Waters) as previously described²¹³. The eluted sample was dried by speed vac and resuspended in 0.1 M HEPES buffer (pH 8.5). Samples were labeled with Tandem Mass Tag™ 6-plex (TMTsixplex™) (Thermo Scientific) with the UV(+) sample labeled with TMT⁶- 128 or 131 reagent, the propofol protection sample labeled with TMT⁶- 126 or 129 reagent and the UV (-) sample labeled with TMT⁶- 127 or 130 reagent

using product instructions. Appropriate corresponding TMTsixplexTM-labeled samples were pooled and dried by speed vac. The combined samples were resuspended in 0.5% acetic acid in water, pH corrected with acetic acid until pH was < 2. 40 µg of protein was desalted with C18 stage tips prepared in house and dried by speed vac.

Samples were resuspended in 10 mM KH₂PO₄ (pH 2.6) 30% ACN (v/v%) in water and fractionated by offline strong cation exchange (SCX) chromatography prior to mass spectrometry (MS) analysis similar to as previously reported²¹³. The full synaptosome proteome control was prepared similarly without TMTsixplexTM labeling.

Mass spectrometry analysis- All TMT samples were analyzed with three-stage mass spectrometry (MS3) TMTsixplexTM quantification workflow previously described²⁰⁷. Spectral analysis was conducted using Thermo Proteome Discoverer 2.0 (Thermo Scientific) and mouse non-redundant (gene-centric) FASTA database. Mascot searches allowed for variable oxidation of methionine (+15.9949 *m/z*) and static modifications of cysteine residues (+57.0215 *m/z*; iodoacetamide alkylation) and TMT6-plex tags on lysine residues and peptide N-termini (+ 229.162932 *m/z*). To establish the base synaptosomal proteome, searches allowed for variable oxidation of methionine (+15.9949 *m/z*) and static modifications of cysteine residues (+57.0215 *m/z*; iodoacetamide alkylation). All studies maintained trypsin enzyme specificity filtered with no greater than 2 missed cleavages. The MS2 spectral assignment was restricted to a specified false positive rate of 1% and a minimum of 2 unique peptides were required for protein identifications. Quantification was based on the theoretical *m/z* of the individual TMTsixplexTM reporter ions as previously reported²⁰⁷. Enrichment factor was defined as

the mean (+)UV/(-)UV TMT ratio. Frequency distribution histograms of Log2 values were generated using GraphPad Prism 7.0.

3.3. Characterization of alkylphenol anesthetic selective GABA_A receptor subunit binding in synaptosomes

Numerous drugs influence GABA_A receptor activity, including propofol, which has been strongly implicated as a modulator of the GABA_A receptor²¹⁴. Relatively low concentrations of this alkylphenol significantly potentiate GABA-induced current, an action that hyperpolarizes the post-synaptic membrane and thereby likely contributes to hypnosis and possibly other anesthesia phenotypes^{215,216}. Furthermore multiple reports indicate that phasic inhibition is particularly sensitive to low concentrations of propofol, suggesting that synaptic GABAergic signaling is a critical pathway for the anesthetic's pharmacological effects²¹⁷⁻²¹⁹.

Investigations have focused on the potential binding sites within heterologously expressed $\alpha\beta\gamma$ GABA_A receptors. A wide range of mutagenesis studies have probed ligand-gated ion channel electrophysiology and have shown that mutation of various residues predicted to reside within subunit interfacial regions alter propofol modulation^{220-222,170}. Particular point mutations within β subunits, such as N265, greatly decreased propofol positive modulation^{216,223}. Previous work using the [³H]AziPm demonstrated frequent labeling of interfacial residues within heterologously expressed Cys-loop superfamily of receptors, including $\alpha_1\beta_3\gamma_2$ GABA_A receptors⁷⁶. These findings further suggest that subunit interfaces are potentially involved in propofol modulation. Structure-activity relationships applying alkylphenol analogues and/or other chemical derivatives^{185,224}, molecular dynamic (MD) simulations^{225,226}, as well as other investigations have

suggested complex physicochemical interactions between propofol and GABA_A receptors²²⁷. Together, these studies have provided insight regarding the potential mechanism by which propofol perturbs GABA_A receptor protein dynamics. However, in addition to the biased nature of using heterologously expressed receptors, it is recognized that each method has experimental limitations that result in the current uncertainty regarding alkylphenol interactions within the receptor.

The objective of this investigation was to advance the current understanding of anesthetic interactions with heteromeric receptors by addressing the interaction(s) of alkylphenols with GABA_A receptors within their native synaptic milieu. Five GABA_A receptor subunits ($\alpha_{1,3}$ and $\beta_{1,3}$) were identified as propofol-specific proteins (see appendix A.5.). All subunits showed a decrease of at least 10 in enrichment factor with propofol protection. This unbiased ABPP capture of the receptor from a complex biological milieu, derived from native tissue, is to our knowledge, the first such demonstration, and it further validates the receptor as a pharmacologically relevant target. To further corroborate the ABPP results and the apparent subunit-level selectivity binding to this single target other approaches were employed. Independent MD simulations using the Alchemical Free Energy Perturbation (AFEP) algorithm²²⁸ were used to predict potential molecular recognition elements within $\alpha_1\beta_3\gamma_2$ GABA_A receptor binding sites. The impact of the molecular recognition elements was examined within the synaptic GABA_A receptors with photoaffinity protection experiments. Jointly, the studies led to the unbiased identification of GABA_A receptor subunits in native synaptic membranes as alkylphenol binding proteins. This investigation further suggested higher affinity for

β^+/α^- and α^+/β^- interfacial sites relative to γ^- containing subunit interfaces with hydrogen bonding as the major recognition element for the alkylphenol/GABA_A receptor complex.

3.3.1. $\alpha_1\beta_2\gamma_{2L}$ GABA_A receptor modulation by AziPm-click(**1c**)

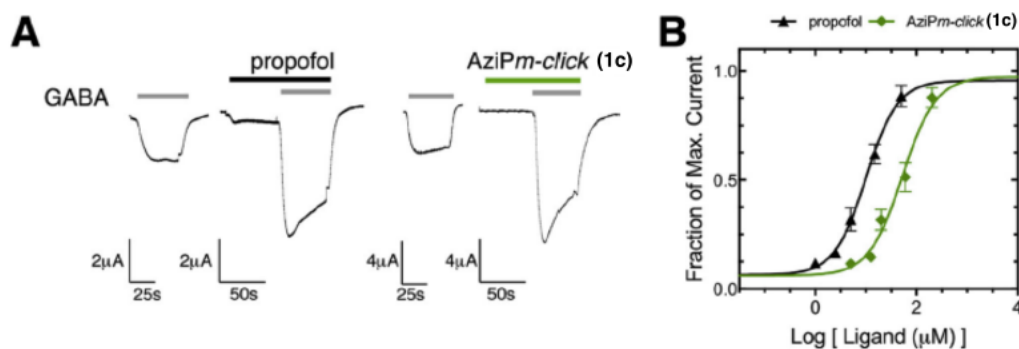


Figure 30. AziPm-click(**1c**) $\alpha_1\beta_2\gamma_{2L}$ GABA_A receptor activity. A) Representative traces of ligand activity on heterologously expressed $\alpha_1\beta_2\gamma_{2L}$ GABA_A receptors in *Xenopus laevis* oocytes. Traces are shown with the oocytes response to GABA EC₁₀ and corresponding modulation propofol (3 μ M) or AziPm-click(**1c**) (20 μ M). B) Concentration-response curves for propofol (black circle) and AziPm-click(**1c**) (green diamond) for the positive modulation of heterologously expressed GABA_A receptor $\alpha_1\beta_2\gamma_{2L}$ in *Xenopus laevis* oocytes. Each point represents the mean of 4 oocytes (n=4) +/- SEM and data was fitted to a sigmoidal dose response curve with variable Hill Slope.

To associate AziPm-click (**1c**) binding to synaptic GABA_A receptor functional activity, electrophysiological studies on heterologously expressed receptors were performed. AziPm-click (**1c**) was functionally active on $\alpha_1\beta_2\gamma_{2L}$ GABA_A receptors expressed in *Xenopus* oocytes. AziPm-click (**1c**) demonstrated similar positive modulation activity as propofol (Figure 30). The EC₅₀ for propofol positive modulation (at a GABA EC₁₀) in our system was 10 μ M (95% CI; 3.3-17). AziPm-click (**1c**) required a higher concentration for a similar response with an EC₅₀ of 49 μ M (95% CI; 38-61). These studies indicate, while with lower potency, that AziPm-click binding does transduce positive modulation similar to that of propofol, likely through the shared binding site.

3.3.2. Alkylphenol anesthetic selective GABA_A receptor subunit binding

In order to understand the apparent subunit specificity noted in the above

experiments, MD simulations for alkylphenol anesthetic binding were generated with an $\alpha_1\beta_3\gamma_2$ GABA_A model derived from an $\alpha_1\beta_1\gamma_2$ GABA_A model used previously¹⁶⁸.

Docking calculations to the entire pentamer identified at least one propofol pose in each subunit interface, β^+/α^- (2 sites), α^+/β^- , α^+/γ^- and γ^+/β^- , as shown in Figure 31A. Other than the channel lumen, no alternate sites were consistently detected over multiple docking runs. Docking of *AziPm-click*(**1c**) to the same model yielded overlapping sites, demonstrating that *AziPm-click*(**1c**) is not sterically hindered from binding to the intersubunit sites, despite the larger molecular size. Furthermore, as shown in Figure 32, *AziPm-click*(**1c**) has sufficiently favorable interactions common to propofol that docking simulations yield similar orientations.

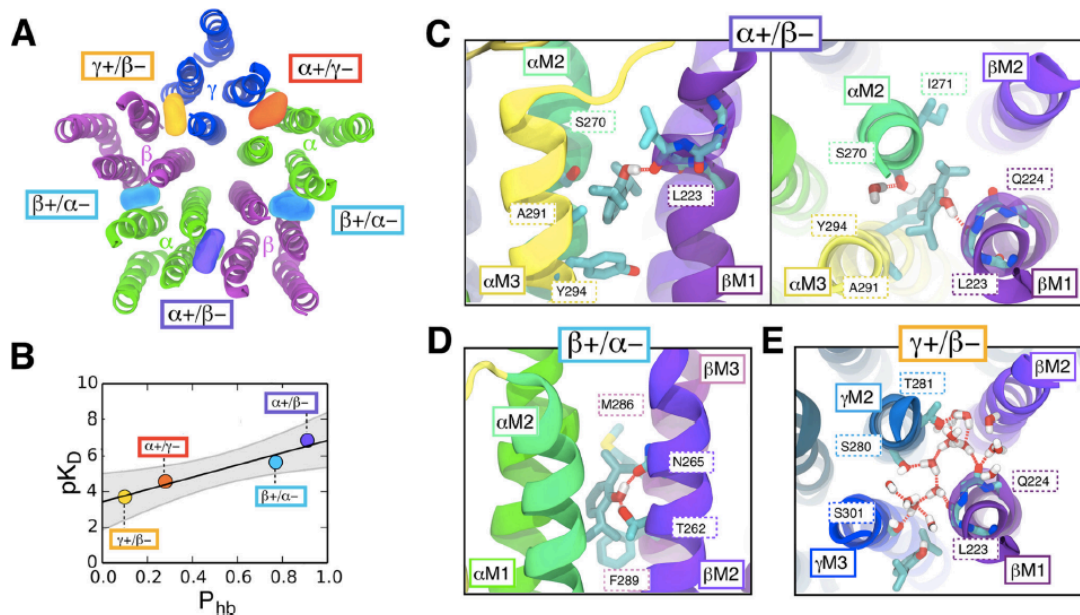


Figure 31. Selectivity of intersubunit propofol binding in an $\alpha_1\beta_3\gamma_2$ GABA_A receptor as predicted by molecular dynamics simulations using the Alchemical Free Energy Perturbation algorithm. (A)

Five propofol molecules (colored surfaces) docked in the GABA_A receptor subunit interfaces (β^+/α^- (2 sites) in cyan; α^+/β^- in violet; α^+/γ^- in red; γ^+/β^- in orange). The transmembrane domain is viewed from the extracellular side along the pore axis, and colored by subunit type; α_1 in green, β_3 in magenta, and γ_2 in blue. B) Computational results for propofol pK_D and its likelihood of hydrogen bonding to protein cavity residues (P_{hb}) can be well fit by the line $pK_D = a(P_{hb}) + b$, where $a = 3.4 \pm 0.8$ and $b = 3.4 \pm 0.1$, and the 95% confidence band is shown in gray. C-E) Interactions of propofol and water in the high-affinity and low-affinity interfacial sites. Hydrogen bonds (red dashed lines). C) Propofol binding in α^+/β^- interface that contained 7

polar residue sidechains (*left*, side view; *right*, top view) forms a persistent hydrogen bonding with a backbone carbonyl group exposed by the M1 helical bulge (β -L223). D) Bound propofol at the β^+/α^- interfacial site, which contained 7 polar residue sidechains, (side view) alternates between hydrogen bonds to $\beta^+M2:T262$ and $\beta^+M2:N265$. For compactness, the image shows a rare frame in which both hydrogen bonds coexist. E) In the γ^+/β^- interface 8 polar residue sidechains were present (top view), these residues favor hydrogen bonding with a water cluster stabilized by polar residues γ^+T281 and γ^+S301 , which are homologous to hydrophobic residues in α and β subunits.

A receptor/propofol complex was constructed with one propofol molecule in the highest scoring pose for each subunit interface (Figure 31A). The complex was embedded in a fully hydrated phosphatidylcholine membrane and simulated for 270 ns using traditional equilibrium MD with atomic resolution. In addition to allowing the propofol in the intersubunit space to equilibrate before the affinity calculations, we used this simulation to characterize and compare the microscopic interactions between propofol and the binding pocket across subunits.

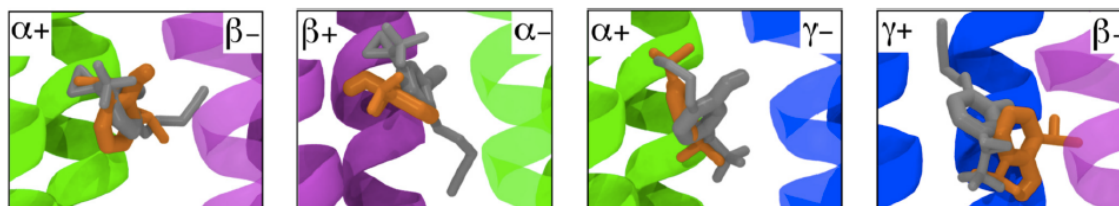


Figure 32. Intersubunit propofol and *AziPm-click* (**1c**) occupancy in an $\alpha_1\beta_3\gamma_2$ GABA_A receptor as predicted by AutoDock Vina simulations. Helices of the four distinct subunit interface pairs (α_1 , green; β_3 , magenta; γ_2 , blue) with the highest scored docking poses for propofol (orange) and *AziPm-click* (**1c**) (gray).

At the conclusion of the traditional MD simulation, standard binding affinities for propofol in each of the four distinct sites were calculated using separate 24 ns Alchemical Free Energy Perturbation (AFEP) simulations. The AFEP method also involves running MD simulations, but is designed to facilitate simultaneous calculation of average quantities appearing in the Zwanzig equation²²⁹, an exact expression for the free energy difference between two states (e.g. bound and unbound) that inherently accounts for all

entropic and enthalpic contributions. The results from the AFEP simulations indicate three higher affinity sites at the α +/ β - and two β +/ α - interfaces, with K_D values similar to propofol EC_{50} . K_D values for the α +/ γ - and $+$ γ / β - interfaces, however, suggest markedly weaker propofol binding to those sites (Table 9).

Table 9. Binding affinities of propofol bound to one of four GABA_A receptor interfacial sites (shown in Figure 31, interfaces notated counter-clockwise), calculated using Alchemical Free Energy Perturbation algorithm.

Interface	K_D (μ M)	$K_D e^{-\delta/RT} - K_D e^{\delta/RT}$ (μ M) ^a
α +/ β -	0.1	0.02-0.7
β +/ α -	2.0	0.4-10
α +/ γ -	30	5-200
γ +/ β -	200	40-1000

^a K_D range corresponding to an uncertainty in ΔG of $\delta = 1$ kcal/mol. Challenges inherent in determining constants required for correction to laboratory conditions contribute significantly to δ ; errors in relative values of K_D are substantially reduced compared to those for absolute K_D .

The particularly low affinity of propofol for the $+\gamma/\beta$ - interfacial cavity, which has one more polar residue than the other interfacial cavities (Figure 33A), seemed potentially contradictory to an essential role for hydrogen bonding. As shown in Figure 33B, however, the pK_D values for different subunit interfaces were found to be strongly correlated ($r^2 = 0.94$) with the probability (P_{hb}) that the propofol hydroxyl would form at least one hydrogen bond with one of the cavity-lining residues. Propofol in either of the two sites with low K_D values (α +/ β - and β +/ α -) had at least $P_{hb} > 0.8$; for the two low-affinity sites this probability was significantly reduced ($P_{hb} < 0.3$). Thus, although propofol affinity is correlated with propofol hydrogen bonding, propofol is less likely to form hydrogen bonds with the more hydrophilic $+\gamma/\beta$ - interfacial cavity. This result was due to stable hydration of the $+\gamma/\beta$ - cavity, due to interactions of water molecules with

γ Ser-301 and γ Thr-281 (Figure 31E). The water molecules compete for hydrogen bonding partners and interact unfavorably with the propofol isopropyl groups.

Within the highest-affinity site at the α +/ β - interface, propofol orients as a hydrogen donor to the carbonyl backbone of Leu-223 within the β M1 transmembrane helix (Figure 31C) where a bulge in backbone hydrogen bonding is observed in crystal structures for both the glutamate-gated chloride channel²³⁰ and the GABA_A receptor β 3 homopentamer²³¹. Similar behavior was observed in simulations of triiodothyronine bound to interfacial sites²³². In the β +/ α - interface, propofol alternates rapidly between serving as a hydrogen acceptor for β M2:Thr-262 and donor for β M2:Asn-265 (Figure 31D). The associated slight reduction in pK_D is consistent with the slight reduction in P_{hb} and the line of best fit.

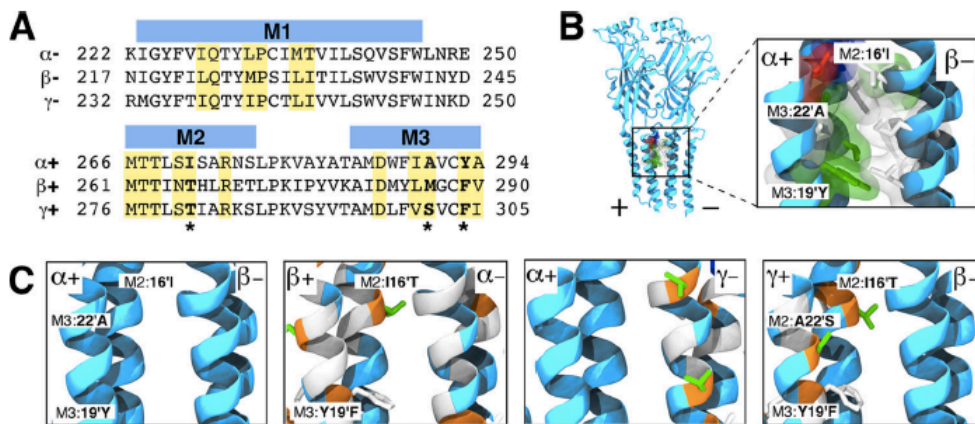


Figure 33. Sequence variation in interfacial binding sites of an $\alpha_1\beta_3\gamma_2$ GABA_A receptor heteropentamer. A) Sequence alignment of + and - subunit interfaces that contribute to the formation of interfacial binding sites. Highlighted residues represent residue sidechains that directly contribute the formation of the binding cavity. Bold and (*) residues denote key sequence variations in the interfacial binding sites. B-C) Helices of the four distinct subunit interface pairs with α +/ β - interface as the reference pair. In all panels, side-chains are colored by residue type: polar (green), hydrophobic (white), acidic (red), basic (blue). B) Extended view and binding site cavity view of the α +/ β - interface reference pair with all cavity contributing sidechain residues represented. C) Helices of the four distinct subunit interface pairs are colored according to sequence differences with the α +/ β - interface as the reference subunit pair displaying identical (light blue), similar (white), change in residue type (orange). Note that for a given interface, coloring of the + and - subunit backbone reflects sequence differences from α_1 and β_3 respectively. Cavity residues are labeled according to a prime-numbering system in which

M2:16' is equivalent to (I271, T266, T281) for α_1 , β_3 , and γ_2 subunits respectively; M3:19' is (Y294, F289, F304) and M3:22' is (A291, M286, S301) with the same ordering.

The AFEP calculations yield an intermediate affinity of propofol for the γ -/ α + interfacial site. Residues of the γ - face, however, are nearly identical to those of the β - face, as shown in (Figure 33B-C), and sequence differences among site residues are unable to account for the moderate differences in hydrogen-bonding and affinity between γ -/ α + and the higher affinity β -/ α + site. Since hydrogen bonding of propofol to the M1 backbone is frequently observed for β - but not γ -, it is possible that sensitivity of fluctuations in M1 secondary structure to non-cavity residues causes the observed weak sequence dependence. If so, the result suggests a further uncertainty in interpretations of mutagenesis experiments and the underlying assumption that identified residues are contact residues.

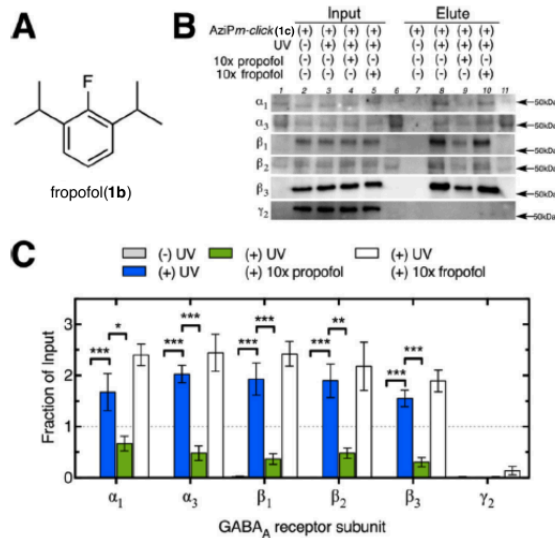


Figure 34. Ligand protection of synaptic GABA_A receptor capture. A) Chemical structure of 2-fluoro-1,3-diisopropylbenzene or propofol(1b). B) Representative western blots for GABA_A receptor subunits of input (lanes 2-5) and the corresponding elution (lanes 7-10) for synaptosomal samples exposed to AziPm-click (1c) (10 μ M) with or without UV irradiation and with or without co-exposure with propofol (100 μ M) or fropofol(1b) (100 μ M). Lane 1, 6 and 11 contain protein ladders. B) Comparison of non-UV and UV capture with or without propofol or fropofol(1b) protection for each GABA_A receptor subunit, values are represented as the mean of four experiments \pm SEM of the fraction of the corresponding input sample. Data was analyzed by 2-

way ANOVA with Tukey's multiple comparison test comparing fraction captured between protection conditions for each subunit. Significant differences from UV irradiated elute without protection ligand are shown (***, $p < 0.001$) (**, $p < 0.01$) (*, $p < 0.05$).

To experimentally evaluate the role of the alkylphenol hydroxyl in selective binding to sites within synaptic GABA_A receptor subunits, the fluorine substituted analogue fropofol(**1b**) (Figure 34A) was applied within protection experiments²³³. Previously, fropofol(**1b**) did not modulate or disrupt propofol potentiation of the GABA_A receptor, and did not cause immobilization at even 100-fold higher concentrations than propofol. On the other hand, fropofol(**1b**) did display similar binding as propofol to protein sites that were not dependent on hydrogen bond interactions²³³. Azide-PEG3-biotin was employed as the reporter tag for streptavidin-affinity isolation of protein targets photoaffinity labeled by *AziPm-click*(**1c**) with or without protection ligands propofol or fropofol(**1b**). Protein levels of GABA_A receptor subunits were determined by western blot before (or 'input') and after (or 'elute') streptavidin capture of biotinylated proteins. All GABA_A receptor subunits were detected within synaptosomes prior to capture (Figure 34), consistent with synaptic localization of these subunits. After capture, only α and β subunits were detected. All GABA_A receptor α and β subunits showed significant decreases in capture efficiency when propofol was present during UV irradiation. Unlike propofol, fropofol(**1b**) was unable to protect GABA_A receptor α and β subunits from capture (Figure 34A-B). The lack of protection by fropofol(**1b**) corroborates MD simulations suggesting that complex hydrogen bond interactions between alkylphenol anesthetics and residues within α/β interface likely facilitates the selectivity for these sites.

3.3.3. Conclusion

Propofol is a positive modulator of the GABA_A receptor, but the mechanistic details, including the relevant binding sites, remain disputed. Previously a photoaffinity tandem bioorthogonal propofol α -PAL, AziPm-click(**1c**), was applied for the unbiased identification of propofol-binding proteins in their native state within mouse synaptosomes. Within the identified proteome was the selective identification of five α or β synaptic GABA_A receptor subunits. Lack of γ 2 subunit capture was not due to low abundance. Electrophysiology studies confirmed that AziPm-click(**1c**) retained GABAergic activity similar to propofol, therefore associating binding to functional activity. Molecular dynamics simulations revealed that the higher affinity interactions for propofol at α/β relative to γ -containing interfaces were likely due to differential hydrogen-bond probability. Application of a hydrogen-bond null propofol derivative propofol(**1b**) supported these results. The investigation provided the first evidence for direct propofol interaction with specific GABA_A receptor subunits within native tissue.

3.3.4. Experimental methods

Heterologous expression of GABA_A receptor subunits and electrophysiological recordings- GABA_A receptor expression in *Xenopus laevis* oocytes was completed as described previously²³³. cDNAs for GABA_A receptor α_1 , β_2 , and γ_{2L} subunits were generously provided by Dr. Robert Pearce (University of Wisconsin). All animal care and experimental procedures involving *X. laevis* frogs were carried out according to a protocol approved by the IACUC of Thomas Jefferson University. GABA_A receptor currents expressed in *X. laevis* oocytes were recorded as previously reported²³³. Data acquisition and initial analysis were performed using pClamp 9.2/10.3 (Molecular Devices, Sunnyvale, CA). Macroscopic currents were low-pass filtered at 1 kHz and

digitized at 2 kHz. Data was fit to a sigmoidal dose-response curve with variable Hill Slope.

Molecular dynamics simulations- A model of the $\alpha_1\beta_3\gamma_2$ GABA_A receptor was built by mutating 31 residues in the β subunits from an $\alpha_1\beta_1\gamma_2$ GABA_A Model 3 reported in Hénin et al., 2014¹⁶⁸. The mutations were made using the MUTATOR plugin of VMD¹⁷⁵. AutoDock Vina¹⁴⁷ was used to generate initial coordinates for propofol; default parameters were used and the search space included the entire pentamer. AutoDock Vina returned at least one pose for each subunit interface; the ligand conformation with the best score was chosen for each site. The complex (GABA_A receptor and 5 propofol molecules) was then placed in a 109 Å x 109 Å phosphatidylcholine (POPC) membrane aligned parallel to the xy plane using CHARMM-GUI Membrane Builder²³⁴. The system was solvated to a total height in z of 139 Å, followed by the addition of sodium and potassium ions that neutralized the system and brought the salt concentration to 0.15 M. The complete simulation system contained about 167000 atoms.

The CHARMM36 forcefield was used for protein^{235,236} and phospholipid²³⁷ parameters, with parameters for TIP3P waters²³⁸ and ions²³⁹ corresponding to those traditionally used with CHARMM-based force fields. Propofol parameters relied on atom types from CHARMM36; as described in LeBard et al., 2012²⁴⁰, further parameterization and use of a CMAP potential was required to accurately enforce coupling between rotation of the hydroxyl and isopropyl groups due to steric clashes.

Atomistic molecular dynamics simulations were run with NAMD v2.10²⁴¹. All simulations used periodic boundary conditions and particle mesh Ewald (PME) electrostatics. Interactions between non-bonded atoms were cutoff at 12 Å, and bonds

involving hydrogen were constrained using the SHAKE/RATTLE algorithm. A Langevin thermostat and barostat were used to maintain a temperature and pressure of 300 K and 1 atm, respectively, and vanishing surface tension was imposed. The simulation timestep was 2 fs. Following the system generation, 30000 minimization steps and a 7 ns equilibration protocol that gradually softened restraints on the protein and ligand were run. Subsequently we ran a 200 ns production run with soft harmonic restraints on the C α atoms ($k = 0.5 \text{ kcal/mol/\AA}^2$). The probability of hydrogen bonding was calculated using a VMD script that measured the fraction of frames in which propofol was hydrogen bonding to any residue in the site, detected using the VMD geometric criterion with a distance cutoff of 3.3 \AA and an angle cutoff of 40 degrees. The first 50 ns of the production run were not included in the analysis.

Binding affinities were calculated using the Alchemical Free Energy Perturbation (AFEP) method, a theoretically exact method that involves gradually decoupling (reducing interaction strength) the ligand and the binding site throughout an MD simulation^{242,243}. The decoupling free energy is then corrected by the ligand solvation free energy, as well as the entropic cost of transferring the ligand from the available volume per molecule in the standard state (1660 \AA^3) to the volume of the ligand binding site, yielding the standard Gibbs free energy of binding, ΔG^0 . The dissociation constant K_D is calculated using the relationship $K_D = \exp(-\Delta G^0/RT)$. Implementation of the method was very closely based on the procedure used in LeBard et al., 2012²⁴⁰ for propofol binding to intrasubunit sites TMD of GLIC. Decoupling of propofol from each of four interfaces was carried out in four separate simulations, over 24 windows, with 1 ns/window for a total of 24 ns per interfacial binding site.

The probability of propofol hydrogen bond formation (P_{hb}) was estimated by calculating the frequency that a single hydrogen bond with the propofol hydroxyl was detected over the course of the equilibrium MD simulation. Molecular images in Figure 31 A and C-E and Figure 32 were generated using VMD ¹⁷⁵, while data in Figure 31 B was plotted and fit using python scripts.

Synaptosomal photoaffinity labeling- Synaptosomes were resuspended to 1 mg protein/mL in HEPES buffer medium (in mM: 140 NaCl, 5 KCl, 5 NaHCO₃, 1.2 NaH₂PO₄, 1 MgCl₂, 10 glucose, and 10 HEPES (pH 7.4)). Concentrations of AziPm-click (**1c**) with or without the presence of concentrations of competitive ligands (propofol or propofol(**1b**)) in dimethyl sulfoxide (DMSO) vehicle (<0.3% v/v) were added and synaptosomes were gently vortexed for 10 s. The samples were allowed to equilibrate for 5 min before being transferred to a parafilm-sealed 1 mm path-length quartz cuvette. The sample was then irradiated for 20 min at a peak band-width of 350 nm (Rayonet RPR-3500 lamp) ~ 6 cm from the light source. Non-irradiated samples were left in the dark at ambient temperature (22-25°C) for 20 min. All remaining procedures were conducted with restricted light exposure.

Biotin conjugation- To 750 µg of photolabeled or control synaptosome sample, 40 µL of 10% SDS and 2 µL of 5 mM DTT in water were added. Samples were then vortexed, heated for 10 min at 65°C, and then briefly cooled. Final concentrations of 150 µM azide-biotin (Click Chemistry Tools), 2 mM THPTA (Sigma), 1 mM ascorbic acid (Sigma), and 1 mM CuSO₄* 5H₂O (Sigma) were added to each sample and vortexed vigorously. The samples were left in the dark at ambient temperature (22-25° C) for 1 hr with mild agitation. Directly to each sample 4X volume chilled methanol, 1.5X chilled

chloroform and 3X chilled ddH₂O were added. Samples were vortexed vigorously and centrifuged at 1,400 x g for 30 min at 4°C. Both liquid layers were carefully removed and the protein pellet was washed with 2 mL of 1:1 (v:v) chilled methanol: chloroform.

Samples were centrifuged at 3,500 x g for 30 min at 4° C. Protein pellets were briefly air dried before further processing.

Western blot for biotin conjugated protein targets- 750 µg of biotin conjugated protein sample was resuspended via sonication in 500 µL of 25 mM NH₄HCO₃ and 6 M urea in water. Following, 150 µL 5% Triton-100X in water, 50 µL 10% SDS in water and 1.5 µL 0.5 M DTT was added. The samples were heated for 15 min at 65° C. Insoluble debris was separated by centrifugation for 10 min at 14,000 x g. The supernatant was diluted to 1 mL with PBS and 50 µL was removed for the input sample. An additional 5 mL of PBS containing 100 uL of 50% strepavidin-agarose resin (Thermo Scientific) was added.

Biotinylated proteins were captured over resin overnight at 4° C with mild agitation. The resin was first washed with 6 mL of 1% SDS in PBS, then 7 mL of 0.1 M urea in PBS followed by 10 mL PBS. The resin underwent final wash with 0.9 mL PBS then was resuspended in 100 uL of 2x SDS Laemmli buffer containing 100 mM DTT. Samples were then incubated with agitation at 37° C for 30 min, centrifuged at 700 x g for 2 min and heated for 15 min at 90°C. 50 µL of 2x SDS Laemmli buffer containing 100 mM DTT was joined to the input sample and heated for 5 min at 90°C. Samples were centrifuged at 14, 000 x g for 10 min prior to electrophoresis using 4-15% SDS-PAGE gels with 10 µL of each sample was introduced into each well. Proteins were then transferred to PDVF membranes. The membranes were blocked for 1 hr with 2.5% BSA in Tris-buffered saline containing 0.1% Tween-20 (v/v%; TBST). Membranes were

incubated with GABA_A receptor subunit antibodies overnight at 4° C. All antibodies for GABA_A receptor subunits were purchased from Santa Cruz Biotechnology, Inc. and included rabbit or goat polyclonal α1 ((A-20): sc-31405), α3 ((J-23)sc122603), β1((N-19)sc-7361), β2 ((C-20): sc-7362), and γ2 ((Q-18): sc- 101963), antibodies and monoclonal β3 ((D-12): sc-376252) antibody. For GABA_A receptor subunit analysis membranes were washed three times with TBST prior to 2 hr incubation with appropriate HRP-conjugated secondary at room temperature. All membranes were then washed twice with TBST and once with Tris-buffered saline (TBS) before being developed with Amersham ECL select reagent and scanned. Only the net ratio of intensity (ROI) detected band(s) between the 75-50 kDa molecular weights were considered. The elution intensities were normalized to the corresponding input sample. Samples showing no detectable band elution were set to a net ROI of 0. Studies were conducted in quadruplicates and are represented as the fraction of the corresponding input. *Statistics*- GraphPad Prism 7.0, unless otherwise noted, was used for preparation and statistical data analysis. Details are given in the figure legends.

CHAPTER 4: CONCLUSIONS

Of all the achievements that have been made within medicine, the ability of general anesthetics to impede the perception of pain, induce immobility, and prevent recall of surgical procedures is one of the greatest. However, general anesthetics are not without their drawbacks. Furthering our knowledge regarding the mechanisms behind their pharmacological effects is critical to continuing the improvement of general anesthetic administration and design. The field of anesthesiology research is rapidly

evolving, incorporating and integrating methods from a full range of science disciplines including molecular and chemical biology. The body of work presented in this thesis utilizes these techniques to help advance our understanding of molecular mechanisms of propofol, sevoflurane, and isoflurane.

Sevoflurane is a volatile anesthetic that is most commonly used within pediatric care. As a comparatively new general anesthetic, much of this agent's mechanism is unclear. The novel *α*-PAL derivative azisevoflurane(**1a**) demonstrated similar physicochemical, functional and biological endpoints of the parent anesthetic and thus shows promise as a tool to further understanding of molecular targets. Azisevoflurane(**1a**) was applied to investigate the mammalian *Shaker* Kv1.2 channel that is a unique target of sevoflurane. An allosteric binding site was identified within a critical location of the channel, the S4-S5 linker, which was supported by mutagenesis studies as a likely site that leads to sevoflurane's voltage-dependent positive modulation of the channel. The study of sevoflurane's action on the Kv1.2 channel also indicated a complex molecular mechanism through at least two binding sites, each with distinctive influence(s) on the channel's activity.

The molecular mechanism of sevoflurane was further explored in a joint investigation with another commonly use volatile anesthetic isoflurane. Both volatile anesthetics have been shown to positively modulate synaptic $\alpha\beta\gamma$ GABA_A receptors, however the binding sites that lead to this enhanced activity was previously unclear. Photoaffinity labeling studies using *α*-PAL derivatives, azisevoflurane(**1a**) and aziisoflurane for sevoflurane and isoflurane respectively, identified likely positive modulatory sites that overlap within the β +/ α - TMD interface and are selective within the

α +/ β - TMD interface. Potential TMD inter- and intrasubunit sites were also identified within γ -containing interfaces; however, how the occupancy of these cavities may alter function of the receptor is less clear.

In addition to the volatile anesthetics, the most commonly used intravenous anesthetic propofol was studied in this work. Reflecting the findings for sevoflurane and isoflurane, the molecular mechanism(s) of propofol were shown to be complex despite the comparatively simple chemical structure of the drug. The novel derivative fropofol(**1b**) demonstrated that the 1-hydroxyl within the propofol structure, and the hydrogen bonding interactions it allows, is critical for overt anesthesia endpoints. The 1-hydroxyl was observed to be specifically significant for the propofol positive modulation of synaptic GABA_A receptors. However the hydrogen bonding properties of propofol did not abolish all the physiological activity of the anesthetic, as fropofol(**1b**) did decrease muscle contractility in a fashion similar to propofol.

An area of contrast between propofol and the volatile anesthetics is their relative protein binding affinities with propofol displaying, in general, a higher affinity. Although the micromolar EC₅₀ concentrations associated with propofol's biological activity still indicates transient interactions with a large range of molecular targets. To determine the propofol-binding proteins a novel tandem anesthetic photoaffinity-click chemistry active ligand called *AziPm-click*(**1c**) was synthesized. Application of *AziPm-click*(**1c**) within a developed ABPP workflow allowed for the identification of the propofol-specific proteome within a synaptosomal system. Of the over 4,500 proteins identified within the synaptosomes, 196 were identified as being likely propofol-binding proteins. These findings expand the repertoire of potential targets for propofol and can be used for future

drug design. Furthermore, many of the identified proteins have been previously suggested as potentially functionally relevant targets *in vitro*, confirming these findings in a system derived from native tissue.

One protein target that was identified as propofol-specific within the synapse was the $\alpha\beta\gamma$ GABA_A receptor. Only the α and β subunits of this receptor were identified as propofol-specific proteins, and the lack of γ subunit was not a result of low abundance within the synaptosomal system. The similar positive modulatory activity of *AziPm-click(1c)* associated the selective binding of the α and β subunits to the enhancement of $\alpha\beta\gamma$ GABA_A receptor activity characteristic of propofol. Independent MD simulations indicated higher affinity within β^+/α^- and α^+/β^- TMD interfaces compared to γ -containing interfaces and that hydrogen bonding is likely the key feature that contributes to the selective binding of subunits. The application of propofol(**1b**) in protection studies further associated this functional significance and confirmed MD predictions of proposed GABA_A receptor sites within the synaptosomal system.

The above investigations displayed intricate anesthetic-protein interactions and likely only scratch the surface of the molecular mechanisms behind general anesthesia. With their higher EC₅₀ concentrations it is anticipated that anesthetics have multiple target proteins that cumulatively result in anesthesia endpoints and/or adverse side effects¹¹⁸ (Figure 35A). This hypothesis is further supported by the studies presented within this work. Anesthetic binding within particular target proteins likely play a larger role in causing overt anesthesia endpoints, one example being the GABA_A receptor. Interestingly, within this single protein target multiple potential general anesthetic binding sites appear to exist. Some of these sites within the same receptor overlap despite

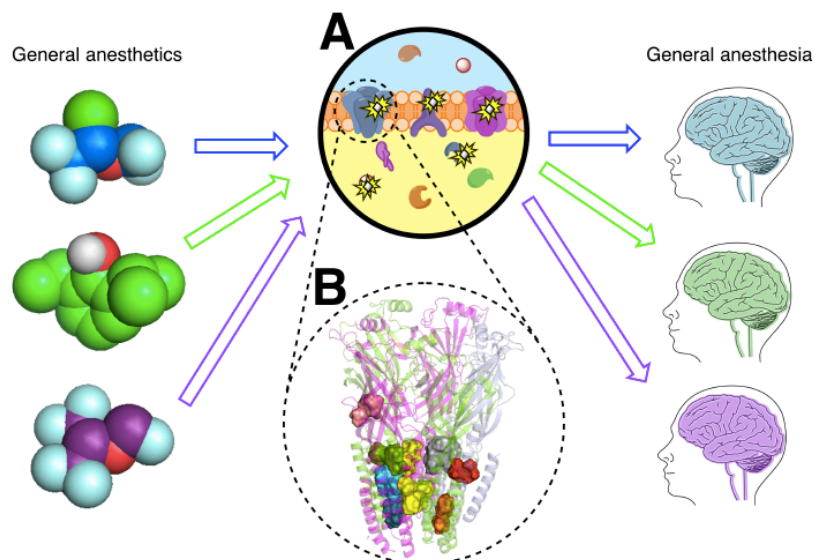


Figure 35. Schematic of the major conclusions presented in this work. A) General anesthetics bind to a complex range of shared and unique macromolecular targets that cumulatively result to distinct general anesthesia states. B) Multiple binding sites might exist within a single protein target that overlap across chemotypes or be unique to an anesthetic. The various potential binding sites have differing influences on the protein activity.

significantly different chemical structures, while others appear to be selective even within the same anesthetic chemotype (Figure 35B). Evidence also suggested at least two sevoflurane binding sites within Kv1.2 channels. Studies indicated that binding within these sites might contribute to different molecular mechanisms that collectively result in the changes in channel's activity. Ultimately, the work provided within this thesis adds to the abundant opportunities that lay within anesthesiology research to further our knowledge of molecular biology and medicine.

APPENDIX

A.1. Equations

Equation 1.

$$T_{1/2} = 0.3 / (\Psi I_0 \epsilon)$$

$T_{1/2}$: half-life of photoactivation

I_0 : intensity of the lamp

ϵ : molar extinction coefficient

Ψ : quantum yield of photoactivation

Equation 2.

$$G = \frac{G_{max}}{\left(1 + e^{\frac{(V_c - V_s)}{k}}\right)^4}$$

G ; peak chord conductance

G_{max} ; maximum conductance

k ; slope factor

V_c ; command voltage

V_s ; activation midpoint voltage of a single subunit

$V_{1/2}$; midpoint voltage of the peak conductance curve

Equation 3.

$$V_{1/2} = 1.665 k + V_s$$

$V_{1/2}$; midpoint voltage of the peak conductance curve

k ; slope factor

V_s ; activation midpoint voltage of a single subunit

Equation 4.

$$z = RT/Fk = 25.5/k$$

z ; equivalent gating charge

R ; gas constant

T ; absolute temperature

F ; Faraday constant

k ; slope factor

A.2. Detailed synthetic methods

A.2.1. 3-(Difluoro((1,1,1,3,3,3-hexafluoropropan-2-yl)oxy)methyl)-3H-diazirine; Azisevoflurane(1a)

Preparation of Ethyl 2-((1,1,1,3,3,3-hexafluoropropan-2-yl)oxy)acetate (2a). A 2 L rbf with large magnetic stir bar was filled with 76.45 g (0.455 mol) of hexafluoroisopropanol, 72.38 g (0.433 mol) of ethyl bromoacetate, 800 mL of acetone and 160.0 g (1.16 mol) of anhydrous K₂CO₃. The flask was fitted with a condenser, and the reaction was stirred vigorously under reflux for 2 h. The mixture was cooled, and 200 mL methylene chloride was added. The mixture was vacuum-filtered through a fritted funnel and the resulting liquid was concentrated *in vacuo*. The product was purified by distillation at atmospheric pressure to yield 87.52 g (80%) of a clear, colorless liquid **2a**, bp 156-160 °C. ¹H NMR (500 MHz, CDCl₃): δ 4.46 (sep, 1 H, J_{H-F} = 5.8 Hz), 4.38 (s, 2 H), 4.22 (q, 2 H, J_{H-H} = 7.2 Hz), 1.27 (t, 3 H, J_{H-H} = 7.2 Hz). ¹³C NMR (500 MHz, CDCl₃): δ 167.88 (s), 121.31 (q, J_{C-F} = 285 Hz), 75.26 (sep, J_{C-F} = 33 Hz), 68.90 (s), 61.48 (s). ¹⁹F NMR (360 MHz, CDCl₃): δ -73.73 (d, 6 F, J_{H-F} = 5.5 Hz). HRMS *m/z* calcd for C₇H₈F₆O₃ (M + Na)⁺ 277.0275; found 277.0271.

Preparation of 2-((1,1,1,3,3,3-Hexafluoropropan-2-yl)oxy)acetic acid (3a). To a 500 mL rbf was added 79.54 g (0.313 mol) of **2a** and 18.79 g (0.470 mol) of NaOH dissolved in 80 mL of H₂O. The biphasic reaction mixture was stirred vigorously overnight. Concentrated HCl (86.0 mL) was then added. The resulting mixture was extracted with methylene chloride (3 x 200 mL) and the organic layer was dried over Na₂SO₄. The solvent was evaporated and the product was dried *in vacuo* to yield 69.54 g (98%) of a white solid **3a**, mp 52-54 °C. ¹H NMR (500 MHz, CDCl₃): δ 9.00 (br s, 1 H), 4.49 (s, 2 H), 4.38 (sep, 1 H, J_{H-F} = 5.7 Hz). ¹³C NMR (500 MHz, CDCl₃): δ 173.29 (s), 121.15 (q, J_{C-F} = 285 Hz), 75.64 (sep, J_{C-F} = 33 Hz), 68.60 (s). ¹⁹F NMR (360 MHz, CDCl₃): δ -73.40 (d, 6 F, J_{H-F} = 5.8 Hz). HRMS *m/z* calcd for C₇H₈F₆O₃ (M)⁺ 226.0065; found 226.0065.

Preparation of 2-((1,1,1,3,3,3-Hexafluoropropan-2-yl)oxy)acetyl chloride (4a). A 1 L rbf with stir bar was filled with 69.54 g (0.307 mol) of **3a** and 500 mL of CH₂Cl₂ and the mixture was stirred until a clear solution. Then 0.25 mL of DMF was added with stirring. In a separate flask 35.1 mL (46.86 g; 0.369 mol) of oxalyl chloride was dissolved in 60 mL CH₂Cl₂. The oxalyl chloride solution was added dropwise over the course of 15 minutes into the solution of **3a**. The mixture was stirred for 1 h at room temperature, and then was heated under reflux for 2 h. Distillation at atmospheric pressure yielded 61.74 g (82%) of a clear, colorless liquid **4a**, bp 128-132 °C. ¹H NMR (500 MHz, CDCl₃): δ 4.74 (s, 2 H), 4.30 (sep, 1 H, J_{H-F} = 5.6 Hz). ¹³C NMR (500 MHz, CDCl₃): δ 169.32 (s), 120.89 (q, J_{C-F} = 285 Hz), 75.79 (sep, J_{C-F} = 33 Hz), 75.65 (s). ¹⁹F NMR (360 MHz, CDCl₃): δ -71.23 (d, 6 F, J_{H-F} = 5.3 Hz). HRMS *m/z* calcd for C₇H₈F₆O₃ (M - F)⁻ 224.9742; found 224.9744.

Preparation of Methyl 2,2-dichloro-2-((1,1,1,3,3,3-hexafluoropropan-2-yl)oxy)acetate (5a). To an annular Pyrex photochemical flask was added 35.2 g (0.144 mol) of **4a** and 2 mL of carbon tetrachloride. Chlorine gas was bubbled through the solution under irradiation by UV light (450W Hanovia Lamp) for 5.5 h. The solution was cooled and air was bubbled through the solution to expel excess chlorine. Methanol (7.0 mL, 5.5 g; 0.17 mol) was added to the crude product and the solution was stirred for 1 h.

Concentration *in vacuo* followed by vacuum distillation (60 torr) yielded 28.82 g (65 % over two steps) of a clear, colorless liquid **5a**, bp₆₀ 91-97 °C. ¹H NMR (500 MHz, CDCl₃): δ 5.14 (sep, 1 H, J_{H-F} = 5.4 Hz), 3.98 (s, 3 H). ¹³C NMR (500 MHz, CDCl₃): δ 161.48 (s), 120.05 (q, J_{C-F} = 285 Hz), 104.08 (s), 72.53 (sep, J_{C-F} = 35 Hz), 55.22 (s). ¹⁹F NMR (360 MHz, CDCl₃): δ -73.62 (d, 6 F, J_{H-F} = 5.4 Hz). HRMS *m/z* calcd for C₇H₈F₆O₃ (M - Cl)⁺ 272.9753; found 272.9760.

Preparation of Methyl 2,2-difluoro-2-((1,1,1,3,3,3-hexafluoropropan-2-yl)oxy)acetate (6a). To a 50 mL rbf with stir bar was added 9.50 g (30.7 mmol) of **5a**, 5.50 g (30.9 mmol) of SbF₃ and 0.35 mL of SbCl₅. The suspension was heated with stirring to 80 °C in an oil bath 1 h. Distillation of the mixture at atmospheric pressure yielded 7.24 g (85%) of a clear, colorless liquid **6a**, bp 119-124 °C. ¹H NMR (500 MHz, CDCl₃): δ 4.95 (sep, 1 H, J_{H-F} = 5.6 Hz), 3.96 (s, 3 H). ¹³C NMR (500 MHz, CDCl₃): 158.40 (t, J_{C-F} = 39 Hz), 119.85 (q, J_{C-F} = 283 Hz), 113.34 (t, J_{C-F} = 279 Hz), 69.42 (m), 54.31 (s). ¹⁹F NMR (360 MHz, CDCl₃): δ -73.69 (q, 6 F, J_{H-F} = J_{F-F} = 4.5 Hz), -79.07 (sept, 2 F, J_{F-F} = 4.5 Hz). HRMS *m/z* calcd for C₇H₈F₆O₃ (M + H)⁺ 277.0111; found 277.0110.

Preparation of N-(tert-Butyl)-2,2-difluoro-2-((1,1,1,3,3,3-hexafluoropropan-2-yl)oxy)ethan-1-imine (7a). Under an inert atmosphere, a 100 mL rbf with stir bar was filled with 6.75 g (24.4 mmol) of ester **6a** and 50 mL of ether. The mixture was cooled to -80 °C in a dry ice/acetone bath and 32 mL (32 mmol; 1 M in hexane) DIBAL-H solution was added dropwise, over the course of 15 minutes. The mixture was stirred at -80 °C for 2 h and was then poured into a cold solution of 5 mL concentrated H₂SO₄ in 275 mL water and stirred vigorously for several minutes. After all of the solid had dissolved, the solution was extracted with ether (3 x 100 mL) and the combined ether extracts were concentrated using a rotary evaporator at room temperature. The resulting oil was dissolved in 50 mL benzene and 5.36 g (73.3 mmol) of *tert*-butylamine was added. The solution was heated to reflux with a Dean-Stark water separator for 4 h after which another 5.36 g (73.3 mmol) *tert*-butylamine was added. The solution was then heated to reflux with a Dean-Stark water separator overnight. Concentration of the solution followed by dynamic transfer under high vacuum to a U-trap cooled in liquid nitrogen yielded 3.21 g (44% over two steps) of a clear, colorless liquid **7a**, which was sufficiently pure for conversion to diaziridine. ¹H NMR (500 MHz, CDCl₃): δ 7.50 (t, 1 H, J_{H-F} = 4.9 Hz), 5.00 (sept, 1 H, J_{H-F} = 5.6 Hz), 1.26 (s, 9 H). ¹³C NMR (500 MHz, CDCl₃): 145.32 (t, J_{C-F} = 33 Hz), 120.16 (q, J_{C-F} = 285 Hz), 117.62 (t, J_{C-F} = 270 Hz), 68.99 (m), 58.91 (s) 28.68 (s). ¹⁹F NMR (360 MHz, CDCl₃): δ -73.46 (q, 6 F, J_{H-F} = J_{F-F} = 4.9 Hz), -77.04 (oct, 2 F, J_{H-F} = J_{F-F} = 4.7 Hz). HRMS *m/z* calcd for C₉H₁₁F₈NO (M + H)⁺ 302.0798; found 302.0791.

Preparation of 1-(tert-Butyl)-3-(difluoro((1,1,1,3,3,3-hexafluoropropan-2-yl)oxy)methyl)diaziridine (8a). To a 25 mL rbf with stir bar was added 1.85 g (6.14 mmol) of imine **7a** dissolved in 3 mL absolute ethanol, and the solution was cooled in an ice bath. A mixture of 0.83 g (7.33 mmol) of hydroxylamine-*O*-sulfonic acid (HOSA) in 4.2 mL absolute ethanol was cooled in an ice bath, and 0.64 g (6.32 mmol) of triethylamine was added slowly, over 5 minutes, with good stirring. The clear, colorless HOSA solution was added dropwise to the solution of **7a**, and the resulting solution was stirred at 0 °C for 20 minutes. The ice bath was removed, and the mixture was stirred at room temperature for 1 h during which a white precipitate formed. Concentration using a

rotary evaporator resulted in a white semisolid that was subsequently triturated with ether (3 x 20 mL). Evaporation of the ether yielded 0.86 g (44 %) of a clear, colorless liquid **8a**, which was sufficiently pure for conversion to diazirine. ¹H NMR (500 MHz, CDCl₃): δ 4.90 (sept, 1 H, J_{H-F} = 5.6 Hz), 3.21 (d, 1 H), 2.16 (s, 1 H), 1.03 (s, 9 H). ¹³C NMR (500 MHz, CDCl₃): δ 121.02 (t, J_{C-F} = 271 Hz), 120.02 (q, J_{C-F} = 283 Hz), 69.00 (m), 55.84 (s), 50.85 (t, J_{C-F} = 36 Hz), 25.21 (s). ¹⁹F NMR (360 MHz, CDCl₃): δ -73.71 (oct, 2 F, J_{H-F} = J_{F-F} = 5.2 Hz), -82.51 (q, 6 F, J_{H-F} = J_{F-F} = 4.7 Hz). HRMS *m/z* calcd for C₇H₈F₆O₃ (M + H)⁺ 317.0900; found 317.0901.

Preparation of 3-(Difluoro((1,1,1,3,3,3-hexafluoropropan-2-yl)oxy)methyl)-3H-diazirine (1a). To a 10 mL conical flask with stir bar was added 0.6 g (1.90 mmol) of **8a** dissolved in 1 mL of 1,2-dichloroethane. The solution was cooled to 0 °C in an ice bath and 0.36 g (2.00 mmol) NBS was added in one portion. The resulting suspension was stirred at 0 °C for 10 minutes and then at room temperature for 1 h. The volatiles were transferred to a U-trap cooled in liquid nitrogen under vacuum. Purification of the solution by preparative gas chromatography was accomplished using a 10 ft x 0.25 in. column packed with 10% SF-96 on Chromasorb W. GC collection conditions were as follows: injector 40 °C; column 30 °C; detector 60 °C; helium flow rate = 120 mL/min. The order of elution was **1**, *tert*-butylbromide, and dichloroethane. Product **1a** was collected in a U-trap cooled in liquid nitrogen. ¹H NMR (500 MHz, CDCl₃): δ 4.83 (sept, 1 H, J_{H-F} = 5.7 Hz), 1.71 (t, 1 H, J_{H-F} = 4.6 Hz). ¹³C NMR (500 MHz, CDCl₃): δ 120.94 (q, J_{C-F} = 283 Hz), 118.98 (t, J_{C-F} = 268 Hz), 69.32 (m), 20.66 (t, J_{C-F} = 42 Hz). ¹⁹F NMR (500 MHz, CDCl₃): δ -73.62 (q, 6 F, J_{H-F} = J_{F-F} = 5.0 Hz), -74.06 (oct, 2 F, J_{H-F} = J_{F-F} = 4.7 Hz).

A. 2.2. 2-fluoro-1,3-diisopropylbenzene; Fropofol (1b)

A 250 mL round bottom flask (rbf) with stir bar was filled with 2.0 g (11.3 mmol) of >99% pure 2,6-diisopropylaniline, water (39 mL), and 48% HBF₄ (5.7 g; 31.1 mmol). This clear, homogeneous solution was cooled to 0°C in an ice-water bath. A solution of NaNO₂ (0.78 g; 11.3 mmol) in water (1.7 mL) was added dropwise over the course of 5min, while keeping the temperature of the stirred solution below 3°C. After stirring for a few additional minutes, the resulting yellow crystals were suction filtered on a fritted glass funnel and then transferred to a 250mL rbf, which was evacuated under aspirator pressure overnight. The next day, the resulting brown liquid residue was extracted with hexanes (3 x 25 mL) and the combined organic layers were washed with 1 N KOH solution (4 x 35 mL), followed by water (3 x 15 mL). The organic layer was dried over magnesium sulfate and concentrated *in vacuo* to yield 1.53 g of a yellow oil. The product was purified by passing it through a plug of silica gel (33 cc) using hexane. Evaporation of the solvent followed by bulb-to-bulb transfer of the residue under dynamic vacuum gave 1.15 g (57%) of fropofol as a clear, colorless liquid. ¹H NMR (500 MHz, CDCl₃): δ 7.14-7.23 (3H, m), 3.41 (2H, sep, J = 7 Hz), 1.40 (12H, d, J = 7 Hz). ¹³C NMR (125 MHz, CDCl₃): δ 158.5 (d, J_{C-F} = 243 Hz), 135.1 (d, J_{C-F} = 15 Hz), 124.4 (d, J_{C-F} = 6.3 Hz), 123.8 (d, J_{C-F} = 3.8 Hz), 27.2 (d, J = 3.8 Hz), 22.8 ppm. ¹⁹F NMR (360 MHz, CDCl₃): δ -126.14 ppm (t, J = 3.6 Hz). HRMS *m/z* calculated for C₁₂H₁₇F (M)⁺ 180.1314; found 180.1311.

A. 2.3. 2-((prop-2-yn-1-yloxy)methyl)-5-(3-(trifluoromethyl)-3H-diazirin-3-yl)phenol; AziPm-click (1c)

2,2,2-Trifluoro-1-(3-(methoxymethoxy)-4-methylphenyl)ethan-1-one (3c): Under an argon atmosphere, a solution of **2** (5.0 g; 21.6 mmol) in dry THF (23 mL) and magnesium metal (0.57 g; 23.5 mmol) were added to a 50 mL rbf equipped with a condenser and stir bar. The flask was heated slowly to initiate the reaction, and then was allowed to react without external heating. Once the exothermic reaction was finished, the contents were heated to reflux for 20 minutes to ensure complete consumption of **2c**. The flask was cooled in an ice-salt bath for 25 minutes, causing a white precipitate to form. The condenser was replaced with an addition funnel containing 2,2,2-trifluoro-1-pyrrolidin-1-ylethanone (2.9 g; 17.4 mmol) in dry THF (4.3 mL) and the amide solution was added dropwise over 30 minutes at 0 °C while stirring. After the addition, the mixture was stirred in the ice bath for 1 hour. The reaction was then quenched with saturated aqueous NH₄Cl solution (6 mL), and the mixture was vacuum-filtered. The resulting liquid was dried over MgSO₄, and the solvent was removed under reduced pressure to give 5.4 g of a yellow liquid. Distillation under high vacuum yielded 3.2 g (72%) of **3** as a yellow liquid, bp 59°C (35 mTorr). ¹H NMR (500 MHz, CDCl₃): δ 7.74 (1 H, s), 7.61 (1 H, d, J = 8 Hz), 7.29 (1 H, d, J = 8 Hz), 5.27 (2 H, s), 3.50 (3 H, s), 2.34 (3 H, s). ¹³C NMR (125 MHz, CDCl₃): δ 179.89 (q, J_{C-F} = 34 Hz), 155.80, 136.95, 131.15, 128.90, 123.81, 116.79 (q, J_{C-F} = 290 Hz), 114.14, 94.43, 56.10, 16.71 ppm. ¹⁹F NMR (340 MHz, CDCl₃): δ -71.2 ppm. HRMS *m/z* calcd for C₁₁H₁₂F₃O₃ (M + H⁺) 249.0738; found 249.0742.

2,2,2-Trifluoro-1-(3-(methoxymethoxy)-4-methylphenyl)ethan-1-one oxime (4c): To a 25 mL rbf with stir bar was added **3** (1.0 g; 4 mmol), hydroxylamine hydrochloride (0.35 g; 4 mmol), and pyridine (10 mL). The flask was heated in an oil bath at 60 °C for 4 hours. The mixture was evaporated to remove volatiles and the residue was partitioned between methylene chloride (25 mL) and water (25 mL), and the separated organic layer was washed with additional water (20 mL). The organic solution was dried (Na₂SO₄) and was evaporated *in vacuo* to give 1.0 g of yellow oil. Crystallization from hexanes produced 600 mg (58%) of **4c** as colorless needles, mp. 101-102 °C. ¹H NMR (500 MHz, CDCl₃): δ 9.19 (1 H, s), 7.26 (2 H, d, J = 8 Hz), 7.09 (1 H, d, J = 8 Hz), 5.25 (2 H, s), 3.52 (3 H, s), 2.31 (3 H, s). ¹³C NMR (125 MHz, CDCl₃): δ 155.28, 147.44 (q, J_{C-F} = 33 Hz), 130.90, 130.62, 124.41, 121.80, 120.64 (q, J_{C-F} = 274 Hz), 114.18, 94.61, 56.18, 16.37 ppm. ¹⁹F NMR (340MHz, CDCl₃): δ - 66.6 ppm. HRMS *m/z* calcd for C₁₁H₁₁F₃NO₃ (M-H)⁻ 262.0691; found 262.0690.

2,2,2-Trifluoro-1-(3-(methoxymethoxy)-4-methylphenyl)ethan-1-one O-tosyl oxime (5c): In a 25 mL rbf with stir bar, **4c** (280 mg; 1.06 mmol) was dissolved in methylene chloride (7.3 mL). While stirring, 4-(N,N-dimethylamino)pyridine (6.2 mg; 0.05 mmol), *p*-toluenesulfonyl chloride (0.21 g; 1.16 mmol), and triethylamine (0.15 g; 208 μL; 1.5 mmol) were added to the flask. The mixture was stirred for 24 hours under nitrogen atmosphere at room temperature. Water (20 mL) and methylene chloride (20 mL) were then added to the reaction mixture, and the separated organic phase was washed with additional water (20 mL). The mixture was concentrated *in vacuo* to give 440 mg of a pale yellow crystalline solid. The crude product was purified by column chromatography with silica gel using 8% EtOAc/hexanes to give 360 mg (81%) of **7c** as a clear crystalline solid, mp 65-66 °C. ¹H NMR (500 MHz, CDCl₃): δ 7.89 (2 H, d, J = 8.5 Hz), 7.38 (2 H, d, J = 8.5 Hz), 7.23 (1 H, d, J = 8 Hz), 7.11 (1 H, s), 6.96 (1 H, d, J = 8 Hz), 5.20 (2 H, s), 3.50 (3 H, s), 2.49 (3 H, s), 2.28 (3 H, s). ¹³C NMR (125 MHz, CDCl₃): δ 155.46, 153.9

(q, $J_{C-F} = 38$ Hz), 146.06, 131.90, 131.34, 131.04, 129.88, 129.26, 122.88, 121.65, 120.78, 118.57, 116.58 (q, $J_{C-F} = 56.6$ Hz), 113.82, 94.66, 56.12, 21.77, 16.56 ppm. ^{19}F NMR (340 MHz, CDCl_3): δ -66.6 ppm. HRMS calcd for $\text{C}_{18}\text{H}_{19}\text{F}_3\text{NO}_5\text{S}$ ($\text{M}+\text{H}$) $^+$ 418.0936; found 418.0928.

3-(3-(Methoxymethoxy)-4-methylphenyl)-3-(trifluoromethyl)diaziridine (6c): To a solution of **5** (340 mg; 0.82 mmol) in diethyl ether (2 mL) in a 50 mL rbf equipped with stir bar and dry ice gas condenser was added excess liquid ammonia at -78 °C. The mixture was stirred overnight and allowed to warm to room temperature. The remaining residue was partitioned between diethyl ether (35 mL) and water (40 mL). The organic layer was washed with additional water (20 mL). The ether solution was dried over Na_2SO_4 , and the solvent was removed to give 215 mg (100%) of **6** as a white solid, mp 79 - 80 °C. ^1H NMR (500 MHz, CDCl_3): δ 7.29 (1 H, s), 7.20-7.15 (2 H, m), 5.23 (1 H, d, $J = 7$ Hz), 5.20 (1 H, d, $J = 7$ Hz), 3.50 (3 H, s), 2.79 (1 H, d, $J = 9$ Hz), 2.26 (3 H, s), 2.24 (1 H, d, $J = 9$ Hz). ^{13}C NMR (125 MHz, CDCl_3): δ 155.50, 130.99, 130.38, 129.78, 123.56 (q, $J_{C-F} = 278$ Hz), 121.21, 113.35, 94.56, 57.93 (q, $J_{C-F} = 35$ Hz), 56.13, 16.19 ppm. ^{19}F NMR (340 MHz, CDCl_3): δ -75.5 ppm. HRMS m/z calcd for $\text{C}_{11}\text{H}_{14}\text{F}_3\text{N}_2\text{O}_2$ ($\text{M}+\text{H}$) $^+$ 263.1007; found 263.1010.

3-(3-(Methoxymethoxy)-4-methylphenyl)-3-(trifluoromethyl)-3H-diazirine (7c): To a 50 mL rbf with stir bar was added **6** (1.0 g; 3.82 mmol), PDC (2.0 g; 5.32 mmol), and methylene chloride (10 mL). The mixture was stirred overnight at room temperature. The solution was diluted with hexanes (10 mL) and flushed through a short plug of silica gel with more hexanes. Evaporation of volatiles left 0.89 g (89%) of **7** as a clear light yellow liquid. ^1H NMR (500 MHz, CDCl_3): δ 7.17 (1 H, d, $J = 8.5$ Hz), 6.85 (1 H, s), 6.80 (1 H, d, $J = 8.5$ Hz), 5.19 (2 H, s), 3.50 (3 H, s), 2.25 (3 H, s). ^{13}C NMR (125 MHz, CDCl_3): δ 155.69, 131.13, 129.59, 127.74, 122.20 (q, $J_{C-F} = 274$ Hz), 119.85, 111.83, 94.56, 56.08, 28.45 (q, $J_{C-F} = 40$ Hz), 16.09 ppm. ^{19}F NMR (340 MHz, CDCl_3): δ -65.3 ppm. HRMS m/z calcd for $\text{C}_{11}\text{H}_{10}\text{F}_3\text{N}_2\text{O}_2$ ($\text{M}-\text{H}$) $^-$ 259.0694; found 259.0695.

3-(4-(Bromomethyl)-3-(methoxymethoxy)phenyl)-3-(trifluoromethyl)-3H-diazirine (8c): In a 10 mL rbf with stir bar, **7** (0.47 g; 1.8 mmol), NBS (0.32 g; 1.8 mmol), and CCl_4 (3.5 mL) were combined. The flask was equipped with a condenser and a nitrogen balloon and placed in an oil bath preheated to 90 °C. Incandescent light was shone directly on the flask. When the reaction was complete as monitored by TLC, the product was dissolved in hexanes (5 mL) and flushed through a pipette containing Celite (2 cc). The resulting mixture was evaporated *in vacuo* to give 0.63 g of a yellow liquid. The product was then flushed through a plug of silica gel (15 cc) with hexanes, and the solvent was evaporated to yield 0.5 g (83%) of **8c** as a colorless liquid. ^1H NMR (500 MHz, CDCl_3): δ 7.37 (1 H, d, $J = 8$ Hz), 6.88-6.84 (2 H, m), 5.27 (2 H, s), 4.53 (2 H, s), 3.52 (3 H, s). ^{13}C NMR (125 MHz, CDCl_3): δ 155.25, 151.46, 131.22, 131.14, 131.05, 128.65, 121.99 (q, $J_{C-F} = 275$ Hz), 120.00, 112.28, 94.74, 94.59, 56.59, 56.44, 56.10, 33.98, 28.42 (q, $J_{C-F} = 40$ Hz), 27.48, 16.11 ppm. ^{19}F NMR (340 MHz, CDCl_3): δ -65.1 ppm. HRMS m/z calcd for $\text{C}_{11}\text{H}_9\text{BrF}_3\text{N}_2\text{O}_2$ ($\text{M}-\text{H}$) $^+$ 336.9799; found 336.9799.

3-(3-(Methoxymethoxy)-4-((prop-2-yn-1-yloxy)methyl)phenyl)-3-(trifluoromethyl)-3H-diazirine (9c): To a 10 mL rbf with stir bar was added 60% dispersion of sodium hydride in mineral oil (0.06 g; 1.50 mmol) under nitrogen. The oil was removed by washing with hexanes (5 mL). Dry THF (2 mL) was then added, forming a cloudy white suspension. The mixture was cooled in an ice-water bath to 0 °C. To this mixture was

added propargyl alcohol (0.08g; 79 μ L; 1.37 mmol) via syringe which caused bubbling. After the bubbling stopped, a solution of **8c** (0.31 g; 0.91 mmol) dissolved in THF (1 mL) was added. The reaction was stirred at room temperature overnight. The mixture was dissolved in water (15 mL) and was extracted with diethyl ether (3 x 15 mL). The combined organic layers were washed with water (3 x 15 mL), and then dried over Na₂SO₄. The mixture was evaporated *in vacuo* to give 0.22 g (77%) of a yellow oil. The product was purified by column chromatography using silica gel and 5% ethyl acetate/hexanes, giving 0.13 g (45%) of **9c** as a colorless oil, R_f = 0.33 (5% EtOAc/hexanes). ¹H NMR (500 MHz, CDCl₃): δ 7.43 (1 H, d, J = 8.5 Hz), 6.89 (1 H, d, J = 8.5 Hz), 6.88 (1H, s), 5.20 (2 H, s), 4.66 (2 H, s), 4.22 (2 H, d, J = 2.5 Hz), 3.48 (3 H, s), 2.46 (1 H, t, J = 2.5 Hz). ¹³C NMR (125 MHz, CDCl₃): δ 154.96, 129.73, 129.35, 128.73, 122.09 (q, J_{C-F} = 275 Hz), 119.99, 111.94, 79.58, 74.66, 66.06, 57.74, 56.27, 28.45 (q, J_{C-F} = 40 Hz) ppm. ¹⁹F NMR (340 MHz, CDCl₃): δ -65.3 ppm. HRMS *m/z* calcd for C₁₄H₁₂F₃N₂O₃ (M-H)⁻ 313.0800; found 313.0812.

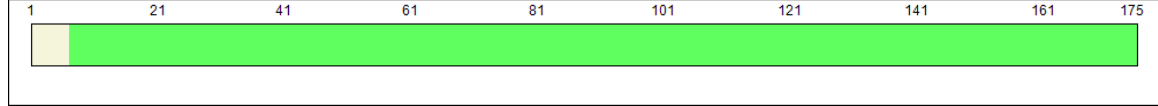
2-((Prop-2-yn-1-yloxy)methyl)-5-(3-(trifluoromethyl)-3H-diazirin-3-yl)phenol (AziPm-click 1c). In a 10 mL rbf with stir bar, **9** (65 mg; 0.21 mmol) was dissolved in methylene chloride (2.3 mL) at room temperature. While stirring, activated (hot) NaHSO₄•SiO₂ (43 mg) was added. After 4 hours the reaction was complete, as shown by TLC, and the mixture was dissolved in methylene chloride (2 mL) and run through a pipette containing silica gel (2 cc). The resulting solution was evaporated *in vacuo* and then evaporated under high vacuum to give 37.3 mg of a clear oil. The product was purified by column chromatography with silica gel using 15% EtOAc/hexanes to give 28.5 mg (52%) of **12**, a colorless oil. R_f = 0.3 (15% EtOAc/hexanes). ¹H NMR (500 MHz, CDCl₃): δ 7.17 (1 H, s), 7.09 (1 H, d, J = 8 Hz), 6.73 (1 H, s), 6.66 (1 H, d, J = 8 Hz), 4.80 (2 H, s), 4.25 (2 H, d, J = 2 Hz), 2.54 (1 H, t, J = 2 Hz). ¹³C NMR (125 MHz, CDCl₃): δ 156.50, 131.12, 129.22, 123.33, 122.21 (1, J_{C-F} = 274 Hz), 118.18, 115.04, 78.19, 76.39, 70.30, 57.94, 28.44 (q, J_{C-F} = 40 Hz) ppm. ¹⁹F NMR (340 MHz, CDCl₃): δ -65.3 ppm. HRMS *m/z* calcd for C₁₂H₉F₃N₂O₂ (M)⁺ 270.0616; found 270.0618.

A.3. Mass spectrometry protein coverage

Protein coverage maps and sequences are provided with detected peptide residues highlighted in green or denoted in bold and underlined.

A.3.1. aF coverage photoaffinity labeled by aziseovflurane(1a)

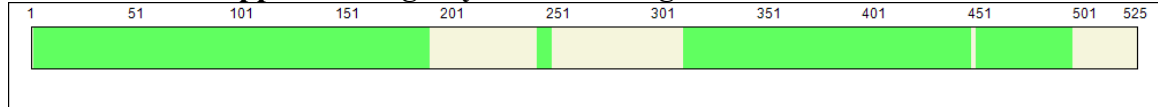
Horse spleen apo-ferritin light chain



<u>MSSQIRQNY</u> S	<u>TEVEAAVNRL</u>	<u>VNLYLRASYT</u>	<u>YLSLGFYFDR</u>
<u>DDVALEGVCH</u>	<u>FFRELAEK</u> R	<u>EGAERLLKMQ</u>	<u>NORGGRALFQ</u>
<u>DLQKPSQDEW</u>	<u>GTTLDAMKAA</u>	<u>IVLEKSLNQA</u>	<u>LLDLHALGSA</u>
<u>QADPHLCDFL</u>	<u>ESHFLDEEVK</u>	<u>LIKKMGDHLT</u>	<u>NIQRLVGSQA</u>
<u>GLGEYLFERL</u>	<u>TLKHD</u>		

A.3.2. Kv1.2 coverage photoaffinity labeled by aziseovflurane(1a)

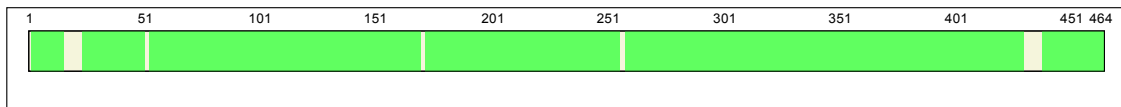
Rat Kv1.2 with appended Arg-Gly-Ser-His10 tag



<u>MTVATGDPVD</u>	<u>EAAALPGHPQ</u>	<u>DTYDPEADHE</u>	<u>CCERVVINIS</u>
<u>GLRFETQLKT</u>	<u>LAQFPETLLG</u>	<u>DPKKRMRYFD</u>	<u>PLRNEYFFDR</u>
<u>NRPSFDAILY</u>	<u>YYQSGGRLRR</u>	<u>PVNVPLDIFS</u>	<u>EEIRFYELGE</u>
<u>EAMEMFREDE</u>	<u>GYIKEERPL</u>	<u>PENEFQRQVW</u>	<u>LLFEYPSSG</u>
<u>PARIIAIVSV</u>	<u>MVILISIVSF</u>	<u>CLETLPIFRD</u>	ENEDMHGGGV
TFHTYSNSTI	GYQQSTSFTD	PFIVETLCI	IWFSFEFLVR
<u>FFACPSKAGF</u>	FTNIMNIIDI	VAIIPYFITL	GTELAEKPED
AQQGQOAMSL	AILRVIRLVR	VFRIFKLSRH	<u>SKGLQILGQT</u>
<u>LKASMRELGL</u>	<u>LIFFLFIGVI</u>	<u>LFSSAVYFAE</u>	<u>ADERDSQFPS</u>
<u>IPDAFWWAVV</u>	<u>SMTTVGYGDM</u>	<u>VPTTIGGKIV</u>	<u>GSLCAIAGVL</u>
<u>TIALPVPVIV</u>	<u>SNFNIFYHRE</u>	<u>TEGEEQAQYL</u>	<u>QVTSCPKIPS</u>
<u>SPDLKKSRSA</u>	<u>STISKSDYME</u>	<u>IQEGVNNSNE</u>	<u>DFREENLKTA</u>
<u>NCTLANTNYV</u>	<u>NITKMLTDVS</u>	GLEVLFOGPN	GARGSHHHHH
HHHHH			

A.3.3. FLAG- $\alpha_1\beta_3\gamma_{2L}$ -L3-1D4 GABA_A receptor coverage photoaffinity labeled by aziseovflurane(1a)

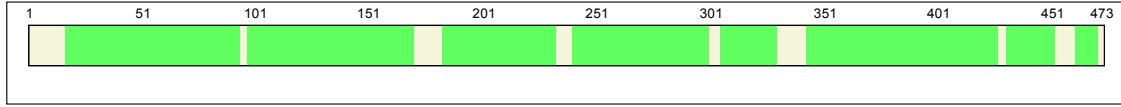
FLAG- α_1 GABA_A receptor subunit



<u>MKKSPGLSDY</u>	<u>LWAWTLFLST</u>	<u>LTGRSYGDYK</u>	<u>DDDDKQPSLQ</u>	<u>DELKDNTTVF</u>
<u>TRILDRLLDG</u>	<u>YDNRLRPGLG</u>	<u>ERVTEVKTDI</u>	<u>FVTSFGPVSD</u>	<u>HDMEYTIIDVF</u>
<u>FRQSWKDERL</u>	<u>KFKGPMTVLR</u>	<u>LNNLMASKIW</u>	<u>TPDTFFHNGK</u>	<u>KSVAHNMTMP</u>
<u>NKLLRITEDG</u>	<u>TLLYTMRLTV</u>	<u>RAECPMHLED</u>	<u>FPMDAHACPL</u>	<u>KFGSYAYTRA</u>
<u>EVVYEWTREP</u>	<u>ARSVVVAEDG</u>	<u>SRLNQYDLLG</u>	<u>QTVDSGIVQS</u>	<u>STGEYVVMTT</u>

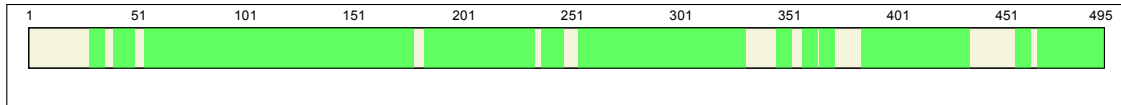
HFHLKRKIGY **FVIQTYLPCI** **MTVILSQVSF** **WLNRESVPAR** **TVFGVTTVLT**
MTTLSISARN **SLPKVAYATA** **MDWFIAVCYA** **FVFSALIEFA** **TVNYFTKRGY**
AWDGKSVVPE **KPKKVKDPLI** **KKNNTYAPTA** **TSYTPNLARG** **DPGLATIAKS**
ATIEPKVKP **ETKPPEPKKT** **FNSVSKIDRL** **SRIAFPLLFG** **IFNLVYWATY**
LNREPQLKAP **TPHQ**

β_3 GABA_A receptor subunit



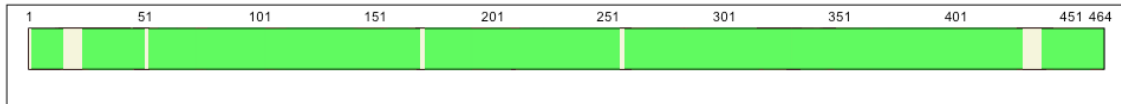
MCSGLLELLL **PIWLSWTLGT** **RGSEPRSVND** **PGNMSFVKET** **VDKLLKGYDI**
RLRPDFGGPP **VCVGMNIDIA** **SIDMVSEVNM** **DYTLTMYFQQ** **YWRDKRLAYS**
GIPNLNLTLDN **RVADQLWVPD** **TYFLNDKKSF** **VHGVTVKNRM** **IRLHPDGTVL**
YGLRITTTAA **CMDLRRYP** **DEQNCTLEIE** **SYGYTTDDIE** **FYWRGGDKAV**
TGVERIELPQ **FSIVEHRLVS** **RNVVFATGAY** **PRLSLSFRLK** **RNIGYFILQT**
YMPSILITIL **SWVSFWINYD** **ASAARVALGI** **TTVLTMTTIN** **THLRETLPKI**
PYVKAIDMYL **MGCFVVFVLA** **LLEYAFVNYI** **FFGRGPQRQK** **KLAEKTAKAK**
NDRSKSESNR **VDAHGNILLT** **SLEVHNEMNE** **VSGGIGDTRN** **SAISFDNSGI**
QYRKQSMPRE **GHGRFLGDRS** **LPHKKTHLRR** **RSSQLKIKIP** **DLTDVNAIDR**
WSRIVFPPTF **SLFNLVYWLY** **YVN**

γ_{2L} -L3-1D4 GABA_A receptor subunit



MSSPNIWSTG **SSVYSTPVFS** **QKMTVWILLL** **LSLYPGFTSQ** **KSDDDYEDYA**
SNKTWVLTPK **VPEGDVTVIL** **NNLLEGYDNK** **LRPDIGVKPT** **LIHTDMYVNS**
IGPVNAINME **YTIDIFFAQT** **WYDRRLKFNS** **TIKVLRLNSN** **MVGKIWIPTD**
FFRNSKKADA **HWITTPNRML** **RIWINDGRVLY** **TLRLTIDAEC** **QLQLHNFPM**
EHSCPLEFSS **YGYPREEIVY** **QWKRSSVEVG** **DTRSWRLYQF** **SFVGLRNTTE**
VVKTTSGDYV **VMSVYFDLSR** **RMGYFTIQTY** **IPCTLIVVLS** **WVSFWINKDA**
VPARTSLGIT **TVLTMTTLST** **IARKSLPKVS** **YVTAMDLFVS** **VCFIFVFSAL**
VEYGTLHYFV **SNRKPSKDKD** **KKKKNPLLRM** **FSFKAPTIDI** **RPRSATIOQN**
NATHLOERDE **EYGYECLDGK** **DCASFFCCFE** **DCRTGAWRHG** **RIHIRIAKMD**
SYARIFFPTA **FCLFNLVYWV** **SYLYLGGSGG** **SGSGKTETS** **QVAPA**

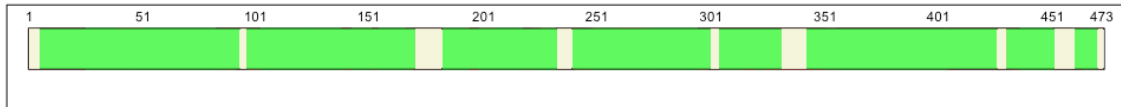
A.3.4. $\alpha_1\beta_3\gamma_{2L}$ GABA_A receptor coverage photoaffinity labeled by aziisoflurane FLAG- α_1 GABA_A receptor subunit



MKKSPGLSDY **LWAWTLFLST** **LTGRSYGDYK** **DDDDKQPSLQ** **DELKDNTTVF**
TRILDRLLDG **YDNRLRPGLG** **ERVTEVKTDI** **FVTSFGPVSD** **HDMEYTIQVF**
FRQSWKDERL **KFKGPMTVLR** **LNNLMASKIW** **TPDTFFHNGK** **KVAHNMTMP**
NKLLRITEDG **TLlyTMRLTV** **RAECPMHLED** **FPMDAHACPL** **KFGSYAYTRA**

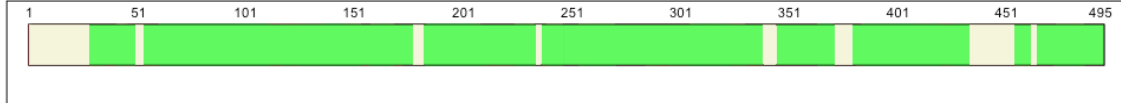
EVVYEWTREP ARSVVVAEDG SRLNQYDLLG QTVDSGIVQS STGEYVVMTT
HFHLKRKIGY FVIQTYLPCI MTVILSQVSF WLNRESVPAR TVFGVTTVLT
MTTLSISARN SLPKVAYATA MDWFIAVCYA FVFSALIEFA TVNYFTKRGY
AWDGKSVVPE KPKKVKDPLI KKNNTYAPTA TSYTPNLARG DPGLATIAKS
ATIEPKEVKP ETKPPEPKKT FNSVSKIDRL SRIAFPLLFG IFNLVYWATY
LNREPQLKAP TPHQ

β_3 GABA_A receptor subunit



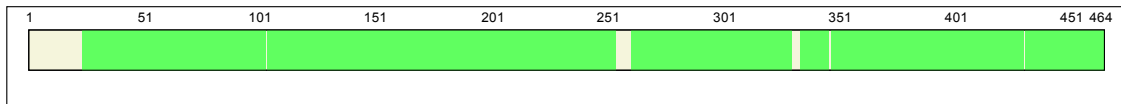
MCSGLELELL PIWLSWTLGT RGSEPRSVND PGNMSFVKET VDKLLKGYDI
RLRPDFGGPP VCVGMNIDIA SIDMVSEVNM DYTLTMYFQQ YWRDKRLAYS
GIPNLTLDN RVADQLWVPD TYFLNDKKSF VHGVTVKNRM IRLHPDGTVL
YGLRITTTAA CMDLRRYPL DEQNCTLEIE SYGYTTDDIE FYWRGGDKAV
TGVERIELPQ FSIVEHRLVS RNVVFATGAY PRLSLSFRLK RNIGYFILQT
YMPSILITIL SWVSFWINYD ASAARVALGI TTVLTMTTIN THLRETLPKI
PYVKAIDMYL MGCFVVFVLA LLEYAFVNYI FFGRGPQRQK KLAEKTAKAK
NDRSKSESNR VDAHGNILLT SLEVHNEMNE VSGGIGDTRN SAISFDNSGI
QYRKQSMPRE GHGRFLGDRS LPHKKTHLRR RSSQLKIKIP DLTDVNAIDR
WSRIVFPPTF SLFNLVYWLY YVN

γ_{2L} -L3-1D4 GABA_A receptor subunit



MSSPNIWSTG SSVYSTPVFS QKMTVWILL LSLYPGFTSQ KSDDDYEDYA
SNKTWVLTPK VPEGDVTVIL NNLLEGYDNK LRPDIGVKPT LIHTDMYVNS
IGPVNAINME YTIDIFFAQT WYDRRLKFNS TIKVLRLNSN MVGKIWIPTD
FFRNSKKADA HWITTPNRML RIWINDGRVLY TLRLTIDAEC QLQLHNFPM
EHSCPLEFSS YGYPREEIVY QWKRSSVEVG DTRSWRLYQF SFVGLRNTTE
VVKTTSGDYV VMSVYFDLSR RMGYFTIQTY IPCTLIVVLS WVSFWINKDA
VPARTSLGIT TVLTM TTLST IARKSLPKVS YVTAMDLFVS VCFIFVFSAL
VEYGLTHYFV SNRKPSKDKD KKKKNPLLRLM FSFKAPTIDI RPRSATIOMN
NATHLQERDE EYGYECLDGK DCASFFCCFE DCRTGAWRHG RIHIRIAKMD
SYARIFFPTA FCLFNLVYWV SYLYLGGSGG SGGSGKTETS QVAPA

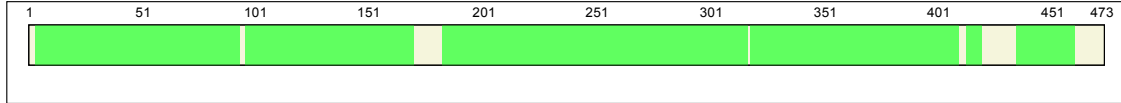
A.3.5. $\alpha_1\beta_3$ GABA_A receptor coverage photoaffinity labeled by azisevoflurane(1a) FLAG- α_1 GABA_A receptor subunit



MKKSPGLSDY LWAWTLFLST LTGRSYGDYK DDDDKQPSLQ DELKDNTTVF
TRILDRLLDG YDNRLRPGLG ERVTEVKTDI FVTSFGPVSD HDMEYTIDVF
FRQSWKDERL KFKGPMTVLR LNNLMASKIW TPDTFFHNGK KSVAHNMTMP

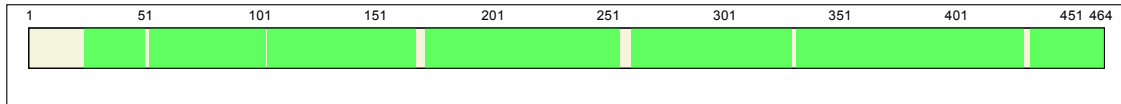
NKLLRITEDG TLLYTMRLTV RAECPMHLED FPMDAHACPL KFGSYAYTRA
EVVYEWTR ARSVVVAEDG SRLNQYDLLG QTVDSGIVQS STGEYVVMTT
HFHLKRKIGY FVIQTYLPCI MTVILSQVSF WLNRESVPAR TVFGVTTVLT
MTTLLSISARN SLPKVAYATA MDWFIAVCYA FVFSALIEFA TVNYFTKRGY
AWDGKSVVPE KPKKVKDPLI KKNNTYAPTA TSYTPNLARG DPGLATIAKS
ATIEPKEVKP ETKPPEPKKT FNSVSKIDRL SRIAFPLLFG IFNLVYWATY
LNREPQLKAP TPHQ

β_3 GABA_A receptor subunit



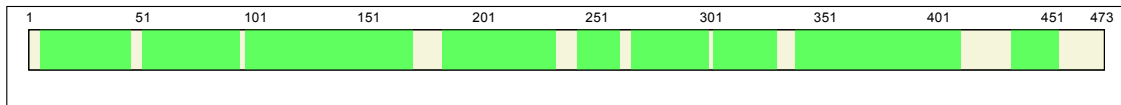
MCSGELLELL PIWLSWTLGT RGSEPRSVND PGNMSFVKET VDKLLKGYDI
RLRPDFGGPP VCVGMNIDIA SIDMVSEVNM DYTLTMYFQQ YWRDKRLAYS
GIPNLTLDN RVADQLWVPD TYFLNDKKSF VHGVTVKNRM IRLHPDGTVL
YGLRITTTAA CMDLRRYPL DEQNCTLEIE SYGYTTDDIE FYWRGGDKAV
TGVERIELPQ FSIVEHRLVS RNVVFATGAY PRLSLSFRLK RNIGYFILQT
YMPSILITIL SWVSFWINYD ASAARVALGI TTVLTMTTIN THLRETLPKI
PYVKAIDMYL MGCFVVFVFLA LLEYAFVNYI FFGRGPQRQK KLAEKTAKAK
NDRSKSESNR VDAHGNILLT SLEVHNEMNE VSGGIGDTRN SAISFDNSGI
QYRKQSMPRE GHGRFLGDRS LPHKKTHLRR RSSQLKIKIP DLTDVNAIDR
WSRIVFPPTF SLFNLVYWLY YVN

A.3.6. $\alpha_1\beta_3$ GABA_A receptor coverage photoaffinity labeled by aziisoflurane
 FLAG- α_1 GABA_A receptor subunit



MKKSPGLSDY LWAWTLFLST LTGRSYGDYK DDDDKQPSLQ DELKDNTTVF
TRILDRLLDG YDNRLRPGLG ERVTEVKTDI FVTSFGPVSD HDMEYIDVF
FRQSWKDERL KFKGPMTVLR LNNLMASKIW TPDTFFHNGK KSVAHNMTMP
NKLLRITEDG TLLYTMRLTV RAECPMHLED FPMDAHACPL KFGSYAYTRA
EVVYEWTR ARSVVVAEDG SRLNQYDLLG QTVDSGIVQS STGEYVVMTT
HFHLKRKIGY FVIQTYLPCI MTVILSQVSF WLNRESVPAR TVFGVTTVLT
MTTLLSISARN SLPKVAYATA MDWFIAVCYA FVFSALIEFA TVNYFTKRGY
AWDGKSVVPE KPKKVKDPLI KKNNTYAPTA TSYTPNLARG DPGLATIAKS
ATIEPKEVKP ETKPPEPKKT FNSVSKIDRL SRIAFPLLFG IFNLVYWATY
LNREPQLKAP TPHQ

β_3 GABA_A receptor subunit



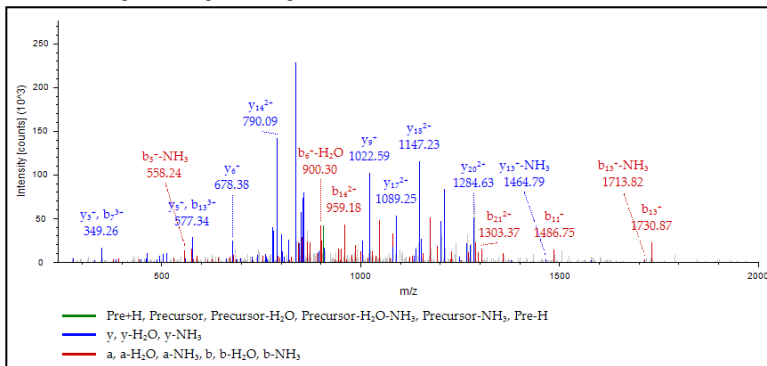
MCSGELLELL PIWLSWTLGT RGSEPRSVND PGNMSFVKET VDKLLKGYDI
RLRPDFGGPP VCVGMNIDIA SIDMVSEVNM DYTLTMYFQQ YWRDKRLAYS

GIPNLTLDN RVADQLWVPD TYFLNDKKSF VHGVTVKNRM IRLHPDGTVL
YGLRITTTAA CMMDLRRYPL DEQNCTLEIE SYGYTTDDIE FYWRGGDKAV
TGVERIELPO FSIVEHRLVS RNVVFATGAY PRLSLSFRLK RNIGYFILQT
YMPSILITIL SWVSFWINYD ASAARVALGI TTVLTMTTIN THLRETLPKI
PYVKAIDMYL MGCFVVFVFLA LLEYAFVNYI FFGRGPQRQK KLAEKTAKAK
NDRSKSESNR VDAHGNILLT SLEVHNEMNE VSGGIGDTRN SAISFDNSGI
QYRKQSMPRE GHGRFLGDRS LPHKKTHLRR RSQKIKIP DLTDVNAIDR
WSRIVFPPTF SLFNLVYWLY YVN

A.4. Mass spectra

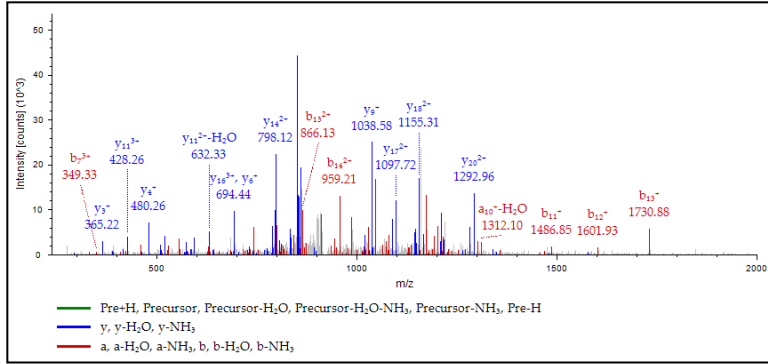
For all spectra, hypothetical fragment ions are listed in the tables, and their predicted positions are indicated on the spectra. Fragment ions that were identified on the spectra are colored in the ion tables. Respective residue modifications are noted within ion tables. Photoaffinity labeled residues are denoted bold and with an (*) and labeled within ion tables for aziseovflurane(**1a**) (AziSev) and aziisovflurane (AziIso)

A.4.1. Apo-ferritin (aF) peptides photoaffinity labeled by aziseovflurane(**1a**) 76-ALFQDL*QKPSQDEWGTTLDAMK-97



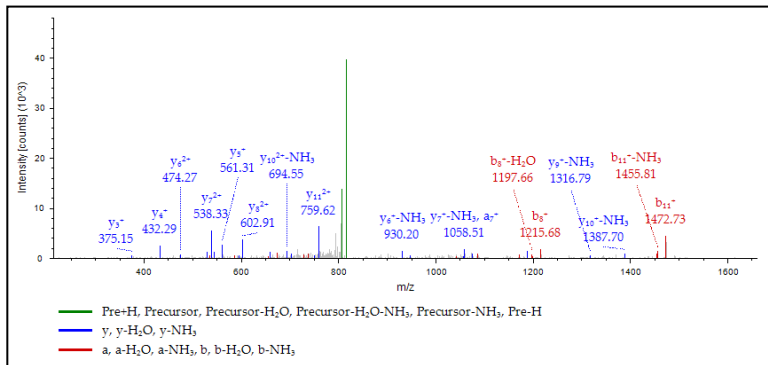
#1	a*	a ²⁺	a ³⁺	b*	b ²⁺	b ³⁺	Seq.	y*	y ²⁺	y ³⁺	#2
1	44.049	22.528	15.355	72.044	36.526	24.686	A				22
2	157.134	79.070	53.049	185.128	93.068	62.381	L	2681.184	1341.096	894.400	21
3	304.202	152.605	102.072	332.197	166.602	111.404	F	2568.100	1284.554	856.705	20
4	432.261	216.634	144.758	460.255	230.631	154.090	Q	2421.031	1211.019	807.682	19
5	547.288	274.147	183.101	575.282	288.145	192.432	D	2292.973	1146.990	764.996	18
6	890.369	445.688	297.461	918.364	459.686	306.793	L-AziSev	2177.946	1089.477	726.654	17
7	1018.428	509.718	340.148	1046.423	523.715	349.479	Q	1834.864	917.936	612.293	16
8	1146.523	573.765	382.846	1174.518	587.763	392.177	K	1706.806	853.906	569.607	15
9	1243.576	622.291	415.197	1271.571	636.289	424.528	P	1578.711	789.859	526.908	14
10	1330.608	665.807	444.207	1358.603	679.805	453.539	S	1481.658	741.333	494.557	13
11	1458.666	729.837	486.894	1486.661	743.834	496.225	Q	1394.626	697.817	465.547	12
12	1573.693	787.350	525.236	1601.688	801.348	534.568	D	1266.567	633.787	422.861	11
13	1702.736	851.872	568.250	1730.731	865.869	577.582	E	1151.540	576.274	384.518	10
14	1888.815	944.911	630.277	1916.810	958.909	639.608	W	1022.498	511.752	341.504	9
15	1945.837	973.422	649.284	1973.832	987.419	658.615	G	836.418	418.713	279.478	8
16	2046.884	1023.946	682.966	2074.879	1037.943	692.298	T	779.397	390.202	260.470	7
17	2147.932	1074.470	716.649	2175.927	1088.467	725.980	T	678.349	339.678	226.788	6
18	2261.016	1131.012	754.344	2289.011	1145.009	763.675	L	577.301	289.154	193.105	5
19	2376.043	1188.525	792.686	2404.038	1202.523	802.017	D	464.217	232.612	155.411	4
20	2447.080	1224.044	816.365	2475.075	1238.041	825.697	A	349.190	175.099	117.068	3
21	2578.121	1289.564	860.045	2606.116	1303.561	869.377	M	278.153	139.580	93.389	2
22							K	147.113	74.060	49.709	1

76-ALFQDLQ*KPSQDEWGTTLDAMK-97



#1	a ⁺	a ²⁺	a ³⁺	b ⁺	b ²⁺	b ³⁺	Seq.	y ⁺	y ²⁺	y ³⁺	#2
1	44.049	22.528	15.355	72.044	36.526	24.686	A				22
2	157.134	79.070	53.049	185.128	93.068	62.381	L	2697.179	1349.093	899.731	21
3	304.202	152.605	102.072	332.197	166.602	111.404	F	2584.095	1292.551	862.036	20
4	432.261	216.634	144.758	460.255	230.631	154.090	Q	2437.026	1219.017	813.014	19
5	547.288	274.147	183.101	575.282	288.145	192.432	D	2308.968	1154.988	770.327	18
6	660.372	330.689	220.795	688.366	344.687	230.127	L	2193.941	1097.474	731.985	17
7	1018.428	509.718	340.148	1046.423	523.715	349.479	Q-AziSev	2080.857	1040.932	694.290	16
8	1146.523	573.765	382.846	1174.518	587.763	392.177	K	1722.800	861.904	574.938	15
9	1243.576	622.291	415.197	1271.571	636.289	424.528	P	1594.705	797.856	532.240	14
10	1330.608	665.807	444.207	1358.603	679.805	453.539	S	1497.653	749.330	499.889	13
11	1458.666	729.837	486.894	1486.661	743.834	496.225	Q	1410.621	705.814	470.878	12
12	1573.693	787.350	525.236	1601.688	801.348	534.568	D	1282.562	641.785	428.192	11
13	1702.736	851.872	568.250	1730.731	865.869	577.582	E	1167.535	584.271	389.850	10
14	1888.815	944.911	630.277	1916.810	958.909	639.608	W	1038.493	519.750	346.836	9
15	1945.837	973.422	649.284	1973.832	987.419	658.615	G	852.413	426.710	284.809	8
16	2046.884	1023.946	682.966	2074.879	1037.943	692.298	T	795.392	398.200	265.802	7
17	2147.932	1074.470	716.649	2175.927	1088.467	725.980	T	694.344	347.676	232.120	6
18	2261.016	1131.012	754.344	2289.011	1145.009	763.675	L	593.296	297.152	198.437	5
19	2376.043	1188.525	792.686	2404.038	1202.523	802.017	D	480.212	240.610	160.742	4
20	2447.080	1224.044	816.365	2475.075	1238.041	825.697	A	365.185	183.096	122.400	3
21	2594.116	1297.561	865.377	2622.110	1311.559	874.708	M-Oxidation	294.148	147.578	98.721	2
22							K	147.113	74.060	49.709	1

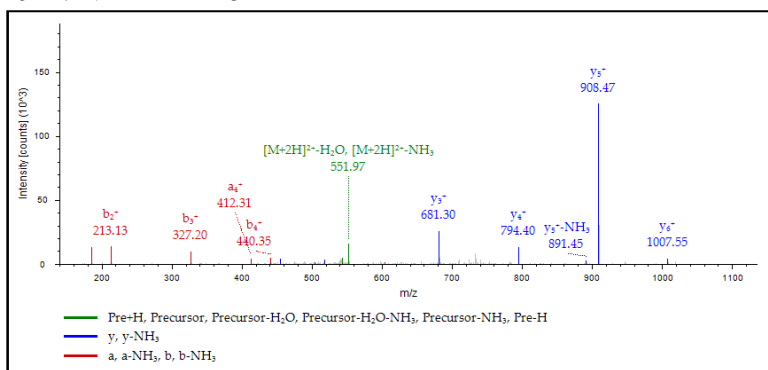
53-ELAAEKR*EGAER-64



7	a ⁺	a ²⁺	b ⁺	b ²⁺	Seq.	y ⁺	y ²⁺	#2
1	102.055	51.531	130.050	65.529	E			12
2	215.139	108.073	243.134	122.071	L	1517.663	759.335	11
3	286.176	143.592	314.171	157.589	A	1404.579	702.793	10
4	415.219	208.113	443.214	222.110	E	1333.542	667.275	9

5	544.261	272.634	572.256	286.632	E	1204.499	602.753	8
6	672.356	336.682	700.351	350.679	K	1075.457	538.232	7
7	1058.455	529.731	1086.450	543.729	R-AziSev	947.362	474.184	6
8	1187.498	594.253	1215.493	608.250	E	561.263	281.135	5
9	1244.519	622.763	1272.514	636.761	G	432.220	216.614	4
10	1315.556	658.282	1343.551	672.279	A	375.199	188.103	3
11	1444.599	722.803	1472.594	736.801	E	304.162	152.584	2
12					R	175.119	88.063	1

19-IVNLYLR*-25

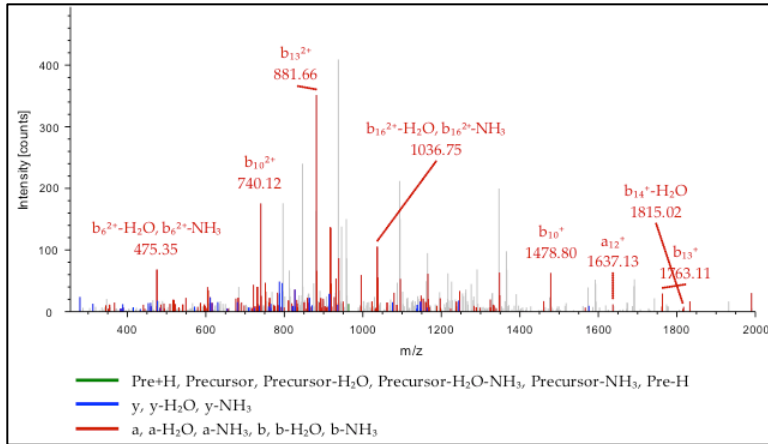


#1	a ⁺	a ²⁺	b ⁺	b ²⁺	Seq.	y ⁺	y ²⁺	#2
1	86.096	43.552	114.091	57.549	L			7
2	185.165	93.086	213.160	107.084	V	1007.460	504.233	6
3	299.208	150.108	327.203	164.105	N	908.391	454.699	5
4	412.292	206.650	440.287	220.647	L	794.348	397.678	4
5	575.355	288.181	603.350	302.179	Y	681.264	341.136	3
6	688.439	344.723	716.434	358.721	L	518.201	259.604	2
7					R-AziSev	405.117	203.062	1

A.4.2. Kv1.2 peptide photoaffinity labeled by azisevoflurane(1a) 313-GLQIL*GQTLK-322 Spectra (See Figure 8)

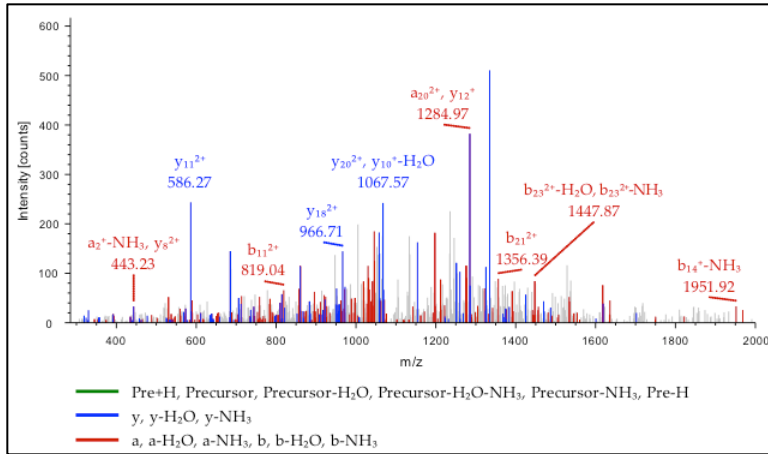
#1	a ⁺	a ²⁺	b ⁺	b ²⁺	Seq.	y ⁺	y ²⁺	#2
1	30.034	15.521	58.029	29.518	G			10
2	143.118	72.063	171.113	86.060	L	1243.633	622.320	9
3	271.176	136.092	299.171	150.089	Q	1130.549	565.778	8
4	384.261	192.634	412.255	206.631	I	1002.491	501.749	7
5	727.342	364.175	755.337	378.172	L-AziSev	889.406	445.207	6
6	784.364	392.686	812.359	406.683	G	546.325	273.666	5
7	912.422	456.715	940.417	470.712	Q	489.303	245.155	4
8	1013.470	507.239	1041.465	521.236	T	361.245	181.126	3
9	1126.554	563.781	1154.549	577.778	L	260.197	130.602	2
10					K	147.113	74.060	1

A.4.3. α₁β₃γ_{2L} GABA_A receptor peptides photoaffinity labeled by azisevoflurane(1a) FLAG-α₁ GABA_A receptor subunit 276-S*QVSFWLNRESVPARTVFGVTTVL-299



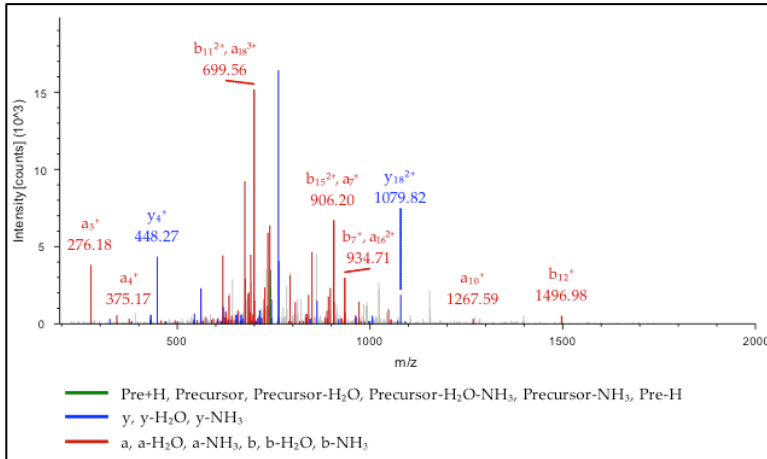
#	a ⁺	a ²⁺	a ³⁺	b ⁺	b ²⁺	b ³⁺	Seq.	y ⁺	y ²⁺	y ³⁺	#
1	290.0421 8	145.5247 3	97.3522 5	318.0371 0	159.5221 9	106.683 88	S-AziSev				2 4
2	419.0847 8	210.0460 3	140.366 44	447.0796 9	224.0434 8	149.698 08	Q-Deamidate d	2608.377 08	1304.692 18	870.130 55	2 3
3	518.1532 0	259.5802 4	173.389 25	546.1481 1	273.5776 9	182.720 89	V	2479.334 49	1240.170 88	827.116 35	2 2
4	605.1852 3	303.0962 5	202.399 93	633.1801 4	317.0937 1	211.731 57	S	2380.266 07	1190.636 67	794.093 54	2 1
5	752.2536 5	376.6304 6	251.422 73	780.2485 6	390.6279 2	260.754 37	F	2293.234 04	1147.120 66	765.082 86	2 0
6	938.3329 7	469.6701 2	313.449 17	966.3278 8	483.6675 8	322.780 81	W	2146.165 62	1073.586 45	716.060 06	1 9
7	1051.417 04	526.2121 6	351.143 86	1079.411 95	540.2096 1	360.475 50	L	1960.086 30	980.5467 9	654.033 62	1 8
8	1166.443 98	583.7256 3	389.486 18	1194.438 90	597.7230 9	398.817 82	N-Deamidate d	1847.002 23	924.0047 5	616.338 93	1 7
9	1322.545 10	661.7761 9	441.519 89	1350.540 02	675.7736 5	450.851 52	R	1731.975 28	866.4912 8	577.996 61	1 6
10	1451.587 70	726.2974 9	484.534 09	1479.582 62	740.2949 5	493.865 72	E	1575.874 16	788.4407 2	525.962 90	1 5
11	1538.619 73	769.8135 1	513.544 76	1566.614 65	783.8109 6	522.876 40	S	1446.831 56	723.9194 2	482.948 70	1 4
12	1637.688 15	819.3477 2	546.567 57	1665.683 07	833.3451 7	555.899 21	V	1359.799 53	680.4034 0	453.938 03	1 3
13	1734.740 92	867.8741 0	578.918 49	1762.735 84	881.8715 6	588.250 13	P	1260.731 11	630.8691 9	420.915 22	1 2
14	1805.778 04	903.3926 6	602.597 53	1833.772 96	917.3901 2	611.929 17	A	1163.678 34	582.3428 1	388.564 30	1 1
15	1961.879 16	981.4432 2	654.631 24	1989.874 08	995.4406 8	663.962 88	R	1092.641 22	546.8242 5	364.885 26	1 0
16	2062.926 84	1031.967 06	688.313 80	2090.921 76	1045.964 52	697.645 44	T	936.5401 0	468.7736 9	312.851 55	9
17	2161.995 26	1081.501 27	721.336 61	2189.990 18	1095.498 73	730.668 24	V	835.4924 2	418.2498 5	279.168 99	8
18	2309.063 8	1155.035 48	770.359 41	2337.058 60	1169.032 94	779.691 05	F	736.4240 0	368.7156 4	246.146 18	7
19	2366.085 15	1183.546 22	789.366 57	2394.080 07	1197.543 67	798.698 21	G	589.3555 8	295.1814 3	197.123 38	6
20	2465.153 57	1233.080 43	822.389 38	2493.148 49	1247.077 88	831.721 01	V	532.3341 1	266.6706 9	178.116 22	5
21	2566.201 25	1283.604 27	856.071 94	2594.196 17	1297.601 72	865.403 57	T	433.2656 9	217.1364 8	145.093 41	4
22	2667.248 93	1334.128 11	889.754 50	2695.243 85	1348.125 56	899.086 13	T	332.2180 1	166.6126 4	111.410 85	3
23	2766.317 35	1383.662 32	922.777 30	2794.312 27	1397.659 77	932.108 94	V	231.1703 3	116.0888 0	77.7282 9	2
24							L	132.1019 1	66.55459	44.70549 9	1

290-R*TVFGV*TTVLTMTTLLSISARNSLPKV-315



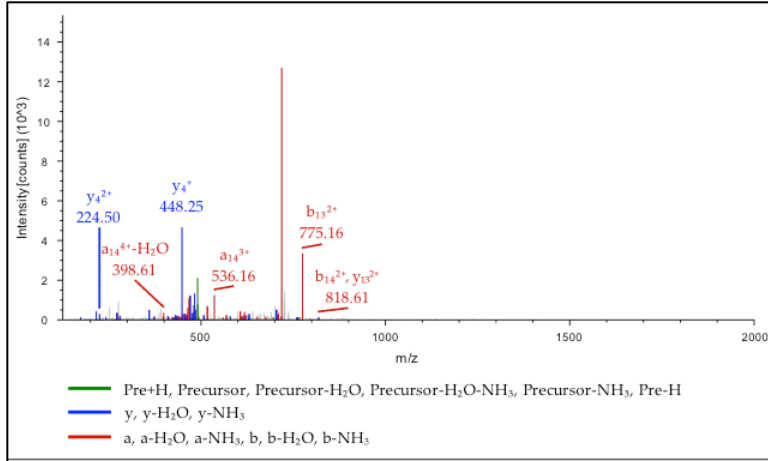
#	a ⁺	a ²⁺	a ³⁺	b ⁺	b ²⁺	b ³⁺	Seq.	y ⁺	y ²⁺	y ³⁺	#
1	359.1112 7	180.0592 7	120.3752 8	387.1061 9	194.0567 3	129.7069 1	R-AziSev				2
2	460.1589 5	230.5831 1	154.0578 4	488.1538 7	244.5805 7	163.3894 7	T	2867.451 08	1434.229 18	956.488 54	2
3	559.2273 7	280.1173 2	187.0806 4	587.2222 9	294.1147 8	196.4122 8	V	2766.403 40	1383.705 34	922.805 98	2
4	706.2957 9	353.6515 3	236.1034 5	734.2907 1	367.6489 9	245.4350 9	F	2667.334 98	1334.171 13	889.783 18	2
5	763.3172 6	382.1622 7	255.1106 1	791.3121 8	396.1597 3	264.4422 4	G	2520.266 56	1260.636 92	840.760 37	2
6	1092.383 47	546.6953 7	364.7993 4	1120.378 39	560.6928 3	374.1309 8	V-AziSev	2463.245 09	1232.126 18	821.753 21	2
7	1193.431 15	597.2192 1	398.4819 0	1221.426 07	611.2166 7	407.8135 4	T	2134.178 88	1067.593 08	712.064 48	2
8	1294.478 83	647.7430 5	432.1644 6	1322.473 75	661.7405 1	441.4961 0	T	2033.131 20	1017.069 24	678.381 92	1
9	1393.547 25	697.2772 6	465.1872 7	1421.542 17	711.2747 2	474.5189 1	V	1932.083 52	966.5454 0	644.699 36	1
10	1506.631 32	753.8193 0	502.8819 6	1534.626 24	767.8167 6	512.2136 0	L	1833.015 10	917.0111 9	611.676 55	1
11	1607.679 00	804.3431 4	536.5645 2	1635.673 92	818.3406 0	545.8961 6	T	1719.931 03	860.4691 5	573.981 86	1
12	1738.719 50	869.8633 9	580.2446 9	1766.714 42	883.8608 5	589.5763 2	M	1618.883 35	809.9453 1	540.299 30	1
13	1839.767 18	920.3872 3	613.9272 5	1867.762 10	934.3846 9	623.2588 8	T	1487.842 85	744.4250 6	496.619 13	1
14	1940.814 86	970.9110 7	647.6098 1	1968.809 78	984.9085 3	656.9414 4	T	1386.795 17	693.9012 2	462.936 57	1
15	2053.898 93	1027.453 10	685.3045 0	2081.893 85	1041.450 56	694.6361 3	L	1285.747 49	643.3773 8	429.254 01	1
16	2140.930 96	1070.969 12	714.3151 7	2168.925 88	1084.966 58	723.6468 1	S	1172.663 42	586.8353 5	391.559 32	1
17	2254.015 03	1127.511 15	752.0098 6	2282.009 95	1141.508 61	761.3415 0	I	1085.631 39	543.3193 3	362.548 65	1
18	2341.047 06	1171.027 17	781.0205 4	2369.041 98	1185.024 63	790.3521 8	S	972.5473 2	486.7773 0	324.853 96	9
19	2412.084 18	1206.545 73	804.6995 8	2440.079 10	1220.543 19	814.0312 2	A	885.5152 9	443.2612 8	295.843 28	8
20	2568.185 30	1284.596 29	856.7332 9	2596.180 22	1298.593 75	866.0649 2	R	814.4781 7	407.7427 2	272.164 24	7
21	2683.212 25	1342.109 76	895.0756 0	2711.207 16	1356.107 22	904.4072 4	N-Deamidated	658.3770 5	329.6921 6	220.130 53	6
22	2770.244 28	1385.625 78	924.0862 8	2798.239 19	1399.623 23	933.4179 2	S	543.3501 0	272.1786 9	181.788 22	5
23	2883.328 35	1442.167 81	961.7809 7	2911.323 26	1456.165 27	971.1126 1	L	456.3180 7	228.6626 7	152.777 54	4
24	2980.381 42	1490.694 20	994.1318 9	3008.376 03	1504.691 65	1003.463 53	P	343.2340 0	172.1206 4	115.082 85	3
25	3108.476 09	1554.741 68	1036.830 21	3136.471 00	1568.739 14	1046.161 85	K	246.1812 3	123.5942 5	82.7319 3	2
26							V	118.0862 6	59.54677	40.0336 0	1

292-VFGVT*TVLTMTTLSISARN-310



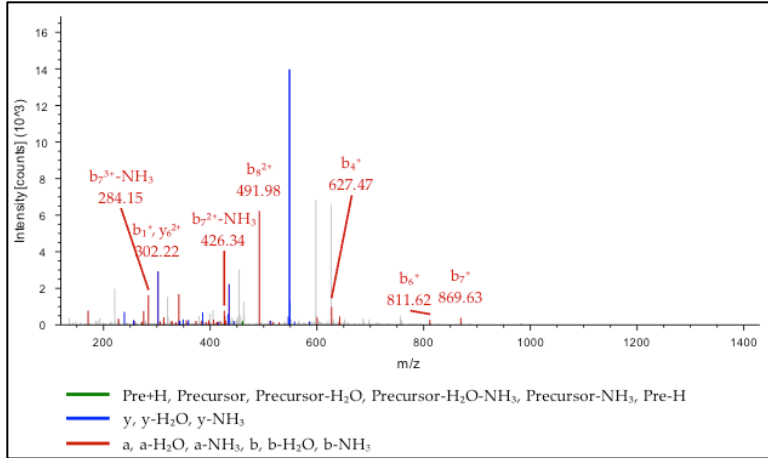
#	a ⁺	a ²⁺	a ³⁺	b ⁺	b ²⁺	b ³⁺	Seq.	y ⁺	y ²⁺	y ³⁺	#
1	72.08078	36.54403	24.6984	100.0757	50.54149	34.0300	V				1
2	219.1492	110.0782	73.7212	247.1441	124.0757	83.0528	F	2158.997	1080.002	720.337	1
3	276.1706	138.5889	92.7284	304.1655	152.5864	102.060	G	2011.929	1006.468	671.314	1
4	375.2390	188.1231	125.751	403.2340	202.1206	135.082	V	1954.907	977.9575	652.307	1
5	706.2845	353.6459	236.099	734.2794	367.6433	245.431	T-AziSev	1855.839	928.4233	619.284	1
6	807.3322	404.1697	269.782	835.3271	418.1672	279.113	T	1524.793	762.9005	508.936	1
7	906.4006	453.7039	302.805	934.3955	467.7014	312.136	V	1423.746	712.3767	475.253	1
8	1019.484	510.2460	340.499	1047.479	524.2434	349.831	L	1324.677	662.8425	442.230	1
9	1120.532	560.7698	374.182	1148.527	574.7673	383.513	T	1211.593	606.3004	404.536	1
10	1267.567	634.2875	423.194	1295.562	648.2850	432.525	M-Oxidation	1110.546	555.7766	370.853	1
11	1368.615	684.8113	456.876	1396.610	698.8088	466.208	T	963.5105	482.2589	321.841	9
12	1469.663	735.3352	490.559	1497.658	749.3326	499.890	T	862.4629	431.7350	288.159	8
13	1582.747	791.8772	528.253	1610.742	805.8747	537.585	L	761.4152	381.2112	254.476	7
14	1669.779	835.3932	557.264	1697.774	849.3907	566.596	S	648.3311	324.6692	216.781	6
15	1782.863	891.9353	594.959	1810.858	905.9327	604.290	I	561.2991	281.1532	187.771	5
16	1869.895	935.4513	623.969	1897.890	949.4487	633.301	S	448.2150	224.6111	150.076	4
17	1940.932	970.9698	647.649	1968.927	984.9673	656.980	A	361.1830	181.0951	121.065	3
18	2097.033	1049.020	699.682	2125.028	1063.017	709.014	R	290.1459	145.5765	97.3868	2
19							N-Deamidated	134.0447	67.52603	45.3531	1

294-GVTTVLT*MTTLSISARN-310



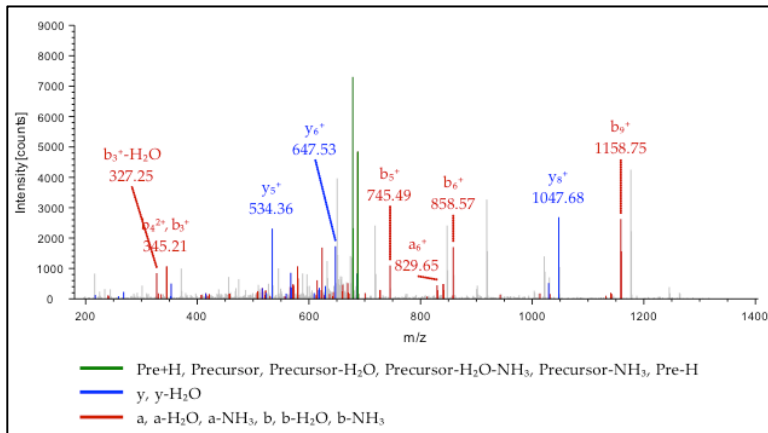
#	a*	a ²⁺	a ³⁺	a ⁴⁺	b*	b ²⁺	b ³⁺	b ⁴⁺	Seq.	y*	y ²⁺	y ³⁺	y ⁴⁺	#
1	30.033	15.52	10.68	8.263	58.028	29.51	20.01	15.26	G					1
	83	055	280	92	75	801	443	264						7
2	129.10	65.05	43.70	33.03	157.09	79.05	53.03	40.02	V	1938.9	969.9	646.9	485.4	1
	225	476	560	102	717	222	724	975		1283	6005	7579	8366	6
3	230.14	115.5	77.38	58.29	258.14	129.5	86.71	65.29	T	1839.8	920.4	613.9	460.7	1
	993	7860	816	294	485	7606	980	167		4441	2584	5299	1656	5
4	331.19	166.1	111.0	83.55	359.19	180.0	120.4	90.55	T	1738.7	869.9	580.2	435.4	1
	761	0244	7072	486	253	9990	0236	359		9673	0200	7043	5464	4
5	430.26	215.6	144.0	108.3	458.26	229.6	153.4	115.3	V	1637.7	819.3	546.5	410.1	1
	603	3665	9353	2197	095	3411	2517	2069		4905	7816	8787	9272	3
6	543.35	272.1	181.7	136.5	571.34	286.1	191.1	143.5	L	1538.6	769.8	513.5	385.4	1
	010	7869	8822	9298	502	7615	1986	9171		8063	4395	6506	2561	2
7	874.39	437.7	292.1	219.3	902.39	451.6	301.4	226.3	T- AziSev	1425.5	713.3	475.8	357.1	1
	557	0142	3671	5435	049	9888	6835	5308		9656	0192	7037	5460	1
8	1005.4	503.2	335.8	252.1	1033.4	517.2	345.1	259.1	M	1094.5	547.7	365.5	274.3	1
	3607	2167	1688	1448	3099	1913	4851	1320		5109	7918	2188	9323	0
9	1106.4	553.7	369.4	277.3	1134.4	567.7	378.8	284.3	T	963.51	482.2	321.8	241.6	9
	8375	4551	9944	7640	7867	4297	3107	7512		059	5893	4171	3310	
1	1207.5	604.2	403.1	302.6	1235.5	618.2	412.5	309.6	T	862.46	431.7	288.1	216.3	8
0	3143	6935	8200	3832	2635	6681	1363	3704		291	3509	5915	7118	
1	1320.6	660.8	440.8	330.9	1348.6	674.8	450.2	337.9	L	761.41	381.2	254.4	191.1	7
	1550	1139	7669	0933	1042	0885	0832	0806		523	1125	7659	0926	
1	1407.6	704.3	469.8	352.6	1435.6	718.3	479.2	359.6	S	648.33	324.6	216.7	162.8	6
2	4753	2740	8736	6734	4245	2486	1900	6607		116	6922	8190	3825	
1	1520.7	760.8	507.5	380.9	1548.7	774.8	516.9	387.9	I	561.29	281.1	187.7	141.0	5
3	3160	6944	8205	3836	2652	6690	1369	3709		913	5320	7123	8024	
1	1607.7	804.3	536.5	402.6	1635.7	818.3	545.9	409.6	S	448.21	224.6	150.0	112.8	4
4	6363	8545	9273	9637	5855	8291	2437	9509		506	1117	7654	0922	
1	1678.8	839.9	560.2	420.4	1706.7	853.9	569.6	427.4	A	361.18	181.0	121.0	91.05	3
5	0075	0401	7177	5565	9567	0147	0341	5437		303	9515	6586	121	
1	1834.9	917.9	612.3	459.4	1862.8	931.9	621.6	466.4	R	290.14	145.5	97.38	73.29	2
6	0187	5457	0548	8093	9679	5203	3711	7965		591	7659	682	193	
1									N- Deamidated	134.04	67.52	45.35	34.26	1
7										479	603	311	665	

**β₃ GABA_A receptor subunit
273-A*ARVALGITTVL-284**



# 1	a ⁺	a ²⁺	a ³⁺	b ⁺	b ²⁺	b ³⁺	Seq.	y ⁺	y ²⁺	y ³⁺	# 2
1	274.0472	137.527	92.0206	302.0421	151.524	101.352	A- AziSev				1
	7	27	1	9	73	25					2
2	345.0843	173.045	115.699	373.0793	187.043	125.031	A	1113.699	557.353	371.904	1
	9	83	65	1	29	29		08	18	54	1
3	501.1855	251.096	167.733	529.1804	265.093	177.064	R	1042.661	521.834	348.225	1
	1	39	36	3	85	99		96	62	50	0
4	600.2539	300.630	200.756	628.2488	314.628	210.087	V	886.5608	443.784	296.191	9
	3	60	16	5	06	80		4	06	80	
5	671.2910	336.149	224.435	699.2859	350.146	233.766	A	787.4924	394.249	263.168	8
	5	16	20	7	62	84		2	85	99	
6	784.3751	392.691	262.129	812.3700	406.688	271.461	L	716.4553	358.731	239.489	7
	2	20	89	4	66	53		0	29	95	
7	841.3965	421.201	281.137	869.3915	435.199	290.468	G	603.3712	302.189	201.795	6
	9	93	05	1	39	69		3	25	26	
8	954.4806	477.743	318.831	982.4755	491.741	328.163	I	546.3497	273.678	182.788	5
	6	97	74	8	43	38		6	52	10	
9	1055.528	528.267	352.514	1083.523	542.265	361.845	T	433.2656	217.136	145.093	4
	34	81	30	26	27	94		9	48	41	
10	1156.576	578.791	386.196	1184.570	592.789	395.528	T	332.2180	166.612	111.410	3
	02	65	86	94	11	50		1	64	85	
11	1255.644	628.325	419.219	1283.639	642.323	428.551	V	231.1703	116.088	77.7282	2
	44	86	67	36	32	30		3	80	9	
12							L	132.1019	66.5545	44.7054	1
								1	9	9	

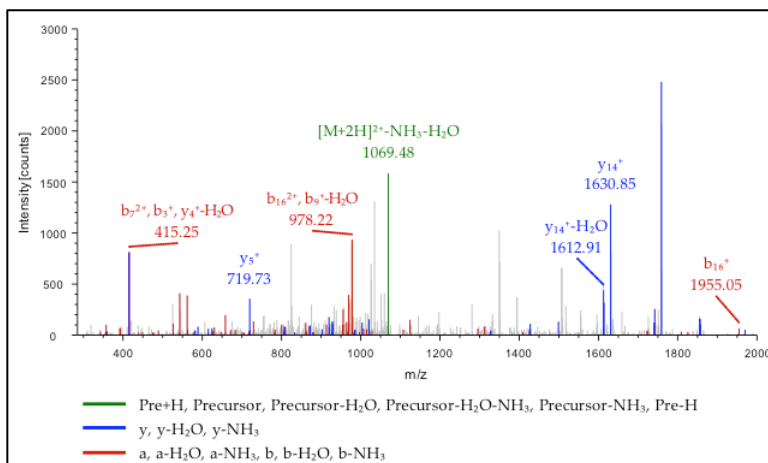
**γ₂L-L3-1D4 GABA_A receptor subunit
304-RTSL*GITTVLT-314**



#1	a ⁺	a ²⁺	b ⁺	b ²⁺	Seq.	y ⁺	y ²⁺	#2
1	129.11348	65.06038	157.10840	79.05784	R			11

2	230.16116	115.58422	258.15608	129.58168	T	1235.58048	618.29388	10
3	317.19319	159.10023	345.18811	173.09769	S	1134.53280	567.77004	9
4	660.27505	330.64116	688.26997	344.63862	L-AziSev	1047.50077	524.25402	8
5	717.29652	359.15190	745.29144	373.14936	G	704.41891	352.71309	7
6	830.38059	415.69393	858.37551	429.69139	I	647.39744	324.20236	6
7	931.42827	466.21777	959.42319	480.21523	T	534.31337	267.66032	5
8	1032.47595	516.74161	1060.47087	530.73907	T	433.26569	217.13648	4
9	1131.54437	566.27582	1159.53929	580.27328	V	332.21801	166.61264	3
10	1244.62844	622.81786	1272.62336	636.81532	L	233.14959	117.07843	2
11					T	120.06552	60.53640	1

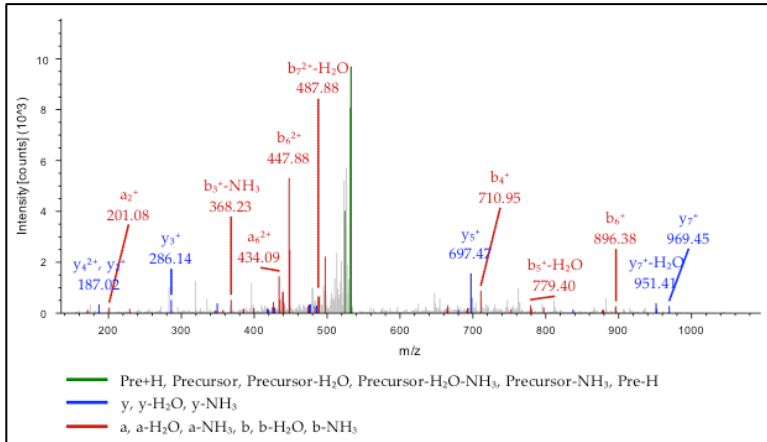
294-WINKDAVPARTSLG*ITTV-312



#1	a*	a2*	b*	b2*	Seq.	y*	y2*	#2
1	159.09168	80.04948	187.08660	94.04694	W			18
2	272.17575	136.59151	300.17067	150.58897	I	1986.97822	993.99275	17
3	387.20270	194.10499	415.19761	208.10244	N-Deamidated	1873.89415	937.45071	16
4	515.29767	258.15247	543.29258	272.14993	K	1758.86720	879.93724	15
5	630.32462	315.66595	658.31953	329.66340	D	1630.77223	815.88975	14
6	701.36174	351.18451	729.35665	365.18196	A	1515.74528	758.37628	13
7	800.43016	400.71872	828.42507	414.71617	V	1444.70816	722.85772	12
8	897.48293	449.24510	925.47784	463.24256	P	1345.63974	673.32351	11
9	968.52005	484.76366	996.51496	498.76112	A	1248.58697	624.79712	10
10	1124.62117	562.81422	1152.61608	576.81168	R	1177.54985	589.27856	9
11	1225.66885	613.33806	1253.66376	627.33552	T	1021.44873	511.22800	8
12	1312.70088	656.85408	1340.69579	670.85153	S	920.40105	460.70416	7
13	1425.78495	713.39611	1453.77986	727.39357	L	833.36902	417.18815	6
14	1712.80421	856.90574	1740.79912	870.90320	G-AziSev	720.28495	360.64611	5
15	1825.88828	913.44778	1853.88319	927.44523	I	433.26569	217.13648	4
16	1926.93596	963.97162	1954.93087	977.96907	T	320.18162	160.59445	3
17	2027.98364	1014.49546	2055.97855	1028.49291	T	219.13394	110.07061	2
18					V	118.08626	59.54677	1

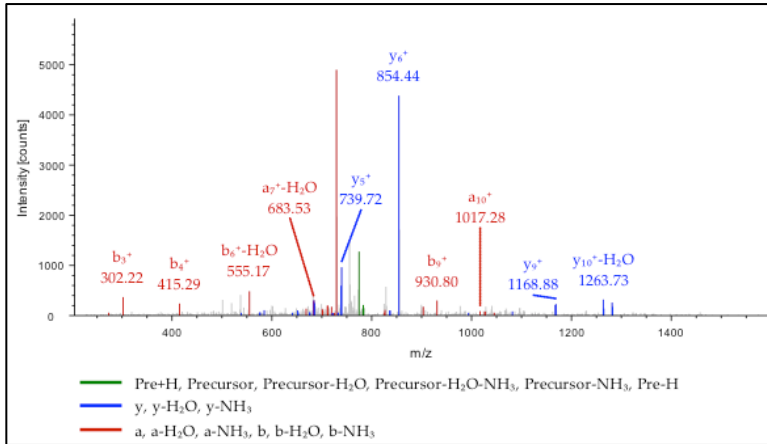
A.4.4. $\alpha_1\beta_3\gamma_{2L}$ GABA_A receptor peptides photoaffinity labeled by aziisoflurane FLAG- α_1 GABA_A receptor subunit

282-LNRE*SVPA-289



#1	a ⁺	a ²⁺	b ⁺	b ²⁺	Seq.	y ⁺	y ²⁺	#2
1	86.09643	43.55185	114.09135	57.54931	L			8
2	201.12338	101.06533	229.11829	115.06278	N-Deamidated	969.35028	485.17878	7
3	357.22450	179.11589	385.21941	193.11334	R	854.32334	427.66531	6
4	682.23853	341.62290	710.23345	355.62036	E-Azilso	698.22222	349.61475	5
5	769.27056	385.13892	797.26548	399.13638	S	373.20818	187.10773	4
6	868.33898	434.67313	896.33390	448.67059	V	286.17615	143.59171	3
7	965.39175	483.19951	993.38667	497.19697	P	187.10773	94.05750	2
8					A	90.05496	45.53112	1

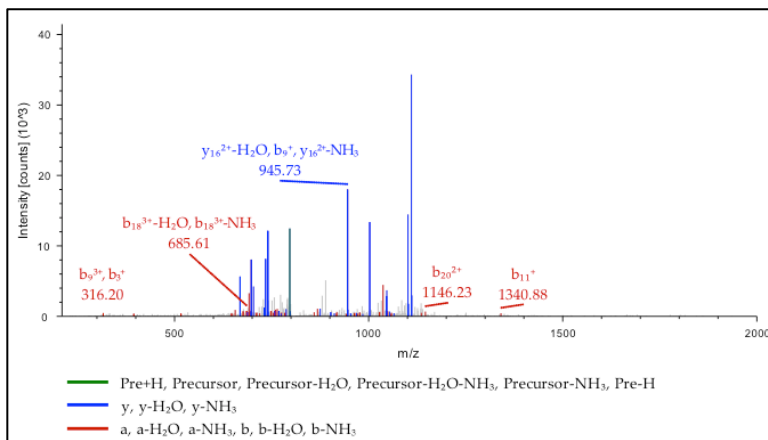
303-TLSISARNSLP*KV-315



#1	a ⁺	a ²⁺	b ⁺	b ²⁺	Seq.	y ⁺	y ²⁺	#2
1	74.06004	37.53366	102.05496	51.53112	T			13
2	187.14411	94.07569	215.13903	108.07315	L	1481.71892	741.36310	12
3	274.17614	137.59171	302.17106	151.58917	S	1368.63485	684.82106	11
4	387.26021	194.13374	415.25513	208.13120	I	1281.60282	641.30505	10
5	474.29224	237.64976	502.28716	251.64722	S	1168.51875	584.76301	9
6	545.32936	273.16832	573.32428	287.16578	A	1081.48672	541.24700	8
7	701.43048	351.21888	729.42540	365.21634	R	1010.44960	505.72844	7
8	816.45743	408.73235	844.45234	422.72981	N-Deamidated	854.34848	427.67788	6
9	903.48946	452.24837	931.48437	466.24582	S	739.32154	370.16441	5

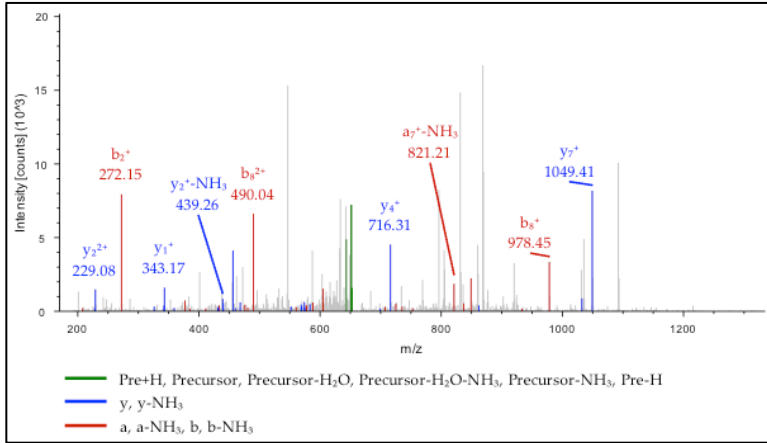
10	1016.57353	508.79040	1044.56844	522.78786	L	652.28951	326.64839	4
11	1309.59773	655.30250	1337.59265	669.29996	P-Azilso	539.20544	270.10636	3
12	1437.69270	719.34999	1465.68762	733.34745	K	246.18123	123.59425	2
13					V	118.08626	59.54677	1

302-TTLLSISARNS*LPKVAYATAMD-222



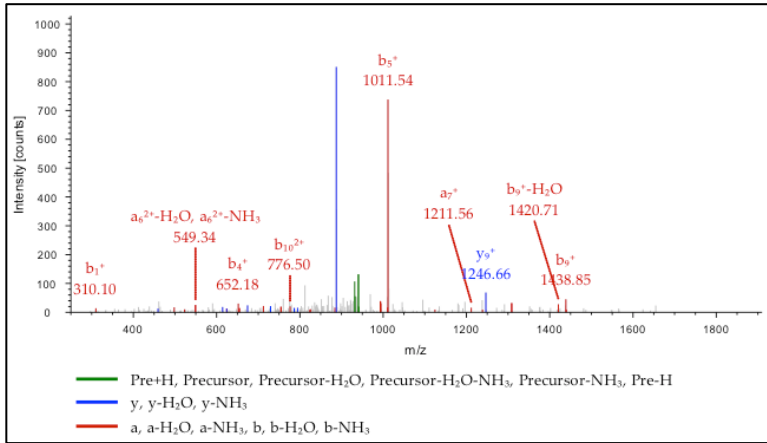
#	a ⁺	a ²⁺	a ³⁺	b ⁺	b ²⁺	b ³⁺	Seq.	y ⁺	y ²⁺	y ³⁺	#
1	74.06004	37.53366	25.35820	102.05496	51.53112	34.68984	T				2
2	175.10772	88.05750	59.04076	203.10264	102.05496	68.37240	T	2322.05133	1161.52930	774.68863	2
3	288.19179	144.59953	96.73545	316.18671	158.59699	106.06709	L	2221.00365	1111.00546	741.00607	1
4	375.22382	188.11555	125.74613	403.21874	202.11301	135.07776	S	2107.91958	1054.46343	703.31138	1
5	488.30789	244.65758	163.44082	516.30281	258.65504	172.77245	I	2020.88755	1010.94741	674.30070	1
6	575.33992	288.17360	192.45149	603.33484	302.17106	201.78313	S	1907.80348	954.40538	636.60601	1
7	646.37704	323.69216	216.13053	674.37196	337.68962	225.46217	A	1820.77145	910.88936	607.59533	1
8	802.47816	401.74272	268.16424	830.47308	415.74018	277.49588	R	1749.73433	875.37080	583.91629	1
9	917.50511	459.25619	306.50655	945.50002	473.25365	315.83819	N-Deamidated	1593.63321	797.32024	531.88259	1
10	1200.50857	600.75792	400.84104	1228.50349	614.75538	410.17268	S-Azilso	1478.60626	739.80677	493.54027	1
11	1313.59264	657.29996	438.53573	1341.58756	671.29742	447.86737	L	1195.60280	598.30504	399.20578	1
12	1410.64541	705.82634	470.88666	1438.6433	719.82380	480.21829	P	1082.51873	541.76300	361.51109	1
13	1538.74038	769.87383	513.58498	1566.73530	783.87129	522.91662	K	985.46596	493.23662	329.16017	9
14	1637.80880	819.40804	546.60779	1665.80372	833.40550	555.93942	V	857.37099	429.18913	286.46185	8
15	1708.84592	854.92660	570.28683	1736.8484	868.92406	579.61846	A	758.30257	379.65492	253.43904	7
16	1871.90924	936.45826	624.64127	1899.90416	950.45572	633.97290	Y	687.26545	344.13636	229.76000	6
17	1942.94636	971.97682	648.32031	1970.94128	985.97428	657.65194	A	524.20213	262.60470	175.40556	5
18	2043.99404	1022.50066	682.00287	2071.98896	1036.49812	691.33450	T	453.16501	227.08614	151.72652	4
19	2115.03116	1058.01922	705.68191	2143.02608	1072.01668	715.01354	A	352.11733	176.56230	118.04396	3
20	2262.06658	1131.53693	754.69371	2290.06149	1145.53438	764.02535	M-Oxidation	281.08021	141.04374	94.36492	2
21							D	134.04479	67.52603	45.35311	1

β_3 GABA_A receptor subunit
241-RNIGYFILQ*-249



#1	a*	a ²⁺	b*	b ²⁺	Seq.	y*	y ²⁺	#2
1	129.11348	65.06038	157.10840	79.05784	R			9
2	244.14043	122.57385	272.13534	136.57131	N-Deamidated	1164.48022	582.74375	8
3	357.22450	179.11589	385.21941	193.11334	I	1049.45328	525.23028	7
4	414.24597	207.62662	442.24088	221.62408	G	936.36921	468.68824	6
5	577.30929	289.15828	605.30420	303.15574	Y	879.34774	440.17751	5
6	724.37771	362.69249	752.37262	376.68995	F	716.28442	358.64585	4
7	837.46178	419.23453	865.45669	433.23198	I	569.21600	285.11164	3
8	950.54585	475.77656	978.54076	489.77402	L	456.13193	228.56960	2
9					Q-Azilso	343.04786	172.02757	1

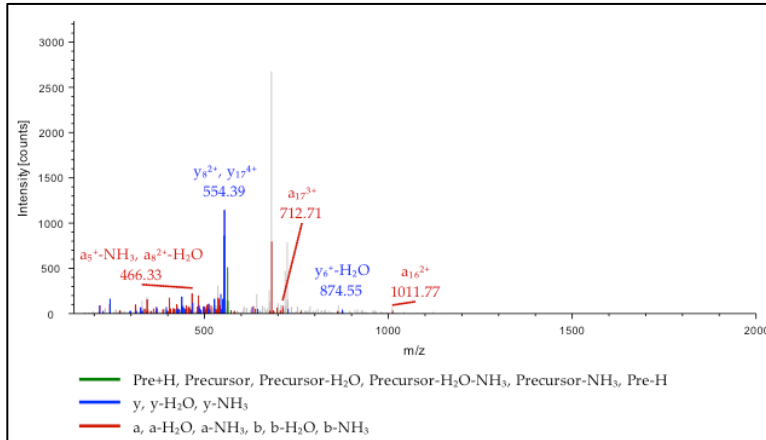
247-I*LQTY*MPSILITI-259



#1	a*	a ²⁺	b*	b ²⁺	Seq.	y*	y ²⁺	#2
1	282.06787	141.53757	310.06278	155.53503	I-Azils			13
2	395.15194	198.07961	423.14685	212.07706	L	1588.75219	794.87973	12
3	523.21052	262.10890	551.20543	276.10635	Q	1475.66812	738.33770	11
4	624.25820	312.63274	652.25311	326.63019	T	1347.60954	674.30841	10
5	983.29295	492.15011	1011.28786	506.14757	Y-Azilso	1246.56186	623.78457	9
6	1114.33345	557.67036	1142.32836	571.66782	M	887.52710	444.26719	8
7	1211.38622	606.19675	1239.38113	620.19421	P	756.48660	378.74694	7

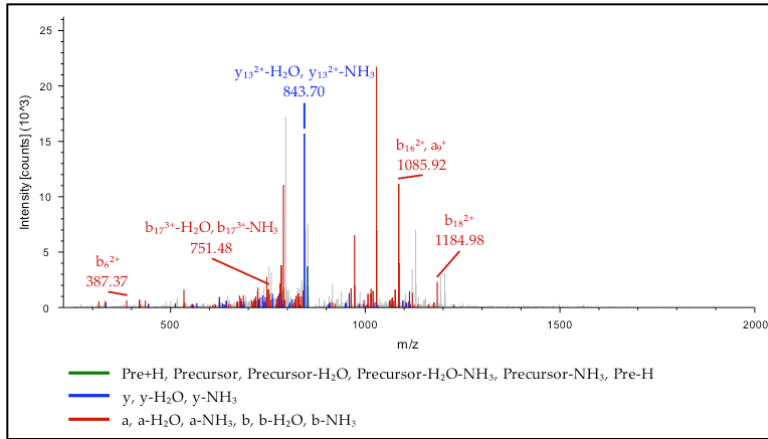
8	1298.41825	649.71276	1326.41316	663.71022	S	659.43383	330.22055	6
9	1411.50232	706.25480	1439.49723	720.25226	I	572.40180	286.70454	5
10	1524.58639	762.79683	1552.58130	776.79429	L	459.31773	230.16250	4
11	1637.67046	819.33887	1665.66537	833.33633	I	346.23366	173.62047	3
12	1738.71814	869.86271	1766.71305	883.86017	T	233.14959	117.07843	2
13					I	132.10191	66.55459	1

274-ARVALGI*TTVLTMTTI*NT-300



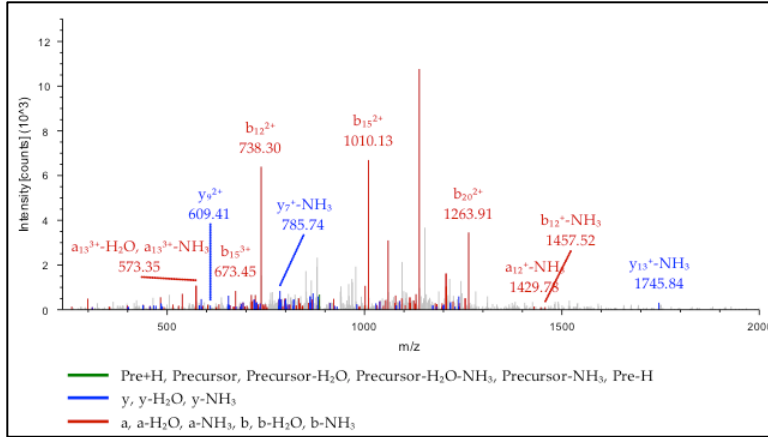
# 1	a ⁺	a ²⁺	a ³⁺	a ⁴⁺	b ⁺	b ²⁺	b ³⁺	b ⁴⁺	Seq.	y ⁺	y ²⁺	y ³⁺	y ⁴⁺	# 2
1	44.049	22.528	15.35	11.76	72.044	36.525	24.68	18.76	A					1
8	48	38	468	783	40	84	632	656						8
2	200.15	100.57	67.38	50.79	228.14	114.57	76.72	57.79	R	2213.9	1107.4	738.6	554.2	1
7	060	894	839	311	552	640	002	184		4198	7463	5218	4095	7
3	299.21	150.11	100.4	75.56	327.21	164.11	109.7	82.55	V	2057.8	1029.4	686.6	515.2	1
6	902	315	1119	021	394	061	4283	894		4086	2407	1847	1567	6
4	370.25	185.63	124.0	93.31	398.25	199.62	133.4	100.3	A	1958.7	979.88	653.5	490.4	1
5	614	171	9023	949	106	917	2187	1822		7244	986	9566	4857	5
5	483.34	242.17	161.7	121.5	511.33	256.17	171.1	128.5	L	1887.7	944.37	629.9	472.6	1
4	021	374	8492	9051	513	120	1656	8924		3532	130	1662	8929	4
6	540.36	270.68	180.7	135.8	568.35	284.68	190.1	142.8	G	1774.6	887.82	592.2	444.4	1
3	168	448	9208	4588	660	194	2372	4461		5125	926	2193	1827	3
7	849.41	425.21	283.8	213.1	877.41	439.20	293.1	220.1	I-Azilso	1717.6	859.31	573.2	430.1	1
2	719	223	1058	0975	210	969	4222	0848		2978	853	1478	6290	2
8	950.46	475.73	317.4	238.3	978.45	489.73	326.8	245.3	T	1408.5	704.79	470.1	352.8	1
1	487	607	9314	7167	978	353	2478	7040		7428	078	9628	9903	1
9	1051.5	526.25	351.1	263.6	1079.5	540.25	360.5	270.6	T	1307.5	654.26	436.5	327.6	1
0	1255	991	7570	3359	0746	737	0734	3232		2660	694	1372	3711	0
1	1150.5	575.79	384.1	288.4	1178.5	589.79	393.5	295.3	V	1206.4	603.74	402.8	302.3	9
0	8097	412	9851	0070	7588	158	3014	9943		7892	310	3116	7519	9
1	1263.6	632.33	421.8	316.6	1291.6	646.33	431.2	323.6	L	1107.4	554.20	369.8	277.6	8
1	6504	616	9320	7172	5995	361	2483	7045		1050	889	0835	0808	8
1	1364.7	682.86	455.5	341.9	1392.7	696.85	464.9	348.9	T	994.32	497.66	332.1	249.3	7
2	1272	000	7576	3364	0763	745	0739	3237		643	685	1366	3706	7
1	1511.7	756.37	504.5	378.6	1539.7	770.37	513.9	385.6	M-Oxidation	893.27	447.14	298.4	224.0	6
3	4813	770	8756	9249	4305	516	1920	9122		875	301	3110	7514	6
1	1612.7	806.90	538.2	403.9	1640.7	820.89	547.6	410.9	T	746.24	373.62	249.4	187.3	5
4	9581	154	7012	5441	9073	900	0176	5314		333	530	1929	1629	5
1	1713.8	857.42	571.9	429.2	1741.8	871.42	581.2	436.2	T	645.19	323.10	215.7	162.0	4
5	4349	538	5268	1633	3841	284	8432	1506		565	146	3673	5437	4
1	2022.8	1011.9	674.9	506.4	2050.8	1025.9	684.3	513.4	I-Azilso	544.14	272.57	182.0	136.7	3
6	9900	5314	7118	8021	9391	5059	0282	7893		797	762	5417	9245	3
1	2137.9	1069.4	713.3	535.2	2165.9	1083.4	722.6	542.2	N-Deamidated	235.09	118.04	79.03	59.52	2
7	2594	6661	1350	3694	2086	6407	4514	3567		247	987	567	857	2
1									T	120.06	60.536	40.69	30.77	1
8										552	40	336	184	1

γ_{2L}-L3-1D4 GABA_A receptor subunit



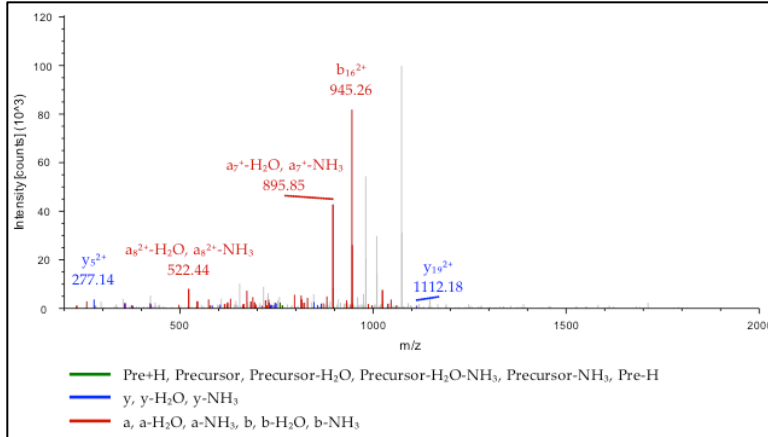
#	a ⁺	a ²⁺	a ³⁺	b ⁺	b ²⁺	b ³⁺	Seq.	y ⁺	y ²⁺	y ³⁺	#
1	129.113 48	65.0603 8	43.7093 5	157.108 40	79.0578 4	53.0409 8	R				2 0
2	276.148 90	138.578 09	92.7211 5	304.143 81	152.575 54	102.052 79	M-Oxidation	2431.11 548	1216.06 138	811.043 35	1 9
3	333.170 37	167.088 82	111.728 31	361.165 28	181.086 28	121.059 94	G	2284.08 007	1142.54 367	762.031 54	1 8
4	496.233 69	248.620 48	166.082 75	524.228 60	262.617 94	175.414 38	Y	2227.05 860	1114.03 294	743.024 38	1 7
5	643.302 11	322.154 69	215.105 55	671.297 02	336.152 15	224.437 19	F	2063.99 528	1032.50 128	688.669 94	1 6
6	744.349 79	372.678 53	248.788 11	772.344 70	386.675 99	258.119 75	T	1916.92 686	958.967 07	639.647 14	1 5
7	857.433 86	429.220 57	286.482 80	885.428 77	443.218 02	295.814 44	I	1815.87 918	908.443 23	605.964 58	1 4
8	985.492 44	493.249 86	329.169 00	1013.48 735	507.247 31	338.500 63	Q	1702.79 511	851.901 19	568.269 89	1 3
9	1086.54 012	543.773 70	362.851 56	1114.53 503	557.771 15	372.183 19	T	1574.73 653	787.871 90	525.583 69	1 2
10	1445.57 487	723.291 07	482.529 81	1473.56 979	737.288 53	491.861 45	Y-Azilso	1473.68 885	737.348 06	491.901 13	1 1
11	1558.65 894	779.833 11	520.224 50	1586.65 386	793.830 57	529.556 14	I	1114.65 410	557.830 69	372.222 88	1 0
12	1655.71 171	828.359 49	552.575 42	1683.70 663	842.356 95	561.907 06	P	1001.57 003	501.288 65	334.528 19	9
13	1815.74 237	908.374 82	605.918 97	1843.73 728	922.372 28	615.250 61	C-Carbamidomet hyl	904.517 26	452.762 27	302.177 27	8
14	1916.79 005	958.898 66	639.601 53	1944.78 496	972.896 12	648.933 17	T	744.486 60	372.746 94	248.833 72	7
15	2029.87 412	1015.44 070	677.296 22	2057.86 903	1029.43 815	686.627 86	L	643.438 92	322.223 10	215.151 16	6
16	2142.95 819	1071.98 273	714.990 91	2170.95 310	1085.98 019	724.322 55	I	530.354 85	265.681 06	177.456 47	5
17	2242.02 661	1121.51 694	748.013 72	2270.02 152	1135.51 440	757.345 36	V	417.270 78	209.139 03	139.761 78	4
18	2341.09 503	1171.05 115	781.036 53	2369.08 994	1185.04 861	790.368 16	V	318.202 36	159.604 82	106.738 97	3
19	2454.17 910	1227.59 319	818.731 22	2482.17 401	1241.59 064	828.062 85	L	219.133 94	110.070 61	73.7161 6	2
20							S	106.049 87	53.5285 7	36.0214 7	1

A.4.5. $\alpha_1\beta_3$ GABA_A receptor peptides photoaffinity labeled by aziseovflurane(**1a**)
FLAG- α_1 GABA_A receptor subunit
 227-SKIWTPDTFFHNG*KKSVAHN-446



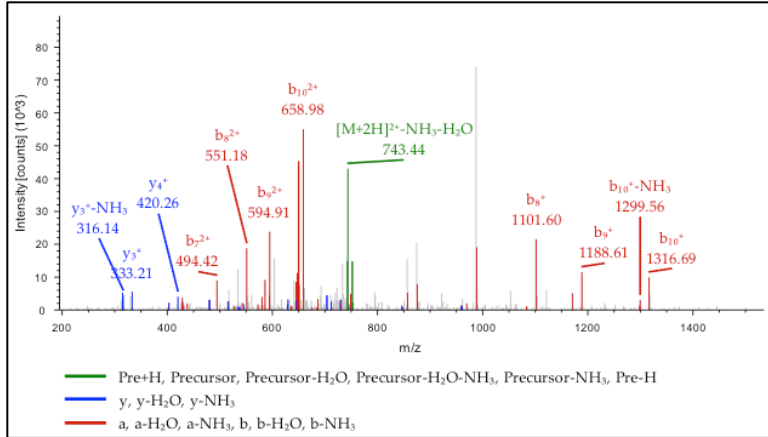
#	a*	a ²⁺	a ³⁺	b*	b ²⁺	b ³⁺	Seq.	y*	y ²⁺	y ³⁺	#
1	60.04439	30.52583	20.68632	88.03931	44.52329	30.01795	S				2
2	188.13936	94.57332	63.38464	216.13428	108.57078	72.71628	K	2604.17399	1302.59063	868.72951	20
3	301.22343	151.11535	101.07933	329.21835	165.11281	110.41097	I	2476.07902	1238.54315	826.03119	19
4	487.30275	244.15501	163.10577	515.29767	258.15247	172.43741	W	2362.99495	1182.00111	788.33650	18
5	588.35043	294.67885	196.78833	616.34535	308.67631	206.11997	T	2176.91563	1088.96145	726.31006	17
6	685.40320	343.20524	229.13925	713.39812	357.20270	238.47089	P	2075.86795	1038.43761	692.62750	16
7	800.43015	400.71871	267.48157	828.42507	414.71617	276.81321	D	1978.81518	989.91123	660.27658	15
8	901.47783	451.24255	301.16413	929.47275	465.24001	310.49577	T	1863.78823	932.39775	621.93426	14
9	1048.54625	524.77676	350.18694	1076.54117	538.77422	359.51857	F	1762.74055	881.87391	588.25170	13
10	1195.61467	598.31097	399.20974	1223.60959	612.30843	408.54138	F	1615.67213	808.33970	539.22889	12
11	1332.67358	666.84043	444.89605	1360.66850	680.83789	454.22768	H	1468.60371	734.80549	490.20609	11
12	1446.71651	723.86189	482.91036	1474.71143	737.85935	492.24199	N	1331.54480	666.27604	444.51978	10
13	1733.73577	867.37152	578.58344	1761.73069	881.36898	587.91508	G-AziSev	1217.50187	609.25457	406.50547	9
14	1861.83074	931.41901	621.28177	1889.82566	945.41647	630.61340	K	930.48261	465.74494	310.83239	8
15	1989.92571	995.46649	663.98009	2017.92063	1009.46395	673.31173	K	802.38764	401.69746	268.13406	7
16	2076.95774	1038.98251	692.99077	2104.95266	1052.97997	702.32240	S	674.29267	337.64997	225.43574	6
17	2176.02616	1088.51672	726.01357	2204.02108	1102.51418	735.34521	V	587.26064	294.13396	196.42506	5
18	2247.06328	1124.03528	749.69261	2275.05820	1138.03274	759.02425	A	488.19222	244.59975	163.40226	4
19	2384.12219	1192.56473	795.37892	2412.11711	1206.56219	804.71055	H	417.15510	209.08119	139.72322	3
20	2498.16512	1249.58620	833.39323	2526.16004	1263.58366	842.72486	N	280.09619	140.55173	94.03691	2
21							M-Oxidation	166.05326	83.53027	56.02260	1

286-SVP*ARTVFGVTTVLTMTTLLS-305



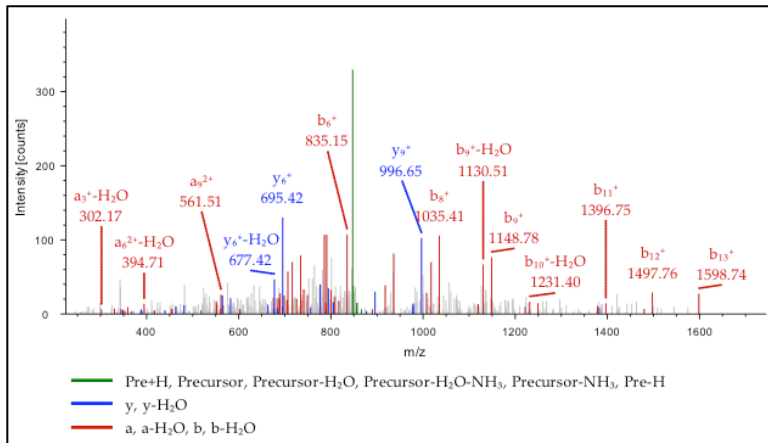
#	a*	a ²⁺	a ³⁺	b*	b ²⁺	b ³⁺	Seq.	y*	y ²⁺	y ³⁺	#
1	60.04439	30.52583	20.6863	88.03931	44.52329	30.0179	S				2
2	159.1128	80.06004	53.7091	187.1077	94.05750	63.0407	V	2224.096	1112.552	742.037	1
3	486.1633	243.5853	162.725	514.1582	257.5827	172.057	P- AziSev	2125.028	1063.017	709.014	1
4	557.2004	279.1038	186.405	585.1954	293.1013	195.736	A	1797.977	899.4926	599.997	1
5	713.3016	357.1544	238.438	741.2965	371.1519	247.770	R	1726.940	863.9740	576.318	1
6	814.3492	407.6782	272.121	842.3442	421.6757	281.452	T	1570.839	785.9235	524.284	1
7	913.4177	457.2124	305.144	941.4126	471.2099	314.475	V	1469.792	735.3996	490.602	1
8	1060.486	530.7467	354.166	1088.481	544.7441	363.498	F	1370.723	685.8654	457.579	1
9	1117.507	559.2574	373.174	1145.502	573.2549	382.505	G	1223.655	612.3312	408.556	1
10	1216.576	608.7916	406.196	1244.570	622.7891	415.528	V	1166.633	583.8205	389.549	1
11	1317.623	659.3154	439.879	1345.618	673.3129	449.211	T	1067.565	534.2863	356.526	1
12	1418.671	709.8393	473.561	1446.666	723.8367	482.893	T	966.5176	483.7624	322.844	9
13	1517.739	759.3735	506.584	1545.734	773.3710	515.916	V	865.4699	433.2386	289.161	8
14	1630.823	815.9155	544.279	1658.818	829.9130	553.611	L	766.4015	383.7044	256.138	7
15	1731.871	866.4394	577.962	1759.866	880.4368	587.293	T	653.3174	327.1623	218.444	6
16	1862.912	931.9596	621.642	1890.906	945.9571	630.973	M	552.2698	276.6385	184.761	5
17	1963.959	982.4835	655.324	1991.954	996.4809	664.656	T	421.2293	211.1182	141.081	4
18	2065.007	1033.007	689.007	2093.002	1047.004	698.338	T	320.1816	160.5944	107.398	3
19	2178.091	1089.549	726.702	2206.086	1103.546	736.033	L	219.1339	110.0706	73.7161	2
20							S	106.0498	53.52857	36.0214	1

268-PC*IMTVILSQVS-279



#1	a*	a ²⁺	b*	b ²⁺	Seq.	y*	y ²⁺	#2
1	70.06513	35.53620	98.06005	49.53366	P			12
2	403.07211	202.03969	431.06703	216.03715	C-AziSev	1423.62469	712.31598	11
3	516.15618	258.58173	544.15110	272.57919	I	1090.61771	545.81249	10
4	647.19668	324.10198	675.19160	338.09944	M	977.53364	489.27046	9
5	748.24436	374.62582	776.23928	388.62328	T	846.49314	423.75021	8
6	847.31278	424.16003	875.30770	438.15749	V	745.44546	373.22637	7
7	960.39685	480.70206	988.39177	494.69952	I	646.37704	323.69216	6
8	1073.48092	537.24410	1101.47584	551.24156	L	533.29297	267.15012	5
9	1160.51295	580.76011	1188.50787	594.75757	S	420.20890	210.60809	4
10	1288.57153	644.78940	1316.56645	658.78686	Q	333.17687	167.09207	3
11	1387.63995	694.32361	1415.63487	708.32107	V	205.11829	103.06278	2
12					S	106.04987	53.52857	1

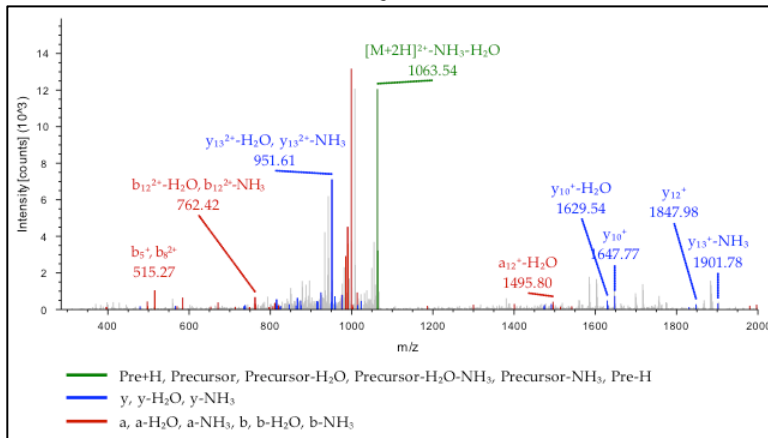
291-TV*FGVTTVLTMTTL-304



#1	a*	a ²⁺	b*	b ²⁺	Seq.	y*	y ²⁺	#2
1	74.06004	37.53366	102.05496	51.53112	T			14
2	403.12625	202.06676	431.12117	216.06422	V-AziSev	1628.75274	814.88001	13
3	550.19467	275.60097	578.18959	289.59843	F	1299.68653	650.34690	12
4	607.21614	304.11171	635.21106	318.10917	G	1152.61811	576.81269	11
5	706.28456	353.64592	734.27948	367.64338	V	1095.59664	548.30196	10
6	807.33224	404.16976	835.32716	418.16722	T	996.52822	498.76775	9

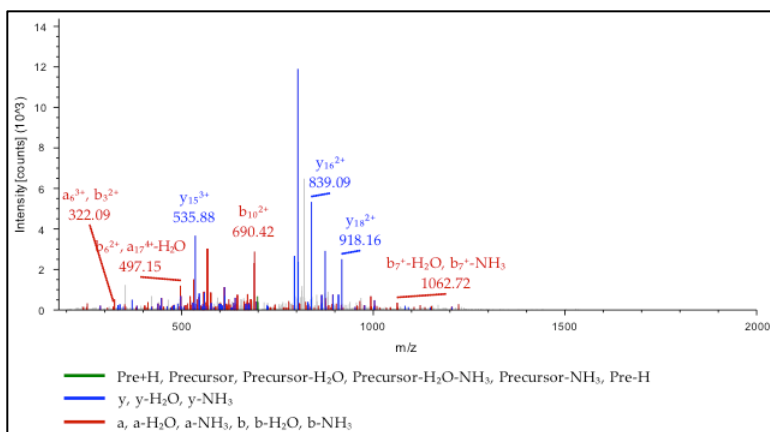
7	908.37992	454.69360	936.37484	468.69106	T	895.48054	448.24391	8
8	1007.44834	504.22781	1035.44326	518.22527	V	794.43286	397.72007	7
9	1120.53241	560.76984	1148.52733	574.76730	L	695.36444	348.18586	6
10	1221.58009	611.29368	1249.57501	625.29114	T	582.28037	291.64382	5
11	1368.61551	684.81139	1396.61042	698.80885	M-Oxidation	481.23269	241.11998	4
12	1469.66319	735.33523	1497.65810	749.33269	T	334.19727	167.60227	3
13	1570.71087	785.85907	1598.70578	799.85653	T	233.14959	117.07843	2
14					L	132.10191	66.55459	1

β_3 GABA_A receptor subunit
197-DKAVTGVE*RIELP*QF-211



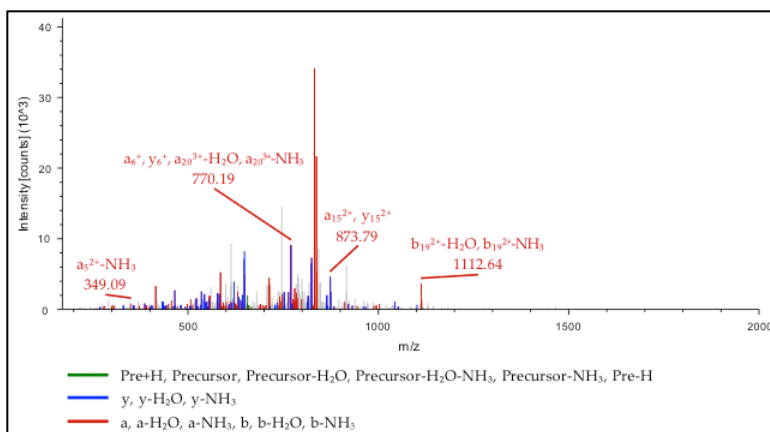
#1	a ⁺	a ²⁺	b ⁺	b ²⁺	Seq.	y ⁺	y ²⁺	#2
1	88.03931	44.52329	116.03423	58.52075	D			15
2	216.13428	108.57078	244.12920	122.56824	K	2046.88573	1023.94650	14
3	287.17140	144.08934	315.16632	158.08680	A	1918.79076	959.89902	13
4	386.23982	193.62355	414.23474	207.62101	V	1847.75364	924.38046	12
5	487.28750	244.14739	515.28242	258.14485	T	1748.68522	874.84625	11
6	544.30897	272.65812	572.30389	286.65558	G	1647.63754	824.32241	10
7	643.37739	322.19233	671.37231	336.18979	V	1590.61607	795.81167	9
8	1002.41778	501.71253	1030.41270	515.70999	E-AziSev	1491.54765	746.27746	8
9	1158.51890	579.76309	1186.51382	593.76055	R	1132.50726	566.75727	7
10	1271.60297	636.30512	1299.59789	650.30258	I	976.40614	488.70671	6
11	1400.64557	700.82642	1428.64049	714.82388	E	863.32207	432.16467	5
12	1513.72964	757.36846	1541.72456	771.36592	L	734.27947	367.64337	4
13	1840.78020	920.89374	1868.77512	934.89120	P-AziSev	621.19540	311.10134	3
14	1968.83878	984.92303	1996.83370	998.92049	Q	294.14484	147.57606	2
15					F	166.08626	83.54677	1

266-W*INYDASAARVALGITTTLMTTI-289



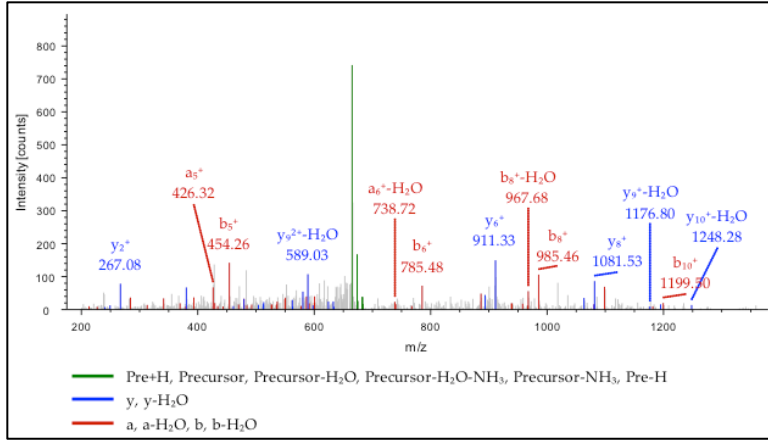
# 1	a ⁺	a ²⁺	a ³⁺	a ⁴⁺	b ⁺	b ²⁺	b ³⁺	b ⁴⁺	Seq.	y ⁺	y ²⁺	y ³⁺	y ⁴⁺	# 2
1	389.08 947	195.04 837	130.3 6801	98.02 783	417.08 439	209.04 583	139.6 9965	105.0 2655	W- AziSev					2 4
2	502.17 354	251.59 041	168.0 6270	126.2 9884	530.16 846	265.58 787	177.3 9434	133.2 9757	I	2411.2 8515	1206.1 4621	804.4 3323	603.5 7674	2 3
3	616.21 647	308.61 187	206.0 7701	154.8 0958	644.21 139	322.60 933	215.4 0865	161.8 0830	N	2298.2 0108	1149.6 0418	766.7 3854	575.3 0573	2 2
4	779.27 979	390.14 353	260.4 3145	195.5 7541	807.27 471	404.14 099	269.7 6309	202.5 7413	Y	2184.1 5815	1092.5 8271	728.7 2423	546.7 9499	2 1
5	894.30 674	447.65 701	298.7 7377	224.3 3214	922.30 166	461.65 447	308.1 0540	231.3 3087	D	2021.0 9483	1011.0 5105	674.3 6979	506.0 2916	2 0
6	965.34 386	483.17 557	322.4 5281	242.0 9142	993.33 878	497.17 303	331.7 8444	249.0 9015	A	1906.0 6788	953.53 758	636.0 2748	477.2 7243	1 9
7	1052.3 7589	526.69 158	351.4 6348	263.8 4943	1080.3 7081	540.68 904	360.7 9512	270.8 4816	S	1835.0 3076	918.01 902	612.3 4844	459.5 1315	1 8
8	1123.4 1301	562.21 014	375.1 4252	281.6 0871	1151.4 0793	576.20 760	384.4 7416	288.6 0744	A	1747.9 9873	874.50 300	583.3 3776	437.7 5514	1 7
9	1194.4 5013	597.72 870	398.8 2156	299.3 6799	1222.4 4505	611.72 616	408.1 5320	306.3 6672	A	1676.9 6161	838.98 444	559.6 5872	419.9 9586	1 6
10	1350.5 5125	675.77 926	450.8 5527	338.3 9327	1378.5 4617	689.77 672	460.1 8691	345.3 9200	R	1605.9 2449	803.46 588	535.9 7968	402.2 3658	1 5
11	1449.6 1967	725.31 347	483.8 7808	363.1 6038	1477.6 1459	739.31 093	493.2 0971	370.1 5910	V	1449.8 2337	725.41 532	483.9 4597	363.2 1130	1 4
12	1520.6 5679	760.83 203	507.5 5712	380.9 1966	1548.6 5171	774.82 949	516.8 8875	387.9 1838	A	1350.7 5495	675.88 111	450.9 2317	338.4 4419	1 3
13	1633.7 4086	817.37 407	545.2 5181	409.1 9067	1661.7 3578	831.37 153	554.5 8344	416.1 8940	L	1279.7 1783	640.36 255	427.2 4413	320.6 8491	1 2
14	1690.7 6233	845.88 480	564.2 5896	423.4 4604	1718.7 5725	859.88 226	573.5 9060	430.4 4477	G	1166.6 3376	583.82 052	389.5 4944	292.4 1390	1 1
15	1803.8 4640	902.42 684	601.9 5365	451.7 1706	1831.8 4132	916.42 430	611.2 8529	458.7 1579	I	1109.6 1229	555.30 978	370.5 4228	278.1 5853	1 0
16	1904.8 9408	952.95 068	635.6 3621	476.9 7898	1932.8 8900	966.94 814	644.9 6785	483.9 7771	T	996.52 822	498.76 775	332.8 4759	249.8 8751	9
17	2005.9 4176	1003.4 7452	669.3 1877	502.2 4090	2033.9 3668	1017.4 7198	678.6 5041	509.2 3963	T	895.48 054	448.24 391	299.1 6503	224.6 2559	8
18	2105.0 1018	1053.0 0873	702.3 4158	527.0 0800	2133.0 0510	1067.0 0619	711.6 7322	534.0 0673	V	794.43 286	397.72 007	265.4 8247	199.3 6367	7
19	2218.0 9425	1109.5 5076	740.0 3627	555.2 7902	2246.0 8917	1123.5 4822	749.3 6791	562.2 7775	L	695.36 444	348.18 586	232.4 5966	174.5 9657	6
20	2319.1 4193	1160.0 7460	773.7 1883	580.5 4094	2347.1 3685	1174.0 7206	783.0 5047	587.5 3967	T	582.28 037	291.64 382	194.7 6497	146.3 2555	5
21	2466.1 7735	1233.5 9231	822.7 3063	617.2 9979	2494.1 7226	1247.5 8977	832.0 6227	624.2 9852	M- Oxidati on	481.23 269	241.11 998	161.0 8241	121.0 6363	4
22	2567.2 2503	1284.1 1615	856.4 1319	642.5 6171	2595.2 1994	1298.1 1361	865.7 4483	649.5 6044	T	334.19 727	167.60 227	112.0 7061	84.30 478	3
23	2668.2 7271	1334.6 3999	890.0 9575	667.8 2363	2696.2 6762	1348.6 3745	899.4 2739	674.8 2236	T	233.14 959	117.07 843	78.38 805	59.04 286	2
24									I	132.10 191	66.554 59	44.70 549	33.78 094	1

274-A*RVALGITTVLTMTTINTHLRE-265



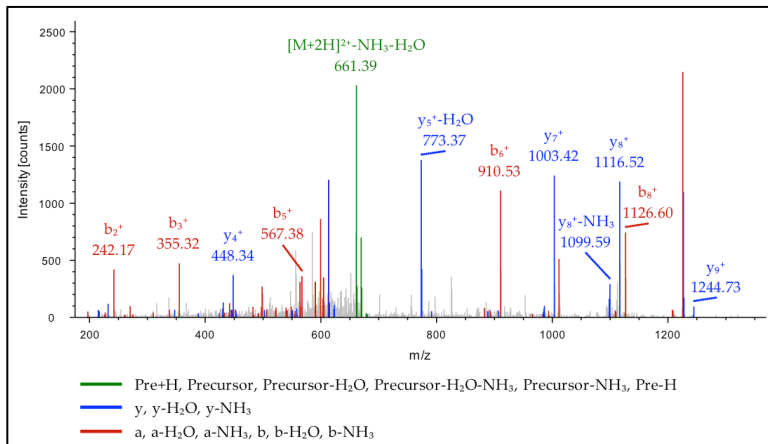
# 1	a ⁺	a ²⁺	a ³⁺	a ⁴⁺	b ⁺	b ²⁺	b ³⁺	b ⁴⁺	Seq.	y ⁺	y ²⁺	y ³⁺	y ⁴⁺	# 2
1	274.04	137.52	92.02	69.26	302.04	151.52	101.3	76.26	A-					2
	727	727	061	728	219	473	5225	600	AziSev					2
2	430.14	215.57	144.0	108.2	458.14	229.57	153.3	115.2	R	2357.2	1179.1	786.4	590.0	2
	839	783	5432	9256	331	529	8595	9128		8581	4654	3346	7691	1
3	529.21	265.11	177.0	133.0	557.21	279.10	186.4	140.0	V	2201.1	1101.0	734.3	551.0	2
	681	204	7712	5966	173	950	0876	5839		8469	9598	9975	5163	0
4	600.25	300.63	200.7	150.8	628.24	314.62	210.0	157.8	A	2102.1	1051.5	701.3	526.2	1
	393	060	5616	1894	885	806	8780	1767		1627	6177	7694	8453	9
5	713.33	357.17	238.4	179.0	741.33	371.17	247.7	186.0	L	2031.0	1016.0	677.6	508.5	1
	800	264	5085	8996	292	010	8249	8869		7915	4321	9790	2525	8
6	770.35	385.68	257.4	193.3	798.35	399.68	266.7	200.3	G	1917.9	959.50	640.0	480.2	1
	947	337	5801	4533	439	083	8965	4405		9508	118	0321	5423	7
7	883.44	442.22	295.1	221.6	911.43	456.22	304.4	228.6	I	1860.9	930.99	620.9	465.9	1
	354	541	5270	1634	846	287	8434	1507		7361	044	9606	9886	6
8	984.49	492.74	328.8	246.8	1012.4	506.74	338.1	253.8	T	1747.8	874.44	583.3	437.7	1
	122	925	3526	7826	8614	671	6690	7699		8954	841	0137	2784	5
9	1085.5	543.27	362.5	272.1	1113.5	557.27	371.8	279.1	T	1646.8	823.92	549.6	412.4	1
	3890	309	1782	4018	3382	055	4946	3891		4186	457	1881	6592	4
1	1184.6	592.80	395.5	296.9	1212.6	606.80	404.8	303.9	V	1545.7	773.40	515.9	387.2	1
0	0732	730	4063	0729	0224	476	7226	0602		9418	073	3625	0400	3
1	1297.6	649.34	433.2	325.1	1325.6	663.34	442.5	332.1	L	1446.7	723.86	482.9	362.4	1
1	9139	933	3532	7831	8631	679	6695	7703		2576	652	1344	3690	2
1	1398.7	699.87	466.9	350.4	1426.7	713.87	476.2	357.4	T	1333.6	667.32	445.2	334.1	1
2	3907	317	1788	4023	3399	063	4951	3895		4169	448	1875	6588	1
1	1545.7	773.39	515.9	387.1	1573.7	787.38	525.2	394.1	M-	1232.5	616.80	411.5	308.9	1
3	7449	088	2968	9908	6940	834	6132	9781	Oxidation	9401	064	3619	0396	0
1	1646.8	823.91	549.6	412.4	1674.8	837.91	558.9	419.4	T	1085.5	543.28	362.5	272.1	9
4	2217	472	1224	6100	1708	218	4388	5973		5860	294	2438	4511	
1	1747.8	874.43	583.2	437.7	1775.8	888.43	592.6	444.7	T	984.51	492.75	328.8	246.8	8
5	6985	856	9480	2292	6476	602	2644	2165		092	910	4182	8319	
1	1860.9	930.98	620.9	465.9	1888.9	944.97	630.3	472.9	I	883.46	442.23	295.1	221.6	7
6	5392	060	8949	9394	4883	805	2113	9267		324	526	5926	2127	
1	1975.9	988.49	659.3	494.7	2003.9	1002.4	668.6	501.7	N-	770.37	385.69	257.4	193.3	6
7	8086	407	3181	5067	7578	9153	6344	4940	Deamidated	917	322	6457	5025	
1	2077.0	1039.0	693.0	520.0	2105.0	1053.0	702.3	527.0	T	655.35	328.17	219.1	164.5	5
8	2854	1791	1437	1259	2346	1537	4600	1132		222	975	2226	9351	
1	2214.0	1107.5	738.7	554.2	2242.0	1121.5	748.0	561.2	H	554.30	277.65	185.4	139.3	4
9	8745	4736	0067	7732	8237	4482	3231	7605		454	591	3970	3159	
2	2327.1	1164.0	776.3	582.5	2355.1	1178.0	785.7	589.5	L	417.24	209.12	139.7	105.0	3
0	7152	8940	9536	4834	6644	8686	2700	4707		563	645	5339	6687	
2	2483.2	1242.1	828.4	621.5	2511.2	1256.1	837.7	628.5	R	304.16	152.58	102.0	76.79	2
1	7264	3996	2907	7362	6756	3742	6070	7235		156	442	5870	585	
2									E	148.06	74.533	50.02	37.77	1
2										044	86	500	057	

275-VALGIT*TVLTM-286



#1	a ⁺	a ²⁺	b ⁺	b ²⁺	Seq.	y ⁺	y ²⁺	#2
1	72.08078	36.54403	100.07570	50.54149	V			11
2	143.11790	72.06259	171.11282	86.06005	A	1265.57331	633.29029	10
3	256.20197	128.60462	284.19689	142.60208	L	1194.53619	597.77173	9
4	313.22344	157.11536	341.21836	171.11282	G	1081.45212	541.22970	8
5	426.30751	213.65739	454.30243	227.65485	I	1024.43065	512.71896	7
6	757.35298	379.18013	785.34790	393.17759	T-AziSev	911.34658	456.17693	6
7	858.40066	429.70397	886.39558	443.70143	T	580.30111	290.65419	5
8	957.46908	479.23818	985.46400	493.23564	V	479.25343	240.13035	4
9	1070.55315	535.78021	1098.54807	549.77767	L	380.18501	190.59614	3
10	1171.60083	586.30405	1199.59575	600.30151	T	267.10094	134.05411	2
11					M-Oxidation	166.05326	83.53027	1

337-IKIPDL*TDVN-446



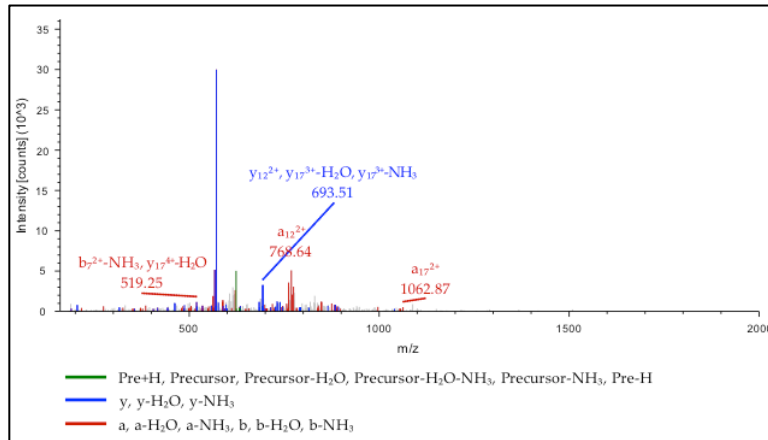
#1	a ⁺	a ²⁺	b ⁺	b ²⁺	Seq.	y ⁺	y ²⁺	#2
1	86.09643	43.55185	114.09135	57.54931	I			10
2	214.19140	107.59934	242.18632	121.59680	K	1244.54444	622.77586	9
3	327.27547	164.14137	355.27039	178.13883	I	1116.44947	558.72837	8
4	424.32824	212.66776	452.32316	226.66522	P	1003.36540	502.18634	7
5	539.35519	270.18123	567.35011	284.17869	D	906.31263	453.65995	6
6	882.43705	441.72216	910.43197	455.71962	L-AziSev	791.28568	396.14648	5
7	983.48473	492.24600	1011.47965	506.24346	T	448.20382	224.60555	4

8	1098.51168	549.75948	1126.50660	563.75694	D	347.15614	174.08171	3
9	1197.58010	599.29369	1225.57502	613.29115	V	232.12919	116.56823	2
10					N	133.06077	67.03402	1

A.4.6. $\alpha_1\beta_3$ GABA_A receptor peptides photoaffinity labeled by aziisoflurane

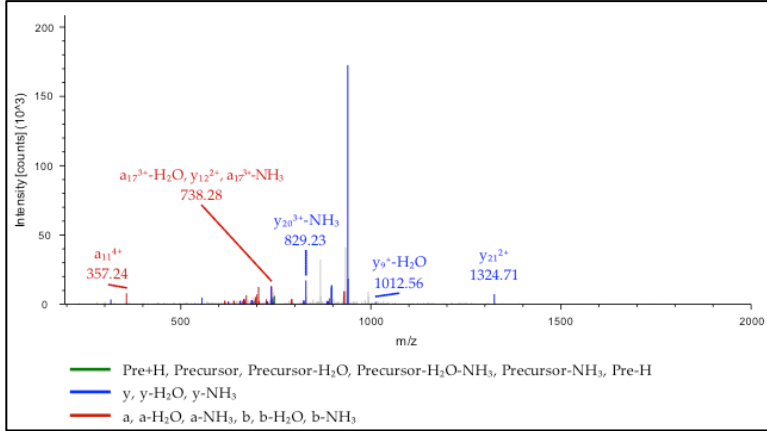
FLAG- α_1 GABA_A receptor subunit

135-FFHN*GKKSVAHNMTMPNKL-154



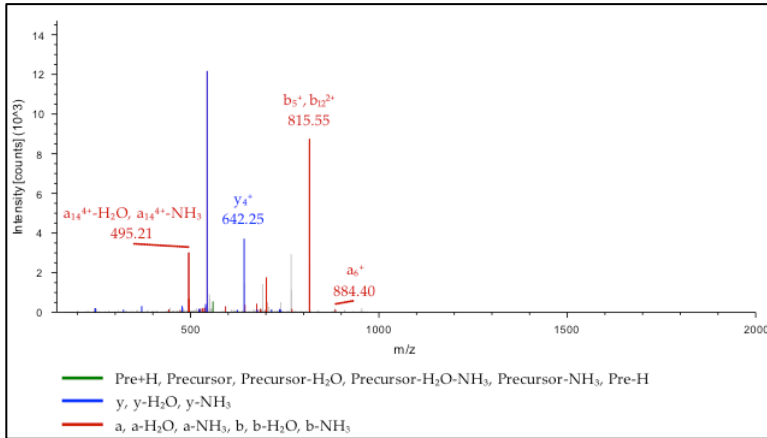
#	a*	a ²⁺	a ³⁺	a ⁴⁺	b*	b ²⁺	b ³⁺	b ⁴⁺	Seq.	y*	y ²⁺	y ³⁺	y ⁴⁺	#
1	120.08	60.544	40.69	30.77	148.07	74.541	50.03	37.77	F					2
	078	03	845	565	570	49	008	438						0
2	267.14	134.07	89.72	67.54	295.14	148.07	99.05	74.54	F	2379.0	1190.0	793.7	595.5	1
	920	824	125	276	412	570	289	149		9276	5002	0244	2865	9
3	404.20	202.60	135.4	101.8	432.20	216.60	144.7	108.8	H	2232.0	1116.5	744.6	558.7	1
	811	769	0756	0749	303	515	3919	0621		2434	1581	7963	6154	8
4	714.22	357.61	238.7	179.3	742.21	371.61	248.0	186.3	N- Azilso	2094.9	1047.9	698.9	524.4	1
	248	488	4568	1108	739	233	7731	0981	G	6543	8635	9333	9682	7
5	771.24	386.12	257.7	193.5	799.23	400.12	267.0	200.5		1784.9	892.97	595.6	446.9	1
	395	561	5283	6644	886	307	8447	6517		5107	917	5521	9322	6
6	899.33	450.17	300.4	225.5	927.33	464.17	309.7	232.5	K	1727.9	864.46	576.6	432.7	1
	892	310	5116	9019	383	055	8279	8892		2960	844	4805	3786	5
7	1027.4	514.22	343.1	257.6	1055.4	528.21	352.4	264.6	K	1599.8	800.42	533.9	400.7	1
	3389	058	4948	1393	2880	804	8112	1266		3463	095	4973	1411	4
8	1114.4	557.73	372.1	279.3	1142.4	571.73	381.4	286.3	S	1471.7	736.37	491.2	368.6	1
	6592	660	6016	7194	6083	405	9179	7067		3966	347	5140	9037	3
9	1213.5	607.27	405.1	304.1	1241.5	621.26	414.5	311.1	V	1384.7	692.85	462.2	346.9	1
	3434	081	8296	3904	2925	826	1460	3777		0763	745	4073	3236	2
1	1284.5	642.78	428.8	321.8	1312.5	656.78	438.1	328.8	A	1285.6	643.32	429.2	322.1	1
	0	7146	937	6200	9832	6637	9364	9705		3921	324	1792	6526	1
1	1421.6	711.31	474.5	356.1	1449.6	725.31	483.8	363.1	H	1214.6	607.80	405.5	304.4	1
	1	3037	882	4831	2528	628	7994	6178		0209	468	3888	0598	0
1	1535.6	768.34	512.5	384.6	1563.6	782.33	521.8	391.6	N	1077.5	539.27	359.8	270.1	9
	2	7330	029	6262	7378	6821	774	9425		4318	523	5258	4125	
1	1666.7	833.86	556.2	417.4	1694.7	847.85	565.5	424.4	M	963.50	482.25	321.8	241.6	8
	3	1380	054	4278	3391	0871	799	7442		025	376	3827	3052	
1	1767.7	884.38	589.9	442.6	1795.7	898.38	599.2	449.6	T	832.45	416.73	278.1	208.8	7
	4	6148	438	2534	9583	5639	183	5698		975	351	5810	7039	
1	1914.7	957.90	638.9	479.4	1942.7	971.89	648.2	486.4	M- Oxidati on	731.41	366.20	244.4	183.6	6
	5	9689	208	3715	5468	9181	954	6879		207	967	7554	0847	
1	2011.8	1006.4	671.2	503.7	2039.8	1020.4	680.6	510.7	P	584.37	292.69	195.4	146.8	5
	6	4966	2847	8807	1787	4458	2593	1971		665	196	6373	4962	
1	2125.8	1063.4	709.3	532.2	2153.8	1077.4	718.6	539.2	N	487.32	244.16	163.1	122.5	4
	7	9259	4993	0238	2861	8751	4739	3402		388	558	1281	8643	
1	2253.9	1127.4	752.0	564.2	2281.9	1141.4	761.3	571.2	K	373.28	187.14	125.0	94.07	3
	8	8756	9742	0070	5235	8248	9488	3234		095	411	9850	570	
1	2367.0	1184.0	789.6	592.5	2395.0	1198.0	799.0	599.5	L	245.18	123.09	82.40	62.05	2
	9	7163	3945	9539	2337	6655	3691	2703		598	663	018	195	
2									L	132.10	66.554	44.70	33.78	1
	0									191	59	549	094	

268-PCIMTVI*LSQVSFWLNRESVPART-301



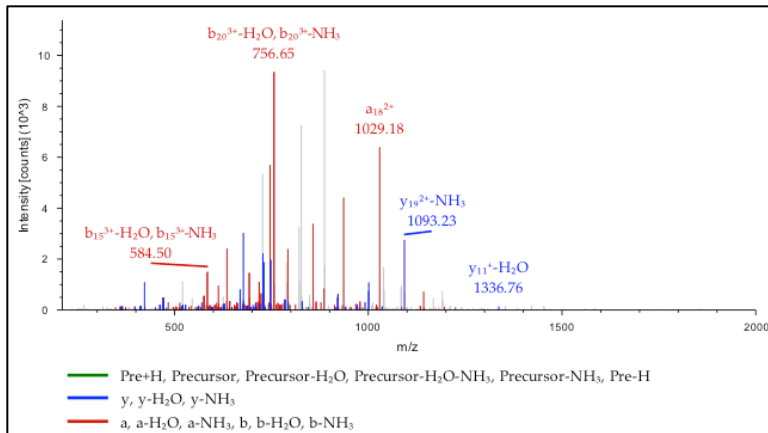
#	a ⁺	a ²⁺	a ³⁺	a ⁴⁺	b ⁺	b ²⁺	b ³⁺	b ⁴⁺	Seq.	y ⁺	y ²⁺	y ³⁺	y ⁴⁺	#
1	70.06	35.53	24.02	18.27	98.06	49.53	33.35	25.27	P					2
	513	620	656	174	005	366	820	047						4
2	230.0	115.5	77.37	58.27	258.0	129.5	86.70	65.27	C- Carbamido methyl	2921. 34035	1461. 17381	974.4 5163	731.0 9054	2 3
	9579	5153	011	940	9070	4899	175	813						
3	343.1	172.0	115.0	86.55	371.1	186.0	124.3	93.54	I	2761. 30969	1381. 15848	921.1 0808	691.0 8288	2 2
	7986	9357	6480	042	7477	9102	9644	915						
4	490.2	245.6	164.0	123.3	518.2	259.6	173.4	130.3	M- Oxidation	2648. 22562	1324. 61645	883.4 1339	662.8 1186	2 1
	1527	1127	7661	0928	1019	0873	0825	0800						
5	591.2	296.1	197.7	148.5	619.2	310.1	207.0	155.5	T	2501. 19021	1251. 09874	834.4 0159	626.0 5301	2 0
	6295	3511	5917	7120	5787	3257	9081	6992						
6	690.3	345.6	230.7	173.3	718.3	359.6	240.1	180.3	V	2400. 14253	1200. 57490	800.7 1903	600.7 9109	1 9
	3137	6932	8197	3830	2629	6678	1361	3703						
7	999.3	500.1	333.8	250.6	1027.	514.1	343.1	257.6	I-Azilso	2301. 07411	1151. 04069	767.6 9622	576.0 2398	1 8
	8688	9708	0048	0218	38179	9453	3211	0090						
8	1112.	556.7	371.4	278.8	1140.	570.7	380.8	285.8	L	1992. 01860	996.5 1294	664.6 7772	498.7 6011	1 7
	47095	3911	9517	7319	46586	3657	2680	7192						
9	1199.	600.2	400.5	300.6	1227.	614.2	409.8	307.6	S	1878. 93453	939.9 7090	626.9 8303	470.4 8909	1 6
	50298	5513	0584	3120	49789	5258	3748	2993						
1	1328.	664.7	443.5	332.8	1356.	678.7	452.8	339.8	Q- Deamidate d	1791. 90250	896.4 5489	597.9 7235	448.7 3108	1 5
0	54557	7642	2004	9185	54049	7388	5168	9058						
1	1427.	714.3	476.5	357.6	1455.	728.3	485.8	364.6	V	1662. 85991	831.9 3359	554.9 5815	416.4 7043	1 4
1	61399	1063	4285	5896	60891	0809	7449	5768						
1	1514.	757.8	505.5	379.4	1542.	771.8	514.8	386.4	S	1563. 79149	782.3 9938	521.9 3535	391.7 0333	1 3
2	64602	2665	5352	1696	64094	2411	8516	1569						
1	1661.	831.3	554.5	416.1	1689.	845.3	563.9	423.1	F	1476. 75946	738.8 8337	492.9 2467	369.9 4532	1 2
3	71444	6086	7633	8407	70936	5832	0797	8280						
1	1847.	924.4	616.6	462.7	1875.	938.3	625.9	469.7	W	1329. 69104	665.3 4916	443.9 0186	333.1 7822	1 1
4	79376	0052	0277	0390	78868	9798	3441	0263						
1	1960.	980.9	654.2	490.9	1988.	994.9	663.6	497.9	L	1143. 61172	572.3 0950	381.8 7542	286.6 5839	1 0
5	87783	4255	9746	7492	87275	4001	2910	7364						
1	2075.	1038.	692.6	519.7	2103.	1052.	701.9	526.7	N- Deamidate d	1030. 52765	515.7 6746	344.1 8073	258.3 8737	9
6	90478	45603	3978	3165	89969	45348	7141	3038						
1	2232.	1116.	744.6	558.7	2260.	1130.	754.0	565.7	R	915.5 0070	458.2 5399	305.8 3842	229.6 3063	8
7	00590	50659	7348	5693	00081	50404	0512	5566						
1	2361.	1181.	787.6	591.0	2389.	1195.	797.0	598.0	E	759.3 9958	380.2 0343	253.8 0471	190.6 0535	7
8	04850	02789	8768	1758	04341	02534	1932	1631						
1	2448.	1224.	816.6	612.7	2476.	1238.	826.0	619.7	S	630.3 5698	315.6 8213	210.7 9051	158.3 4470	6
9	08053	54390	9836	7559	07544	54136	3000	7432						
2	2547.	1274.	849.7	637.5	2575.	1288.	859.0	644.5	V	543.3 2495	272.1 6611	181.7 7983	136.5 8670	5
0	14895	07811	2117	4269	14386	07557	5280	4142						
2	2644.	1322.	882.0	661.8	2672.	1336.	891.4	668.8	P	444.2 5653	222.6 3190	148.7 5703	111.8 1959	4
1	20172	60450	7209	0589	19663	60195	0373	0462						
2	2715.	1358.	905.7	679.5	2743.	1372.	915.0	686.5	A	347.2 0376	174.1 0552	116.4 0610	87.55 640	3
2	23884	12306	5113	6517	23375	12051	8277	6390						
2	2871.	1436.	957.7	718.5	2899.	1450.	967.1	725.5	R	276.1 6664	138.5 8696	92.72 706	69.79 712	2
3	33996	17362	8484	9045	33487	17107	1647	8918						
2									T	120.0 6552	60.53 640	40.69 336	30.77 184	1
4														

263-IQT*YLPCIMTVIL*SQV-278



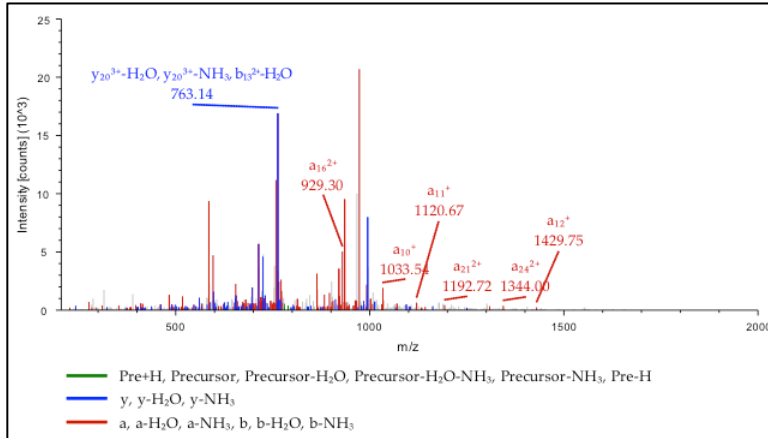
#	a ⁺	a ²⁺	a ³⁺	a ⁴⁺	b ⁺	b ²⁺	b ³⁺	b ⁴⁺	Seq.	y ⁺	y ²⁺	y ³⁺	y ⁴⁺	#
1	86.09 643	43.55 185	29.37 033	22.27 957	114.0 9135	57.54 931	38.70 197	29.27 829	I					1 6
2	214.1 5501	107.5 8114	72.05 652	54.29 421	242.1 4993	121.5 7860	81.38 816	61.29 294	Q	2157. 86562	1079. 43645	719.9 6006	540.2 2186	1 5
3	511.1 7413	256.0 9070	171.0 6289	128.5 4899	539.1 6904	270.0 8816	180.3 9453	135.5 4772	T-Azilso	2029. 80704	1015. 40716	677.2 7387	508.2 0722	1 4
4	674.2 3745	337.6 2236	225.4 1733	169.3 1482	702.2 3236	351.6 1982	234.7 4897	176.3 1355	Y	1732. 78793	866.8 9760	578.2 6749	433.9 5244	1 3
5	787.3 2152	394.1 6440	263.1 1202	197.5 8584	815.3 1643	408.1 6185	272.4 4366	204.5 8457	L	1569. 72461	785.3 6594	523.9 1305	393.1 8661	1 2
6	884.3 7429	442.6 9078	295.4 6295	221.8 4903	912.3 6920	456.6 8824	304.7 9458	228.8 4776	P	1456. 64054	728.8 2391	486.2 1836	364.9 1559	1 1
7	1044. 40494	522.7 0611	348.8 0650	261.8 5669	1072. 39985	536.7 0357	358.1 3814	268.8 5542	C- Carbamido methyl	1359. 58777	680.2 9752	453.8 6744	340.6 5240	1 0
8	1157. 48901	579.2 4814	386.5 0119	290.1 2771	1185. 48392	593.2 4560	395.8 3283	297.1 2644	I	1199. 55712	600.2 8220	400.5 2389	300.6 4474	9
9	1288. 52951	644.7 6839	430.1 8135	322.8 8783	1316. 52442	658.7 6585	439.5 1299	329.8 8656	M	1086. 47305	543.7 4016	362.8 2920	272.3 7372	8
1	1389. 57719	695.2 9223	463.8 6391	348.1 4975	1417. 57210	709.2 8969	473.1 9555	355.1 4848	T	955.4 3255	478.2 1991	319.1 4903	239.6 1359	7
1	1488. 64561	744.8 2644	496.8 8672	372.9 1686	1516. 64052	758.8 2390	506.2 1836	379.9 1559	V	854.3 8487	427.6 9607	285.4 6647	214.3 5167	6
1	1601. 72968	801.3 6848	534.5 8141	401.1 8788	1629. 72459	815.3 6594	543.9 1305	408.1 8661	I	755.3 1645	378.1 6186	252.4 4367	189.5 8457	5
1	1910. 78518	955.8 9623	637.5 9991	478.4 5175	1938. 78010	969.8 9369	646.9 3155	485.4 5048	L-Azilso	642.2 3238	321.6 1983	214.7 4898	161.3 1355	4
1	1997. 81721	999.4 1225	666.6 1059	500.2 0976	2025. 81213	1013. 40970	675.9 4223	507.2 0849	S	333.1 7687	167.0 9207	111.7 3047	84.04 968	3
4	2125. 87579	1063. 44154	709.2 9678	532.2 2441	2153. 87071	1077. 43899	718.6 2842	539.2 2313	Q	246.1 4484	123.5 7606	82.71 980	62.29 167	2
1									V	118.0 8626	59.54 677	40.03 360	30.27 702	1

286-V*PARTVFGVTTVLTMTTLLSIS*ARNSLP-313



#	a*	a ²⁺	a ³⁺	a ⁴⁺	b*	b ²⁺	b ³⁺	b ⁴⁺	Seq.	y*	y ²⁺	y ³⁺	y ⁴⁺	#
1	268.05 222	134.52 975	90.022 26	67.76 851	296.04 713	148.52 720	99.353 89	74.76 724	V- Azils o					2 7
2	365.10 499	183.05 613	122.37 318	92.03 170	393.09 990	197.05 359	131.70 482	99.03 043	P	2929.4 6833	1465.2 3780	977.1 6096	733.1 2254	2 6
3	436.14 211	218.57 469	146.05 222	109.7 9098	464.13 702	232.57 215	155.38 386	116.7 8971	A	2832.4 1556	1416.7 1142	944.8 1004	708.8 5935	2 5
4	592.24 323	296.62 525	198.08 593	148.8 1626	620.23 814	310.62 271	207.41 756	155.8 1499	R	2761.3 7844	1381.1 9286	921.1 3100	691.1 0007	2 4
5	693.29 091	347.14 909	231.76 849	174.0 7818	721.28 582	361.14 655	241.10 012	181.0 7691	T	2605.2 7732	1303.1 4230	869.0 9729	652.0 7479	2 3
6	792.35 933	396.68 330	264.79 129	198.8 4529	820.35 424	410.68 076	274.12 293	205.8 4402	V	2504.2 2964	1252.6 1846	835.4 1473	626.8 1287	2 2
7	939.42 775	470.21 751	313.81 410	235.6 1239	967.42 266	484.21 497	323.14 574	242.6 1112	F	2405.1 6122	1203.0 8425	802.3 9192	602.0 4576	2 1
8	996.44 922	498.72 825	332.82 126	249.8 6776	1024.4 4413	512.72 570	342.15 289	256.8 6649	G	2258.0 9280	1129.5 5004	753.3 6912	565.2 7866	2 0
9	1095.5 1764	548.26 406	365.84 406	274.6 3487	1123.5 1255	562.25 991	375.17 570	281.6 3360	V	2201.0 7133	1101.0 3930	734.3 6196	551.0 2329	1 9
10	1196.5 6532	598.78 630	399.52 662	299.8 9679	1224.5 6023	612.78 375	408.85 826	306.8 9552	T	2102.0 0291	1051.5 0509	701.3 3915	526.2 5618	1 8
11	1297.6 1300	649.31 014	433.20 918	325.1 5871	1325.6 0791	663.30 759	442.54 082	332.1 5744	T	2000.9 5523	1000.9 8125	667.6 5659	500.9 9426	1 7
12	1396.6 8142	698.84 435	466.23 199	349.9 2581	1424.6 7633	712.84 180	475.56 363	356.9 2454	V	1899.9 0755	950.45 741	633.9 7403	475.7 3234	1 6
13	1509.7 6549	755.38 638	503.92 668	378.1 9683	1537.7 6040	769.38 384	513.25 832	385.1 9556	L	1800.8 3913	900.92 320	600.9 5123	450.9 6524	1 5
14	1610.8 1317	805.91 022	537.60 924	403.4 5875	1638.8 0808	819.90 768	546.94 088	410.4 5748	T	1687.7 5506	844.38 117	563.2 5654	422.6 9422	1 4
15	1741.8 5367	871.43 047	581.28 941	436.2 1887	1769.8 4858	885.42 793	590.62 104	443.2 1760	M	1586.7 0738	793.85 733	529.5 7398	397.4 3230	1 3
16	1842.9 0135	921.95 431	614.97 197	461.4 8079	1870.8 9626	935.95 177	624.30 360	468.4 7952	T	1455.6 6688	728.33 708	485.8 9381	364.6 7218	1 2
17	1943.9 4903	972.47 815	648.65 453	486.7 4271	1971.9 4394	986.47 561	657.98 616	493.7 4144	T	1354.6 1920	677.81 324	452.2 1125	339.4 1026	1 1
18	2057.0 3310	1029.0 2019	686.34 922	515.0 1373	2085.0 2801	1043.0 1764	695.68 085	522.0 1246	L	1253.5 7152	627.28 940	418.5 2869	314.1 4834	1 0
19	2144.0 6513	1072.5 3620	715.35 989	536.7 7174	2172.0 6004	1086.5 3366	724.69 153	543.7 7047	S	1140.4 8745	570.74 736	380.8 3400	285.8 7732	9
20	2257.1 04920	1129.0 7824	753.05 458	565.0 4276	2285.1 4411	1143.0 7569	762.38 622	572.0 4149	I	1053.4 5542	527.23 135	351.8 2332	264.1 1931	8
21	2540.1 5266	1270.5 7997	847.38 907	635.7 9362	2568.1 4757	1284.5 7743	856.72 071	642.7 9235	S- Azils o	940.37 135	470.68 931	314.1 2863	235.8 4829	7
22	2611.1 8978	1306.0 9853	871.06 811	653.5 5290	2639.1 8469	1320.0 9599	880.39 975	660.5 5163	A	657.36 788	329.18 758	219.7 9414	165.0 9743	6
23	2767.2 9090	1384.1 4909	923.10 182	692.5 7818	2795.2 8581	1398.1 4655	932.43 346	699.5 7691	R	586.33 076	293.66 902	196.1 1510	147.3 3815	5
24	2881.3 3383	1441.1 7055	961.11 613	721.0 8891	2909.3 2874	1455.1 6801	970.44 777	728.0 8764	N	430.22 964	215.61 846	144.0 8140	108.3 1287	4
25	2968.3 6586	1484.6 8657	990.12 680	742.8 4692	2996.3 6077	1498.6 8403	999.45 844	749.8 4565	S	316.18 671	158.59 699	106.0 6709	79.80 214	3
26	3081.4 4993	1541.2 2860	1027.8 2149	771.1 1794	3109.4 4484	1555.2 2606	1037.1 5313	778.1 1667	L	229.15 468	115.08 098	77.05 641	58.04 413	2
27									P	116.07	58.538	39.36	29.77	1

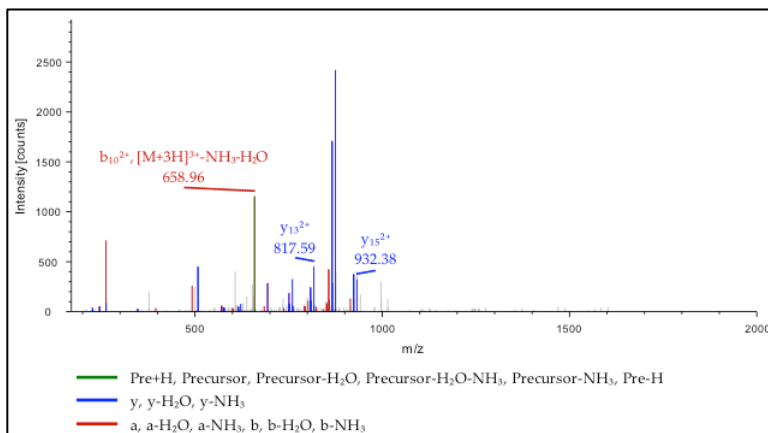
295-VTTVLTMTLSI*SARNSLPKVAYATAMD-322



#	a*	a ²⁺	a ³⁺	a ⁴⁺	b*	b ²⁺	b ³⁺	b ⁴⁺	Seq.	y*	y ²⁺	y ³⁺	y ⁴⁺	#
1	72.08 078	36.54 403	24.69 845	18.77 565	100.0 7570	50.54 149	34.03 008	25.77 438	V					2 8
2	173.1 2846	87.06 787	58.38 101	44.03 757	201.1 2338	101.0 6533	67.71 264	51.03 630	T	3053. 44012	1527. 22370	1018. 48489	764.1 1549	2 7
3	274.1 7614	137.5 9171	92.06 357	69.29 949	302.1 7106	151.5 8917	101.3 9520	76.29 822	T	2952. 39244	1476. 69986	984.8 0233	738.8 5357	2 6
4	373.2 4456	187.1 2592	125.0 8637	94.06 660	401.2 3948	201.1 2338	134.4 1801	101.0 6533	V	2851. 34476	1426. 17602	951.1 1977	713.5 9165	2 5
5	486.3 2863	243.6 6795	162.7 8106	122.3 3762	514.3 2355	257.6 6541	172.1 1270	129.3 3634	L	2752. 27634	1376. 64181	918.0 9696	688.8 2454	2 4
6	587.3 7631	294.1 9179	196.4 6362	147.5 9954	615.3 7123	308.1 8925	205.7 9526	154.5 9826	T	2639. 19227	1320. 09977	880.4 0227	660.5 5353	2 3
7	718.4 1681	359.7 1204	240.1 4379	180.3 5966	746.4 1173	373.7 0950	249.4 7543	187.3 5839	M	2538. 14459	1269. 57593	846.7 1971	635.2 9161	2 2
8	819.4 6449	410.2 3588	273.8 2635	205.6 2158	847.4 5941	424.2 3334	283.1 5799	212.6 2031	T	2407. 10409	1204. 05568	803.0 3955	602.5 3148	2 1
9	920.5 1217	460.7 5972	307.5 0891	230.8 8350	948.5 0709	474.7 5718	316.8 4055	237.8 8223	T	2306. 05641	1153. 53184	769.3 5699	577.2 6956	2 0
10	1033. 59624	517.3 0176	345.2 0360	259.1 5452	1061. 59116	531.2 9922	354.5 3524	266.1 5325	L	2205. 00873	1103. 00800	735.6 7443	552.0 0764	1 9
11	1120. 62827	560.8 1777	374.2 1428	280.9 1253	1148. 62319	574.8 1523	383.5 4591	287.9 1125	S	2091. 92466	1046. 46597	697.9 7974	523.7 3662	1 8
12	1429. 68378	715.3 4553	477.2 3278	358.1 7640	1457. 67869	729.3 4298	486.5 6441	365.1 7513	I-Azilso	2004. 89263	1002. 94995	668.9 6906	501.9 7862	1 7
13	1516. 71581	758.8 6154	506.2 4345	379.9 3441	1544. 71072	772.8 5900	515.5 7509	386.9 3314	S	1695. 83713	848.4 2220	565.9 5056	424.7 1474	1 6
14	1587. 75293	794.3 8010	529.9 2249	397.6 9369	1615. 74784	808.3 7756	539.2 5413	404.6 9242	A	1608. 80510	804.9 0619	536.9 3988	402.9 5673	1 5
15	1743. 85405	872.4 3066	581.9 5620	436.7 1897	1771. 84896	886.4 2812	591.2 8784	443.7 1770	R	1537. 76798	769.3 8763	513.2 6084	385.1 9745	1 4
16	1858. 88099	929.9 4413	620.2 9852	465.4 7571	1886. 87591	943.9 4159	629.6 3015	472.4 7443	N-Deamidated	1381. 66686	691.3 3707	461.2 2714	346.1 7217	1 3
17	1945. 91302	973.4 6015	649.3 0919	487.2 3371	1973. 90794	987.4 5761	658.6 4083	494.2 3244	S	1266. 63991	633.8 2359	422.8 8482	317.4 1544	1 2
18	2058. 99709	1030. 00218	687.0 0388	515.5 0473	2086. 99201	1043. 99964	696.3 3552	522.5 0346	L	1179. 60788	590.3 0758	393.8 7414	295.6 5743	1 1
19	2156. 04986	1078. 52857	719.3 5481	539.7 6792	2184. 04478	1092. 52603	728.6 8644	546.7 6665	P	1066. 52381	533.7 6554	356.1 7945	267.3 8641	1 0
20	2284. 14483	1142. 57605	762.0 5313	571.7 9167	2312. 13975	1156. 57351	771.3 8477	578.7 9039	K	969.4 7104	485.2 3916	323.8 2853	243.1 2322	9
21	2383. 21325	1192. 11026	795.0 7594	596.5 5877	2411. 20817	1206. 10772	804.4 0757	603.5 5750	V	841.3 7607	421.1 9167	281.1 3021	211.0 9948	8
22	2454. 25037	1227. 62882	818.7 5498	614.3 1805	2482. 24529	1241. 62628	828.0 8661	621.3 1678	A	742.3 0765	371.6 5746	248.1 0740	186.3 3237	7
23	2617. 31369	1309. 16048	873.1 0942	655.0 8388	2645. 30861	1323. 15794	882.4 4105	662.0 8261	Y	671.2 7053	336.1 3890	224.4 2836	168.5 7309	6
24	2688. 35081	1344. 67904	896.7 8846	672.8 4316	2716. 34573	1358. 67650	906.1 2009	679.8 4189	A	508.2 0721	254.6 0724	170.0 7392	127.8 0726	5
25	2789. 39849	1395. 20288	930.4 7102	698.1 0508	2817. 39341	1409. 20034	939.8 0265	705.1 0381	T	437.1 7009	219.0 8868	146.3 9488	110.0 4798	4

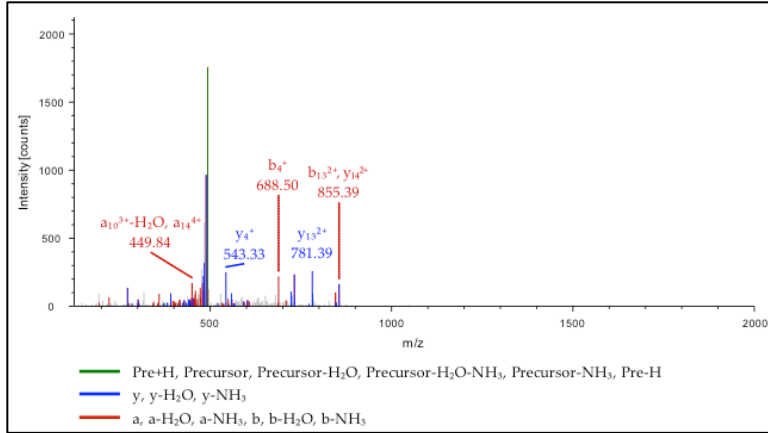
2	2860.	1430.	954.1	715.8	2888.	1444.	963.4	722.8	A	336.1	168.5	112.7	84.78	3
6	43561	72144	5006	6436	43053	71890	8169	6309		2241	6484	1232	606	
2	2991.	1496.	997.8	748.6	3019.	1510.	1007.	755.6	M	265.0	133.0	89.03	67.02	2
7	47611	24169	3022	2449	47103	23915	16186	2321		8529	4628	328	678	
2									D	134.0	67.52	45.35	34.26	1
8										4479	603	311	666	

β_3 GABA_A receptor subunit 65-MNIDIA*SIDMVSEVNM-80



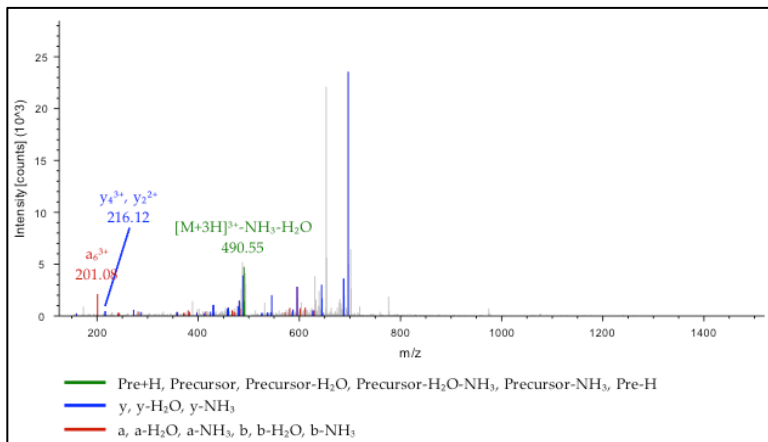
#	a ⁺	a ²⁺	a ³⁺	b ⁺	b ²⁺	b ³⁺	Seq.	y ⁺	y ²⁺	y ³⁺	#
1	120.0477	60.5275	40.6874	148.0426	74.5249	50.0190	M-				1
6	8	3	4	9	8	8	Oxidation				6
2	234.0907	117.548	78.7017	262.0856	131.546	88.0333	N	1862.737	931.872	621.584	1
5	1	99	5	2	45	9		78	53	11	5
3	347.1747	174.091	116.396	375.1696	188.088	125.728	I	1748.694	874.851	583.569	1
4	8	03	44	9	48	08		85	06	80	4
4	462.2017	231.604	154.738	490.1966	245.601	164.070	D	1635.610	818.309	545.875	1
3	3	50	76	4	96	40		78	03	11	3
5	575.2858	288.146	192.433	603.2807	302.143	201.765	I	1520.583	760.795	507.532	1
2	0	54	45	1	99	09		83	55	79	2
6	842.2943	421.650	281.436	870.2892	435.648	290.767	A-Azilso	1407.499	704.253	469.838	1
1	5	81	30	7	27	94		76	52	10	1
7	929.3263	465.166	310.446	957.3213	479.164	319.778	S	1140.491	570.749	380.835	1
8	8	83	98	0	29	62		21	24	25	0
8	1042.410	521.708	348.141	1070.405	535.706	357.473	I	1053.459	527.233	351.824	9
9	45	86	67	37	32	31		18	23	58	
9	1157.437	579.222	386.483	1185.432	593.219	395.815	D	940.3751	470.691	314.129	8
8	40	34	98	32	80	62		1	19	89	
1	1288.477	644.742	430.164	1316.472	658.740	439.495	M	825.3481	413.177	275.787	7
0	90	59	15	82	05	79		6	72	57	
1	1387.546	694.276	463.186	1415.541	708.274	472.518	V	694.3076	347.657	232.107	6
1	32	80	96	24	26	60		6	47	40	
1	1474.578	737.792	492.197	1502.573	751.790	501.529	S	595.2392	298.123	199.084	5
2	35	81	63	27	27	27		4	26	60	
1	1603.620	802.314	535.211	1631.615	816.311	544.543	E	508.2072	254.607	170.073	4
3	95	11	83	87	57	47		1	24	92	
1	1702.689	851.848	568.234	1730.684	865.845	577.566	V	379.1646	190.085	127.059	3
4	37	32	64	29	78	28		1	94	72	
1	1816.732	908.869	606.248	1844.727	922.867	615.580	N	280.0961	140.551	94.0369	2
5	30	79	95	22	25	59		9	73	1	
1							M-	166.0532	83.5302	56.0226	1
6							Oxidation	6	7	0	

315-V*FVFLALLEYAFVNY-329



#	a*	a ²⁺	a ³⁺	a ⁴⁺	b*	b ²⁺	b ³⁺	b ⁴⁺	Seq.	y*	y ²⁺	y ³⁺	y ⁴⁺	#
1	268.05	134.5	90.02	67.76	296.04	148.5	99.35	74.76	V-Azilso					1
	222	2975	226	851	713	2720	389	724						5
2	415.12	208.0	139.0	104.5	443.11	222.0	148.3	111.5	F	1709.8	855.4	570.6	428.2	1
	064	6396	4506	3562	555	6141	7670	3435		8258	4493	3238	2610	4
3	514.18	257.5	172.0	129.3	542.18	271.5	181.3	136.3	V	1562.8	781.9	521.6	391.4	1
	906	9817	6787	0272	397	9562	9951	0145		1416	1072	0957	5900	3
4	661.25	331.1	221.0	166.0	689.25	345.1	230.4	173.0	F	1463.7	732.3	488.5	366.6	1
	748	3238	9068	6983	239	2983	2231	6856		4574	7651	8676	9189	2
5	774.34	387.6	258.7	194.3	802.33	401.6	268.1	201.3	L	1316.6	658.8	439.5	329.9	1
	155	7441	8537	4084	646	7187	1700	3957		7732	4230	6396	2479	1
6	845.37	423.1	282.4	212.1	873.37	437.1	291.7	219.0	A	1203.5	602.3	401.8	301.6	1
	867	9297	6441	0012	358	9043	9604	9885		9325	0026	6927	5377	0
7	958.46	479.7	320.1	240.3	986.45	493.7	329.4	247.3	L	1132.5	566.7	378.1	283.8	9
	274	3501	5910	7114	765	3246	9073	6987		5613	8170	9023	9449	
8	1071.5	536.2	357.8	268.6	1099.5	550.2	367.1	275.6	L	1019.4	510.2	340.4	255.6	8
	4681	7704	5379	4216	4172	7450	8542	4089		7206	3967	9554	2347	
9	1200.5	600.7	400.8	300.9	1228.5	614.7	410.1	307.9	E	906.38	453.6	302.8	227.3	7
	8941	9834	6799	0281	8432	9580	9962	0154		799	9763	0085	5245	
10	1363.6	682.3	455.2	341.6	1391.6	696.3	464.5	348.6	Y	777.34	389.1	259.7	195.0	6
	5273	3000	2243	6864	4764	2746	5406	6737		539	7633	8665	9180	
11	1434.6	717.8	478.9	359.4	1462.6	731.8	488.2	366.4	A	614.28	307.6	205.4	154.3	5
	8985	4856	0147	2792	8476	4602	3310	2665		207	4467	3221	2597	
12	1581.7	791.3	527.9	396.1	1609.7	805.3	537.2	403.1	F	543.24	272.1	181.7	136.5	4
	5827	8277	2427	9502	5318	8023	5591	9375		495	2611	5317	6669	
13	1680.8	840.9	560.9	420.9	1708.8	854.9	570.2	427.9	V	396.17	198.5	132.7	99.79	3
	2669	1698	4708	6213	2160	1444	7872	6086		653	9190	3036	959	
14	1795.8	898.4	599.2	449.7	1823.8	912.4	608.6	456.7	N-Deamidated	297.10	149.0	99.70	75.03	2
	5363	3045	8940	1887	4855	2791	2103	1759		811	5769	755	248	
15									Y	182.08	91.54	61.36	46.27	1
										116	422	524	575	

280-ITTVLMTTINT*-291



#1	a ⁺	a ²⁺	a ³⁺	b ⁺	b ²⁺	b ³⁺	Seq.	y ⁺	y ²⁺	y ³⁺	#2
1	86.09643	43.55185	29.37033	114.0913 5	57.54931	38.70197	I				1 2
2	187.1441 1	94.07569	63.05289	215.1390 3	108.0731 5	72.38453	T	1391.595 35	696.3013 1	464.5366 3	1 1
3	288.1917 9	144.5995 3	96.73545	316.1867 1	158.5969 9	106.0670 9	T	1290.547 67	645.7774 7	430.8540 7	1 0
4	387.2602 1	194.1337 4	129.7582 6	415.2551 3	208.1312 0	139.0898 9	V	1189.499 99	595.2536 3	397.1715 1	9
5	500.3442 8	250.6757 8	167.4529 5	528.3392 0	264.6732 4	176.7845 8	L	1090.431 57	545.7194 2	364.1487 1	8
6	601.3919 6	301.1996 2	201.1355 1	629.3868 8	315.1970 8	210.4671 4	T	977.3475 0	489.1773 9	326.4540 2	7
7	732.4324 6	366.7198 7	244.8156 7	760.4273 8	380.7173 3	254.1473 1	M	876.2998 2	438.6535 5	292.7714 6	6
8	833.4801 4	417.2437 1	278.4982 3	861.4750 6	431.2411 7	287.8298 7	T	745.2593 2	373.1333 0	249.0912 9	5
9	934.5278 2	467.7675 5	312.1807 9	962.5227 4	481.7650 1	321.5124 3	T	644.2116 4	322.6094 6	215.4087 3	4
10	1047.611 89	524.3095 8	349.8754 8	1075.606 81	538.3070 4	359.2071 2	I	543.1639 6	272.0856 2	181.7261 7	3
11	1161.654 82	581.3310 5	387.8897 9	1189.649 74	595.3285 1	397.2214 3	N	430.0798 9	215.5435 8	144.0314 8	2
12							T- Azilso	316.0369 6	158.5221 2	106.0171 7	1

A.5. Table of Propofol-specific proteome as determined by AziPm-click(1c) activity-based protein profiling

Please Refer to Associated excel file (A.5. Table of Propofol-specific proteome as determined by AziPm-click(1c) activity-based protein profiling) for table A.5.

BIBLIOGRAPHY

1. Meyer, H. Zur Theorie der Alkoholnarkose. *Arch. für Exp. Pathol. und Pharmakologie* **42**, 109–118 (1899).
2. Overton, C. E. *Studien über die Narkose zugleich ein Beitrag zur allgemeinen Pharmakologie*. (Gustav Fischer, 1901).
3. Premachandra, B. R., Kalra, V. K. & Baker, R. F. Photoaffinity labeling of procaine-binding sites in normal and sickle cell membranes. *Biochim. Biophys. Acta* **550**, 245–258 (1979).
4. Bayley, H. *Photogenerated Reagents in Biochemistry and Molecular Biology. Laboratory Techniques in Biochemistry and Molecular Biology* **12**, (Elsevier, 1983).
5. Dubinsky, L., Krom, B. P. & Meijler, M. M. Diazirine based photoaffinity labeling. *Bioorg. Med. Chem.* **20**, 554–570 (2012).
6. Rudolph, U. & Antkowiak, B. Molecular and neuronal substrates for general anaesthetics. *Nat Rev Neurosci* **5**, 709–720 (2004).
7. Company., B. W. and & Association., A. M. Anæsthetics: antient and modern: an historical sketch of anæsthesia. 176, [4], xii (1907).
8. Chidiac, E. J., Kaddoum, R. N. & Fuleihan, S. F. Special article: mandragora: anesthetic of the ancients. *Anesth. Analg.* **115**, 1437–1441 (2012).
9. Pedanius, D. & Beck, L. Y. *De Materia Medica*. (Olms-Weidmann, 2005).
10. Pioreschi, P. Medieval anesthesia--the spongia somnifera. *Med. Hypotheses* **61**, 213–219 (2003).
11. Houghton, I. T. Some observations on early military anaesthesia. *Anaesth. Intensive Care* **34 Suppl 1**, 6–15 (2006).
12. Haridas, R. P. Humphry Davy. *Anesthesiology* **116**, 225; author reply 225-6 (2012).
13. West, J. B. Humphry Davy, nitrous oxide, the Pneumatic Institution, and the Royal Institution. *Am. J. Physiol. Lung Cell. Mol. Physiol.* **307**, L661-7 (2014).
14. Haridas, R. P. Horace wells' demonstration of nitrous oxide in Boston. *Anesthesiology* **119**, 1014–1022 (2013).
15. Haridas, R. P. 'Gentlemen! This Is No Humbug': Did John Collins Warren, M.D., Proclaim These Words on October 16, 1846, at Massachusetts General Hospital, Boston? *Anesthesiology* **124**, 553–560 (2016).
16. Whalen, F. X., Bacon, D. R. & Smith, H. M. Inhaled anesthetics: an historical overview. *Best Pract. Res. Clin. Anaesthesiol.* **19**, 323–330 (2005).
17. Vitchea, J. F. A history of Forane. *Anesthesiology* **35**, 4–7 (1971).
18. Bovill, J. G. Inhalation anaesthesia: from diethyl ether to xenon. *Handb. Exp. Pharmacol.* 121–142 (2008). doi:10.1007/978-3-540-74806-9_6
19. Krantz, J. C. Recent advances in anesthesia. *J. Am. Pharm. Assoc.* **32**, 287–293 (1943).
20. Robinson, D. H. & Toledo, A. H. Historical development of modern anesthesia. *J. Invest. Surg.* **25**, 141–149 (2012).
21. López-Muñoz, F., Ucha-Udabe, R. & Alamo, C. The history of barbiturates a century after their clinical introduction. *Neuropsychiatr. Dis. Treat.* **1**, 329–343 (2005).
22. Roberts, M. & Jagdish, S. A History of Intravenous Anesthesia in War (1656-

- 1988). *J. Anesth. Hist.* **2**, 13–21 (2016).
23. Doubrava, S. M. & Larson, E. Ketamine anesthesia. *S. D. J. Med.* **24**, 13–18 (1971).
 24. Black, G. W. & Clarke, R. S. Recently introduced anesthetic drugs. *Int. Anesthesiol. Clin.* **9**, 171–196 (1971).
 25. Giese, J. L. & Stanley, T. H. Etomidate: a new intravenous anesthetic induction agent. *Pharmacotherapy* **3**, 251–258 (1983).
 26. Sebel, P. S. & Lowdon, J. D. Propofol: a new intravenous anesthetic. *Anesthesiology* **71**, 260–277 (1989).
 27. Darnobid, J. A. The pharmacology of total intravenous anesthesia. *Int. Anesthesiol. Clin.* **53**, 13–27 (2015).
 28. Berthoud, M. C. & Reilly, C. S. Adverse effects of general anaesthetics. *Drug Saf.* **7**, 434–459 (1992).
 29. Weiser, T. G. *et al.* An estimation of the global volume of surgery: a modelling strategy based on available data. *Lancet* **372**, 139–144 (2008).
 30. Katoh, T. & Ikeda, K. The minimum alveolar concentration (MAC) of sevoflurane in humans. *Anesthesiology* **66**, 301–303 (1987).
 31. Smith, C. *et al.* The interaction of fentanyl on the Cp50 of propofol for loss of consciousness and skin incision. *Anesthesiology* **81**, 820–8; discussion 26A (1994).
 32. Istaphanous, G. K. & Loepke, A. W. General anesthetics and the developing brain. *Curr. Opin. Anesthesiol.* **22**, 368–373 (2009).
 33. Arora, S. S., Gooch, J. L. & Garcia, P. S. Postoperative cognitive dysfunction, Alzheimer’s disease, and anesthesia. *Int. J. Neurosci.* **124**, 236–242 (2014).
 34. Eckenhoff, R. G. & Laudansky, K. F. Anesthesia, surgery, illness and Alzheimer’s disease. *Prog. Neuropsychopharmacol. Biol. Psychiatry* **47**, 162–166 (2013).
 35. Sagner, M. *et al.* The P4 Health Spectrum - A Predictive, Preventive, Personalized and Participatory Continuum for Promoting Healthspan. *Prog. Cardiovasc. Dis.* (2016). doi:10.1016/j.pcad.2016.08.002
 36. Potter, D. E. & Choudhury, M. Ketamine: repurposing and redefining a multifaceted drug. *Drug Discov. Today* **19**, 1848–1854 (2014).
 37. Eckenhoff, R. G. & Shuman, H. Halothane binding to soluble proteins determined by photoaffinity labeling. *Anesthesiology* **79**, 96–106 (1993).
 38. Woll, K. A., Pinch, B. P., Dailey, W. P. & Eckenhoff, R. G. ‘Clickable’ - Photoactive Propofol Analogue for the Identification of Anesthetic Targets. *Biophys. J.* **106**, 478A (2014).
 39. Woll, K. A. *et al.* A Novel Bifunctional Alkylphenol Anesthetic Allows Characterization of GABAA Receptor Subunit Binding Selectivity in Synaptosomes. *J. Biol. Chem.* (2016). doi:10.1074/jbc.M116.736975
 40. Weiser, B. P., Woll, K. A., Dailey, W. P. & Eckenhoff, R. G. Mechanisms revealed through general anesthetic photolabeling. *Curr Anesth. Rep* **4**, 57–66 (2014).
 41. Martinu, T. & Dailey, W. P. Synthesis of carboalkoxychloro- and bromodiazirines. *J. Org. Chem.* **69**, 7359–7362 (2004).
 42. Brunner, J. New photolabeling and crosslinking methods. *Annu. Rev. Biochem.* **62**, 483–514 (1993).
 43. Zhang, Y., Burdzinski, G., Kubicki, J. & Platz, M. S. Direct observation of carbene

- and diazo formation from aryldiazirines by ultrafast infrared spectroscopy. *J. Am. Chem. Soc.* **130**, 16134–16135 (2008).
44. Das, J. Photoincorporation of azialcohol to the C1B domain of PKCdelta is buffer dependent. *J. Photochem. Photobiol. B.* **95**, 185–188 (2009).
 45. Seydel, U. & Gerace, L. A 28,000-Da GDP/GTP-binding protein specific to the nuclear envelope. *J. Biol. Chem.* **266**, 7602–7608 (1991).
 46. Chen, Z.-W. *et al.* A neurosteroid analogue photolabeling reagent labels the colchicine-binding site on tubulin: a mass spectrometric analysis. *Electrophoresis* **33**, 666–674 (2012).
 47. Wang, J., Kubicki, J., Peng, H. & Platz, M. S. Influence of solvent on carbene intersystem crossing rates. *J. Am. Chem. Soc.* **130**, 6604–6609 (2008).
 48. Weiser, B. P. *et al.* Macroscopic and Macromolecular Specificity of Alkylphenol Anesthetics for Neuronal Substrates. *Sci. Rep.* **5**, (2015).
 49. Sigrist, H., Muhlemann, M. & Dolder, M. Philicity of amino-acid side-chains for photogenerated carbenes. *J. Photochem. Photobiol. B-Biology* **7**, 277–287 (1990).
 50. Eckenhoff, R. G. *et al.* Azi-isoflurane, a Photolabel Analog of the Commonly Used Inhaled General Anesthetic Isoflurane. *Acs Chem. Neurosci.* **1**, 139–145 (2010).
 51. Das, J. Aliphatic Diazirines as Photoaffinity Probes for Proteins: Recent Developments. *Chem. Rev.* **111**, 4405–4417 (2011).
 52. Ziebell, M. R., Nirthanan, S., Husain, S. S., Miller, K. W. & Cohen, J. B. Identification of binding sites in the nicotinic acetylcholine receptor for H-3 azietomidate, a photoactivatable general anesthetic. *J. Biol. Chem.* **279**, 17640–17649 (2004).
 53. Pratt, M. B., Husain, S. S., Miller, K. W. & Cohen, J. B. Identification of sites of incorporation in the nicotinic acetylcholine receptor of a photoactivatable general anesthetic. *J. Biol. Chem.* **275**, 29441–29451 (2000).
 54. Hamouda, A. K., Stewart, D. S., Husain, S. S. & Cohen, J. B. Multiple transmembrane binding sites for p-trifluoromethyldiaziriny-etomidate, a photoreactive Torpedo nicotinic acetylcholine receptor allosteric inhibitor. *J. Biol. Chem.* **286**, 20466–20477 (2011).
 55. Husain, S. S. *et al.* Synthesis of trifluoromethylaryl diazirine and benzophenone derivatives of etomidate that are potent general anesthetics and effective photolabels for probing sites on ligand-gated ion channels. *J Med Chem* **49**, 4818–4825 (2006).
 56. Johansson, J. S., Scharf, D., Davies, L. A., Reddy, K. S. & Eckenhoff, R. G. A designed four-alpha-helix bundle that binds the volatile general anesthetic halothane with high affinity. *Biophys. J.* **78**, 982–993 (2000).
 57. Chiara, D. C., Dangott, L. J., Eckenhoff, R. G. & Cohen, J. B. Identification of nicotinic acetylcholine receptor amino acids photolabeled by the volatile anesthetic halothane. *Biochemistry* **42**, 13457–13467 (2003).
 58. Addona, G. H., Husain, S. S., Stehle, T. & Miller, K. W. Geometric isomers of a photoactivatable general anesthetic delineate a binding site on adenylate kinase. *J. Biol. Chem.* **277**, 25685–25691 (2002).
 59. Arevalo, E. *et al.* An alcohol binding site on the neural cell adhesion molecule L1. *Proc. Natl. Acad. Sci. U. S. A.* **105**, 371–375 (2008).

60. Das, J. *et al.* Identification of a general anesthetic binding site in the diacylglycerol-binding domain of protein kinase Cdelta. *J. Biol. Chem.* **279**, 37964–37972 (2004).
61. Das, J., Pany, S., Rahman, G. M. & Slater, S. J. PKC epsilon has an alcohol-binding site in its second cysteine-rich regulatory domain. *Biochem. J.* **421**, 405–413 (2009).
62. Pany, S. & Das, J. Alcohol binding in the C1 (C1A+C1B) domain of protein kinase C epsilon. *Biochim. Biophys. Acta* **1850**, 2368–2376 (2015).
63. Shanmugasundararaj, S. *et al.* The location and nature of general anesthetic binding sites on the active conformation of firefly luciferase; a time resolved photolabeling study. *PLoS One* **7**, e29854 (2012).
64. Yuki, K. *et al.* Isoflurane binds and stabilizes a closed conformation of the leukocyte function-associated antigen-1. *FASEB J. Off. Publ. Fed. Am. Soc. Exp. Biol.* **26**, 4408–4417 (2012).
65. Yuki, K., Bu, W., Shimaoka, M. & Eckenhoff, R. Volatile anesthetics, not intravenous anesthetic propofol bind to and attenuate the activation of platelet receptor integrin alphaIIb beta3. *PLoS One* **8**, e60415 (2013).
66. Chiara, D. C. *et al.* Time-resolved photolabeling of the nicotinic acetylcholine receptor by [3H]azietomidate, an open-state inhibitor. *Mol. Pharmacol.* **75**, 1084–1095 (2009).
67. Li, G.-D. *et al.* Identification of a GABAA receptor anesthetic binding site at subunit interfaces by photolabeling with an etomidate analog. *J. Neurosci.* **26**, 11599–11605 (2006).
68. Li, G. D., Chiara, D. C., Cohen, J. B. & Olsen, R. W. Neurosteroids allosterically modulate binding of the anesthetic etomidate to gamma-aminobutyric acid type A receptors. *J Biol Chem* **284**, 11771–11775 (2009).
69. Li, G. D., Chiara, D. C., Cohen, J. B. & Olsen, R. W. Numerous classes of general anesthetics inhibit etomidate binding to gamma-aminobutyric acid type A (GABAA) receptors. *J Biol Chem* **285**, 8615–8620 (2010).
70. Nirthanan, S., Garcia, G. 3rd, Chiara, D. C., Husain, S. S. & Cohen, J. B. Identification of binding sites in the nicotinic acetylcholine receptor for TDBzl-etomidate, a photoreactive positive allosteric effector. *J. Biol. Chem.* **283**, 22051–22062 (2008).
71. Chiara, D. C. *et al.* Mapping General Anesthetic Binding Site(s) in Human alpha 1 beta 3 gamma-Aminobutyric Acid Type A Receptors with H-3 TDBzl-Etomidate, a Photoreactive Etomidate. *Biochemistry* **51**, 836–847 (2012).
72. Hamouda, A. K. *et al.* Identifying barbiturate binding sites in a nicotinic acetylcholine receptor with [3H]allyl m-trifluoromethyldiazirine mephobarbital, a photoreactive barbiturate. *Mol. Pharmacol.* **85**, 735–746 (2014).
73. Chiara, D. C. *et al.* Specificity of Intersubunit General Anesthetic-binding Sites in the Transmembrane Domain of the Human alpha 1 beta 3 gamma 2 gamma-Aminobutyric Acid Type A (GABAA) Receptor. *J Biol Chem* **288**, 19343–19357 (2013).
74. Chen, Z. W. *et al.* Neurosteroid Analog Photolabeling of a Site in the Third Transmembrane Domain of the beta 3 Subunit of the GABA(A) Receptor. *Mol. Pharmacol.* **82**, 408–419 (2012).

75. Jayakar, S. S., Dailey, W. P., Eckenhoff, R. G. & Cohen, J. B. Identification of Propofol Binding Sites in a Nicotinic Acetylcholine Receptor with a Photoreactive Propofol Analog. *J. Biol. Chem.* **288**, 6178–6189 (2013).
76. Jayakar, S. S. *et al.* Multiple Propofol Binding Sites in a gamma-Aminobutyric Acid Type A Receptor (GABAAR) Identified Using a Photoreactive Propofol Analog. *J Biol Chem* **1**, 581728 (2014).
77. Chiara, D. C. *et al.* Photoaffinity labeling the propofol binding site in GLIC. *Biochemistry* **53**, 135–142 (2014).
78. Hall, M. A. *et al.* m-Azipropofol (AziPm) a photoactive analogue of the intravenous general anesthetic propofol. *J Med Chem* **53**, 5667–5675 (2010).
79. Yuki, K., Bu, W., Xi, J., Shimaoka, M. & Eckenhoff, R. Propofol Shares the Binding Site with Isoflurane and Sevoflurane on Leukocyte Function-Associated Antigen-1. *Anesth. Analg.* **117**, 10.1213/ANE.0b013e3182a00ae0 (2013).
80. Weiser, B. P. & Eckenhoff, R. G. Propofol inhibits SIRT2 deacetylase through a conformation-specific, allosteric site. *J. Biol. Chem.* **290**, 8559–8568 (2015).
81. Weiser, B. P., Bu, W., Wong, D. & Eckenhoff, R. G. Sites and functional consequence of VDAC-alkylphenol anesthetic interactions. *FEBS Lett.* **588**, 4398–403 (2014).
82. Stewart, D. S. *et al.* p-(4-Azipentyl)propofol: A Potent Photoreactive General Anesthetic Derivative of Propofol. *J. Med. Chem.* **54**, 8124–8135 (2011).
83. Yip, G. M. *et al.* A propofol binding site on mammalian GABA receptors identified by photolabeling. *Nat Chem Biol* **22**, (2013).
84. Moya-Barrios, R., Cozens, F. L. & Schepp, N. P. Absolute reactivity of halo(pyridyl)carbenes. *J. Org. Chem.* **74**, 1148–1155 (2009).
85. Husain, S. S. *et al.* p-Trifluoromethyldiaziriny-etomidate: a potent photoreactive general anesthetic derivative of etomidate that is selective for ligand-gated cationic ion channels. *J Med Chem* **53**, 6432–6444 (2010).
86. Chiara, D. C. *et al.* Mapping general anesthetic binding site(s) in human alpha1beta3 gamma-aminobutyric acid type A receptors with [(3)H]TDBzl-etomidate, a photoreactive etomidate analogue. *Biochemistry* **51**, 836–847 (2012).
87. Vedula, L. S. *et al.* A Unitary Anesthetic Binding Site at High Resolution. *J. Biol. Chem.* **284**, 24176–24184 (2009).
88. Liu, R., Loll, P. J. & Eckenhoff, R. G. Structural basis for high-affinity volatile anesthetic binding in a natural 4-helix bundle protein. *Faseb J* **19**, 567–576 (2005).
89. Eckenhoff, R. G., Petersen, C. E., Ha, C. E. & Bhagavan, N. V. Inhaled anesthetic binding sites in human serum albumin. *J. Biol. Chem.* **275**, 30439–30444 (2000).
90. Bhattacharya, A. A., Curry, S. & Franks, N. P. Binding of the general anesthetics propofol and halothane to human serum albumin. High resolution crystal structures. *J Biol Chem* **275**, 38731–38738 (2000).
91. Husain, S. S. *et al.* 2-(3-Methyl-3H-diaziren-3-yl)ethyl 1-(1-phenylethyl)-1H-imidazole-5-carboxylate: a derivative of the stereoselective general anesthetic etomidate for photolabeling ligand-gated ion channels. *J. Med. Chem.* **46**, 1257–1265 (2003).
92. Zhong, H. J., Rusch, D. & Forman, S. A. Photo-activated azi-etomidate, a general anesthetic photolabel, irreversibly enhances gating and desensitization of gamma-aminobutyric acid type A receptors. *Anesthesiology* **108**, 103–112 (2008).

93. Weiser, B. P., Kelz, M. B. & Eckenhoff, R. G. In vivo activation of azipropofol prolongs anesthesia and reveals synaptic targets. *J Biol Chem* **288**, 1279–1285 (2013).
94. Marshall, A. G., Hendrickson, C. L. & Jackson, G. S. Fourier transform ion cyclotron resonance mass spectrometry: A primer. *MASS Spectrom. Rev.* **17**, 1–35 (1998).
95. Han, X., Aslanian, A. & Yates III, J. R. Mass spectrometry for proteomics. *Curr. Opin. Chem. Biol.* **12**, 483–490 (2008).
96. Nagar, S., Argikar, U. A. & Tweedie, D. J. Enzyme kinetics in drug metabolism: fundamentals and applications. *Methods in molecular biology (Clifton, N.J.)* **1113**, 1–6 (2014).
97. Zhang, Y., Wen, Z., Washburn, M. P. & Florens, L. Refinements to label free proteome quantitation: how to deal with peptides shared by multiple proteins. *Anal Chem* **82**, 2272–2281 (2010).
98. Chahrour, O., Cobice, D. & Malone, J. Stable isotope labelling methods in mass spectrometry-based quantitative proteomics. *J. Pharm. Biomed. Anal.* **113**, 2–20 (2015).
99. Li, Z. *et al.* Systematic comparison of label-free, metabolic labeling, and isobaric chemical labeling for quantitative proteomics on LTQ Orbitrap Velos. *J Proteome Res* **11**, 1582–1590 (2012).
100. Mobert, J., Zahler, S., Becker, B. F. & Conzen, P. F. Inhibition of neutrophil activation by volatile anesthetics decreases adhesion to cultured human endothelial cells. *Anesthesiology* **90**, 1372–1381 (1999).
101. Reutershan, J., Chang, D., Hayes, J. K. & Ley, K. Protective effects of isoflurane pretreatment in endotoxin-induced lung injury. *Anesthesiology* **104**, 511–517 (2006).
102. Yuki, K. *et al.* The volatile anesthetic isoflurane perturbs conformational activation of integrin LFA-1 by binding to the allosteric regulatory cavity. *FASEB J. Off. Publ. Fed. Am. Soc. Exp. Biol.* **22**, 4109–4116 (2008).
103. Savechenkov, P. Y. *et al.* Allyl m-Trifluoromethyl diazirine Mephobarbital: An Unusually Potent Enantioselective and Photoreactive Barbiturate General Anesthetic. *J. Med. Chem.* **55**, 6554–6565 (2012).
104. Darbandi-Tonkabon, R. *et al.* Photoaffinity Labeling with a neuroactive steroid analogue - 6-AZI-Pregnanolone labels voltage-dependent anion channel-1 in rat brain. *J. Biol. Chem.* **278**, 13196–13206 (2003).
105. Emerson, D. J. *et al.* Direct modulation of microtubule stability contributes to anthracene general anesthesia. *J. Am. Chem. Soc.* **135**, 5389–5398 (2013).
106. Darbandi-Tonkabon, R. *et al.* Neuroactive steroid interactions with voltage-dependent anion channels: lack of relationship to GABA(A) receptor modulation and anesthesia. *J. Pharmacol. Exp. Ther.* **308**, 502–511 (2004).
107. Weiser, B. P., Kelz, M. B. & Eckenhoff, R. G. In Vivo Activation of Azi-propofol Prolongs Anesthesia and Reveals Synaptic Targets. *J Biol Chem* **26**, 26 (2012).
108. Herring, B. E., Xie, Z., Marks, J. & Fox, A. P. Isoflurane inhibits the neurotransmitter release machinery. *J. Neurophysiol.* **102**, 1265–1273 (2009).
109. Herring, B. E. Etomidate and propofol inhibit the neurotransmitter release machinery at different sites (vol 589, pg 1103, 2011). *J. Physiol.* **589**, 4633 (2011).

110. Lapinsky, D. J. Tandem photoaffinity labeling-bioorthogonal conjugation in medicinal chemistry. *Bioorg. Med. Chem.* **20**, 6237–47 (2012).
111. Booth, H. S. & Bixby, E. M. Fluorine Derivatives of Chloroform. *Ind. Eng. Chem.* **24**, 637–641 (1932).
112. McBee, E. T. Halogenation. *Ind. Eng. Chem.* **40**, 1611–1619 (9AD).
113. McBee, E. T. Fluorine Chemistry. *Ind. Eng. Chem.* **39**, 236–237 (3AD).
114. BRADBURY, F. R., SUCKLING, C. W. & MCCARTHY, M. C. PATTERNS OF INNOVATION .2. ANESTHETIC HALOTHANE. *Chem. Ind.* 105- (1972).
115. Smith, I., Nathanson, M. & White, P. F. Sevoflurane--a long-awaited volatile anaesthetic. *Br. J. Anaesth.* **76**, 435–445 (1996).
116. Hitt, B. A., Mazze, R. I., Cook, T. L., Beppu, W. J. & Kosek, J. C. Thermoregulatory defect in rats during anesthesia. *Anesth. Analg.* **56**, 9–15 (1977).
117. Corbett, T. H. Cancer and congenital anomalies associated with anesthetics. *Ann. N. Y. Acad. Sci.* **271**, 58–66 (1976).
118. Eckenhoff, R. G. Promiscuous ligands and attractive cavities: how do the inhaled anesthetics work? *Mol Interv* **1**, 258–268 (2001).
119. Wallin, R. F., Regan, B. M., Napoli, M. D. & Stern, I. J. Sevoflurane: a new inhalational anesthetic agent. *Anesth. Analg.* **54**, 758–766 (1975).
120. Villani, A. *et al.* A prospective, randomized clinical comparison of sevoflurane and halothane in children. *Minerva Anesthesiol.* **64**, 3–10 (1998).
121. Lerman, J. Inhalation agents in pediatric anaesthesia - an update. *Curr. Opin. Anaesthesiol.* **20**, 221–226 (2007).
122. Eckenhoff, R. G., Knoll, F. J., Greenblatt, E. P. & Dailey, W. P. Halogenated diazirines as photolabel mimics of the inhaled haloalkane anesthetics. *J. Med. Chem.* **45**, 1879–1886 (2002).
123. Krespan, C. G. & Dixon, D. A. Perhalodioxins and Perhalodihydrodioxins. *J. Org. Chem.* **56**, 3915–3923 (1991).
124. Huang, C. G., Rozov, L. A., Hapler, D. F. & Vernice, G. G. Preparation of the isoflurane enantiomers. *J. Org. Chem.* **58**, 7382–7387 (1993).
125. Xi, J. *et al.* Photoactive analogues of the haloether anesthetics provide high-resolution features from low-affinity interactions. *ACS Chem. Biol.* **1**, 377–384 (2006).
126. Butts, C. A. *et al.* Identification of a fluorescent general anesthetic, 1-aminoanthracene. *Proc Natl Acad Sci U S A* **106**, 6501–6506 (2009).
127. McKinstry-Wu, A. R. *et al.* Discovery of a Novel General Anesthetic Chemotype Using High-throughput Screening. *Anesthesiology* **122**, 325–333 (2015).
128. Zhou, J.-X., Luo, N.-F., Liang, X.-M. & Liu, J. The efficacy and safety of intravenous emulsified isoflurane in rats. *Anesth. Analg.* **102**, 129–134 (2006).
129. Barber, A. F., Liang, Q. & Covarrubias, M. Novel activation of voltage-gated K(+) channels by sevoflurane. *J Biol Chem* **287**, 40425–40432 (2012).
130. Liang, Q. *et al.* Positive Allosteric Modulation of Kv Channels by Sevoflurane: Insights into the Structural Basis of Inhaled Anesthetic Action. *PLoS One* **10**, e0143363 (2015).
131. Kenny, J. D., Westover, M. B., Ching, S., Brown, E. N. & Solt, K. Propofol and sevoflurane induce distinct burst suppression patterns in rats. *Front. Syst. Neurosci.* **8**, 237 (2014).

132. Wulff, H., Castle, N. A. & Pardo, L. A. Voltage-gated Potassium Channels as Therapeutic Drug Targets. *Nat. Rev. Drug Discov.* **8**, 982–1001 (2009).
133. Alkire, M. T., Asher, C. D., Franciscus, A. M. & Hahn, E. L. Thalamic microinfusion of antibody to a voltage-gated potassium channel restores consciousness during anesthesia. *Anesthesiology* **110**, 766–773 (2009).
134. Lioudyno, M. I. *et al.* Shaker-related potassium channels in the central medial nucleus of the thalamus are important molecular targets for arousal suppression by volatile general anesthetics. *J Neurosci* **33**, 16310–16322 (2013).
135. Trott, O. & Olson, A. J. AutoDock Vina: improving the speed and accuracy of docking with a new scoring function, efficient optimization, and multithreading. *J. Comput. Chem.* **31**, 455–61 (2010).
136. Barber, A. F., Liang, Q., Amaral, C., Treptow, W. & Covarrubias, M. Molecular mapping of general anesthetic sites in a voltage-gated ion channel. *Biophys J* **101**, 1613–1622 (2011).
137. Zhang, J., Qu, X., Covarrubias, M. & Germann, M. W. Insight into the modulation of Shaw2 Kv channels by general anesthetics: structural and functional studies of S4-S5 linker and S6 C-terminal peptides in micelles by NMR. *Biochim. Biophys. Acta* **1828**, 595–601 (2013).
138. Covarrubias, M., Barber, A. F., Carnevale, V., Treptow, W. & Eckenhoff, R. G. Mechanistic Insights into the Modulation of Voltage-Gated Ion Channels by Inhalational Anesthetics. *Biophys. J.* **109**, 2003–2011 (2016).
139. Long, S. B., Campbell, E. B. & Mackinnon, R. Voltage sensor of Kv1.2: structural basis of electromechanical coupling. *Science* **309**, 903–908 (2005).
140. Batulan, Z., Haddad, G. A. & Blunck, R. An intersubunit interaction between S4-S5 linker and S6 is responsible for the slow off-gating component in Shaker K⁺ channels. *J. Biol. Chem.* **285**, 14005–14019 (2010).
141. Nishizawa, M. & Nishizawa, K. Coupling of S4 helix translocation and S6 gating analyzed by molecular-dynamics simulations of mutated Kv channels. *Biophys. J.* **97**, 90–100 (2009).
142. Han, M. & Zhang, J. Z. H. Molecular dynamic simulation of the Kv1.2 voltage-gated potassium channel in open and closed state conformations. *J. Phys. Chem. B* **112**, 16966–16974 (2008).
143. Cheng, T. *et al.* Computation of octanol-water partition coefficients by guiding an additive model with knowledge. *J Chem Inf Model* **47**, 2140–2148 (2007).
144. Irwin, J. J., Sterling, T., Mysinger, M. M., Bolstad, E. S. & Coleman, R. G. ZINC: A Free Tool to Discover Chemistry for Biology. *J. Chem. Inf. Model.* **52**, 1757–1768 (2012).
145. Tao, X., Lee, A., Limapichat, W., Dougherty, D. A. & MacKinnon, R. A Gating Charge Transfer Center in Voltage Sensors. *Science* **328**, 67–73 (2010).
146. Morris, G. M. *et al.* AutoDock4 and AutoDockTools4: Automated Docking with Selective Receptor Flexibility. *J. Comput. Chem.* **30**, 2785–2791 (2009).
147. Trott, O. & Olson, A. J. Software News and Update AutoDock Vina: Improving the Speed and Accuracy of Docking with a New Scoring Function, Efficient Optimization, and Multithreading. *J. Comput. Chem.* **31**, 455–461 (2010).
148. Olsen, R. W. & Sieghart, W. International union of pharmacology. LXX. Subtypes of gamma-aminobutyric Acid(A) receptors: Classification on the basis of subunit

- composition, pharmacology, and function. Update. *Pharmacol. Rev.* **60**, 243–260 (2008).
149. Wu, X. *et al.* γ -aminobutyric acid type A (GABA A) receptor α subunits play a direct role in synaptic Versus extrasynaptic targeting. *J. Biol. Chem.* **287**, 27417–27430 (2012).
 150. Hentschke, H. *et al.* Altered GABAA,slow inhibition and network oscillations in mice lacking the GABAA receptor beta3 subunit. *J. Neurophysiol.* **102**, 3643–3655 (2009).
 151. Kullmann, D. M. *et al.* Presynaptic, extrasynaptic and axonal GABA(A) receptors in the CNS: where and why? *Prog. Biophys. Mol. Biol.* **87**, 33–46 (2005).
 152. Baumann, S. W., Baur, R. & Sigel, E. Subunit arrangement of gamma-aminobutyric acid type A receptors. *J. Biol. Chem.* **276**, 36275–36280 (2001).
 153. Baumann, S. W., Baur, R. & Sigel, E. Forced subunit assembly in alpha1beta2gamma2 GABAA receptors. Insight into the absolute arrangement. *J. Biol. Chem.* **277**, 46020–46025 (2002).
 154. Baur, R., Minier, F. & Sigel, E. A GABA(A) receptor of defined subunit composition and positioning: concatenation of five subunits. *FEBS Lett.* **580**, 1616–1620 (2006).
 155. Curtis, D. R., Duggan, A. W., Felix, D. & Johnston, G. A. Bicuculline, an antagonist of GABA and synaptic inhibition in the spinal cord of the cat. *Brain Res* **32**, 69–96 (1971).
 156. Mihic, S. J., McQuilkin, S. J., Eger 2nd, E. I., Ionescu, P. & Harris, R. A. Potentiation of gamma-aminobutyric acid type A receptor-mediated chloride currents by novel halogenated compounds correlates with their abilities to induce general anesthesia. *Mol Pharmacol* **46**, 851–857 (1994).
 157. Brown, C. L. & Martin, I. L. Photoaffinity labelling of the benzodiazepine receptor cannot be used to predict ligand efficacy. *Neurosci. Lett.* **35**, 37–40 (1983).
 158. Brown, C. L. & Martin, I. L. Photoaffinity labelling of the benzodiazepine receptor compromises the recognition site but not its effector mechanism. *J. Neurochem.* **43**, 272–273 (1984).
 159. Forman, S. A. & Miller, K. W. Mapping General Anesthetic Sites in Heteromeric gamma-Aminobutyric Acid Type A Receptors Reveals a Potential For Targeting Receptor Subtypes. *Anesth. Analg.* **123**, 1263–1273 (2016).
 160. Nishikawa, K. & Harrison, N. L. The actions of sevoflurane and desflurane on the gamma-aminobutyric acid receptor type A: effects of TM2 mutations in the alpha and beta subunits. *Anesthesiology* **99**, 678–684 (2003).
 161. Dai, S., Perouansky, M. & Pearce, R. A. Isoflurane enhances both fast and slow synaptic inhibition in the hippocampus at amnestic concentrations. *Anesthesiology* **116**, 816–823 (2012).
 162. Hall, A. C., Rowan, K. C., Stevens, R. J. N., Kelley, J. C. & Harrison, N. L. The effects of isoflurane on desensitized wild-type and alpha 1(S270H) gamma-aminobutyric acid type A receptors. *Anesth. Analg.* **98**, 1297–304, table of contents (2004).
 163. Lambert, S., Arras, M., Vogt, K. E. & Rudolph, U. Isoflurane-induced surgical tolerance mediated only in part by beta3-containing GABA(A) receptors. *Eur. J. Pharmacol.* **516**, 23–27 (2005).

164. Dostalova, Z. *et al.* Human $\alpha 1\beta 3\gamma 2L$ gamma-aminobutyric acid type A receptors: High-level production and purification in a functional state. *Protein Sci.* **23**, 157–166 (2014).
165. Hinkle, D. J. & Macdonald, R. L. Beta subunit phosphorylation selectively increases fast desensitization and prolongs deactivation of $\alpha 1\beta 1\gamma 2L$ and $\alpha 1\beta 3\gamma 2L$ GABA(A) receptor currents. *J. Neurosci.* **23**, 11698–11710 (2003).
166. Chiara, D. C. *et al.* Mapping general anesthetic binding site(s) in human $\alpha 1\beta 3\gamma$ -aminobutyric acid type A receptors with [(3)H]TDBzl-etomidate, a photoreactive etomidate analog(). *Biochemistry* **51**, 836–847 (2012).
167. Dostalova, Z. *et al.* High-level expression and purification of Cys-loop ligand-gated ion channels in a tetracycline-inducible stable mammalian cell line: GABAA and serotonin receptors. *Protein Sci.* **19**, 1728–1738 (2010).
168. Hénin, J., Salari, R., Murlidaran, S. & Brannigan, G. A predicted binding site for cholesterol on the GABAA receptor. *Biophys. J.* **106**, 1938–49 (2014).
169. Kinde, M. N. *et al.* Common Anesthetic-binding Site for Inhibition of Pentameric Ligand-gated Ion Channels. *Anesthesiology* **124**, 664–673 (2016).
170. Olsen, R. W. & Li, G. D. GABA(A) receptors as molecular targets of general anesthetics: identification of binding sites provides clues to allosteric modulation. *Can J Anaesth* **58**, 206–215 (2011).
171. Pan, J. *et al.* Structure of the Pentameric Ligand-Gated Ion Channel GLIC Bound with Anesthetic Ketamine. *Structure* **20**, 1463–1469 (2012).
172. Nury, H. *et al.* X-ray structures of general anaesthetics bound to a pentameric ligand-gated ion channel. *Nature* **469**, 428–431 (2011).
173. Kittler, J. T. *et al.* Phospho-dependent binding of the clathrin AP2 adaptor complex to GABA(A) receptors regulates the efficacy of inhibitory synaptic transmission. *Proc. Natl. Acad. Sci. U. S. A.* **102**, 14871–14876 (2005).
174. Zhang, X. & Miller, K. W. Dodecyl maltopyranoside enabled purification of active human GABA type A receptors for deep and direct proteomic sequencing. *Mol. Cell. Proteomics* **14**, 724–738 (2015).
175. Humphrey, W., Dalke, A. & Schulten, K. VMD: visual molecular dynamics. *J. Mol. Graph.* **14**, 27-28-38 (1996).
176. James, R. & Glen, J. B. Synthesis, biological evaluation, and preliminary structure-activity considerations of a series of alkylphenols as intravenous anesthetic agents. *J Med Chem* **23**, 1350–1357 (1980).
177. Franks, N. P., Jenkins, A., Conti, E., Lieb, W. R. & Brick, P. Structural basis for the inhibition of firefly luciferase by a general anesthetic. *Biophys J* **75**, 2205–2211 (1998).
178. Franks, N. P. & Lieb, W. R. Molecular and cellular mechanisms of general anaesthesia. *Nature* **367**, 607–614 (1994).
179. Woll, K. A., Dailey, W. P., Brannigan, G. & Eckenhoff, R. G. Shedding Light on Anesthetic Mechanisms: Application of Photoaffinity Ligands. *Anesth. Analg.* (2016). doi:10.1213/ANE.0000000000001365
180. Leon, I. *et al.* Exploring microsolvation of the anesthetic propofol. *Phys Chem Chem Phys* **14**, 4398–4409 (2012).
181. Leon, I. *et al.* Formation of water polyhedrons in propofol-water clusters. *Phys*

- Chem Chem Phys* **15**, 568–575 (2013).
182. Leon, I. *et al.* Mimicking anesthetic-receptor interactions in jets: the propofol-isopropanol cluster. *Phys Chem Chem Phys* **9**, 9 (2014).
 183. Eckenhoff, R. G., Tanner, J. W. & Johansson, J. S. Steric hindrance is not required for n-alkanol cutoff in soluble proteins. *Mol Pharmacol* **56**, 414–418 (1999).
 184. Krasowski, M. D., Hong, X. A., Hopfinger, A. J. & Harrison, N. L. 4D-QSAR analysis of a set of propofol analogues: Mapping binding sites for an anesthetic phenol on the GABA(A) receptor. *J. Med. Chem.* **45**, 3210–3221 (2002).
 185. Krasowski, M. D. *et al.* General anesthetic potencies of a series of propofol analogs correlate with potency for potentiation of gamma-aminobutyric acid (GABA) current at the GABA(A) receptor but not with lipid solubility. *J Pharmacol Exp Ther* **297**, 338–351 (2001).
 186. Rai, G. *et al.* *Discovery of Novel General Anesthetics Using Apoferritin as a Surrogate System.* (2012).
 187. Hall, M. A. *et al.* m-Azipropofol (AziPm) a Photoactive Analogue of the Intravenous General Anesthetic Propofol. *J. Med. Chem.* **53**, 5667–5675 (2010).
 188. Liu, R. Y. *et al.* Comparative binding character of two general anaesthetics for sites on human serum albumin. *Biochem. J.* **380**, 147–152 (2004).
 189. Liu, R., Yang, J., Ha, C. E., Bhagavan, N. V & Eckenhoff, R. G. Truncated human serum albumin retains general anaesthetic binding activity. *Biochem J* **388**, 39–45 (2005).
 190. Hardegger, L. A. *et al.* Systematic investigation of halogen bonding in protein-ligand interactions. *Angew Chem Int Ed Engl* **50**, 314–318 (2011).
 191. Pavan, M. S., Durga Prasad, K. & Row, T. N. Halogen bonding in fluorine: experimental charge density study on intermolecular F...F and F...S donor-acceptor contacts. *Chem Commun* **49**, 7558–7560 (2013).
 192. Politzer, P., Lane, P., Concha, M. C., Ma, Y. & Murray, J. S. An overview of halogen bonding. *J Mol Model* **13**, 305–311 (2007).
 193. Hewapathirane, D. S., Dunfield, D., Yen, W., Chen, S. & Haas, K. In vivo imaging of seizure activity in a novel developmental seizure model. *Exp Neurol* **211**, 480–488 (2008).
 194. Simons, P. J. *et al.* Distribution in female rats of an anaesthetic intravenous dose of ¹⁴C-propofol. *Xenobiotica* **21**, 1325–1335 (1991).
 195. Fang, Z. *et al.* Anesthetic and convulsant properties of aromatic compounds and cycloalkanes: implications for mechanisms of narcosis. *Anesth Analg* **83**, 1097–1104 (1996).
 196. Orser, B. A., Wang, L. Y., Pennefather, P. S. & MacDonald, J. F. Propofol modulates activation and desensitization of GABAA receptors in cultured murine hippocampal neurons. *J Neurosci* **14**, 7747–7760 (1994).
 197. Hill-Venning, C., Belelli, D., Peters, J. A. & Lambert, J. J. Subunit-dependent interaction of the general anaesthetic etomidate with the gamma-aminobutyric acid type A receptor. *Br J Pharmacol* **120**, 749–756 (1997).
 198. Lam, D. W. & Reynolds, J. N. Modulatory and direct effects of propofol on recombinant GABAA receptors expressed in xenopus oocytes: influence of alpha- and gamma2-subunits. *Brain Res.* **784**, 179–187 (1998).
 199. Fujinaka, W. *et al.* Effects of propofol on left ventricular mechanoenergetics in the

- excised cross-circulated canine heart. *Acta Med Okayama* **66**, 435–442 (2012).
200. Royse, C. F., Liew, D. F. L., Wright, C. E., Royse, A. G. & Angus, J. A. Persistent depression of contractility and vasodilation with propofol but not with sevoflurane or desflurane in rabbits. *Anesthesiology* **108**, 87–93 (2008).
 201. Kale, L. *et al.* NAMD2: Greater scalability for parallel molecular dynamics. *J. Comput. Phys.* **151**, 283–312 (1999).
 202. Ding, W. *et al.* Reversal of isoflurane-induced depression of myocardial contraction by nitroxyl via myofilament sensitization to Ca²⁺. *J Pharmacol Exp Ther* **339**, 825–831 (2011).
 203. Gao, W. D., Liu, Y. G. & Marban, E. Selective effects of oxygen free radicals on excitation-contraction coupling in ventricular muscle - Implications for the mechanism of stunned myocardium. *Circulation* **94**, 2597–2604 (1996).
 204. Weyermann, Gisselbrecht, Boudon, Diederich & Gross. Dendritic Iron Porphyrins with Tethered Axial Ligands: New Model Compounds for Cytochromes. *Angew. Chem. Int. Ed. Engl.* **38**, 3215–3219 (1999).
 205. Breton, G. W. Selective monoacetylation of unsymmetrical diols catalyzed by silica gel-supported sodium hydrogen sulfate. *J. Org. Chem.* **62**, 8952–8954 (1997).
 206. Lea, W. A. *et al.* A high-throughput approach for identification of novel general anesthetics. *PLoS One* **4**, 7150 (2009).
 207. Ting, L., Rad, R., Gygi, S. P. & Haas, W. MS3 eliminates ratio distortion in isobaric multiplexed quantitative proteomics. *Nat Methods* **8**, 937–940 (2011).
 208. Eckenhoff, R. G., Xi, J. & Dailey, W. P. Inhalational anesthetic photolabeling. *Methods Mol. Biol.* **617**, 437–443 (2010).
 209. Orser, B. A., Bertlik, M., Wang, L. Y. & Macdonald, J. F. Inhibition by propofol-(2,6-di-isopropylphenol) of the N-Methyl-D-Aspartate subtype of glutamate receptor in cultured hippocampal-neurons. *Br. J. Pharmacol.* **116**, 1761–1768 (1995).
 210. Tibbs, G. R. *et al.* HCN1 channels as targets for anesthetic and nonanesthetic propofol analogs in the amelioration of mechanical and thermal hyperalgesia in a mouse model of neuropathic pain. *J Pharmacol Exp Ther* **345**, 363–373 (2013).
 211. Fassel, J., High, K. M., Stephenson, E. R., Yarotsky, V. & Elmslie, K. S. The Intravenous Anesthetic Propofol Inhibits Human L-Type Calcium Channels by Enhancing Voltage-Dependent Inactivation. *J. Clin. Pharmacol.* **51**, 719–730 (2011).
 212. Olsen, R. W. *et al.* Structural models of ligand-gated ion channels: sites of action for anesthetics and ethanol. *Alcohol. Clin. Exp. Res.* **38**, 595–603 (2014).
 213. Villen, J. & Gygi, S. P. The SCX/IMAC enrichment approach for global phosphorylation analysis by mass spectrometry. *Nat Protoc* **3**, 1630–1638 (2008).
 214. Olsen, R. W. Allosteric ligands and their binding sites define γ -aminobutyric acid (GABA) type A receptor subtypes. *Adv. Pharmacol.* **73**, 167–202 (2015).
 215. Zecharia, A. Y. *et al.* The involvement of hypothalamic sleep pathways in general anesthesia: testing the hypothesis using the GABAA receptor beta3N265M knock-in mouse. *J. Neurosci.* **29**, 2177–2187 (2009).
 216. Sanchis-Segura, C., Cline, B., Jurd, R., Rudolph, U. & Spanagel, R. Etomidate and propofol-hyposensitive GABAA receptor beta3(N265M) mice show little changes

- in acute alcohol sensitivity but enhanced tolerance and withdrawal. *Neurosci. Lett.* **416**, 275–8 (2007).
217. Eckle, V. S., Rudolph, U., Antkowiak, B. & Grasshoff, C. Propofol modulates phasic and tonic GABAergic currents in spinal ventral horn interneurons. *Br. J. Anaesth.* **114**, 491–498 (2015).
 218. McDougall, S. J., Bailey, T. W., Mendelowitz, D. & Andresen, M. C. Propofol enhances both tonic and phasic inhibitory currents in second-order neurons of the solitary tract nucleus (NTS). *Neuropharmacology* **54**, 552–563 (2008).
 219. Nishikawa, K. [Roles of glutamatergic and GABAergic nervous system in hypnotic and analgesic actions of general anesthetics]. *Masui.* **60**, 534–543 (2011).
 220. Chang, C. S., Olcese, R. & Olsen, R. W. A single M1 residue in the beta2 subunit alters channel gating of GABAA receptor in anesthetic modulation and direct activation. *J Biol Chem* **278**, 42821–42828 (2003).
 221. Eaton, M. *et al.* Mutational Analysis of the Putative High-Affinity Propofol Binding Site in Human beta3 Homomeric GABAA Receptors. *Mol. Pharmacol.* (2015). doi:10.1124/mol.115.100347
 222. Krasowski, M. D., Nishikawa, K., Nikolaeva, N., Lin, A. & Harrison, N. L. Methionine 286 in transmembrane domain 3 of the GABAA receptor beta subunit controls a binding cavity for propofol and other alkylphenol general anesthetics. *Neuropharmacology* **41**, 952–964 (2001).
 223. Jonsson Fagerlund, M., Sjodin, J., Krupp, J. & Dabrowski, M. A. Reduced effect of propofol at human {alpha}1{beta}2(N289M){gamma}2 and {alpha}2{beta}3(N290M){gamma}2 mutant GABA(A) receptors. *Br J Anaesth* **104**, 472–481 (2010).
 224. Krasowski, M. D., Hong, X., Hopfinger, A. J. & Harrison, N. L. 4D-QSAR analysis of a set of propofol analogues: mapping binding sites for an anesthetic phenol on the GABA(A) receptor. *J Med Chem* **45**, 3210–3221 (2002).
 225. Olsen, R. W. Allosteric ligands and their binding sites define gamma-aminobutyric acid (GABA) type A receptor subtypes. *Adv. Pharmacol.* **73**, 167–202 (2015).
 226. Bertaccini, E. J., Yoluk, O., Lindahl, E. R. & Trudell, J. R. Assessment of homology templates and an anesthetic binding site within the gamma-aminobutyric acid receptor. *Anesthesiology* **119**, 1087–1095 (2013).
 227. Leon, I. *et al.* Mimicking anaesthetic-receptor interaction: a combined spectroscopic and computational study of propofol...phenol. *Phys Chem Chem Phys* **14**, 8956–8963 (2012).
 228. Jiang, W. *et al.* Generalized Scalable Multiple Copy Algorithms for Molecular Dynamics Simulations in NAMD. *Comput. Phys. Commun.* **185**, 908–916 (2014).
 229. Zwanzig, R. W. High- temperature equation of state by a perturbation method. 1. Nonpolar gases. *J. Chem. Phys.* **22**, 1420–1426 (1954).
 230. Hibbs, R. E. & Gouaux, E. Principles of activation and permeation in an anion-selective Cys-loop receptor. *Nature* **474**, 54–60 (2011).
 231. Miller, P. S. & Aricescu, A. R. Crystal structure of a human GABAA receptor. *Nature* **512**, 270–275 (2014).
 232. Westergard, T., Salari, R., Martin, J. V & Brannigan, G. Correction: Interactions of L-3,5,3'-Triiodothyronine, Allopregnanolone, and Ivermectin with the GABAA Receptor: Evidence for Overlapping Intersubunit Binding Modes. *PloS one* **10**,

- e0142514 (2015).
233. Woll, K. A. *et al.* Role for the Propofol Hydroxyl in Anesthetic Protein Target Molecular Recognition. *ACS Chem. Neurosci.* (2015). doi:10.1021/acscemneuro.5b00078
 234. Jo, S., Lim, J. B., Klauda, J. B. & Im, W. CHARMM-GUI Membrane Builder for Mixed Bilayers and Its Application to Yeast Membranes. *Biophys. J.* **97**, 50–58 (2009).
 235. Best, R. B., Mittal, J., Feig, M. & MacKerell, A. D. Inclusion of Many-Body Effects in the Additive CHARMM Protein CMAP Potential Results in Enhanced Cooperativity of α -Helix and β -Hairpin Formation. *Biophys. J.* **103**, 1045–1051 (2012).
 236. MacKerell, a D. *et al.* All-atom empirical potential for molecular modeling and dynamics studies of proteins. *J. Phys. Chem. B* **102**, 3586–616 (1998).
 237. Klauda, J. B. *et al.* Update of the CHARMM all-atom additive force field for lipids: Validation on six lipid types. *J. Phys. Chem. B* **114**, 7830–7843 (2010).
 238. Jorgensen, W. L., Chandrasekhar, J., Madura, J. D., Impey, R. W. & Klein, M. L. Comparison of simple potential functions for simulating liquid water. *J. Chem. Phys.* **79**, 926–935 (1983).
 239. Beglov, D. & ROUX, B. Finite representation of an infinite bulk system: Solvent boundary potential for computer simulations. *J. Chem. Phys.* **100**, 9050–9063 (1994).
 240. LeBard, D. N., Hénin, J., Eckenhoff, R. G., Klein, M. L. & Brannigan, G. General Anesthetics Predicted to Block the GLIC Pore with Micromolar Affinity. *PLoS Comput. Biol.* **8**, e1002532 (2012).
 241. Phillips, J. C. *et al.* Scalable molecular dynamics with NAMD. *J. Comput. Chem.* **26**, 1781–1802 (2005).
 242. Gilson, M. K., Given, J. A., Bush, B. L. & McCammon, J. A. The statistical-thermodynamic basis for computation of binding affinities: a critical review. *Biophys. J.* **72**, 1047–1069 (1997).
 243. Woo, H.-J. & Roux, B. Calculation of absolute protein-ligand binding free energy from computer simulations. *Proc. Natl. Acad. Sci. U. S. A.* **102**, 6825–6830 (2005).